Engineering layer-by-layer nanoparticles for the targeted delivery of therapeutics to ovarian cancer

By

Santiago Correa

B.S. Biomedical Engineering
Yale University, 2012

Submitted to the Department of Biological Engineering in partial fulfillment of the
requirements for the degree of

Doctor of Philosophy in Biological Engineering
at the
MASSACHUSETTS INSTITUTE OF TECHNOLOGY

September 2018

Signature of author:.... **Signature redacted** ....

Santiago Correa
Department of Biological Engineering
August 14, 2018

Signature redacted

Certified by:..........

Paula T. Hammond
David H. Koch Professor of Engineering
Department Head of Chemical Engineering
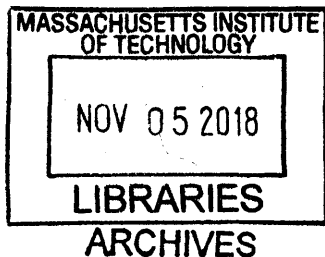Thesis Supervisor

Signature redacted

Accepted by:..................

Forest White
Professor of Biological Engineering
Graduate Program Chair

1

Certified by: ....

Signature redacted

Darrell J. Irvine
Professor of Materials Science & Engineering
Graduate Committee Chair

Signature redacted

Certified by: ....

K. Dane Wittrup
Carbon P. Dubbs Professor of Chemical Engineering & Biological Engineering
Co-advisor

Signature redacted

Certified by: ....

Sangeeta N. Bhatia
John J. and Dorothy Wilson Professor of Health Sciences and Technology and
of Electrical Engineering and Computer Science

2

Engineering layer-by-layer nanoparticles for the targeted delivery of therapeutics to ovarian cancer

By

Santiago Correa

B.S. Biomedical Engineering
Yale University, 2012

ABSTRACT

Survival rates for ovarian cancer haven't meaningfully improved in thirty years. Ovarian cancer is particularly difficult to treat because it is usually discovered after it has metastasized and it quickly develops resistance to the few drugs that are initially effective at controlling it. Nanomedicine has the potential to change the paradigm for ovarian cancer treatment by delivering complex combinations of conventional drugs plus next-generation therapies like small interfering RNA (siRNA) and immunotherapy. However, nanoparticles must be tailored to the particular drug-delivery challenges and opportunities posed by ovarian cancer. In this thesis, we designed layer-by-layer (LbL) nanoparticles (NPs) to target ovarian cancer using library-based approaches. Using this approach, we identified promising formulations for developing an advanced nanotheranostic that both treats and detects ovarian cancer. In order to develop LbL NPs for treating ovarian cancer, we identified and overcame process engineering and fundamental materials challenges, thereby improving synthesis robustness, throughput and scale. Chapter 2 describes how modern tangential flow filtration significantly improves throughput and scalability in colloidal LbL assembly. Chapter 3 implements this improved synthetic approach to generate a small library of LbL NPs that screen for tumor-targeting properties on ovarian cancer cells, both in vitro and in vivo. Our results demonstrate that ovarian cancer cells have a high affinity to carboxylated LbL NPs, and we report several tumor-targeting formulations with distinct subcellular trafficking patterns. Chapter 4 explores the role of salt in LbL colloidal assembly, and we develop strategies for robustly synthesizing LbL-modified liposomes with high loading of siRNA. Chapter 5 advances a promising formulation identified by our surface chemistry screen, which we developed into an advanced nanotheranostic device that delivers siRNA and mediates urinary-based tumor detection. Future work that continues to improve the synthesis of LbL NPs will be essential to generate larger and more ambitious LbL NP libraries. In turn, these libraries will facilitate systematic studies that further tailor the LbL platform to specific diseases and biomedical applications.

Thesis Supervisor: Paula T. Hammond

Title: David H. Koch Professor of Engineering and Department Head of Chemical Engineering

Acknowledgements

Completing a PhD is no small feat, as anyone who has survived one will gladly tell you. Graduate school is somehow amazing, frustrating, exhilarating, painful, and yet affirming all at once. It's a tumultuous time of self-discovery and character-building, and without all the incredible people in my life I don't think I would have been able to accomplish this. Getting to this point requires a lot of behind-the-scenes actors to mentor, support and cultivate you during the good times and the bad times. It may take a village to raise a child, but it may take something more like an army to raise a PhD.

First, I have to acknowledge the people who convinced me that research and the scientific endeavor were ridiculously cool. (Cool enough to spend the rest of my life doing, at least.) My undergraduate research advisor, Themis Kyriakides, gave me the opportunity to learn what it was like to do research. Themis put me to work with his postdoc Andrew Sawyer, who showed me what it was like to try and solve a problem using approaches nobody had ever tried before. I was also incredibly lucky to learn from one of the most talented scientists I have ever met, Susan MacLauchlan, who as a graduate student in her last two years still offered me her wisdom and experience, and no small amount of patience. Susan, having now lived out these last two years of grad school I am so impressed and grateful that you were able to be such a wonderful mentor to me during that time. Outside of lab, Dr. Jay Humphrey instilled in me a deep appreciation for the process of science and the evolution of our field.

At MIT, I have to thank first and foremost my advisor Paula Hammond, who I think must be a superhuman composed of boundless kindness, patience and positive energy. Paula, I could not have asked for a more wonderful guide for this process. You allowed me to explore and build and tinker my way to a thesis that neither of us could have envisioned at the start. And you helped me make it through the hard times, times where I thought things were never going to work out, and times of terrible personal tribulation. Your ability to face every challenge with a smile will always motivate me to keep going. I'll never be able to thank you enough for everything you've given me.

I was very lucky to have Sangeeta Bhatia, Darrell Irvine and Dane Wittrup as members of my thesis committee. Being able to get feedback and advice from this group of science rock-stars was one of the best things about graduate school. Thank you all so much for the time you put into helping me, and for all the help you gave me as I began charting my future career paths.

You learn so much in graduate school from the senior students and postdocs that are there when you're first getting started. Stephen Morton, one of the most delightful people I've ever worked with, helped me understand the Hammond Lab culture. He also showed me that it's possible to have a life while doing research. Stephen, thank you so much for your optimism, advice, and generosity with your time. Even after graduating, Stephen made time to answer questions and give advice on moving forward in my career as a scientist. For that, I will always be grateful.

I was extremely fortunate to be surrounded by excellent postdocs from the start in the Hammond Lab. I'm incredibly grateful to Kevin Shopsowitz, who introduced me to the wonders of Canada (and particularly its music festivals) as well as the world of R programming. Kevin would always help me with my projects, even as it diverged from his own. He was instrumental as I explored novel ways to synthesize LbL nanoparticles, and a constant source of encouragement. I also must extend a heartfelt thanks to Ki Young Choi, the formidable postdoc who helped us to tame

4

the beast that is hyaluronic acid, and an all-around great guy who looks out for his friends. Mohi Quadir, your boundless positivity rivals that of Paula's! Thank you so much for listening to all my crazy chemistry ideas and helping me do the feasible ones. Erik Christopher Dreaden has been one of my most formative mentors in many respects, a model from everything from research and experimental design to professionalism and doggedly pursuing your goals. Erik, thank you so much for your constant, patient guidance throughout the years – I will never forget it.

To the later crop of folks in the Hammond Lab, thank you all for making the lab a fun place to be. Brett Geiger, my conspirator in all things coffee-related, thank you for upholding a high standard for research and just being a great person to have a conversation with. I'm so excited to see what you do next, because I know it will be magnificent. To Tony Barbario, it was such a privilege to introduce you to nanotechnology and to see you grow into the researcher you are today. You always make the lab a more fun place to be. Sheryl Wang, running into you always brightened my day. Thank you for being a wonderful, selfless person and for humoring all my antics. Wade Wang, you are the chemist who holds this group together, and yet you're so humble and down to earth and willing to engage with anyone about anything. Working with you has been a joy. Elad Deiss-Yehiely, it's been such a pleasure to work with you through your first year. Your positivity and work ethic are inspiring, and I wish you the very best on your PhD journey. Joelle and Sean – we haven't had the chance to work together for long, but I'm so grateful for the time that we have spent together. Xiuyun Hou, thank you so much for bringing structure and order to our lab when I needed it the most. And thank you to the rest of the Hammond Lab, who each taught me important lessons in their own ways. And to my undergraduate students – Aria Shi, Benjamin Oberlton, Esperanza Hernandez and Mariam Ahmed – I extend the most heartfelt gratitude. Working with each of you has been a tremendous joy, and I am *so proud* to watch you grow into the people you are today.

I must make a special note for Natalie Boehnke, who I've been extraordinarily lucky to work with over the past year. Natalie, I only wish that we had had more time to further develop our collaboration, which has been one of the most rewarding and fruitful partnerships of my career. Your incomparable standards for scientific research and professionalism will take you incredibly far, even if you can't recognize a good gyro to save your life. I hope we will continue to fight and argue and become better scientists together for years to come.

I must thank the KI for all the resources it put at my fingertips these past six years. To Jaime Cheah and Christian Soule– I cannot express to you how grateful I am to have found you. You taught me the world of high throughput science, and turned your core facility into a haven for me when I needed it most. I know you've done the same for many others, and I want you to know how much it means to us. To Jeff Wyckoff and Eliza Vasile, thank you so much for your time and care in teaching me the art and science of microscopy. The most stunning images of this dissertation are due to your remarkable patience and encouragement. To Glenn Paradis, thank you for establishing such an incredible flow cytometry facility. Your core facility became as familiar to me as the Hammond Lab. To Kathy Cormier, thank you for your painstaking efforts to help me with the unconventional histology required for this dissertation. I learned so much about histology from you in a short time, and I'm incredibly grateful for it.

The structure, comprehensibility, and overall quality of this thesis is due in no small part to gifted writers who have helped me over the years. Raymond Malewitz, my undergraduate English professor, may have been one of my all-time most influential teachers. I was a terrible writer when I

5

began his class, and I felt like I would hopelessly remain so forever. Ray took such time and care with me that he somehow turned me into a pretty good writer, and for that I will be eternally grateful. Although we've never met, Jean Luc-Doumont and his teachings have been instrumental in my development as a scientific writer. Likewise, the work of Joseph M. Williams helped hone my writing into something a bit more elegant, for which I am very grateful. Maxine Jonas at MIT has also been a great asset and friend during the editing of this dissertation. (Shawn has pretty much copy-edited this whole thing, but more on him later.)

Outside of lab, I've been blessed with wonderful friends who saw me through everything life threw at me these past six years. Mark Guttag, Brittany Thomas, Katerina Mantzavinou, Raj Banerjee, Ari Stern, Holly Tarnower, Annie Kozakiewicz, Kunal Bhutani and Marianna Sofman – thank you for always being there when I needed you most. Thank you especially for the good times we had together — I'll always cherish those memories.

I have been inexplicably lucky to count my roommates among my best friends. Living the past five years in what can only be described as a grad student commune has been a constant source of stability and inspiration. It's been such a pleasure and a joy to live with some of the most talented and brilliant scientists I have ever met! So, to Kelly Moynihan, Ryan Truby, Griffin Clausen, Frances Liu, Khoi Nguyen and Claire Duvallet – thank you all so much for sharing your lives with me. Even though we won't live together for now — although I'm open to living in a giant communal compound in the future — I know we'll continue to strengthen this friendship for the rest of our lives. To me, you are all family.

To Shawn Musgrave, my wonderful, brilliant, and devilishly handsome partner and love-of-my-life – what can I say? To you I owe more gratitude than to anyone else. You've been my foundation since pretty much the first few weeks I started living here in Boston. And let's be honest, I'm pretty sure you're the only reason I survived the past year. I'm eager to be your foundation on our next great adventure, so I can start paying back your limitless patience and willingness to help me on everything from coding to writing to preparing oral presentations. Seriously, he did a lot of coding for me. A *lot*.

Finally, but certainly not least, I must recognize my family who made all this possible. The incredible love and support I had growing up planted so many seeds for what I am today. I want to thank my loving (and much older) siblings Catalina and David Correa. Thank you guys, for taking care of me and looking after me for my entire life. To my mother, Maria, I want to express special gratitude for her endless love and support. My mother has always helped me reach my goals, no matter what they were. She taught me to look at the world through the lens of aestheticism and to value the role of art in everyday life. Thank you, Mom, I love you.

Finally, I dedicate this thesis to my late father, Jorge. I am so unbelievably lucky to have had my father's life and guidance to help me become the person I am today. He always led by example, and his tireless work ethic, his uncompromising standards of ethics and honesty, and his infinite capacity to help others in need will always be in my heart. During his battle with cancer, his optimism kept us all going. Whenever we asked him how he felt, he always replied with his favorite saying: "Mejor que ayer, menos bien que mañana" — "Better than yesterday, not as good as tomorrow." Dad, I will always remember your greatest lesson – to work hard, with honesty and humility, and everything will work out in the end. Thank you Dad, I love you.

Table of Contents

Chapter 1. Introduction

This chapter is in part adapted from:
Correa, S.; Dreaden, E. C.; Gu, L.; Hammond, P. T., Engineering nanolayered particles for modular drug delivery. *J Control Release* **2016**, *240*, 364-386.

The National Cancer Act of 1971 marked the beginning of a concerted effort by American scientists and engineers to develop a cure for cancer. As we approach fifty years of America's war on cancer, significant challenges remain to be conquered even as we learn more about this formidable foe. We now properly recognize that cancer is a multi-faceted disease with tremendous heterogeneity that complicates the search for curative treatments[1-2]. Focus has shifted away from a universal cure and instead towards personalized treatment[3-8]. This strategy is enabled by powerful - but highly specific - new technologies like monoclonal antibodies[9], small molecule inhibitors[10] and genetically-modified immune cells[11] that have begun to be deployed to the front lines.

Nanotechnology is a major advancement in improving the sophistication of the anti-cancer arsenal[12]. Like a battleship, nanoparticles ferry potent drugs and therapeutics directly to enemy territory. Therapeutic payloads can be encapsulated within nanoparticle drug delivery vehicles, or nanocarriers, which in turn help to navigate those payloads through the body. The nanocarrier protects its payload from premature release into healthy tissue, where the payload can cause toxic side effects or degrade before reaching the target. By harnessing emerging biological and chemical engineering approaches, nanocarriers can mediate complex interactions with biological barriers – avoiding immune recognition clearance, negotiating passage through endothelial barriers, and finally docking and entering cancer cells to unleash their payloads.

The potential for nanoparticle-based medicine, or nanomedicine, in the clinic is significant. Major advances have already been made in improving the safety of encapsulated drugs[13]. And recent efforts showed that nanocarriers that deliver combination chemotherapy can achieve superior results over free drugs alone[14]. The potential of nanomedicine is now being aimed at enduring challenges such as glioblastoma, pancreatic and ovarian cancer. This thesis focuses on the development of nanotherapeutics for the treatment of ovarian cancer, where survival rates haven't improved in over thirty years.

Introduction

The main target, high-grade serous ovarian cancer (HGSOC), accounts for 70% of all epithelial ovarian cancers and kills roughly two-thirds of women who develop ovarian cancer[15-17]. Drug resistance is the modus operandi of this disease, because while up to 85% of patients respond favorably to frontline platinum-based therapies like cisplatin, this initial response is only a short reprieve for the majority of patients. Within a year, roughly 75% of HGSOCs recur with a platinum-resistant phenotype that renders chemotherapy ineffective[18-19]. If nanomedicines can be engineered to deliver cisplatin alongside next-generation therapeutics like small interfering RNA (siRNA) or small molecule inhibitors that specifically disable key biological pathways that mediate resistance, then perhaps meaningful improvements can be made in treating ovarian cancer. Because siRNA can target genes that are otherwise undruggable, it is a particularly promising approach towards shutting down mechanisms of resistance. And because of their relative fragility and inability to cross cellular membranes, siRNA treatments require a nanoparticle delivery vehicle in order to be used effectively.

This dissertation describes the systematic development of layer-by-layer (LbL) nanoparticles optimized to specifically target therapeutics and diagnostics to HGSOC. This strategy expands on traditional nanoparticle formulations of small molecule drugs by utilizing the LbL technique to add further functionality to liposomal drug carriers, namely siRNA delivery capabilities and tumor-targeting properties. Chapter 2 documents innovation in the synthesis and preparation of LbL nanoparticles that provided the necessary throughput, scalability, and yield needed to carry out the studies described in Chapters 3. This improvement in throughput led to the development of a small library of LbL nanoparticles that facilitated a systematic study of the role of surface chemistry in mediating specific interactions with ovarian cancer cells both in vitro and in vivo, as described in Chapter 3. The identification of tumor-targeting LbL films in Chapter 3 and the improvements in siRNA encapsulation in Chapter 4 lay the groundwork for Chapter 5, which documents the development of a theranostic LbL nanoparticle that delivers therapeutic siRNA while simultaneously providing a urinary biomarker diagnostic utility. Together, this work establishes a basis for the fabrication and development of a number of therapeutic and diagnostic nanoparticles for interventions in ovarian cancer.

This work rests squarely on decades of foundational materials, biological, and chemical research that is discussed at length in the following sections. Section 1.1 briefly reviews the impact and

role of nanomedicine in medical oncology, as well as its current shortcomings and path forward. Section 1.2 discusses the fundamentals of the layer-by-layer method and its advantages for nanomedicine. Sections 1.3.1 and 1.3.2 offer a more comprehensive review of specific facets of LbL technology that motivate Chapter 3. Likewise, Sections 1.3.3 and 1.3.4 are the foundation for Chapter 5. Section 1.4, which motivates the work described in Chapter 2 and Chapter 4, discusses potential obstacles for clinical translation and offers logistical insight into commercialization of this technology.

1.1. Nanomedicine and the era of targeted drug delivery

Until recently, medicine has largely consisted of enteral (absorption via the gastrointestinal tract, e.g., oral or sublingual dosing) and parenteral (not absorbed via the GI tract, e.g., intravenous or intramuscular injection) administration of free drugs. Clinicians optimize these administration methods to carefully balance the pharmacokinetics of a drug to achieve a therapeutic concentration while minimizing toxic side effects, a range termed the therapeutic window. This approach has yielded successful pharmaceuticals for managing a myriad of chronic health issues ranging from epilepsy to heart disease. However, within the realm of medical oncology the balancing act becomes untenable due to the very nature of chemotherapy – drugs used precisely for their toxicity to proliferating cells. In this scenario, clinicians must moderate the dosage of chemotherapy to limit severe side effects, such as thrombocytopenia, neutropenia, anemia, neurotoxicity, nephrotoxicity, cardiotoxicity, and severe digestive side effects. Administering chemotherapeutic regimens at tolerable dosages provides limited anticancer activity and ample opportunity for cancer to adapt and evolve new resistance mechanisms. Sadly, the cancer adapts while our healthy tissues cannot, eventually closing the therapeutic window and rendering the drugs useless.

Chemotherapy suffers from an extremely tight therapeutic window because traditional drug administration leads to comparable (and sometimes greater) concentrations of the drug in off-target tissues. This is an inevitable consequence of the delivery of small molecules, which eventually find their way to the blood compartment and are spread efficiently throughout the body. Fortunately, this paradigm has been disrupted by the development of nanoscale drug-delivery vehicles that can help to steer therapeutics towards target tissues, thereby limiting side effects. With nanotechnology, therapeutics are encapsulated within delivery vehicles ranging from 10-200 nanometers, roughly the scale of a virus. Like viruses, these carriers navigate the body in a unique, way – their large size, relative to their cargo, prevents them from escaping the bloodstream through capillary beds or through the kidneys. In healthy individuals, nanocarriers are eventually removed from circulation through the action of the mononuclear phagocytic system (MPS)[a], composed largely of professional phagocytic cells of the liver and the spleen. However, in organisms bearing tumors, a phenomenon known as the enhanced permeability and retention (EPR) effect leads to leaky vasculature and sluggish lymphatic drainage within the tumor that allows nanoparticles to perfuse

---

a Also known as the reticuloendothelial system, or RES.

13

and reside within neoplastic tissue[b]. With the ability to preferentially accumulate within tumor tissue, nanotherapeutics have the potential to significantly contribute towards solving the drug delivery problem inherent to chemotherapy.

In the 1990s, the chemotherapeutic doxorubicin was the first drug to benefit from encapsulation into a nanocarrier known as Doxil®[20]. Doxil is a liposomal formulation decorated with the polymer poly(ethylene glycol) (PEG), which is actively loaded with doxorubicin via a pH gradient method to achieve high (ca. 10 weight percent) loading. The PEG brush provides a very hydrophilic surface that helps prevent protein adsorption and clearance of the nanoparticle via the MPS, and thereby significantly extends the circulation time of the nanoparticle. Doxil® is just as effective as doxorubicin in treating cancer, but significantly reduces risk of a fatal side effect of doxorubicin – cardiomyopathy[13]. Interestingly, Doxil® presented a new dose-limiting toxicity, a rash of the hands and feet termed palmar-plantar erythrodysthesias. However, a non-PEGylated liposomal formulation approved in the European Union avoids this side effect without impacting effectiveness and still reduces overall cardiotoxicity[21].

Subsequent work aimed to reformulate a variety of chemotherapeutics into nanotherapeutics with reduced toxicity, and with the hope of improved efficacy. Because nanocarriers have the potential to preferentially increase drug concentrations in neoplastic tissues, there is the possibility that much higher doses can be achieved than could be possible with free-drug administration. This would naturally translate towards greater anti-cancer effects and improved therapeutic efficacy. Work in the EU developing PEGylated liposomal cisplatin (Lipoplatin®) presented results that supported this concept of improved accumulation in humans. Notably, Boulikas et al. reported a 10-200 fold increase in platinum concentration in tumor tissue relative to surrounding healthy tissue[22]. But in spite of this preferential accumulation within tumors, phase II and III clinical trials of Lipoplatin did not find increased efficacy over free cisplatin, though the improvement in safety

---

b Initially, it was thought that the EPR effect was a universal cancer trait, and would be sufficient for nanocarriers to accumulate to a great extent in malignant tissues. We now know that the EPR effect is highly heterogenous, varying between cancer types and even patients bearing the same disease. The EPR effect also appears to be exaggerated in the most common animal models for cancer, exacerbating the field's reliance on passive targeting. Fortunately, new research that incorporates active transport through endothelial barriers is ongoing and leading to promising new strategies to improve nanoparticle accumulation in tumor tissue.

was dramatic[23-24]. Liposomal cisplatin significantly reduced nephrotoxicity , neuropathy, nausea and vomiting in clinical trials relative to free cisplatin, both in single-drug regimens and combination therapy[22-23].

This overall trend has continued for monotherapy nanoparticles, wherein nanoparticle encapsulation of single agents have generally improved the safety profile of the cargo drug but not the therapeutic efficacy[25-30]. This may be due in part to an overreliance on passive targeting mechanisms such as the EPR effect, or it may be a limitation of the drug itself. In the case of the latter, the field of nanomedicine may be poised to benefit from a renaissance similar to that of chemotherapy in the 1960s, when the first combined chemotherapy regimens came about. These regimens combined some of the most potent chemotherapeutic agents at the time (vincristine, amethopterin, 6-mercapto-purine, and prednisone in childhood acute leukemia and nitrogen mustard, vincristine, and methotrexate or procarbazine, and prednisone in adult Hodgkin's Disease). Both of these treatment plans showed immense benefits, improving the remission rate for Hodgkin's disease from less than 5% to nearly 80%[31]. Remarkably, 60% of patients never relapsed over the course of the 40-year study. The impressive clinical impact of these therapies helped to eliminate the negative view of chemotherapy treatments and combination therapies in oncology at the time. Ultimately, these breakthroughs allowed for new research in rational combination treatments using the extensive catalog of anti-cancer therapies already in the clinic[32].

Since the 1960s there have been many new combinations successfully tested in the clinic showing superior outcomes compared to standard treatment[33-37]. In a recent example, Conroy et al. reported the effective use of a combination therapy including oxaliplatin, irinotecan, and fluorouracil-leucovorin (FOLFIRINOX) against single agent gemcitabine for the treatment of metastatic pancreatic cancer. This regimen presented the first major improvement in this disease in decades, extending median overall survival to 11.1 months compared to 6.8 months seen with gemcitabine monotherapy[34-35]. Similarly, Grothey et al. showed that FOLFIROINOX is more effective than dual combinations of Fluorouracil-leucovorin with a single agent across multiple clinical trials in colorectal cancer, providing a 3.5 month increase in median overall survival when used as a first-line treatment[36]. Despite the significant benefits in efficacy, FOLFIRINOX also showed much higher occurrence of adverse events when compared to standard treatment, limiting its use to patients with good performance status[34-35]. The FOLFIRINOX combination treatment is an

excellent example of the possibilities for these combination therapies in the clinic, and how their implementation can be limited by toxicity.

Nanomedicine provides significant advantages for the delivery of potent combination chemotherapy that extends beyond the reduction of toxic side effects. While multi-drug nanoparticles likely will provide significant safety benefits, they will also provide unparalleled control over the presentation of the combination therapy to cancer cells. Free-drug combination therapies are challenged by the disparate pharmacokinetic and pharmacodynamics profiles of the individual drugs, which often possess wildly different physiochemical properties. Smorenburg et al. illustrate this point with a comprehensive study of multiple antimetabolite/taxane combination therapies, showing that drug combinations must be considered in terms of their activity and pharmacokinetics to avoid toxicity and achieve the highest efficacy. This work further showed that whether or not a treatment is effective can be strongly schedule dependent, with improper scheduling leading to an antagonistic effect in some cases such as 5-fluorouracil followed by paclitaxel[38].

On the other hand, nanocarriers can be engineered to co-encapsulate precise ratios of different drugs to provide a dual benefit. First, co-encapsulation simplifies the scheduling issue of administering drugs with different pharmacokinetics and biodistributions by forcing the drugs to share the pharmacokinetics of the carrier[39]. Second, the ability to encapsulate exact ratios of drugs allow researchers to guarantee that cancer cells that interact with the nanomedicine will be exposed to a synergistic drug ratio. This approach has met with great success with the FDA approval of the liposomal co-encapsulation of cytarabine and daunorubicin (Vyxeos®). Vyxeos demonstrated highly successful results in a recent phase III clinical trial, enhancing overall survival in high-risk acute myeloid leukemia patients to 9.56 months over the free-drug combination regimen which had an overall survival of only 5.95 months[14]. The suspected mechanism behind the success of Vyxeos is the precise 5:1 molar ratio between cytarabine and daunorubicin, supporting the notion that nanocarriers can be used to deliver regimens in a tightly controlled stoichiometry to improve efficacy over free-drug administration. The success of this approach should highlight the value of revisiting currently approved drugs to build new and improved treatments.

Multi-drug nanocarriers may enhance the efficacy of their cargo, but the benefits of improving the safety profile of combination therapies cannot be understated. This is because nanoparticle

formulations of a single FDA-approved drug already possess a somewhat reasonable therapeutic window, otherwise they wouldn't have any clinical utility. On the other hand, there are numerous combination therapies (composed of drugs that are individually FDA-approved) that have shown improved efficacy but unacceptable toxicity. These combination therapies represent lost potential in the clinic, a regimen that could be effective but lacks a practical therapeutic window. In this way, previously undeliverable regimens may become viable as a nanoparticle formulation that adequately manages toxic side effects. The clinical impact of mitigating toxicity using multi-drug nanocarriers may be significant, because combinations of free chemotherapy drugs often show synergistic toxicities and require careful management[40-43]. Recent efforts to develop combination regimens that involve next-generation small molecule inhibitors are also facing major obstacles with regards to unexpected toxicity[44-47]. For example, Liu et al. recently showed that combining small molecule inhibitors of PARP and VEGF led to dramatically increased toxicity, with 70% of combination therapy patients experiencing grade 3 or higher adverse events compared to just 10% in PARP inhibitor monotherapy[47]. However, the combination therapy also increased progression free survival by 8.7 months over monotherapy. Results such as these suggest that promising combination therapies are being stymied by toxicity issues. Fortunately, nanoparticles may offer a means to revisit promising combination therapies that are otherwise too toxic to administer as free drugs.

Nanomedicine may also hold the key to delivering next-generation therapeutics that have struggled to be implemented in the clinic – such as gene therapies and immuno-modulating cytokines[48-50] [51-52]. Gene therapy in particular has promising applications for addressing genetic disease, cancer, and even for the development of vaccines. These approaches offer new avenues for anticancer therapies, where the ability to silence or restore specific genes could provide ways to prevent or reverse drug resistance mechanisms in neoplastic tissue. But gene delivery is highly challenging due to the ubiquitous presence of nucleases in the body and the inability for nucleic acids to penetrate cell membranes. Nanoparticles provide the means to protect encapsulated nucleic acids from premature degradation while simultaneously guiding them into target cells to mediate transfection, with numerous encouraging examples reported in the literature[53-60]. Promisingly, several nanoparticle formulations for siRNA are now in clinical trials[61-62].

The rise of nanoscale drug carriers is creating new opportunities in medicine, and the current

achievements in the field of nanomedicine have highlighted both its potential and enduring challenges. Clear progress has been made in improving the safety profiles of encapsulated drugs, but significant work remains in order to improve the efficacy of nanoparticle formulations beyond that of the free-drug. Using nanotechnology to deliver combination therapies may provide major improvements in efficacy, especially as nanoparticles begin to leverage potent therapeutics such as siRNA alongside traditional chemotherapeutics. But simultaneous efforts must be made to systematically engineer nanocarriers that can actively bypass the biological barriers that limit accumulation in tumors and other tissues of interest. In the following sections, we will explore how the layer-by-layer platform offers the means to actively explore all of these avenues towards improved nanomedicines.

1.2. Modular nanotechnology through layer-by-layer self-assembly

In this Section, we will discuss the application of Layer-by-layer (LbL) nanotechnology towards anti-cancer drug delivery. We will focus on the numerous distinct and novel formulations that have been developed to tackle a variety of biomedical challenges to demonstrate the variety of directions the field has moved towards. But we also aim to show that considerable parameter space available to LbL nanoparticles has led to a dispersion of efforts in the field, which makes it difficult to connect the lessons from the different studies. Consequently, it is challenging to develop a thorough understanding of the importance of different parameters in LbL nanoparticles and how they impact drug delivery. So while these studies form an important basis for the field, the next steps to advance LbL technology will benefit greatly from systematic studies that begin to define
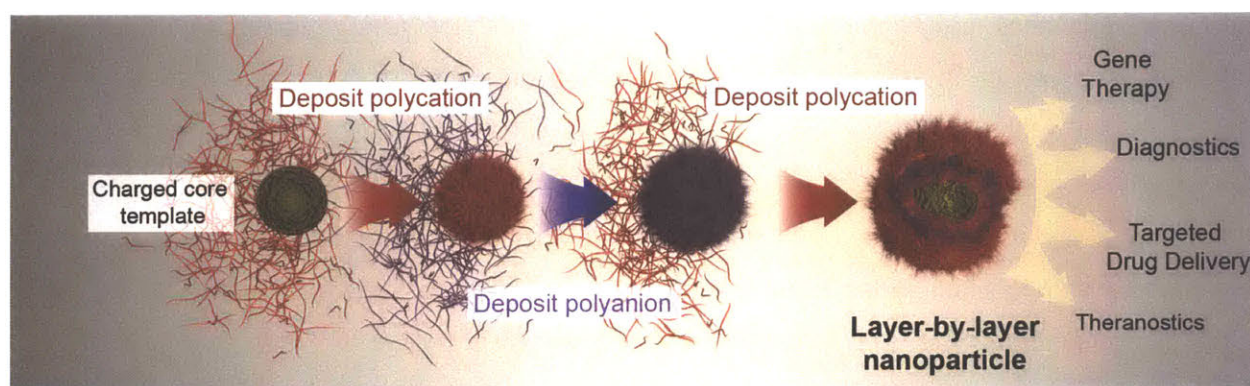
Figure 1.1. The layer-by-layer self-assembly technique can be applied to colloidal templates to build hierarchically organized nanoparticle composites. Generally mediated via electrostatic interactions, the process involves the sequential deposition of polyelectrolytes, or other charged macromolecules, onto a charged colloid. The resulting nanomaterials can contain therapeutics and stimuli-responsive elements that provide biomedical functionalities ranging from targeted drug delivery to diagnostics.

how important parameters like surface chemistry, polyelectrolyte identity, substrate and synthetic conditions impact critical nanoparticle functions like tumor targeting, transfection efficiency, biodistribution and industrial scalability. This section therefore surveys the state of the field, and sets up the reader for a better understanding of the systematic studies discussed in later chapters.

LbL self-assembly of nanoparticles is an emerging and powerful method to develop multifunctional and tissue-responsive nanomedicines for a broad range of diseases. This unique assembly technique is able to confer a high degree of modularity, versatility, and compositional heterogeneity to nanoparticles via the sequential deposition of alternately charged polyelectrolytes onto a colloidal template **(Figure 1.1)**. LbL assembly can provide added functionality by directly incorporating a

range of functional materials within the multilayers including nucleic acids, synthetic polymers, polypeptides, polysaccharides, and functional proteins. These materials can be used to generate heterogeneous, but hierarchically ordered, thin films on an extensive range of both traditional and novel nanoscale colloidal templates, providing the opportunity to engineer precise nanocomposites capable of performing the numerous tasks required for systemic drug delivery.

The LbL technique, beginning with the fundamental concept of alternating electrostatic assembly, was first described by Iler in 1966[63-69]. Since then, LbL assembly has become a well-established technique for the solution-phase synthesis of hierarchical and multifunctional nanoscale therapeutics[70-72]. LbL nanoparticles can possess a range of desirable properties for drug and gene delivery due to the versatility granted by the technique. In its most frequently employed form, LbL assembly is driven by the electrostatic interaction between oppositely charged polyelectrolytes and a charged substrate. Possible substrates include colloids such as gold, polymer, silica, and liposomal nanoparticles, amongst others[73-78]. Along with the flexibility in the choice of a core substrate, any polyelectrolyte with a multivalent charge can be incorporated into an LbL construct, including native polysaccharides, nucleic acids, linear polypeptides, and synthetic polymers[73, 79-81]. In addition to electrostatics, LbL assembly can be driven by a multitude of intermolecular interactions that include hydrogen bonding, covalent bonding, and biologically specific interactions[82]. More recently, research into LbL nanomaterials has yielded important developments for a variety of fields including chemical sensing, catalysis, energy storage, optics, and drug delivery[78, 83-87].

There are several advantages that LbL nanoparticles provide in developing sophisticated drug delivery vehicles. First, deposition of polyelectrolytes of alternating charge generates an ionically crosslinked thin film that acts as a gate for regulating drug release from the core nanoparticle template. This film can also be engineered to possess a characteristic isoelectric point that responds to pH at the target tissue, such as the acidic tumor microenvironment or the interior of a lysosome, to accelerate drug release or to mediate other critical functionalities for successful drug delivery. Extensive discussion of this capability is provided in Section 1.3.2.

Another advantage is that LbL nanoparticles can incorporate diverse materials into the multilayered film, including charged polypeptides, polysaccharides, synthetic polymers and nucleic acids. Because the incorporation of these materials occurs under aqueous conditions, a number

of sensitive biologic drugs like peptides, siRNA, mRNA and plasmid DNA can be readily incorporated into the film itself. This capability enables the intermediate LbL bilayers to serve not only as regulators of drug release, but as drug carriers that can contain high loads of drug – ranging from 10 to 20% by weight of the LbL film, to potentially as high as 50% or more based on the assembly process, which enables one to approach near-stoichiometric amounts of material for charge compensation. These loadings contrast significantly with the more typical 1-3% weight loadings observed in many solid polymer films and coatings, and thus enables an ultrathin film coating that is only a few tens of nanometers thick to contain significant amounts of therapeutic wrapped around the nanoparticle core.

Finally, the outer bilayers of the nanoparticle system play a critical role in the interactions of the nanoparticle with cells, and ultimately in the routing of nanoparticles within the body. The layer-by-layer approach involves the adsorption of polyelectrolyte chains onto an oppositely charged polyion layer, and it is known that depending on the degree of ionization of the polyion adsorbed and the underlying polymer, one can achieve dense, brush-like layers that can present relatively high charge density. These dense, brush-like or loopy chain conformations can yield hydrated and highly charged particle systems that regulate protein opsonization and monocyte uptake in the bloodstream, providing key "stealth" properties for systemic delivery in the blood stream. Furthermore, the free functional groups on the polyelectrolyte outer layer provide opportunities for further chemical functionalization, and the attachment of ligands including small molecules, peptides, glycans, and antibodies, all of which may be used for molecular targeting of specific organs and cell types. Alternatively, the use of polycations as the final layer of a nanoparticle may be used to engage a number of non-specific mechanisms of cell uptake.

The parameter space available to LbL nanoparticles is large, as each element – the core and individual layers within the LbL film – can be swapped out for another similarly charged material. As a result, films can be developed with unique properties and then applied to disparate colloidal templates to study the role of size and shape of nanoparticles while maintaining the same surface chemistry[88]. Alternatively, elements of the film can be varied to study the role each constituent plays in the nanocomposite. Overall, the platform offers researchers the ability to systematically alter one component of a nanoparticle formulation to fully optimize it for a particular application. The ability to change both the core and the inner and outer layers of the multilayered system en-

21

ables incorporation of additional functionality such as imaging or light-activated therapies, which can enable the development of theranostic nanocarriers. The broad range of new therapies that can be introduced using this nanoparticle technology provides an exciting route to next-generation tumor targeting cancer therapies.

1.3. Developing cancer therapies using LbL nanotechnology

The following sections describe the engineering of LbL nanoparticle systems toward specific cancer therapies, including some of the *in vitro* research that forms the underpinnings of understanding of how these nanoparticle systems interact with cells. It will not attempt to cover the large body of work involving layer-by-layer hollow microcapsule systems, which are well captured elsewhere[89-96]. Instead, it will focus mainly on LbL formulations using nanoparticle cores within the range of 10 to 200 nm, typically thought to be relevant for targeted nanoparticles in systemic delivery applications. The work in LbL nanoparticles thus far will illustrate how this modular system can be adapted or utilized for systemic drug delivery of nanoparticles for therapeutic, diagnostic, and theranostic applications, as well as potential additional routes for targeted delivery. Finally, we investigate the translational potential of this technology, and advances toward bringing these highly promising nanoparticle systems to the clinic. This background will ultimately form the foundation from which the work described in this thesis emerges.

1.3.1. LbL films as biofunctional nanoparticle surfaces

The modular nature of LbL nanoparticles [97-106] allows their cellular and physiological interactions to be chemically tuned for a range of diagnostic and therapeutic applications. Following administration, these biological interactions occur first with the outermost layers of the particles; thus, rationally engineering the interactions of these terminal LbL layers (or the lack thereof) is of critical importance. In the following section, we review how the various physiochemical properties of LbL nanoparticles (e.g. size, charge, compressibility, etc.) dictate their interactions with cells in the body and, in Section 2.2, how these surface properties can be chemically modulated to direct outcomes and achieve targeting to specific tissues or cell types in vivo.

Size, surface charge, and structure

A key issue that may be considered in the design of LbL nanoparticle systems is the effect of an additive process on particle size. In applications where prolonged circulation is desired, for example in tissue-targeting or drug delivery, LbL nanoparticles should be somewhat larger than the renal clearance threshold (<6 nm), but smaller than 200-250 nm in hydrodynamic diameter

(HD) in order to avoid efficient splenic clearance. Particles are able to maintain longer plasma half-lives and more effectively accumulate in tumors when they are under 100 nm [107], which fits the NCI definition of a nanoparticle [108]. Once extravasated from circulation, optimal sizes can range widely depending on anatomical site and application, however smaller particles are often preferred in tumor-targeting applications where desmoplasia (stromal compaction) is often a significant barrier to efficient transport. Other important size-dependent barriers, reviewed elsewhere [109-111], include the blood-brain-barrier (ca.15 nm), the nuclear pore complex (ca. 20-40 nm), the lung periciliary layer (20-40 nm), and transmucosal mesh size (ca. 340 nm).

LbL assembly onto nanoparticles can be achieved using a range of approaches (refer to Section 1.4) with subsequent sizes largely dictated by the nanoparticle core itself and the thickness of the surrounding polymer layers. For centrifugal-based LbL colloidal assembly with polymers lacking significant secondary structure, individual layers typically add 4-5 nm to the total particle hydrodynamic diamter[105, 112-113]. Spray-based methods[114] often yield nominally thicker shell layers, adding 5-8 nm to particle diameter per adsorbed layer. Biopolymers such as hyaluronic acid (HA), which present complex secondary structure, can often adsorb with layer thicknesses [106, 115-116] many times greater than polyelectrolytes such as poly(L-lysine) (PLK) or dextran sulfate (DXS) [117-118]. Charge density on the initial particle core can further dictate subsequent layer thickness, with denser adsorbed layers required for efficient charge reversal. Thus, depending on the end-application, LbL systems with multiple layers can be utilized without compromising function. In applications such as imaging in which much smaller nanoparticles are coated, much can be achieved with just 2 to 4 layers in an LbL coating, as will be discussed in upcoming sections.

Surface charge is another key design parameter for LbL nanoparticles used in biomedical applications. As with other nanoscale diagnostics and therapeutics, positively charged constructs should be avoided due to attraction to the negatively charged luminal surface of blood vessels [119], the kidney globular basement membrane [120], and epithelial cell membrane surface [121], as well as their tendency for erythrolysis of sialic acid-rich red blood cell surfaces [122]. Electrostatically stabilized (polyanionic) LbL nanoparticles, while capable of relatively long circulation, can also interact with various extracellular matrix (ECM) components including collagen type I. Wilson et al.[123] for example, found that polyanion-terminated gold nanoparticles could reduce the lag (nucleation) phase of collagen self-assembly and increase the dynamic shear modulus of polymerized collagen gels **(Figure 1.2a)**. In contrast, polycation-terminated LbL nanoparticles had no effect on the mechanical properties of the collagen. Interestingly, both polyanion- and polycation-terminated
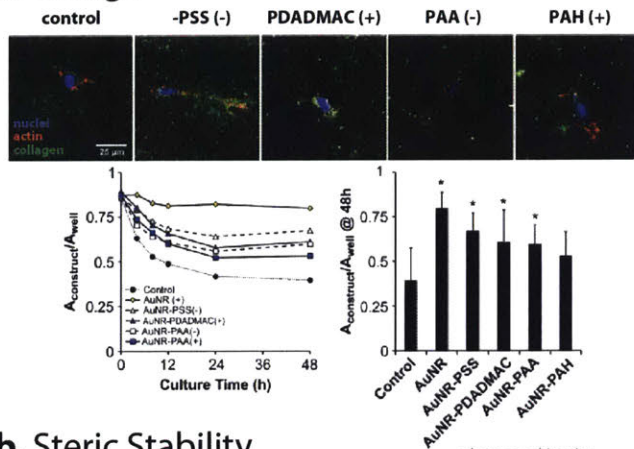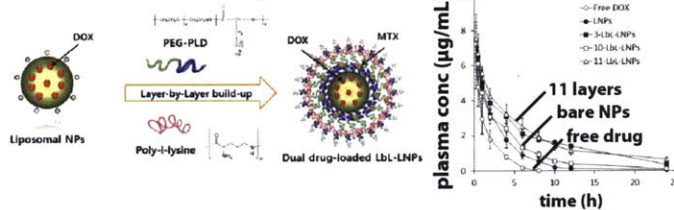
a. Charge

b. Steric Stability

Figure 1.2. Modular LbL nanoparticle architecture provide diverse biophysical interactions. a) Collagen interactions from LbL nanoparticles of varying charge (top) and particle-inhibited gel contraction by cardiac fibroblasts (bottom). b) Poly(ethylene glycol)-block-poly(L-aspartic acid) stabilized liposomal doxorubicin (left) and LbL stabilization-dependent circulation kinetics in Sprague Dawley rats. Reprinted with permission from (a) [123] and (b) [134]. Copyright (a) 2009 and (b) 2014 Elsevier.

nanoparticles inhibited gel contraction by cardiac fibroblasts, suggesting that these LbL nanoparticle architectures influence cell behavior via multiple mechanisms. As demonstrated above, the biophysical interactions of LbL nanoparticles are highly dependent on their physiochemical properties and while, size- and charge-dependent interactions are well-described in many cases, others such as shape [114, 124-126], surface topography (roughness) [127], and mechanical stiffness [128-130] - recently explored with micron and submicron LbL particles – have yet to be fully described with nanoscale LbL particles. Future research in these areas will no-doubt expand the diversity of potential biomedical applications utilizing these novel structures.

Chemically tailoring LbL films

Chemical modification of the final LbL nanoparticle can provide added control over important parameters including steric stability and introduce new functionalities like affinity-targeting. More specifically, steric stability – from both synthetic and native biopolymers – can greatly improve the in vivo stability of nanoparticles. This phenomena is attributed, in part, to decreased serum protein adsorption (i.e., protein corona formation[131-132]) and opsonin binding, the latter of which can contribute to efficient clearance by the mononuclear phagocyte system. For this reason, LbL nanoparticles allow the advantageous use of highly negatively charged polyelectrolytes as the final outer layer of nanoparticles designed for systemic delivery. A dense negative charge yields significant repulsion between the nanoparticle and many of the negatively charged serum proteins, as well as cells that the particle may encounter, which have net negative outer membranes due to the charged polysaccharides bound to most mammalian cells. Furthermore, polyanion

25

functional groups that introduce a number of bound water molecules at physiological conditions may provide additional energetic barriers that enable longer plasma half-lives. Antifouling bio-polymers such as polyanionic hyaluronic acid [106, 115-116] and alginate [113] for example, allow LbL nanoparticles to circulate for significantly longer residence times – in some cases as long as 24 to 28 hour elimination half-lives [104, 112] – than their non-sterically shielding anionic counterparts. The density of the macromolecular brushes generated on the nanoparticle surface is a function of the underlying charge of the positively charged layer as well as the charge density and size of the polyanion adsorbed as the final layer – both of these parameters are readily adapted with pH, ionic strength and choice of polyion in generating the LbL film. The resulting outer layer may in some cases present a much denser and therefore more effective brush layer than those generated using other means such as covalent chain grafting to particle surfaces. Because a number of native extracellular matrix molecules may be used in this process, it may also be possible to optimize these systems to achieve lowered recognition by the immune system or some form of self-recognition that avoids monocyte uptake.

Along with the use of intrinsically charged polyions, it is possible to incorporate neutral stabilizing polymer layers. Due to their intrinsic ability to block adsorption [133], such steric stabilizers are typically appended to already-adsorbed polymer layers in a "grafting-to" type fashion. As with other biomedical colloids, PEG is the most common steric polymer employed with LbL nanoparticles, however poly(2-ethyl-2-oxazoline) (PEO), poly(vinyl alcohol) (PVA), and other water-borne polymers provide opportunities for further research. In its simplest form, a neutral steric stabilizing layer can be achieved using a polyelectrolyte-containing block copolymer such as poly(ethylene glycol-b-L-aspartate)[134], many of which are commercially available.

Kim and coworkers[134] demonstrate the use of a PEG block copolymer to sterically stabilize LbL-functionalized liposomes, here, with the block copolymer incorporated as both the terminal and intermediate polyanion layers. Doxorubicin-containing cationic liposomes were layered with 5.5 bilayers of poly(ethylene glycol-b-L-aspartate) and PLK, resulting in a neutral (ca.-5 mV) PEG-stabilized nanoparticle. In this block copolymer multilayer format, layer thicknesses were relatively large, adding ca. 15 nm to particle diameter per adsorbed layer (**Figure 1.2b**). Interestingly, drug release kinetics were significantly slowed for nanoparticles of identical terminal composition but increased multilayer numbers; circulation half-lives in mice, however, were identical for composi-

tionally related LbL nanoparticles (ca. 5.8 h, first order).

Click-type and carbodiimide coupling chemistries are also highly amenable to the installation of steric polymers onto LbL nanoparticle surfaces. Polyelectrolytes containing biorthogonal azide and alkyne moieties, or transcyclooctene (TCO) and tetrazine groups, are also widely available or obtained in high yield and allow for the facile conjugation of end-functional linear polymers such as PEG-azide or PEG-tetrazine, respectively. Carbodiimide coupling is an attractive option for LbL nanoparticles terminated with weak polyelectrolytes such as polyacids and polyamines and allows for the addition of a wide variety of linear and/or branched stabilizers. For example, Shen and coworkers [135] used carbodiimide coupling to covalently conjugate PEG to the surfaces of PLGA submicron particles coated with PEI/PAA multilayers. The authors demonstrated significant reduction in the magnitude of anionic surface charge (ca. -37 to -12 mV), interestingly, in the absence of interparticle crosslinking as indicated by dynamic light scattering (DLS) measurements. Lastly, although less-explored with nanoscale LbL particles, surface stabilization can also be achieved via living polymerization (e.g. atom-transfer radical-polymerization, ATRP [130]) off of particles bearing surface-bound initiator groups, allowing for radially heterogenous multilayered coating with antifouling terminal groups such as hyaluronic acid [106, 116].

Another powerful aspect of LbL nanoparticle modularity is the ability to further decorate particle surfaces with affinity ligands that can bind or associate with a given cell type, organ, or tissue of interest. With LbL nanoparticles, this targeting can be directed towards surface proteins on diseased or peripheral cells and often initiates ATP-dependent cell uptake through various mechanisms including phagocytosis, caveolin- or clathrin-mediated endocytosis, micropinocytosis, and other pathways. Common LbL nanoparticle affinity ligands include small molecules [136-137], peptides [136], glycopolymers [138], aptamers [139-140], and antibodies [141]. For modifications with poorly water soluble targeting ligands such as folic acid, carboxamide coupling [142] is an attractive option for the amidation of polyacids that can proceed in both aqueous and methanol solvents. For example, we previously used carboxamide coupling to install hydroxyapatite-binding bisphosphonate alendronate ligands onto PAA which was used to terminally layer doxorubicin-containing LbL nanoparticles [143]. 143B osteosarcoma xenograft-bearing mice intravenously treated with the particles exhibited progressive disease from the untargeted constructs, but significant disease stabilization from the targeted nanoparticles, reflecting the altered biodistribution profiles of actively

27

targeted LbL nanoparticles. Lin and coworkers [136] have also explored the use of affinity targeting to develop an LbL nanoparticle-based magnetic resonance imaging (MRI) contrast agent based on Gd^{3+}-conjugated silica nanoparticles. By electrostatically adsorbing a cationic, integrin-binding K_7RDG peptide onto the PSS-terminal LbL nanoparticles, in vitro targeting and T1-weighted MRI contrast from HT-29 colon cancer cells was markedly improved. Boyer et al. [138] employed a related approach whereby a copolymer synthesized by reversible addition-fragmentation (RAFT) polymerization was side chain modified with glucose and galactose, the latter of which can specifically bind with hepatic galactose/N-acetylgalactosamine receptors. The particles underwent crosslinking in the presence of the glucose-binding lectin, concavalin A, and were competitively displaced by free sugar, demonstrating target-specific binding by the LbL nanoparticles.

Stimuli-responsive LbL films

The outer layers can serve as outstanding passive targeting agents; however, LbL systems can be tuned to be responsive to microenvironments that are medically relevant. In prior work [104, 111], we demonstrated a biotin-avidin conjugation approach to prepare pH-responsive multilayered nanoparticles via a biotinylated cationic terminal layer. Using neutravidin as an intermediate linker, iminobiotin-labeled PEG was installed on the outer particle surface, shielding an underlying cell-penetrating polycation surface that was revealed at hypoxic tumor pH conditions [106, 116]. While particles displaying both iminobiotin-PEG and pH-nonresponsive biotin-PEG freely circulated for > 24 h, only pH-sheddable LbL nanoparticles efficiently targeted breast tumor xenografts for extended periods in vivo, colocalizing with hypoxia inducible factor 1 α (HIF1α) and decreasing relative hepatic accumulation.

On the other hand, it is also possible to take advantage of the physicochemical nature of an LbL film to devise a bilayer of two weak polyelectrolytes (e.g. polyacid and polybase) that exhibit a shift in charge at a given pH. A pH responsive outer layer LbL film of (PLK/HA) is a strongly negatively charged particle at bloodstream pH that swells, increases in surface roughness, and loses cell-repulsive anionic surface charge at hypoxic tumor pH[106, 116], thus causing significant uptake in hypoxic tumor regions; the same HA terminated film also targets the CD44 receptor, which is overexpressed highly in many aggressive cancer types including ovarian and lung cancer, thus imparting multiple targeting mechanisms within a singular bilayer thin film.

Another means of enabling cell-responsive behavior is to utilize other aspects of the cellular microenvironment, such as the more highly reducing cytoplasmic environment. Yang et al. [144] have developed methods for the efficient cellular delivery of LbL nanoparticles by making use of a pH responsive, 'bioreducible' polymer layer consisting of a disulfide crosslinked low molecular weight BPEI obtained by reaction with dithiobis(succinimidyl propionate) (DTSSP, Lomat's reagent). The thiol-modified polyamine was used to condense siRNA and was subsequently shielded using a polycation-b-PEG copolymer containing poly(2-(2-aminoethyoxy)ethoxy) phosphazene) (PAEP). At pH 6.8, cell internalization and in vitro cell killing was augmented ca. 4- and 2.8-fold, respectively, compared with physiologic pH (7.4). In vivo, the pH-responsive LbL nanoparticles targeted subcutaneous tumor xenografts >2-fold more efficiently than non-pH responsive constructs, with tumor-specific mRNA silencing improved ca. 2.4-fold.

1.3.2. LbL films as regulators of drug release kinetics

While the outer layers of LbL-modified drug carriers can bestow favorable in vivo stability and active targeting properties, the rest of the film is capable of additional functionalities useful for drug delivery. In this section we address the ability to regulate the release of therapeutics encapsulated in the core template through the generation of an LbL membrane around the core, which acts as a nanoscale drug reservoir. This useful feature is highly tunable through the rational selection of LbL film constituents, which can work in concert to provide a desirable release profile for numerous applications ranging from cancer therapy to oral insulin administration. This section is organized by the identity of the core template for various LbL formulations, but it should be noted that any of the LbL films discussed below could be formed on any suitable template as needed.

LbL films as regulators of drug release

One of the great strengths of the LbL platform is its broad applicability towards modifying conventional nanoparticles that have already been extensively characterized. This includes important drug-carriers such as poly(lactide-co-glycolide) (PLGA) [135, 145-146], mesoporous silica [136, 147], and liposomal [76, 148] colloidal systems. Each of these vectors has attractive properties for drug delivery, but each also has weaknesses that have hindered their clinical translation. This section reviews

29

how recent work in the LbL community is addressing some of these weaknesses through further functionalizing these important drug-carriers with multifunctional LbL films.

LbL modification of PLGA cores

PLGA particles are well studied materials that can encapsulate a variety of cargo, including small molecule drugs, proteins and nucleic acids[145], commonly through emulsification techniques[149]. These templates benefit from LbL modification in several ways, the first being increased specific targeting and avoidance of MPS clearance, as discussed in *Section 1.3.1*. Another major benefit, and what will be focused on in this section, is greater control over drug release by minimizing the initial burst-release of cargo, as well as by extending the duration of release. For example, Venkatraman and coworkers[150] characterized the effects of LbL-modification on submicrometer sized PLGA particles, and found that LbL coatings of either PAH/PSS or PLK/DXS were able to suppress burst release of FITC-dextran (4 kDa) and extend its release over 4 days under physiological conditions in vitro **(Figure 1.3a-b)**. While both PAH/PSS and PLK/DXS films slowed release of the model drug in these systems, only PAH/PSS films benefited from increased layer depositions. This is likely due to differences in the binding affinity that holds these films together, and hydrophobicity of the polymer backbones involved, leading to a more swollen and permeable film in the case of PLK/DXS. Once crosslinks were introduced however, both films efficiently reduced burst release (ca. 3 fold) and extended the duration of release.

Morton at el.[113] described the in vitro and in vivo regulation of small molecule drug release from several LbL-modified PLGA nanoparticles. This work demonstrated that three different LbL formulations (PLGA-(PLK/DXS)$_3$, PLGA-([PLK/DXS]$_2$/PLK/Alginate), and PLGA-([PLK/DXS]$_2$/PLK/HA)) could reduce initial burst-release from 35% (uncoated PLGA) to less than 20% of the entrapped doxorubicin under physiological conditions in vitro, and extended drug release over the course of 5 days **(Figure 1.3c)**. This work also demonstrated that alginate and HA-terminated formulations could sustain the delivery of the model drug cardiogreen (indocyanine green dye) in vivo for up to 24 hours, in stark contrast to bare PLGA cores that release their full cargo within 8 hours **(Figure 1.3d)**.
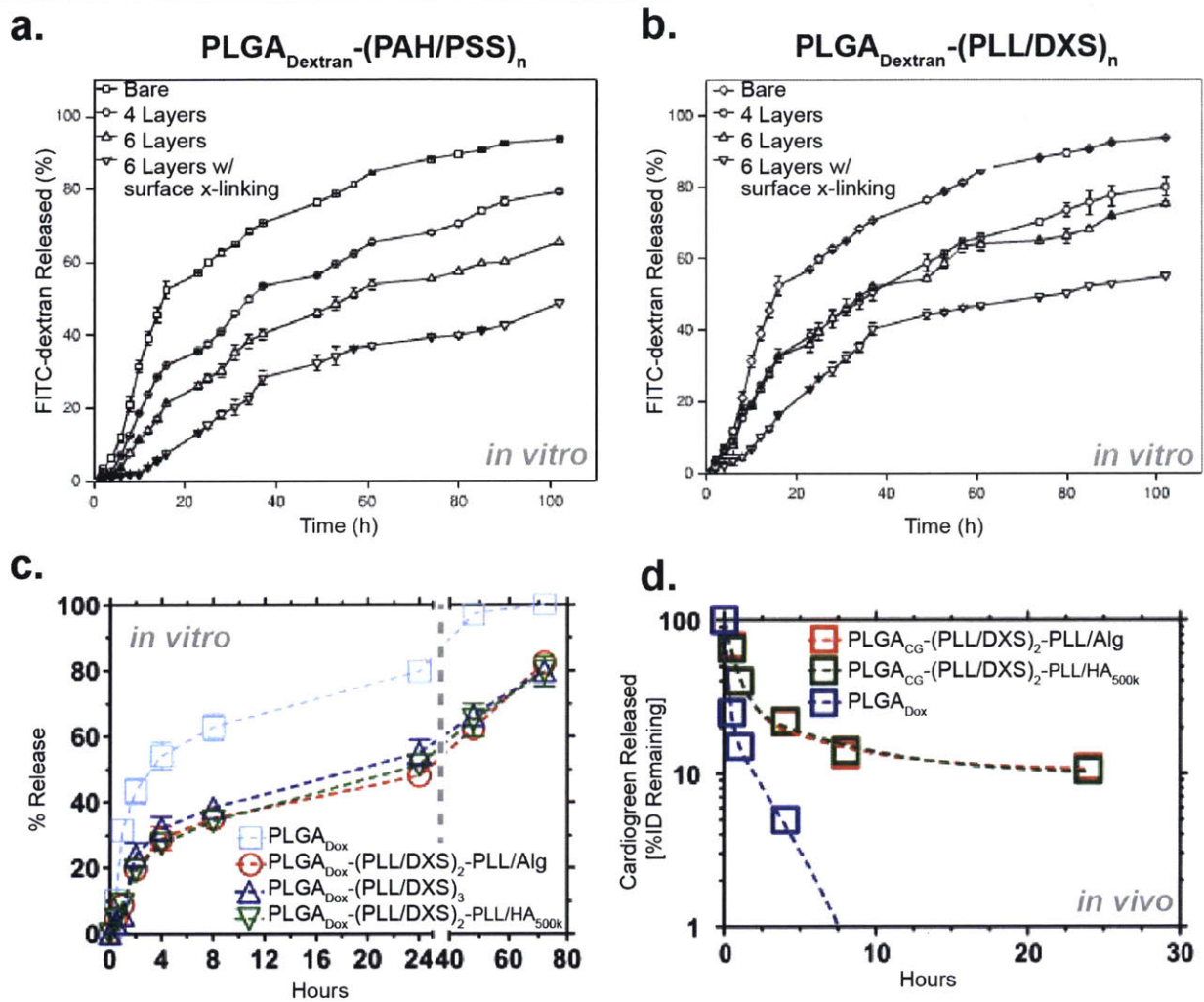
LbL modification of mesoporous silica cores

30

Figure 1.3. LbL films regulate the release of drugs encapsulated in the core template, allowing for extended release and reduced burst-release both in vitro and in vivo. a) Submicrometer PLGA particles can be coated with poly(allylamine hydrochloride) (PAH) and poly(styrene sulfonate) (PSS) to slow the release of the model drug FITC-dextran (4 kDa) from the core. Additional layers further slow release, and crosslinking of the amines in the film (via glutaraldehyde) provides the slowest release profile. b) Similarly, coating these particles with poly(L-lysine) (PLK) and dextran sulfate (DXS) slowed release, but differ from PAH/PSS films in that additional layers do not slow release, highlighting the differences in permeability between different LbL films. c) PLGA nanoparticles also benefit from LbL modification, and can be coated with PLK, DXS, alginate (Alg), and hyaluronic acid (HA) to significantly slow the release of doxorubicin from the PLGA core. d) These observations carry over to in vivo experiments, where PLGA nanoparticles coated with biocompatible LbL films prolong the release of a model drug, cardiogreen (CG), over 24 hours. Reprinted with permission from (a-b) [150], (c-d) [113]. Copyright (a-b) 2012 WILEY-VCH Verlag GmbH & Co., (c-d) 2013 Elsevier.

Another excellent template for LbL assembly is colloidal mesoporous silica (MS), a highly characterized material system with great potential for multifunctionality [151]. Sub-100 nm MS nanopar-

ticles can be prepared at large scales [152], and with extensive control over their porosity [153], which subsequently dictates their drug loading and release behaviors. The versatility of MS drug-carriers is highlighted by their capacity to carry either hydrophilic [154] or hydrophobic cargo [155], depending on the loading technique employed. MS particles are naturally amenable to LbL-modification due to their innate negative charge, but can be chemically modified to yield cationic particles as well [156]. Due to their stability in organic solvents, these materials can also be functionalized through hydrogen-bonding driven LbL assembly [157]. While MS drug-carriers provide several distinct advantages, their clinical translatability has been hindered by toxicity concerns [158-159]. However, in LbL-modified MS systems, it appears that problems with toxicity can be resolved either by core-dissolution to remove silica from the final carrier [156, 160] or by introduction of biocompatible surfaces [147].

Several stimuli-responsive LbL formulations have been prepared from silica templates, which highlight the capacity for LbL films to be more than passive diffusion barriers. By exploiting the well-characterized pH-dependent swelling of LbL films[161], Chen and coworkers[162] were able to design LbL drug carriers templated from MS nanotubes that exhibited pH-specific drug release in vitro depending on the choice of film constituents. This approach takes advantage of the pH-dependency of LbL assembly, where it is generally found that the ideal pH is that which maximizes the charges of the precursor polyelectrolytes. By titrating away from this ideal pH value, the electrostatic forces that hold the LbL film together weaken and allow for swelling, becoming more permeable to the diffusion of cargo. Therefore, by carefully choosing the polyelectrolytes for a given application, an LbL nanoparticle can selectively respond to pH of the target tissue to initiate drug release. This effect is demonstrated nicely by Shu et al.[160], who designed smart LbL carriers suitable for oral delivery of an encapsulated protein. In this system, BSA-loaded MS nanoparticles were coated with low molecular weight (6 kDa) water-soluble chitosan (WSC) and DXS. By using WSC, which is only cationic under acidic conditions, the nanoparticles were highly stable in conditions similar to the stomach environment (pH 1.4, 37°C, and agitation) and prevented release (<10%) of the encapsulated protein **(Figure 1.4a)**. However, at the neutral pH found in the intestinal lumen, WSC loses its cationic charge and the capsules readily release their cargo. This platform was later modified by replacing WSC with cysteine-conjugated chitosan (CS-SH) in order to generate disulfide crosslinks within the LbL film [156], which prevented drug release at neutral pH until exposure to intracellular levels of glutathione **(Figure 1.4b-c)**. By generating CS-SH

32

with different degrees of cysteine conjugation, the authors were able to generate a crosslinking gradient within the film, which they demonstrate is more effective in preventing burst-release after GSH addition. Importantly, this approach highlights the broad range of release profiles achievable with the use of an LbL system, and the ability to introduce orthogonal responsive elements in a hierarchical manner to specifically control not only when release occurs, but also the kinetics once release is initiated.

The pH-responsive functionality of LbL films is not limited to electrostatically stabilized formulations, as was recently demonstrated by Li et al.[163] with a biomolecular LbL particle templated from MS nanoparticles. In this system, MS nanoparticles were electrostatically coated with a layer of PEI and concanavalin A (Con-A). Con-A is a carbohydrate-binding protein that can be adsorbed onto surfaces via hydrophobic attraction, and allows for subsequent bio-templated LbL assembly with the neutral polysaccharide glycogen or galactomannan[164]. Con-A loses its carbohydrate-binding ability at acidic pH, causing the LbL film to rapidly disassemble and release doxorubicin encapsulated in the core. These types of films are also sensitive to degradation via competitive binding [161], wherein Con-A dissociates from glycogen in favor of a carbohydrate to which it has
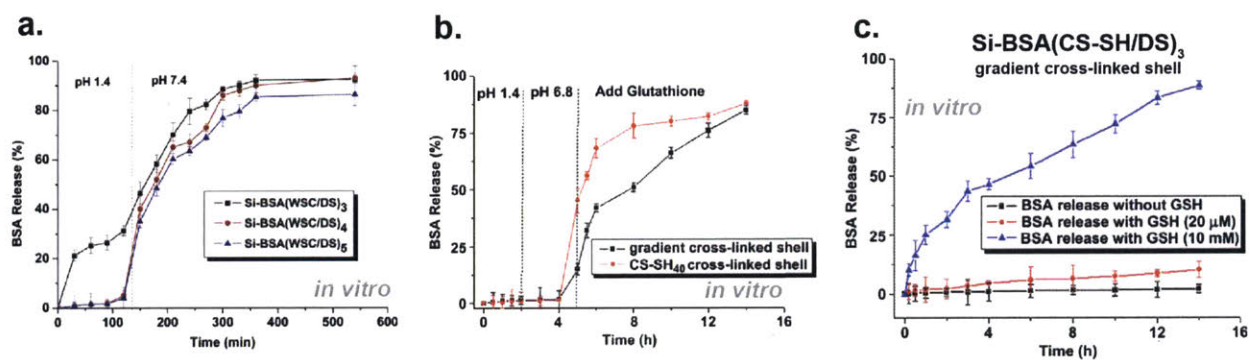

Figure 1.4. Careful selection of LbL film constituents generates smart, responsive films that regulate the release of drugs from the core template. Such films can significantly reduce payload leakage outside of the targeted environment through several means. a) LbL films can be triggered to degrade and release drugs by changes in pH, and in this case a film constructed from water-soluble chitosan (WSC) and dextran sulfate (DS) exhibits stability at acidic pH (WSC protonated) but begins to disassemble at neutral pH (WSC deprotonated). [Si = silica nanoparticle, BSA = bovine serum albumin] b) Introduction of bio-responsive elements adds further control to such films, and in this case silica nanoparticles were coated with cysteine-conjugated chitosan (CS-SH) in order to form disulfide crosslinks throughout the film. These crosslinks prevent release of cargo until exposure to intracellular, disulfide-breaking enzymes (glutathione, GSH). Additional control over release is introduced by spatially controlling crosslinking density through the film by using CS-SH with differing degrees of cysteine conjugation. c) Disulfide-crosslinked LbL films are stable at extracellular GSH concentration but slowly release cargo over 14 hours at intracellular concentrations of GSH. Reprinted with permission from (a) [160], (b-c) [156]. Copyright (a-c) 2010 Elsevier.

greater binding affinity towards, such as glucose.

LbL modification of liposomal cores

Highly biocompatible liposomal drug carriers are among the most promising templates for LbL modification. Liposomes are of particular interest due to their versatility and use in some of the most well-known and readily produced nanomaterials for therapeutic applications, such as Doxil, Onivyde and Vyxeos. Like other traditional nanoparticle cores, liposomal drug carriers can be modified via LbL assembly to improve stability and drug release characteristics while simultaneously providing new stimuli-responsive behavior and targeted biological interactions. Work by Fukui and Fujimoto[148] demonstrated that chitosan and dextran sulfate-coated liposomes exhibited increased stability against surfactants and improved drug-retention. This work tested the retention of several model drugs (1-hydroxy pyrene-3,6,8-trisulfonic acid (HPTS), alendronate, and glucose) and observed prolonged in vitro cargo-retention over 60, 85, and 144 hours, respectively. Interestingly, if the films were built using DNA instead of DXS, then heating the liposomes to 60°C could trigger release, likely via denaturation of the adsorbed DNA **(Figure 1.5a)**. Along these lines, Kim and colleagues [134] described an LbL-modified liposome loaded with doxorubicin, which exhibits a pH dependent release profile under physiological conditions in vitro **(Figure 1.5b)**. This formulation leveraged the pH-sensitivity of LbL films composed of weak polyelectrolytes, in this case PLK and the block co-polymer poly(ethylene glycol-b-L-aspartate). At slightly acidic pH, such as in the tumor microenvironment, protonation of aspartic acid's carboxylic acid side chain initiates film breakdown down and release of cargo. However, at pH 7.4 the films are stable, and improve drug retention significantly relative to bare liposomes after deposition of only 3 layers.

Liposomal cores present a special advantage due to their ability to easily co-encapsulate drugs, including the simultaneous loading of hydrophilic and hydrophobic payloads [165-166]. Combining this capability with responsive LbL films can drastically improve the efficacy of liposomal combination therapies, as was demonstrated by Dreaden et al.[116] with a nanoparticle formulation consisting of dual-inhibitor loaded liposomes functionalized with a bilayer of PLK and HA. With the aid of the pH-responsive and CD44 receptor-targeted functionality of the LbL film, this nanoparticle successfully and safely delivered a synergistic inhibitor pair in a murine model of triple-negative breast cancer, leading to disease stabilization and a 4-fold decrease in tumor size compared to

controls **(Figure 1.5d)**. Notably, use of a non-responsive and non-targeting drug-loaded liposome (coated with PLK/DXS) exhibited less therapeutic efficacy, whereas drug-free vehicles of the PLK/HA formulation exhibited a small but significant (ca. 1.6 fold) reduction in tumor size. This intriguing result may indicate an antiproliferative role of the LbL film itself, though further work is required
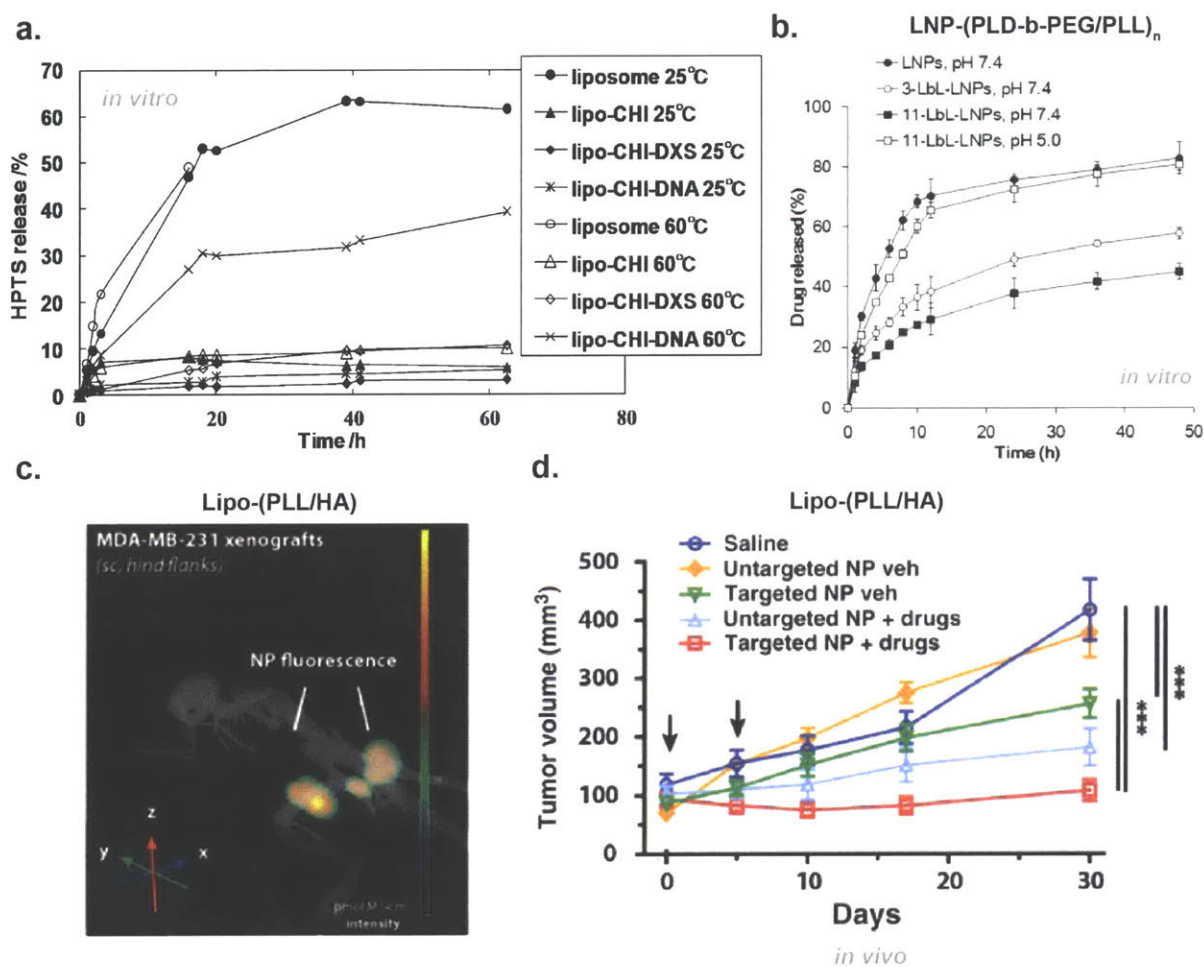

Figure 1.5. LbL films introduce multiple avenues of control over the delivery and release of drugs from clinically-approved drug carriers like liposomes. a) Temperature-responsive film constituents can allow a thermally-triggered release profile, as is achieved in this nanoparticle formulation where 1-hydroxy pyrene-3,6,8-trisulfonic acid (HPTS)-loaded liposomes were coated with chitosan (CHI) and DNA. Heating the particles to the denaturation point of DNA disrupts the film and allows slow leakage of the cargo over 60 hours. b) Use of weak polyelectrolytes such as poly(L-aspartic acid)-b-polyethylene glycol (PLD-b-PEG) and poly(L-lysine) to generate LbL films produces nanoparticles that begin to disassemble at acidic pH, such as in the hypoxic tumor microenvironment. [LNP = liposomes]. c) Films composed of PLK and hyaluronic acid (HA) combine the pH sensitivity of weak polyelectrolyte-based LbL films with receptor-ligand targeting via HA-CD44 binding. This bimodal targeting allows for favorable accumulation of liposomes into tumors in vivo, and d) maximizes the effect of the drug cargo to stabilize disease progression in a model of triple-negative breast cancer. Reprinted with permission from (a) [148], (b) [134], (c-d) [116]. Copyright (a) 2009 American Chemical Society, (b) 2014 Elsevier, (c-d) 2015 American Association of Cancer Research.

to fully characterize the possible mechanisms at play. Importantly, this approach overcame the profound hepatotoxicity associated with free administration of this combination therapy.

Overall, responsive LbL films highlight the versatile and tunable multifunctionality offered by LbL nanomedicines. Importantly, the functionality provided by the LbL film is independent of the identity of the core template, introducing the possibility to develop modular therapies that can be adapted to different templates as needed. By careful selection of the individual components of the film, as well as clever use of chemical modifications after film assembly, researchers can develop highly specialized materials to control the release of therapeutics from a diverse range of nanoparticle drug-carriers.

1.3.3. LbL films as a drug carrier and vector for combination therapy

A key advantage to the LbL platform is the capacity to incorporate therapeutics directly into the LbL film itself. This can be achieved through a variety of means, including direct adsorption of charged biopolymers including proteins [167], peptides [168], and nucleic acids [169], as well as through the incorporation of synthetic drug-conjugated or drug–loaded polymers [170]. Because the drug is adsorbed into the nanocomposite, and deposition steps can be repeated, very high weight percentage loading is possible [171-174]. This section discusses how researchers have leveraged this capability to successfully deliver therapies without a drug-loadable template. Additionally, this section covers formulations that combine drug-loaded templates with therapeutic-containing films to create sophisticated combination therapy vectors.

Gene delivery from responsive LbL films

One of the most promising applications of therapeutic LbL films is gene therapy. Incorporation of DNA into planar LbL films was first described in 1993 by Lvov and colleagues[175], and subsequent work in the early 2000s extended this to colloidal templates[176-179]. Soon after, efforts with DNA-loaded LbL microcapsules demonstrated the ability to successfully transfect cells in vitro[180]. By 2008, Fuller et al. demonstrated the in vitro transfection capability of silica "C dot" nanoparticles coated with PEI and DNA. Shortly thereafter, Breunig and colleagues[181] fabricated LbL particles composed of gold nanoparticles coated with PEI/siRNA/PEI. This formulation dem-

onstrated significantly reduced polymer-mediated cytotoxicity compared to free PEI and mediated gene-specific knockdown in CHO-K1 cells in vitro. Notably, this platform was capable of effective siRNA delivery even in the presence of serum. Follow-up work by this group[182] demonstrated that the same platform could deliver plasmid DNA to cells in vitro, though expression of exogenous genes was not reported. Subsequent research focused on developing robust gene delivery vectors capable of both in vitro and in vivo gene delivery by optimizing the parameters that influence nucleic acid stabilization in vivo[183], efficient uptake into cells[112], desirable sub-cellular trafficking via endosomal escape[184], and efficient cytosolic release of the nucleic acid cargo[185]. In particular, clever selection of LbL film constituents, particularly cationic elements, has shown promise in mediating endosomal escape and cytosolic cargo release.

Previous work found that the choice of the cationic polymer can strongly influence transfection efficiency with polyplexes in vitro[186]. Green and colleagues[187] recently demonstrated that this principle holds for LbL nanoparticles as well by demonstrating how different combinations of PEI and custom biodegradable polycations (SS37 and 447) impacted nucleic acid loading and transfection efficiency. Notably, non-degradable PEI exhibited significantly higher loading (ca. 5-fold) of nucleic acid into the LbL film relative to the biodegradable polycations (**Figure 1.6a**). The authors also found that the degree of terminal layer saturation played an important role in final in vitro transfection efficiency, implying the need to explore this parameter more closely (**Figure 1.6b**). Although not all permutations of the LbL film were fully explored, this study touches on critical parameters for the design of LbL films for gene therapy, namely the balancing between nucleic acid loading efficiency, polycation toxicity, and endosomal escape capability. Important future work should systematically compare the transfection efficiency, toxicity, and sub-cellular localization of nanoparticles composed with different polycations, including more detailed trafficking studies that can examine the mechanism of endosomal escape and release in these unique systems in comparison to more typical synthetic gene vectors.

Responsive LbL films show promise for mediating endosomal escape and subsequent release of nucleic acid cargo. In particular, implementation of charge-reversing polymers for LbL assembly appears to be an effective strategy for triggering disassembly of the nanoparticle within an acidifying endosome. Guo et al. [185] demonstrated this approach by using poly(allylamine hydrochloride)-citraconic anhydride (PAH-Cit), nucleic acids, and PEI in an LbL assembly templated from gold

nanoparticles. PAH-Cit exhibits a negative charge at neutral pH, but at pH 5 becomes cationic and rapidly destabilizes the LbL film through electrostatic repulsion **(Figure 1.6c)**. Nanoparticles consisting of gold core-(PEI/PAH-Cit/PEI/Nucleic acid) exhibited improved in vitro gene transfection and silencing, approximately 3 and 2-fold, respectively, compared to free PEI and lipofectamine **(Figure 1.6d-e)**. Subsequent work by this group extended this platform towards therapeutic gene
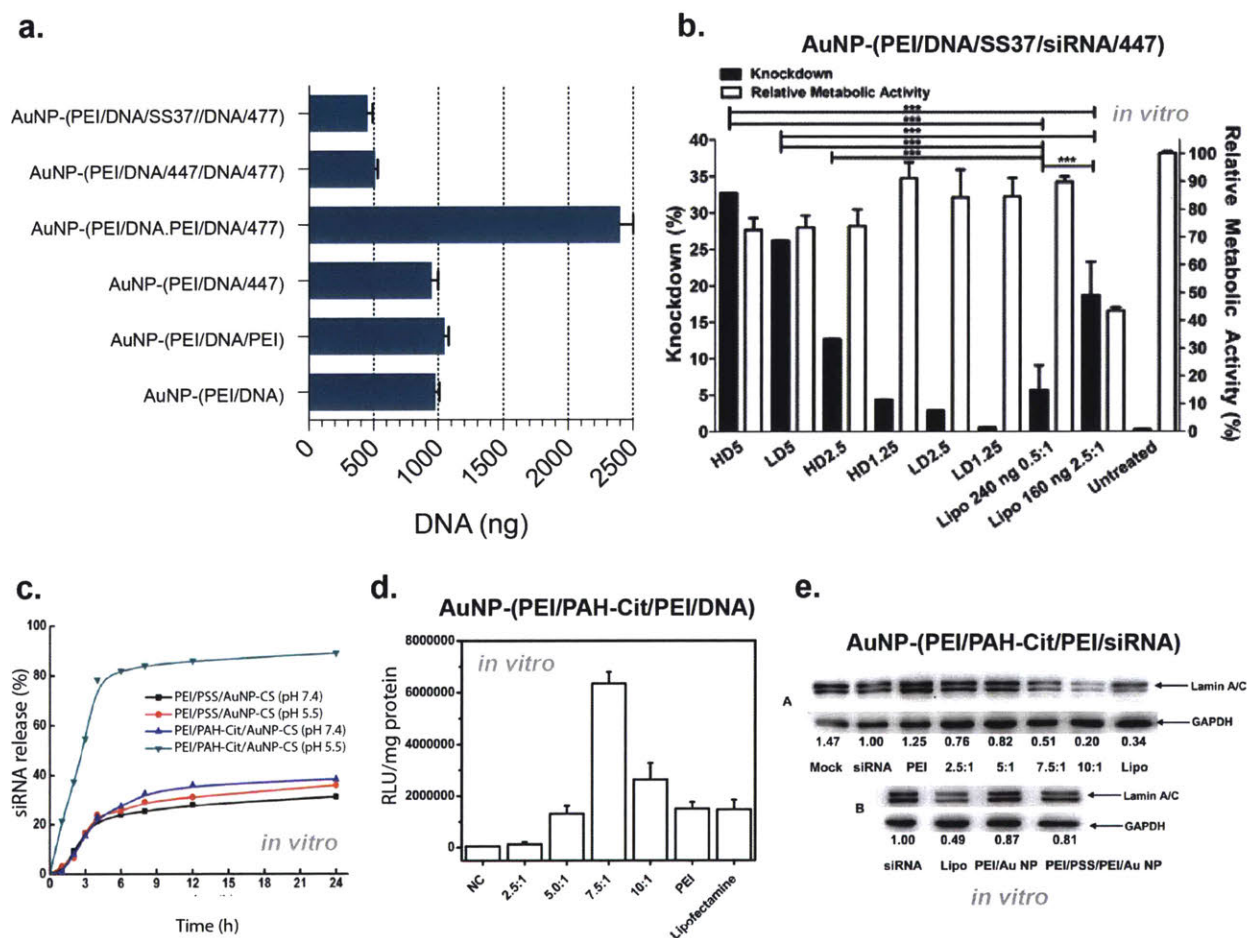

Figure 1.6. Gene delivery through LbL films presents the opportunity to build sophisticated nanostructures to optimize transfection efficiency. Multiple variables are involved in the development of successful LbL gene carriers, and among the most important to optimize is the cationic elements of the LbL film. a) Different nucleic acid loading efficiencies have been observed between nondegradable polyethylenimine (PEI) and biodegradable poly(beta-amino-esters) like SS37 and 447. Chart generated from raw data from [146]. b) Additional consideration should be given to the degree of functionalization of outer cationic layers, and in this case improved biocompatibility and transfection occurred if the surface was less saturated. [LD = low dose, HD = high dose, Lipo = lipofectamine; the fold excess of polycation to core during assembly is given by the number following LD or HD]. c) Responsive polymers, such as charge-reversing poly(allylamine hydrochloride)-citraconic anhydride (PAH-Cit), facilitate the release of nucleic acid cargo at lysosomal pH where they become cationic and trigger film disassembly. In contrast, LbL nanoparticles built from nonresponsive poly(styrene sulfonate) (PSS) films retained their cargo. d) Charge-reversing elements within the film improved gene delivery significantly, and e) similarly aided in gene silencing via siRNA delivery. Reprinted with permission from (b) [187] and (c-e) [185]. Copyright (b) 2015 Elsevier, (c) 2012 American Chemical Society, (d-e) 2010 American Chemical Society.

delivery [188] and silencing [189] in several drug-resistant cancer cell lines in vitro.

In a similar approach, Chen at al. [190] designed charge-reversing LbL carriers of plasmid DNA encoding small hairpin RNA (shRNA) for gene silencing in vivo. This work used chitosan-aconitic anhydride (CS-Aco) as an anionic constituent in a gold-(PEI/CS-A/PEI/shRNA) formulation. In the acidic lysosome, the CS-Aco polymer is hydrolyzed into cationic chitosan to trigger film disassembly and cargo release. Importantly, this formulation was stable and nontoxic in vivo, mediating efficient silencing of the drug-resistance protein ABCG2 in HepG2 liver cancer cells. Mice harboring HepG2 xenografts exhibited improved tumor reduction using the charge-reversing formulation alongside doxorubicin. These results are interesting given that the nanoparticle's outermost layer is composed of the nucleic acid cargo, which could be damaged by nucleases during delivery. Other reports [191-192] also demonstrate that nucleic acids are resistant to degradation after adsorption onto an LbL particle in vitro, but further documentation of the limitations of this stability should be explored. Nonetheless, additional outer layers can provide critical benefits to LbL nanoparticles that include extended blood circulation times and active targeting properties, as discussed in *Section 1.3.1*.

Combination therapies from therapeutic LbL films and functional cores

One of the key strengths of the LbL nanoparticle approach is the ability to introduce two or more drug types within the layers and the core of the nanoparticle. Combining therapeutic-loaded LbL films with functional core templates is a powerful means to deliver combination therapies that can attack disease from multiple angles. Multipronged therapeutics are gaining a great deal of interest, particularly for the treatment of drug-resistant cancer with molecules that can engage or silence genes to enhance the effects of chemotherapy. Because of the modular nature of the LbL platform, nanomedicines can be designed that combine various therapies into a single particle, thereby guaranteeing co-delivery to target cells. Moreover, recent efforts [134] to modulate the temporal release from these systems indicate the potential to stage drug release in such a way as to maximize the effects of each drug.

Deng et al.[112] have recently demonstrated the therapeutic efficacy of a targeted LbL combination therapy platform that co-delivers siRNA and chemotherapy to a subcutaneous murine model of
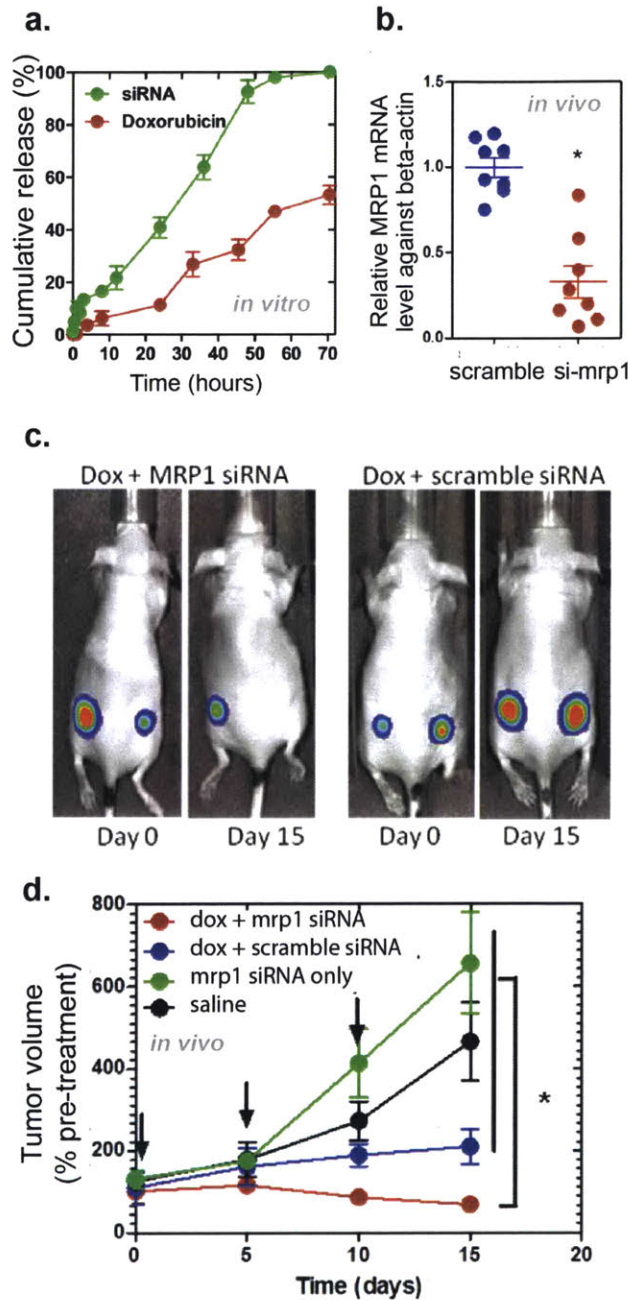
a.

b.

Figure 1.7. Assembly of a therapeutic LbL film onto a drug-loaded core can generate sophisticated carriers of synergistic combination therapies. In this case, a doxorubicin-loaded liposome is coated with a gene-delivering LbL film composed of poly(L-arginine), siRNA against MRP1, and hyaluronic acid (PLA/siRNA/PLA/HA). a) This approach allows for differential release profiles of the therapeutics, with siRNA being released prior to the cytotoxic agent. b) The resulting nanoparticles efficiently silence expression of MRP1, a drug-resistance protein, within triple-negative breast cancer xenografts. c) The combination of gene therapy with chemotherapy provides significant improvements in therapeutic efficacy over monotherapy. Reprinted with permission from [112], 2013 American Chemical Society.

c.

d.

triple-negative breast cancer. This approach functionalizes a doxorubicin-loaded liposome with a functional, therapeutic-containing LbL film composed of PLA/siRNA/PLA/HA. In this formulation, the highly hydrated outer HA coating promotes biostability by reducing opsonization and nonspecific uptake, while simultaneously mediating receptor-mediated endocytosis via the CD44 receptor commonly overexpressed in breast cancer. Meanwhile, the biodegradable cationic PLA layers help to mediate endosomal escape and siRNA release into the cytoplasm. More specifically, this work aimed to overcome drug-resistance towards doxorubicin in triple-negative breast cancer, which is often mediated by enhanced drug efflux via upregulation of transmembrane drug efflux pumps, like the multidrug resistance protein 1 (MRP1). To that end, the applied therapy introduced siRNA against MRP1 (siMRP1) to break down the cancer's defense mechanisms and thereby maximize the effect of the co-delivered cytotoxic agent. The combination of siMRP1 with and doxorubicin led to both efficient in vivo gene silencing and synergistic therapeutic efficacy when compared to the effects of monotherapy **(Fig-**

ure 1.7). Notably, this work reported a differential release profile of the siRNA and chemotherapeutic, demonstrating the potential for staggered release from an LbL nanoparticle platform. This provides a key advantage, as it allows the siRNA time to sensitize the cell before the cytotoxic agent is released.

Overall, LbL technology facilitates the development of multifunctional nanocarriers that can control the delivery of synergistic combinations of drugs. The approach allows researchers to carefully select different therapeutics and incorporate them into the carrier in such a way as to individually regulate their release. Simultaneously, careful selection of film constituents can provide further control over the biodistribution, pharmacokinetics, and stimuli-responsive drug release of these systems.

1.3.4. LbL nanoparticles as theranostics

The LbL approach also lends itself towards other important biomedical applications such as imaging-based diagnostics through the incorporation of an imaging core of the linking of appropriate dye molecules to one of the thin film components. Moreover, because the LbL approach is highly modular, it is possible to simultaneously achieve all the advantages and functionalities as discussed in the previous section to develop sophisticated diagnostic and theranostic systems.

Theranostic nanoparticles provide a single nanocarrier which integrates diagnostics and therapy[193]. Although still in its early stages, this approach is already generating interesting results. For example, Cheng el al.[194] have used LbL assembly to coat superparamagnetic iron oxide (SPIO) and gold nanoparticles onto lanthanide-doped rare-earth up-conversion nanoparticle (UCNP) cores, yielding multifunctional theranostic nanoparticles. Here, the diagnostic functionality is provided by the luminescent UCNP core and the MRI-compatible SPIO nanoparticles in the film. Simultaneously, the SPIO nanoparticles also help to guide nanoparticles to the tumor via exogenous magnetic cues, and the gold nanoparticles provide a photothermal therapeutic effect upon light activation (**Figure 1.8**). Promisingly, using magnetic guidance and light activated photothermal therapy, suppressed tumor growth and prolonged survival, indicating the potential to provide effective therapeutic treatments alongside multimodal diagnostics (**Figure 1.8d-e**).
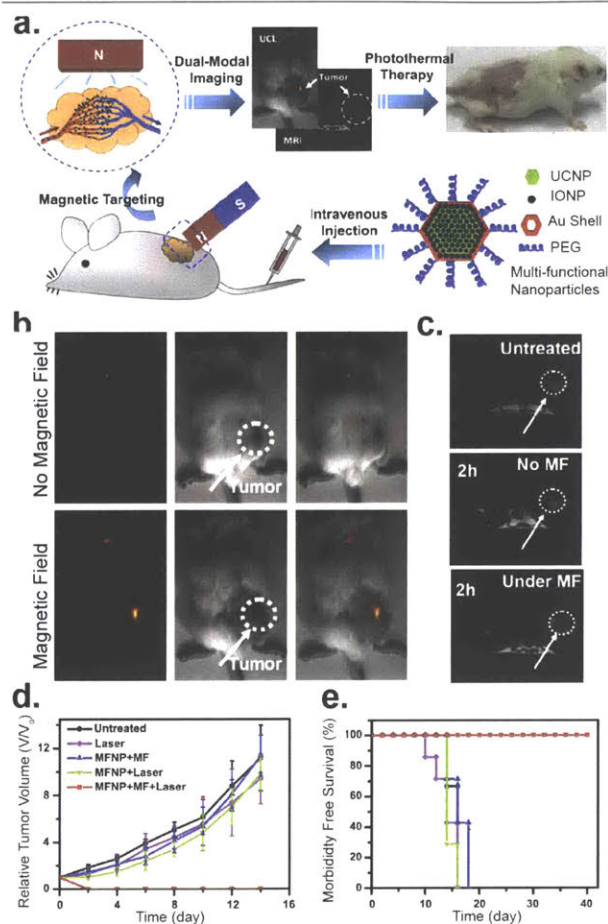
Figure 1.8. LbL modification allows the preparation of potent theranostic nanoparticles. a) Schematic illustration showing the composition of LbL assembled theranostic nanoparticles and the concept of in vivo imaging-guided magnetically targeted PTT. b) Representative in vivo upconversion luminescent images of tumor-bearing mice with or without magnetic field (MF). c) Representative T2 weighted images of tumor-bearing mice. d) The tumor growth curve under different treatment groups. e) Survival curve of tumor-bearing mice after different treatment groups. Reprinted with permission from [194], copyright 2012

One avenue for LbL theranostics takes advantage of the photoresponsive nature of certain core templates, like gold or UCNPs, to initiate phototherapy in addition to triggering drug release from therapeutic-loaded films. For example, Wang and colleagues[195] described the assembly of a therapeutic LbL film onto a NIR-responsive UCNP. In this system the UCNP is coated with PAA and PEI, loaded with the photosensitizing molecule chlorin e6, and finally terminated with siRNA against the oncogene Plk1. This nanoparticle could silence Plk1 in HeLa cells in vitro, and interestingly exhibited better performance in serum-containing media relative to serum-free media. Excitation of the UCNP by NIR light also caused entrapped chlorin e6 molecules to generate cytotoxic singlet oxygen, and combination of this photodynamic therapy with delivery of functional siRNA exhibited a stronger antiproliferative effect in vitro than either treatment by itself. Shen et al.[191] have employed a related approach, using PEI-terminal LbL gold nanorods to complex anionic siRNA. These multifunctional nucleic acid carriers silenced their target protein, pyruvate kinase isoenzyme type M2 (PKM2), in vitro and provided spatially-resolved near-infrared laser photothermal cell killing in triple-negative breast cancer monolayer cultures (808 nm, 500 mW, 7 min).

Chen et al.[196] evaluated the in vivo efficacy of a similar approach, using noble metal-based photothermal contrast agents[110, 197-203] to fabricate polyelectrolyte-coated (PDADMAC/PSS) gold nanorods that could be loaded with doxorubicin post-synthesis. Following tissue-penetrant near-

infrared laser exposure of immunocompetent mice bearing S180 murine sarcoma xenografts (765 nm, 1.8 W cm^{-2}, 5 min), tumor progression was markedly slowed compared with equivalent doses of free doxorubicin.

In current theranostic platforms, diagnostic tools can be a limiting factor for promising disease detection because of their intrinsic drawbacks. For example, MRI is of high cost and requires sophisticated magnetic tuning and prolonged imaging processing incompatible with real-time tracking. Current fluorescence imaging tools, including UCNP, QD, and organic dyes, are within the visible or first window of NIR region, which has limitations in tissue penetration and imaging resolution. Fluorescence imaging in the second window of the NIR region (NIR-II, 1000 nm – 1700 nm) has attracted much attention as it can enhance the penetration and provide high-resolution images in a real-time scale and low cost[204-209]. A variety of systems such as polymeric micelles[207], lipids[205-206], and bacteria phages[210] have been used for NIR-II imaging; however, these systems lack the modularity to package multiple functionalities such as stealth, targeting, and therapeutics. LbL-based NIR-II imaging is a promising future approach towards addressing these concerns. In a different vein, incorporation of non-invasive diagnostic utilities into nanoparticle platforms, such as urinary based biomarker systems, can transform drug carriers into diagnostic devices that require no specialized imaging equipment. This approach is used in Chapter 5 of this thesis to develop a novel LbL theranostic device that mediates both gene silencing and urinary tracking of tumor burden.

## 1.4. Current obstacles for clinical translation

The LbL platform is a promising means to develop modular and multifunctional nanoparticles with important biomedical applications that span drug delivery and diagnostics. However, before this technology can be successfully translated to the clinic, the field must focus on resolving persistent barriers limiting the preparation of these materials. In this section, we discuss efforts to develop automatable fabrication processes for LbL nanoparticles that can be scaled to meet the needs of clinical and industrial implementation. Additionally, efforts to characterize the long-term stability of LbL nanoparticles, both in aqueous and lyophilized states, will be discussed.

1.4.1. Scalable manufacturing

LbL assembly is a facile technique that generally only involves repeating two key steps: (1) exposing the substrate to a solution of adsorbable polymer, and (2) washing of the substrate to remove excess polymer. This simplicity is fully realized for the LbL functionalization of macroscopic materials, which can make use of hands-off automatable devices such as dipping robots. In contrast, colloidal LbL assembly lacks such an automatable and robust synthetic approach because the washing step becomes highly nontrivial at the submicron- and nanometer scale. The necessity for efficient purification between layer depositions has been well documented through systematic experiments by Decher and colleagues[211], who demonstrate that LbL nanoparticle assembly requires a significant excess of polyelectrolytes relative to the core template to fully saturate the surface and avoid particle flocculation. Excess polymer must then be removed prior to the addition of the subsequent layer, otherwise flocculation and the generation of a polyplex byproduct will occur. Traditionally, this has been carried out through extensive centrifugal wash steps following each layer deposition. Centrifugation is time intensive, requires manual handling of materials at every step, necessitates extensive optimization, and is notorious for losing significant product by driving the formation of insoluble aggregated pellets[212].

Soon after colloidal LbL assembly was first described, efforts were underway to solve the problem of fabrication. Reports spanning the past 16 years have yielded several interesting options for automating the production of large (>5 micrometer) particles [213-217]. Several promising options have also been presented for preparing LbL nanoparticles, such as an innovative template-free
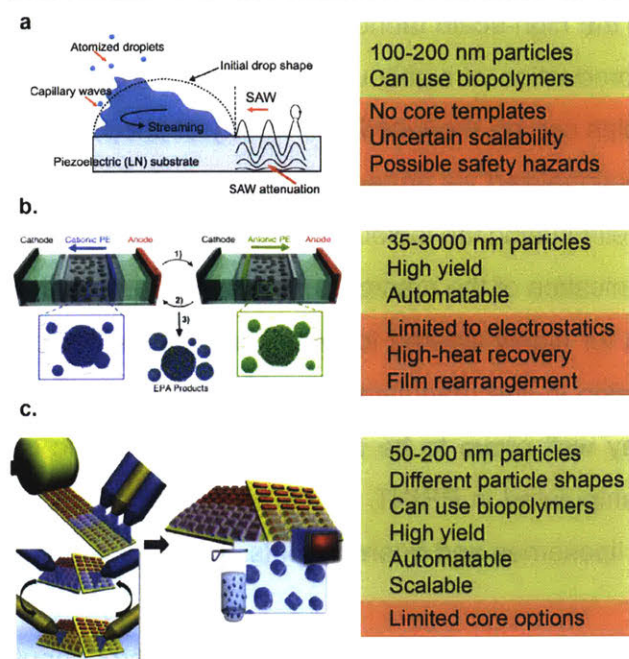
Figure 1.9. This figure summarizes the major advances in LbL nanoparticle fabrication and highlights each method's key strengths and weaknesses. For details on these methodologies, refer to the main text. Reprinted with permission from (a) [218], (b) [219], (c) [114]. Copyright (a) 2011 American Chemical Society, (b) 2013 WILEY-VCH Verlag GmbH & Co, (c) 2013 WILEY-VCH Verlag GmbH & Co.

approach to LbL assembly described by Yeo and colleagues[218]. In this work, LbL was carried out through a series of atomization and suspension steps, and produced particles on the order of 100-200 nm composed entirely of assembled polymers **(Figure 1.9a)**. This approach successfully creates nanoscale LbL nanoparticles, but at the expense of being able to functionalize a core nanoparticle template. As such, it limits the ability to incorporate promising functionalities such as imaging cores and drug-loaded cores. Furthermore, it is unclear whether the atomization technique could limit the types of polyelectrolytes introduced into this system. The potential to aerosolize biologically active nanoparticles into the workspace also necessitates serious investigation of potential safety hazards associated with this technique.

In 2013, Richardson et al.[219] described a novel LbL assembly method in which core templates could be immobilized in agarose gel, and then coated through the systematic electrophoresis of charges species through the gel **(Figure 1.9b)**. This approach generated both micro and nanometer scale LbL colloidal systems (3 μm to 35 nm) at high yields (85%). The main drawback of this approach is the need to melt the agarose to recover the LbL nanoparticles, which could damage sensitive formulations. Indeed, this work observed that regardless of the charge of the terminal layer, all formulations exhibited a negative charge. This was attributed to potential re-arrangement of the films during the agarose melting step. Such rearrangement could initiate premature release of cargo located in the film, and could conceal elements of the outer layer that may be needed for biostability and active targeting.

A novel synthetic approach described by Morton et al.[114] leverages PRINT (particle replication

in non-wetting templates) technology to facilitate the high-scale fabrication of LbL nanoparticles **(Figure 1.9c)**. PRINT technology allows for the production of highly uniform PLGA nanoparticle arrays onto planar surfaces. Notably, these particles can be produced in a variety of shapes and sizes ranging from 50 to 200 nm, and can be functionalized via aqueous spray-assisted LbL assembly while still immobilized on the planar array, eliminating the tedious centrifugal washing step. Subsequent recovery of the NPs requires only sonication of the macroscopic array to release the particles into solution, providing high yields even for highly layered formulations. This approach has significant potential to be automated to develop in-line manufacturing of LbL nanoparticles in a high-throughput, roll-to-roll fashion, and may well prove to be a solution for polymeric or biomacromolecular core particles that can be manipulated in PRINT. However, this technique is unable to use alternative core materials, such as liposomes and quantum dots.

Despite these efforts, the manufacture of LbL nanocarriers at a scale and higher throughput that is also widely accessible to academic laboratories remains a challenge. Work described in Chapter 2 aims to provide new tools towards establishing fabrication processes that provide these features.

1.4.2. Long-term stability and shelf life

With the growing reports of clinically relevant LbL nanomedicines, it is becoming increasingly important to satisfy important questions about the long-term stability of LbL therapeutics. Unfortunately, little documentation exists on the shelf lives of different LbL formulations, particularly those that are drug-loaded and may experience leakage during storage. These questions are vital for the eventual commercial success of these materials, both in terms of stockpiling, shipping, and storage in the clinic.

Full reports on this matter are lacking, but important information can be inferred from the characterizations of various drug-loaded systems. For example, during characterization of their surface-enhanced Raman spectroscopy LbL nanoprobes, DeVetter et al. [220] observed temperature-dependent encapsulation stability. In these studies a Raman-active small molecule, methylene blue, differentially diffused out from an LbL film composed of PAA and PAH over the course of 5 weeks, depending on the storage temperature. Samples stored at 22°C and 37°C exhibit a notable decay

46

in spontaneous Raman signal over 5 weeks, suggesting outward diffusion of methylene blue away from the gold core. Samples stored at 4°C provided more stable Raman spectra over 5 weeks, but still displayed some loss of signal. The authors then explored the effect of cross-linking on the stability of these probes, and found that crosslinking the amines on the outer PAH layer could significantly improve signal retention at 4°C over the course of 5 weeks. These results are interesting, and provide insight on how drug-loaded LbL nanoparticles may behave under prolonged aqueous storage conditions, as well as means to extend their shelf lives. Work from this thesis contributes additional knowledge on this front, as described in Chapter 2.

1.5. Scope of thesis

This dissertation documents improvements made to the fabrication of LbL nanoparticles, it documents the application of these new synthetic methods towards the systematic study of the role of LbL nanoparticle surface chemistry in the specific context of improving drug delivery to ovarian cancer, it also documents the engineering of a multifunctional nanoparticle for combined gene therapy and noninvasive tumor detection.

The introductory Sections 1.2 and 1.4 provide the background on which Chapters 2 and 4 build from in the development of an improved synthetic method based on tangential flow filtration and optimization of solution conditions and the LbL substrate. Innovation in the purification methods for the intermediate steps of LbL assembly provide the throughput, scale and yield of synthesis needed for later studies. Study of the solution conditions and substrate for LbL synthesis provide a basis for more stable nanocarriers with favorable siRNA encapsulation efficiency.

Sections 1.3.1 and 1.3.2 are the basis for the work of Chapter 3, where the methodical comparison of different LbL nanoparticle surface chemistries yields insights into ovarian cancer-targeting formulations with unique subcellular trafficking and the most advantageous means of administering these nanocarriers in vivo. These studies reveal the discrimination between sulfated and carboxylated LbL nanoparticles, and that ovarian cancer cells interact differently with LbL nanoparticles relative to uncoated particles bearing similar surface chemistry. Notably, ovarian cancer cells distinguish minute differences in LbL nanoparticle surface chemistry, translating to unique subcellular fates between formulations with similar surface coatings. Significant advantages are reported for administration methods that take advantage of intraperitoneal injection, which yields highly specific localization of nanoparticle to tumor tissue in a metastatic model of ovarian cancer.

The work for Chapter 5 is framed by the introductory Sections 1.3.3 and 1.3.4, a primer on combination therapy and theranostic nanomedicine. This portion of the dissertation documents the design and fabrication of an LbL-modified liposome for simultaneous siRNA delivery and detection of tumor burden. The diagnostic utility is incorporated into the LbL nanoparticle through click-chemistry modification of the terminal layer to introduce a biosensing peptide developed by collaborators in the Bhatia lab at MIT. This peptide is cleaved by tumor proteases, producing a

small peptide fragment that is readily excreted in the urine for noninvasive detection of tumors. The theranostic nanoparticle is validated in several metastatic model of cancer, including ovarian. The successful delivery of siRNA is documented in ovarian cancer, and the role of introducing additional targeting ligands via click-conjugation is explored.

1.6. References

1.   von Eschenbach, A. C., A vision for the National Cancer Program in the United States. *Nat Rev Cancer* **2004,** *4* (10), 820-8.

2.   Gerlinger, M.; Rowan, A. J.; Horswell, S.; Math, M.; Larkin, J.; Endesfelder, D.; Gronroos, E.; Martinez, P.; Matthews, N.; Stewart, A.; Tarpey, P.; Varela, I.; Phillimore, B.; Begum, S.; McDonald, N. Q.; Butler, A.; Jones, D.; Raine, K.; Latimer, C.; Santos, C. R.; Nohadani, M.; Eklund, A. C.; Spencer-Dene, B.; Clark, G.; Pickering, L.; Stamp, G.; Gore, M.; Szallasi, Z.; Downward, J.; Futreal, P. A.; Swanton, C., Intratumor heterogeneity and branched evolution revealed by multiregion sequencing. *N Engl J Med* **2012,** *366* (10), 883-892.

3.   Chin, L.; Andersen, J. N.; Futreal, P. A., Cancer genomics: from discovery science to personalized medicine. *Nat Med* **2011,** *17* (3), 297-303.

4.   Dias-Santagata, D.; Akhavanfard, S.; David, S. S.; Vernovsky, K.; Kuhlmann, G.; Boisvert, S. L.; Stubbs, H.; McDermott, U.; Settleman, J.; Kwak, E. L.; Clark, J. W.; Isakoff, S. J.; Sequist, L. V.; Engelman, J. A.; Lynch, T. J.; Haber, D. A.; Louis, D. N.; Ellisen, L. W.; Borger, D. R.; Iafrate, A. J., Rapid targeted mutational analysis of human tumours: a clinical platform to guide personalized cancer medicine. *EMBO Mol Med* **2010,** *2* (5), 146-58.

5.   Ross, J. S.; Slodkowska, E. A.; Symmans, W. F.; Pusztai, L.; Ravdin, P. M.; Hortobagyi, G. N., The HER-2 receptor and breast cancer: ten years of targeted anti-HER-2 therapy and personalized medicine. *Oncologist* **2009,** *14* (4), 320-68.

6.   Stenson, P. D.; Mort, M.; Ball, E. V.; Shaw, K.; Phillips, A.; Cooper, D. N., The Human Gene Mutation Database: building a comprehensive mutation repository for clinical and molecular genetics, diagnostic testing and personalized genomic medicine. *Hum Genet* **2014,** *133* (1), 1-9.

7.   van't Veer, L. J.; Bernards, R., Enabling personalized cancer medicine through analysis of gene-expression patterns. *Nature* **2008,** *452* (7187), 564-70.

8.   Weston, A. D.; Hood, L., Systems biology, proteomics, and the future of health care: toward predictive, preventative, and personalized medicine. *J Proteome Res* **2004,** *3* (2), 179-96.

9.   Slamon, D. J.; Leyland-Jones, B.; Shak, S.; Fuchs, H.; Paton, V.; Bajamonde, A.; Fleming, T.; Eiermann, W.; Wolter, J.; Pegram, M.; Baselga, J.; Norton, L., Use of chemotherapy plus a monoclonal antibody against HER2 for metastatic breast cancer that overexpresses HER2. *N Engl J Med* **2001,** *344* (11), 783-92.

10.   Zhang, J.; Yang, P. L.; Gray, N. S., Targeting cancer with small molecule kinase inhibitors. *Nat Rev Cancer* **2009,** *9* (1), 28-39.

11.   Johnson, L. A.; June, C. H., Driving gene-engineered T cell immunotherapy of cancer. *Cell Res* **2017,** *27* (1), 38-58.

12.   Bertrand, N.; Wu, J.; Xu, X.; Kamaly, N.; Farokhzad, O. C., Cancer nanotechnology: the impact of passive and active targeting in the era of modern cancer biology. *Adv Drug Deliv Rev* **2014,** *66,* 2-25.

13.   O'Brien, M. E.; Wigler, N.; Inbar, M.; Rosso, R.; Grischke, E.; Santoro, A.; Catane, R.; Kieback, D. G.; Tomczak, P.; Ackland, S. P.; Orlandi, F.; Mellars, L.; Alland, L.; Tendler, C.; Group, C. B. C. S., Reduced cardiotoxicity and comparable efficacy in a phase III trial of pegylated liposomal doxorubicin HCl (CAELYX/Doxil) versus conventional doxorubicin for first-line treatment of metastatic breast cancer. *Ann Oncol* **2004,** *15* (3), 440-9.

14.   Brunetti, C.; Anelli, L.; Zagaria, A.; Specchia, G.; Albano, F., CPX-351 in acute myeloid leukemia: can a new formulation maximize the efficacy of old compounds? *Expert Rev Hematol* **2017,** *10* (10), 853-862.

15.   Prat, J., New insights into ovarian cancer pathology. *Ann Oncol* **2012,** *23 Suppl 10,* x111-7.

16.   Koonings, P. P.; Campbell, K.; Mishell, D. R., Jr.; Grimes, D. A., Relative frequency of primary

ovarian neoplasms: a 10-year review. *Obstet Gynecol* **1989,** *74* (6), 921-6.

17.　　Seidman, J. D.; Horkayne-Szakaly, I.; Haiba, M.; Boice, C. R.; Kurman, R. J.; Ronnett, B. M., The histologic type and stage distribution of ovarian carcinomas of surface epithelial origin. *Int J Gynecol Pathol* **2004,** *23* (1), 41-4.

18.　　Cooke, S. L.; Brenton, J. D., Evolution of platinum resistance in high-grade serous ovarian cancer. *Lancet Oncol* **2011,** *12* (12), 1169-74.

19.　　Pfisterer, J.; Ledermann, J. A., Management of platinum-sensitive recurrent ovarian cancer. *Semin Oncol* **2006,** *33* (2 Suppl 6), S12-6.

20.　　Barenholz, Y., Doxil(R)--the first FDA-approved nano-drug: lessons learned. *J Control Release* **2012,** *160* (2), 117-34.

21.　　Rafiyath, S. M.; Rasul, M.; Lee, B.; Wei, G.; Lamba, G.; Liu, D., Comparison of safety and toxicity of liposomal doxorubicin vs. conventional anthracyclines: a meta-analysis. *Exp Hematol Oncol* **2012,** *1* (1), 10.

22.　　Boulikas, T., Clinical overview on Lipoplatin: a successful liposomal formulation of cisplatin. *Expert Opin Investig Drugs* **2009,** *18* (8), 1197-218.

23.　　Stathopoulos, G. P.; Antoniou, D.; Dimitroulis, J.; Michalopoulou, P.; Bastas, A.; Marosis, K.; Stathopoulos, J.; Provata, A.; Yiamboudakis, P.; Veldekis, D.; Lolis, N.; Georgatou, N.; Toubis, M.; Pappas, C.; Tsoukalas, G., Liposomal cisplatin combined with paclitaxel versus cisplatin and paclitaxel in non-small-cell lung cancer: a randomized phase III multicenter trial. *Ann Oncol* **2010,** *21* (11), 2227-32.

24.　　Mylonakis, N.; Athanasiou, A.; Ziras, N.; Angel, J.; Rapti, A.; Lampaki, S.; Politis, N.; Karanikas, C.; Kosmas, C., Phase II study of liposomal cisplatin (Lipoplatin) plus gemcitabine versus cisplatin plus gemcitabine as first line treatment in inoperable (stage IIIB/IV) non-small cell lung cancer. *Lung Cancer* **2010,** *68* (2), 240-7.

25.　　Davis, M. E.; Chen, Z. G.; Shin, D. M., Nanoparticle therapeutics: an emerging treatment modality for cancer. *Nat Rev Drug Discov* **2008,** *7* (9), 771-82.

26.　　Allen, T. M.; Cullis, P. R., Liposomal drug delivery systems: from concept to clinical applications. *Adv Drug Deliv Rev* **2013,** *65* (1), 36-48.

27.　　Chan, S.; Davidson, N.; Juozaityte, E.; Erdkamp, F.; Pluzanska, A.; Azarnia, N.; Lee, L. W., Phase III trial of liposomal doxorubicin and cyclophosphamide compared with epirubicin and cyclophosphamide as first-line therapy for metastatic breast cancer. *Ann Oncol* **2004,** *15* (10), 1527-34.

28.　　Leonard, R. C.; Williams, S.; Tulpule, A.; Levine, A. M.; Oliveros, S., Improving the therapeutic index of anthracycline chemotherapy: focus on liposomal doxorubicin (Myocet). *Breast* **2009,** *18* (4), 218-24.

29.　　Zhang, H., Onivyde for the therapy of multiple solid tumors. *Onco Targets Ther* **2016,** *9*, 3001-7.

30.　　Gradishar, W. J.; Tjulandin, S.; Davidson, N.; Shaw, H.; Desai, N.; Bhar, P.; Hawkins, M.; O'Shaughnessy, J., Phase III trial of nanoparticle albumin-bound paclitaxel compared with polyethylated castor oil-based paclitaxel in women with breast cancer. *J Clin Oncol* **2005,** *23* (31), 7794-803.

31.　　DeVita, V. T., Jr.; Chu, E., A history of cancer chemotherapy. *Cancer Res* **2008,** *68* (21), 8643-53.

32.　　Al-Lazikani, B.; Banerji, U.; Workman, P., Combinatorial drug therapy for cancer in the post-genomic era. *Nat Biotechnol* **2012,** *30* (7), 679-92.

33.　　Neijt, J. P.; Engelholm, S. A.; Tuxen, M. K.; Sorensen, P. G.; Hansen, M.; Sessa, C.; de Swart, C. A.; Hirsch, F. R.; Lund, B.; van Houwelingen, H. C., Exploratory phase III study of paclitaxel and cisplatin versus paclitaxel and carboplatin in advanced ovarian cancer. *J Clin Oncol* **2000,** *18* (17), 3084-92.

34.　　Conroy, T.; Desseigne, F.; Ychou, M.; Bouche, O.; Guimbaud, R.; Becouarn, Y.; Adenis, A.; Raoul, J. L.; Gourgou-Bourgade, S.; de la Fouchardiere, C.; Bennouna, J.; Bachet, J. B.; Khemissa-Akouz, F.; Pere-Verge, D.; Delbaldo, C.; Assenat, E.; Chauffert, B.; Michel, P.; Montoto-Grillot, C.; Ducreux, M.; Groupe Tumeurs Digestives of, U.; Intergroup, P., FOLFIRINOX versus gemcitabine for metastatic pancreatic cancer. *N Engl J Med* **2011,** *364* (19), 1817-25.

35.   Conroy, T.; Paillot, B.; Francois, E.; Bugat, R.; Jacob, J. H.; Stein, U.; Nasca, S.; Metges, J. P.; Rixe, O.; Michel, P.; Magherini, E.; Hua, A.; Deplanque, G., Irinotecan plus oxaliplatin and leucovorin-modulated fluorouracil in advanced pancreatic cancer--a Groupe Tumeurs Digestives of the Federation Nationale des Centres de Lutte Contre le Cancer study. *J Clin Oncol* **2005,** *23* (6), 1228-36.

36.   Grothey, A.; Sargent, D.; Goldberg, R. M.; Schmoll, H. J., Survival of patients with advanced colorectal cancer improves with the availability of fluorouracil-leucovorin, irinotecan, and oxaliplatin in the course of treatment. *J Clin Oncol* **2004,** *22* (7), 1209-14.

37.   Cassidy, J.; Clarke, S.; Diaz-Rubio, E.; Scheithauer, W.; Figer, A.; Wong, R.; Koski, S.; Lichinitser, M.; Yang, T. S.; Rivera, F.; Couture, F.; Sirzen, F.; Saltz, L., Randomized phase III study of capecitabine plus oxaliplatin compared with fluorouracil/folinic acid plus oxaliplatin as first-line therapy for metastatic colorectal cancer. *J Clin Oncol* **2008,** *26* (12), 2006-12.

38.   Smorenburg, C. H.; Sparreboom, A.; Bontenbal, M.; Verweij, J., Combination chemotherapy of the taxanes and antimetabolites: its use and limitations. *Eur J Cancer* **2001,** *37* (18), 2310-23.

39.   Hu, T.; Cao, H.; Yang, C.; Zhang, L.; Jiang, X.; Gao, X.; Yang, F.; He, G.; Song, X.; Tong, A.; Guo, G.; Gong, C.; Li, R.; Zhang, X.; Wang, X.; Zheng, Y., LHD-Modified Mechanism-Based Liposome Coencapsulation of Mitoxantrone and Prednisolone Using Novel Lipid Bilayer Fusion for Tissue-Specific Colocalization and Synergistic Antitumor Effects. *ACS Appl Mater Interfaces* **2016,** *8* (10), 6586-601.

40.   Chaudhry, V.; Rowinsky, E. K.; Sartorius, S. E.; Donehower, R. C.; Cornblath, D. R., Peripheral neuropathy from taxol and cisplatin combination chemotherapy: clinical and electrophysiological studies. *Ann Neurol* **1994,** *35* (3), 304-11.

41.   Miles, D.; von Minckwitz, G.; Seidman, A. D., Combination versus sequential single-agent therapy in metastatic breast cancer. *Oncologist* **2002,** *7 Suppl 6,* 13-9.

42.   Gralow, J. R., Optimizing the treatment of metastatic breast cancer. *Breast Cancer Res Treat* **2005,** *89 Suppl 1,* S9-S15.

43.   Dunton, C. J., Management of treatment-related toxicity in advanced ovarian cancer. *Oncologist* **2002,** *7 Suppl 5,* 11-9.

44.   du Bois, A.; Vergote, I.; Wimberger, P.; Ray-Coquard, I.; Harter, P.; Curtis, L. B.; Mitrica, I., Open-label feasibility study of pazopanib, carboplatin, and paclitaxel in women with newly diagnosed, untreated, gynaecologic tumours: a phase I/II trial of the AGO study group. *Br J Cancer* **2012,** *106* (4), 629-32.

45.   Seidman, A.; Hudis, C.; Pierri, M. K.; Shak, S.; Paton, V.; Ashby, M.; Murphy, M.; Stewart, S. J.; Keefe, D., Cardiac dysfunction in the trastuzumab clinical trials experience. *J Clin Oncol* **2002,** *20* (5), 1215-21.

46.   Shimizu, T.; Tolcher, A. W.; Papadopoulos, K. P.; Beeram, M.; Rasco, D. W.; Smith, L. S.; Gunn, S.; Smetzer, L.; Mays, T. A.; Kaiser, B.; Wick, M. J.; Alvarez, C.; Cavazos, A.; Mangold, G. L.; Patnaik, A., The clinical effect of the dual-targeting strategy involving PI3K/AKT/mTOR and RAS/MEK/ERK pathways in patients with advanced cancer. *Clin Cancer Res* **2012,** *18* (8), 2316-25.

47.   Liu, J. F.; Barry, W. T.; Birrer, M.; Lee, J. M.; Buckanovich, R. J.; Fleming, G. F.; Rimel, B.; Buss, M. K.; Nattam, S.; Hurteau, J.; Luo, W.; Quy, P.; Whalen, C.; Obermayer, L.; Lee, H.; Winer, E. P.; Kohn, E. C.; Ivy, S. P.; Matulonis, U. A., Combination cediranib and olaparib versus olaparib alone for women with recurrent platinum-sensitive ovarian cancer: a randomised phase 2 study. *Lancet Oncol* **2014,** *15* (11), 1207-14.

48.   Rosi, N. L.; Giljohann, D. A.; Thaxton, C. S.; Lytton-Jean, A. K.; Han, M. S.; Mirkin, C. A., Oligonucleotide-modified gold nanoparticles for intracellular gene regulation. *Science* **2006,** *312* (5776), 1027-30.

49.   Davis, M. E.; Zuckerman, J. E.; Choi, C. H.; Seligson, D.; Tolcher, A.; Alabi, C. A.; Yen, Y.; Heidel, J. D.; Ribas, A., Evidence of RNAi in humans from systemically administered siRNA via targeted nanoparticles. *Nature* **2010,** *464* (7291), 1067-70.

50.   Slowing, II; Vivero-Escoto, J. L.; Wu, C. W.; Lin, V. S., Mesoporous silica nanoparticles as controlled release drug delivery and gene transfection carriers. *Adv Drug Deliv Rev* **2008,** *60* (11), 1278-88.

Introduction

51.   Visaria, R. K.; Griffin, R. J.; Williams, B. W.; Ebbini, E. S.; Paciotti, G. F.; Song, C. W.; Bischof, J. C., Enhancement of tumor thermal therapy using gold nanoparticle-assisted tumor necrosis factor-alpha delivery. *Mol Cancer Ther* **2006,** *5* (4), 1014-20.

52.   Mejias, R.; Perez-Yague, S.; Gutierrez, L.; Cabrera, L. I.; Spada, R.; Acedo, P.; Serna, C. J.; Lazaro, F. J.; Villanueva, A.; Morales Mdel, P.; Barber, D. F., Dimercaptosuccinic acid-coated magnetite nanoparticles for magnetically guided in vivo delivery of interferon gamma for cancer immunotherapy. *Biomaterials* **2011,** *32* (11), 2938-52.

53.   Wang, Y.; Gao, S.; Ye, W. H.; Yoon, H. S.; Yang, Y. Y., Co-delivery of drugs and DNA from cationic core-shell nanoparticles self-assembled from a biodegradable copolymer. *Nat Mater* **2006,** *5* (10), 791-6.

54.   Dengler, E. C.; Liu, J.; Kerwin, A.; Torres, S.; Olcott, C. M.; Bowman, B. N.; Armijo, L.; Gentry, K.; Wilkerson, J.; Wallace, J.; Jiang, X.; Carnes, E. C.; Brinker, C. J.; Milligan, E. D., Mesoporous silica-supported lipid bilayers (protocells) for DNA cargo delivery to the spinal cord. *J Control Release* **2013,** *168* (2), 209-24.

55.   Sun, M.; Yang, C.; Zheng, J.; Wang, M.; Chen, M.; Le, D. Q. S.; Kjems, J.; Bunger, C. E., Enhanced efficacy of chemotherapy for breast cancer stem cells by simultaneous suppression of multidrug resistance and antiapoptotic cellular defense. *Acta Biomater* **2015,** *28*, 171-182.

56.   Xu, X.; Xie, K.; Zhang, X. Q.; Pridgen, E. M.; Park, G. Y.; Cui, D. S.; Shi, J.; Wu, J.; Kantoff, P. W.; Lippard, S. J.; Langer, R.; Walker, G. C.; Farokhzad, O. C., Enhancing tumor cell response to chemotherapy through nanoparticle-mediated codelivery of siRNA and cisplatin prodrug. *Proc Natl Acad Sci U S A* **2013,** *110* (46), 18638-43.

57.   Babu, A.; Wang, Q.; Muralidharan, R.; Shanker, M.; Munshi, A.; Ramesh, R., Chitosan coated polylactic acid nanoparticle-mediated combinatorial delivery of cisplatin and siRNA/Plasmid DNA chemosensitizes cisplatin-resistant human ovarian cancer cells. *Mol Pharm* **2014,** *11* (8), 2720-33.

58.   Ashley, C. E.; Carnes, E. C.; Epler, K. E.; Padilla, D. P.; Phillips, G. K.; Castillo, R. E.; Wilkinson, D. C.; Wilkinson, B. S.; Burgard, C. A.; Kalinich, R. M.; Townson, J. L.; Chackerian, B.; Willman, C. L.; Peabody, D. S.; Wharton, W.; Brinker, C. J., Delivery of small interfering RNA by peptide-targeted mesoporous silica nanoparticle-supported lipid bilayers. *ACS Nano* **2012,** *6* (3), 2174-88.

59.   Uchida, S.; Kinoh, H.; Ishii, T.; Matsui, A.; Tockary, T. A.; Takeda, K. M.; Uchida, H.; Osada, K.; Itaka, K.; Kataoka, K., Systemic delivery of messenger RNA for the treatment of pancreatic cancer using polyplex nanomicelles with a cholesterol moiety. *Biomaterials* **2016,** *82*, 221-8.

60.   Uchida, H.; Itaka, K.; Nomoto, T.; Ishii, T.; Suma, T.; Ikegami, M.; Miyata, K.; Oba, M.; Nishiyama, N.; Kataoka, K., Modulated protonation of side chain aminoethylene repeats in N-substituted polyaspartamides promotes mRNA transfection. *J Am Chem Soc* **2014,** *136* (35), 12396-405.

61.   Zuckerman, J. E.; Davis, M. E., Clinical experiences with systemically administered siRNA-based therapeutics in cancer. *Nat Rev Drug Discov* **2015,** *14* (12), 843-56.

62.   Wagner, M. J.; Mitra, R.; McArthur, M. J.; Baze, W.; Barnhart, K.; Wu, S. Y.; Rodriguez-Aguayo, C.; Zhang, X.; Coleman, R. L.; Lopez-Berestein, G.; Sood, A. K., Preclinical Mammalian Safety Studies of EPHARNA (DOPC Nanoliposomal EphA2-Targeted siRNA). *Mol Cancer Ther* **2017,** *16* (6), 1114-1123.

63.   Iler, R. K., Multilayers of colloidal particles. *J. Colloid Interface Sci.* **1966,** *21* (6), 569-594.

64.   Decher, G.; Hong, J.-D., Buildup of ultrathin multilayer films by a self-assembly process, 1 consecutive adsorption of anionic and cationic bipolar amphiphiles on charged surfaces. *Makromol. Chem., Macromol. Symp.* **1991,** *46* (1), 321-327.

65.   Decher, G.; Hong, J. D.; Schmitt, J., Buildup of ultrathin multilayer films by a self-assembly process: III. Consecutively alternating adsorption of anionic and cationic polyelectrolytes on charged surfaces. *Thin Solid Films* **1992,** *210*, 831-835.

66.   Keller, S. W.; Johnson, S. A.; Brigham, E. S.; Yonemoto, E. H.; Mallouk, T. E., Photoinduced Charge Separation in Multilayer Thin Films Grown by Sequential Adsorption of Polyelectrolytes. *J. Am. Chem. Soc.* **1995,** *117* (51), 12879-12880.

67.   Donath, E.; Sukhorukov, G. B.; Caruso, F.; Davis, S. A.; Möhwald, H., Novel Hollow Polymer Shells by Colloid-Templated Assembly of Polyelectrolytes. *Angew. Chem. Int. Ed.* **1998,** *37* (16), 2201-2205.

68.   Sukhorukov, G. B.; Donath, E.; Davis, S.; Lichtenfeld, H.; Caruso, F.; Popov, V. I.; Möhwald, H., Stepwise polyelectrolyte assembly on particle surfaces: a novel approach to colloid design. *Polym. Adv. Technol.* **1998,** *9* (10-11), 759-767.

69.   Caruso, F.; Caruso, R. A.; Mohwald, H., Nanoengineering of Inorganic and Hybrid Hollow Spheres by Colloidal Templating. *Science* **1998,** *282* (5391), 1111-4.

70.   Caruso, F., Nanoengineering of particle surfaces. *Adv. Mater.* **2001,** *13* (1).

71.   Hammond, P. T., Form and Function in Multilayer Assembly: New Applications at the Nanoscale. *Adv. Mater.* **2004,** *16* (15), 1271-1293.

72.   Hammond, P. T., Polyelectrolyte multilayered nanoparticles: using nanolayers for controlled and targeted systemic release. *Nanomedicine* **2012,** *7* (5), 619-22.

73.   Poon, Z.; Lee, J. B.; Morton, S. W.; Hammond, P. T., Controlling in vivo stability and biodistribution in electrostatically assembled nanoparticles for systemic delivery. *Nano Lett.* **2011,** *11* (5), 2096-103.

74.   Morton, S. W.; Shah, N. J.; Quadir, M. A.; Deng, Z. J.; Poon, Z.; Hammond, P. T., Osteotropic therapy via targeted layer-by-layer nanoparticles. *Adv. Healthcare Mater.* **2014,** *3* (6), 867-75.

75.   Wang, Y.; Yan, Y.; Cui, J.; Hosta-Rigau, L.; Heath, J. K.; Nice, E. C.; Caruso, F., Encapsulation of water-insoluble drugs in polymer capsules prepared using mesoporous silica templates for intracellular drug delivery. *Adv. Mater.* **2010,** *22* (38), 4293-7.

76.   Fujimoto, K.; Toyoda, T.; Fukui, Y., Preparation of Bionanocapsules by the Layer-by-Layer Deposition of Polypeptides onto a Liposome. *Macromolecules* **2007,** *40* (14), 5122-5128.

77.   Gittins, D. I.; Caruso, F., Tailoring the Polyelectrolyte Coating of Metal Nanoparticles. *J. Phys. Chem. B* **2001,** *105* (29), 6846-6852.

78.   Morton, S. W.; Poon, Z.; Hammond, P. T., The architecture and biological performance of drug-loaded LbL nanoparticles. *Biomaterials* **2013,** *34* (21), 5328-35.

79.   Elbakry, A.; Zaky, A.; Liebl, R.; Rachel, R.; Goepferich, A.; Breunig, M., Layer-by-layer assembled gold nanoparticles for siRNA delivery. *Nano Lett.* **2009,** *9* (5), 2059-64.

80.   Poon, Z.; Chang, D.; Zhao, X.; Hammond, P. T., Layer-by-layer nanoparticles with a pH-sheddable layer for in vivo targeting of tumor hypoxia. *ACS Nano* **2011,** *5* (6), 4284-92.

81.   Shutava, T. G.; Balkundi, S. S.; Vangala, P.; Steffan, J. J.; Bigelow, R. L.; Cardelli, J. A.; O'Neal, D. P.; Lvov, Y. M., Layer-by-Layer-Coated Gelatin Nanoparticles as a Vehicle for Delivery of Natural Polyphenols. *ACS Nano* **2009,** *3* (7), 1877-85.

82.   Borges, J.; Mano, J. F., Molecular interactions driving the layer-by-layer assembly of multilayers. *Chem Rev* **2014,** *114* (18), 8883-942.

83.   Del Mercato, L. L.; Abbasi, A. Z.; Ochs, M.; Parak, W. J., Multiplexed sensing of ions with barcoded polyelectrolyte capsules. *ACS Nano* **2011,** *5* (12), 9668-74.

84.   Del Mercato, L. L.; Abbasi, A. Z.; Parak, W. J., Synthesis and characterization of ratiometric ion-sensitive polyelectrolyte capsules. *Small* **2011,** *7* (3), 351-63.

85.   Kazakova, L. I.; Shabarchina, L. I.; Sukhorukov, G. B., Co-encapsulation of enzyme and sensitive dye as a tool for fabrication of microcapsule based sensor for urea measuring. *Phys. Chem. Chem. Phys.* **2011,** *13* (23), 11110-7.

86.   Shchukin, D. G.; Sukhorukov, G. B., Nanoparticle Synthesis in Engineered Organic Nanoscale Reactors. *Adv. Mater.* **2004,** *16* (8), 671-682.

87.   Ariga, K.; Hill, J. P.; Ji, Q., Layer-by-layer assembly as a versatile bottom-up nanofabrication technique for exploratory research and realistic application. *Phys. Chem. Chem. Phys.* **2007,** *9* (19), 2319-40.

88.   Dang, X.; Gu, L.; Qi, J.; Correa, S.; Zhang, G.; Belcher, A. M.; Hammond, P. T., Layer-by-layer assembled fluorescent probes in the second near-infrared window for systemic delivery and detection of

ovarian cancer. *Proc Natl Acad Sci U S A* **2016**, *113* (19), 5179-84.

89.   Ai, H., Layer-by-layer capsules for magnetic resonance imaging and drug delivery. *Adv. Drug Del. Rev.* **2011**, *63* (9), 772-788.

90.   Such, G. K.; Johnston, A. P. R.; Caruso, F., Engineered hydrogen-bonded polymer multilayers: from assembly to biomedical applications. *Chem. Soc. Rev.* **2011**, *40* (1), 19-29.

91.   Shutava, T.; Prouty, M.; Kommireddy, D.; Lvov, Y., pH responsive decomposable layer-by-layer nanofilms and capsules on the basis of tannic acid. *Macromolecules* **2005**, *38* (7), 2850-2858.

92.   De Temmerman, M.-L.; Demeester, J.; De Vos, F.; De Smedt, S. C., Encapsulation Performance of Layer-by-Layer Microcapsules for Proteins. *Biomacromolecules* **2011**, *12* (4), 1283-1289.

93.   Ochs, C. J.; Such, G. K.; Caruso, F., Modular Assembly of Layer-by-Layer Capsules with Tailored Degradation Profiles. *Langmuir* **2011**, *27* (4), 1275-1280.

94.   Vergaro, V.; Scarlino, F.; Bellomo, C.; Rinaldi, R.; Vergara, D.; Maffia, M.; Baldassarre, F.; Giannelli, G.; Zhang, X.; Lvov, Y. M.; Leporatti, S., Drug-loaded polyelectrolyte microcapsules for sustained targeting of cancer cells. *Adv. Drug Del. Rev.* **2011**, *63* (9), 847-863.

95.   Tong, W.; Song, X.; Gao, C., Layer-by-layer assembly of microcapsules and their biomedical applications. *Chem. Soc. Rev.* **2012**, *41* (18), 6103-6124.

96.   Yoon, H.-J.; Lim, T. G.; Kim, J.-H.; Cho, Y. M.; Kim, Y. S.; Chung, U. S.; Kim, J. H.; Choi, B. W.; Koh, W.-G.; Jang, W.-D., Fabrication of Multifunctional Layer-by-Layer Nanocapsules toward the Design of Theragnostic Nanoplatform. *Biomacromolecules* **2014**, *15* (4), 1382-1389.

97.   Hammond, P. T., Polyelectrolyte multilayered nanoparticles: using nanolayers for controlled and targeted systemic release. *Nanomedicine* **2012**, *7* (5), 619-622.

98.   Caruso, F.; Caruso, R. A.; Möhwald, H., Nanoengineering of inorganic and hybrid hollow spheres by colloidal templating. *Science* **1998**, *282* (5391), 1111-1114.

99.   Donath, E.; Sukhorukov, G. B.; Caruso, F.; Davis, S. A.; Möhwald, H., Novel Hollow Polymer Shells by Colloid-Templated Assembly of Polyelectrolytes. *Angew. Chemie. Int. Ed.* **1998**, *37* (16), 2201-2205.

100.   Shutava, T. G.; Balkundi, S. S.; Vangala, P.; Steffan, J. J.; Bigelow, R. L.; Cardelli, J. A.; O'Neal, D. P.; Lvov, Y. M., Layer-by-Layer-Coated Gelatin Nanoparticles as a Vehicle for Delivery of Natural Polyphenols. *ACS Nano* **2009**, *3* (7), 1877-1885.

101.   Schneider, G.; Decher, G., From Functional Core/Shell Nanoparticles Prepared via Layer-by-Layer Deposition to Empty Nanospheres. *Nano Lett.* **2004**, *4* (10), 1833-1839.

102.   Zahr, A. S.; de Villiers, M.; Pishko, M. V., Encapsulation of drug nanoparticles in self-assembled macromolecular nanoshells. *Langmuir* **2005**, *21* (1), 403-410.

103.   Agarwal, A.; Lvov, Y.; Sawant, R.; Torchilin, V., Stable nanocolloids of poorly soluble drugs with high drug content prepared using the combination of sonication and layer-by-layer technology. *J. Controlled Release* **2008**, *128* (3), 255-260.

104.   Poon, Z.; Chang, D.; Zhao, X.; Hammond, P. T., Layer-by-Layer Nanoparticles with a pH-Sheddable Layer for in Vivo Targeting of Tumor Hypoxia. *Acs Nano* **2011**, *5* (6), 4284-4292.

105.   Poon, Z.; Lee, J. B.; Morton, S. W.; Hammond, P. T., Controlling in Vivo Stability and Biodistribution in Electrostatically Assembled Nanoparticles for Systemic Delivery. *Nano Lett.* **2011**, *11* (5), 2096-2103.

106.   Dreaden, E. C.; Morton, S. W.; Shopsowitz, K. E.; Choi, J.-H.; Deng, Z. J.; Cho, N.-J.; Hammond, P. T., Bimodal Tumor-Targeting from Microenvironment Responsive Hyaluronan Layer-by-Layer (LbL) Nanoparticles. *ACS Nano* **2014**, *8* (8), 8374-8382.

107.   Perrault, S. D.; Walkey, C.; Jennings, T.; Fischer, H. C.; Chan, W. C. W., Mediating Tumor Targeting Efficiency of Nanoparticles Through Design. *Nano Lett.* **2009**, *9* (5), 1909-1915.

108.   NCI Dictionary of Cancer Terms. National Cancer Institute: 2015.

109.   Dreaden, E. C.; El-Sayed, M. A.; El-Sayed, I. H., Nanotechnology and Nanostructures Applied to

Head and Neck Cancer. In *Nanomedicine and Cancer*, Preedy, V. R.; Srirajaskanthan, R., Eds. Science Publishers: Enfield, NH, 2011.

110.   Dreaden, E.; El-Sayed, I.; El-Sayed, M., Structure-Activity Relationships For Tumor-Targeting Gold nanoparticles. In *Frontiers of Nanobiomedical Research*, World Scientific: Hackensack: 2014; Vol. 1.

111.   Shah, N. J.; Hsu, B. B.; Dreaden, E. C.; Hammond, P. T., Engineering Layer-by-Layer Thin Films for Multiscale and Multidrug Delivery Applications. In *Layer-by-Layer Films for Biomedical Applications*, Picart, C.; Caruso, F.; Voegel, J.-C., Eds. Wiley-VCH: Weinheim: 2014.

112.   Deng, Z. J.; Morton, S. W.; Ben-Akiva, E.; Dreaden, E. C.; Shopsowitz, K. E.; Hammond, P. T., Layer-by-Layer Nanoparticles for Systemic Codelivery of an Anticancer Drug and siRNA for Potential Triple-Negative Breast Cancer Treatment. *ACS Nano* **2013,** *7* (11), 9571-9584.

113.   Morton, S. W.; Poon, Z.; Hammond, P. T., The architecture and biological performance of drug-loaded LbL nanoparticles. *Biomaterials* **2013,** *34* (21), 5328-5335.

114.   Morton, S. W.; Herlihy, K. P.; Shopsowitz, K. E.; Deng, Z. J.; Chu, K. S.; Bowerman, C. J.; DeSimone, J. M.; Hammond, P. T., Scalable Manufacture of Built-to-Order Nanomedicine: Spray-Assisted Layer-by-Layer Functionalization of PRINT Nanoparticles. *Adv. Mater.* **2013,** *25* (34), 4707-4713.

115.   Roh, Y. H.; Lee, J. B.; Shopsowitz, K. E.; Dreaden, E. C.; Morton, S. W.; Poon, Z.; Hong, J.; Yamin, I.; Bonner, D. K.; Hammond, P. T., Layer-by-Layer Assembled Antisense DNA Microsponge Particles for Efficient Delivery of Cancer Therapeutics. *ACS Nano* **2014,** *8* (10), 9767-9780.

116.   Dreaden, E. C.; Kong, Y. W.; Morton, S. W.; Correa, S.; Choi, K. Y.; Shopsowitz, K. E.; Renggli, K.; Drapkin, R.; Yaffe, M. B.; Hammond, P. T., Tumor-Targeted Synergistic Blockade of MAPK and PI3K from a Layer-by-Layer Nanoparticle. *Clin. Cancer. Res.* **2015,** *21* (19), 4410-4419.

117.   Choi, J.-H.; Kim, S.-O.; Linardy, E.; Dreaden, E. C.; Zhdanov, V. P.; Hammond, P. T.; Cho, N.-J., Adsorption of hyaluronic acid on solid supports: Role of pH and surface chemistry in thin film self-assembly. *J. Coll. Interface Sci.* **2015,** *448*, 197-207.

118.   Choi, J.-H.; Kim, S.-O.; Linardy, E.; Dreaden, E. C.; Zhdanov, V. P.; Hammond, P. T.; Cho, N.-J., Influence of pH and Surface Chemistry on Poly(l-lysine) Adsorption onto Solid Supports Investigated by Quartz Crystal Microbalance with Dissipation Monitoring. *J. Phys. Chem. B* **2015,** *119* (33), 10554-10565.

119.   Srinivasan, S.; Sawyer, P. N., Role of surface charge of the blood vessel wall, blood cells, and prosthetic materials in intravascular thrombosis. *J. Coll. Interface Sci.* **1970,** *32* (3), 456-463.

120.   Zuckerman, J. E.; Choi, C. H. J.; Han, H.; Davis, M. E., Polycation-siRNA nanoparticles can disassemble at the kidney glomerular basement membrane. *Proc. Natl. Acad. Sci. U.S.A.* **2012,** *109* (8), 3137-3142.

121.   Alkilany, A. M.; Nagaria, P. K.; Hexel, C. R.; Shaw, T. J.; Murphy, C. J.; Wyatt, M. D., Cellular Uptake and Cytotoxicity of Gold Nanorods: Molecular Origin of Cytotoxicity and Surface Effects. *Small* **2009,** *5* (6), 701-708.

122.   Eylar, E. H.; Madoff, M. A.; Brody, O. V.; Oncley, J. L., The Contribution of Sialic Acid to the Surface Charge of the Erythrocyte. *J. Biol. Chem.* **1962,** *237* (6), 1992-2000.

123.   Wilson, C. G.; Sisco, P. N.; Gadala-Maria, F. A.; Murphy, C. J.; Goldsmith, E. C., Polyelectrolyte-coated gold nanorods and their interactions with type I Collagen. *Biomaterials* **2009,** *30* (29), 5639-5648.

124.   Chithrani, B. D.; Ghazani, A. A.; Chan, W. C. W., Determining the Size and Shape Dependence of Gold Nanoparticle Uptake into Mammalian Cells. *Nano Lett.* **2006,** *6* (4), 662-668.

125.   Shimoni, O.; Yan, Y.; Wang, Y.; Caruso, F., Shape-Dependent Cellular Processing of Polyelectrolyte Capsules. *ACS Nano* **2013,** *7* (1), 522-530.

126.   Zan, X.; Garapaty, A.; Champion, J. A., Engineering Polyelectrolyte Capsules with Independently Controlled Size and Shape. *Langmuir* **2015,** *31* (27), 7601-7608.

127.   Wurster, E.-C.; Liebl, R.; Michaelis, S.; Robelek, R.; Wastl, D. S.; Giessibl, F. J.; Goepferich, A.; Breunig, M., Oligolayer-Coated Nanoparticles: Impact of Surface Topography at the Nanobio Interface. *ACS Appl. Mater. Interfaces* **2015,** *7* (15), 7891-7900.

128.   Ejima, H.; Yanai, N.; Best, J. P.; Sindoro, M.; Granick, S.; Caruso, F., Near-Incompressible Faceted Polymer Microcapsules from Metal-Organic Framework Templates. *Adv. Mater.* **2013,** *25* (40), 5767-5771.

129.   Hartmann, R.; Weidenbach, M.; Neubauer, M.; Fery, A.; Parak, W. J., Stiffness-Dependent In Vitro Uptake and Lysosomal Acidification of Colloidal Particles. *Angew. Chemie Int. Ed.* **2015,** *54* (4), 1365-1368.

130.   Sun, H.; Wong, E. H. H.; Yan, Y.; Cui, J.; Dai, Q.; Guo, J.; Qiao, G. G.; Caruso, F., The role of capsule stiffness on cellular processing. *Chem. Sci.* **2015,** *6* (6), 3505-3514.

131.   Monopoli, M.; Walczyk, D.; Campbell, A.; Elia, G.; Lynch, I., Physical-chemical aspects of protein corona: relevance to in vitro and in vivo biological impacts of nanoparticles. *J. Am. Chem. Soc.* **2011,** *133*, 2525.

132.   Lundqvist, M.; Stigler, J.; Elia, G.; Lynch, I.; Cedervall, T.; Dawson, K., Nanoparticle size and surface properties determine the protein corona with possible implications for biological impacts. *Proc. Natl. Acad. Sci. U.S.A.* **2008,** *105*, 14265.

133.   Nel, A. E.; Mädler, L.; Velegol, D.; Xia, T.; Hoek, E. M. V.; Somasundaran, P.; Klaessig, F.; Castranova, V.; Thompson, M., Understanding biophysicochemical interactions at the nano-bio interface. *Nat. Mater.* **2009,** *8* (7), 543-557.

134.   Ramasamy, T.; Haidar, Z. S.; Tran, T. H.; Choi, J. Y.; Jeong, J.-H.; Shin, B. S.; Choi, H.-G.; Yong, C. S.; Kim, J. O., Layer-by-layer assembly of liposomal nanoparticles with PEGylated polyelectrolytes enhances systemic delivery of multiple anticancer drugs. *Acta Biomater.* **2014,** *10* (12), 5116-5127.

135.   Zhou, J.; Moya, S.; Ma, L.; Gao, C.; Shen, J., Polyelectrolyte Coated PLGA Nanoparticles: Templation and Release Behavior. *Macromol. Biosci.* **2009,** *9* (4), 326-335.

136.   Kim, J. S.; Rieter, W. J.; Taylor, K. M. L.; An, H.; Lin, W.; Lin, W., Self-Assembled Hybrid Nanoparticles for Cancer-Specific Multimodal Imaging. *J. Am. Chem. Soc.* **2007,** *129* (29), 8962-8963.

137.   Zhou, J.; Romero, G.; Rojas, E.; Ma, L.; Moya, S.; Gao, C., Layer by layer chitosan/alginate coatings on poly(lactide-co-glycolide) nanoparticles for antifouling protection and Folic acid binding to achieve selective cell targeting. *J. Coll. Interface Sci.* **2010,** *345* (2), 241-247.

138.   Boyer, C.; Bousquet, A.; Rondolo, J.; Whittaker, M. R.; Stenzel, M. H.; Davis, T. P., Glycopolymer Decoration of Gold Nanoparticles Using a LbL Approach. *Macromolecules* **2010,** *43* (8), 3775-3784.

139.   Xie, L.; Tong, W.; Yu, D.; Xu, J.; Li, J.; Gao, C., Bovine serum albumin nanoparticles modified with multilayers and aptamers for pH-responsive and targeted anti-cancer drug delivery. *J. Mater. Chem.* **2012,** *22* (13), 6053-6060.

140.   Liao, W.-C.; Lu, C.-H.; Hartmann, R.; Wang, F.; Sohn, Y. S.; Parak, W. J.; Willner, I., Adenosine Triphosphate-Triggered Release of Macromolecular and Nanoparticle Loads from Aptamer/DNA-Cross-Linked Microcapsules. *ACS Nano* **2015,** *9* (9), 9078-9086.

141.   Masereel, B.; Dinguizli, M.; Bouzin, C.; Moniotte, N.; Feron, O.; Gallez, B.; Vander Borght, T.; Michiels, C.; Lucas, S., Antibody immobilization on gold nanoparticles coated layer-by-layer with polyelectrolytes. *J. Nanopart. Res.* **2011,** *13* (4), 1573-1580.

142.   Kunishima, M.; Kawachi, C.; Hioki, K.; Terao, K.; Tani, S., Formation of carboxamides by direct condensation of carboxylic acids and amines in alcohols using a new alcohol- and water-soluble condensing agent: DMT-MM. *Tetrahedron* **2001,** *57* (8), 1551-1558.

143.   Morton, S. W.; Shah, N. J.; Quadir, M. A.; Deng, Z. J.; Poon, Z.; Hammond, P. T., Osteotropic Therapy via Targeted Layer-by-Layer Nanoparticles. *Adv. Healthcare Mater.* **2014,** *3* (6), 867-875.

144.   Yang, X.-Z.; Du, J.-Z.; Dou, S.; Mao, C.-Q.; Long, H.-Y.; Wang, J., Sheddable Ternary Nanoparticles for Tumor Acidity-Targeted siRNA Delivery. *ACS Nano* **2012,** *6* (1), 771-781.

145.   Panyam, J.; Labhasetwar, V., Biodegradable nanoparticles for drug and gene delivery to cells and tissue. *Adv. Drug Del. Rev.* **2003,** *55* (3), 329-347.

146.   Zhou, J.; Romero, G.; Rojas, E.; Ma, L.; Moya, S.; Gao, C., Layer by layer chitosan/alginate coat-

ings on poly(lactide-co-glycolide) nanoparticles for antifouling protection and Folic acid binding to achieve selective cell targeting. *J. Colloid Interface Sci.* **2010,** *345* (2), 241-247.

147.   Liu, G.; Tian, J.; Liu, C.; Ai, H.; Gu, Z.; Gou, J.; Mo, X., Cell labeling efficiency of layer-by-layer self-assembly modified silica nanoparticles. *J. Mater. Res.* **2009,** *24* (04), 1317-1321.

148.   Fukui, Y.; Fujimoto, K., The Preparation of Sugar Polymer-Coated Nanocapsules by the Layer-by-Layer Deposition on the Liposome. *Langmuir* **2009,** *25* (17), 10020-10025.

149.   Kwon, H.-Y.; Lee, J.-Y.; Choi, S.-W.; Jang, Y.; Kim, J.-H., Preparation of PLGA nanoparticles containing estrogen by emulsification–diffusion method. *Colloids Surf., A* **2001,** *182* (1–3), 123-130.

150.   Luo, R.; Neu, B.; Venkatraman, S. S., Surface Functionalization of Nanoparticles to Control Cell Interactions and Drug Release. *Small* **2012,** *8* (16), 2585-2594.

151.   Argyo, C.; Weiss, V.; Bräuchle, C.; Bein, T., Multifunctional Mesoporous Silica Nanoparticles as a Universal Platform for Drug Delivery. *Chem. Mater.* **2014,** *26* (1), 435-451.

152.   Zhang, K.; Xu, L.-L.; Jiang, J.-G.; Calin, N.; Lam, K.-F.; Zhang, S.-J.; Wu, H.-H.; Wu, G.-D.; Albela, B.; Bonneviot, L.; Wu, P., Facile Large-Scale Synthesis of Monodisperse Mesoporous Silica Nanospheres with Tunable Pore Structure. *J. Am. Chem. Soc.* **2013,** *135* (7), 2427-2430.

153.   Gao, Y.; Chen, Y.; Ji, X.; He, X.; Yin, Q.; Zhang, Z.; Shi, J.; Li, Y., Controlled Intracellular Release of Doxorubicin in Multidrug-Resistant Cancer Cells by Tuning the Shell-Pore Sizes of Mesoporous Silica Nanoparticles. *ACS Nano* **2011,** *5* (12), 9788-9798.

154.   Meng, H.; Liong, M.; Xia, T.; Li, Z.; Ji, Z.; Zink, J. I.; Nel, A. E., Engineered Design of Mesoporous Silica Nanoparticles to Deliver Doxorubicin and P-Glycoprotein siRNA to Overcome Drug Resistance in a Cancer Cell Line. *ACS Nano* **2010,** *4* (8), 4539-4550.

155.   Lu, J.; Liong, M.; Zink, J. I.; Tamanoi, F., Mesoporous Silica Nanoparticles as a Delivery System for Hydrophobic Anticancer Drugs. *Small* **2007,** *3* (8), 1341-1346.

156.   Shu, S.; Zhang, X.; Wu, Z.; Wang, Z.; Li, C., Gradient cross-linked biodegradable polyelectrolyte nanocapsules for intracellular protein drug delivery. *Biomaterials* **2010,** *31* (23), 6039-6049.

157.   Wang, Y.; Yan, Y.; Cui, J.; Hosta-Rigau, L.; Heath, J. K.; Nice, E. C.; Caruso, F., Encapsulation of Water-Insoluble Drugs in Polymer Capsules Prepared Using Mesoporous Silica Templates for Intracellular Drug Delivery. *Adv. Mater.* **2010,** *22* (38), 4293-+.

158.   Hudson, S. P.; Padera, R. F.; Langer, R.; Kohane, D. S., The biocompatibility of mesoporous silicates. *Biomaterials* **2008,** *29* (30), 4045-4055.

159.   Chen, Y.; Chen, H.; Shi, J., In Vivo Bio-Safety Evaluations and Diagnostic/Therapeutic Applications of Chemically Designed Mesoporous Silica Nanoparticles. *Adv. Mater.* **2013,** *25* (23), 3144-3176.

160.   Shu, S.; Sun, C.; Zhang, X.; Wu, Z.; Wang, Z.; Li, C., Hollow and degradable polyelectrolyte nanocapsules for protein drug delivery. *Acta Biomater.* **2010,** *6* (1), 210-217.

161.   Wohl, B. M.; Engbersen, J. F. J., Responsive layer-by-layer materials for drug delivery. *J. Controlled Release* **2012,** *158* (1), 2-14.

162.   Yang, Y.-J.; Tao, X.; Hou, Q.; Ma, Y.; Chen, X.-L.; Chen, J.-F., Mesoporous silica nanotubes coated with multilayered polyelectrolytes for pH-controlled drug release. *Acta Biomater.* **2010,** *6* (8), 3092-3100.

163.   Li, J.; Qu, X.; Payne, G. F.; Zhang, C.; Zhang, Y.; Li, J.; Ren, J.; Hong, H.; Liu, C., Biospecific Self-Assembly of a Nanoparticle Coating for Targeted and Stimuli-Responsive Drug Delivery. *Adv. Funct. Mater.* **2015,** *25* (9), 1404-1417.

164.   Zhang, C.; Qu, X.; Li, J.; Hong, H.; Li, J.; Ren, J.; Payne, G. F.; Liu, C., Biofabricated Nanoparticle Coating for Liver-Cell Targeting. *Adv. Healthcare Mater.* **2015,** *4* (13), 1972-81.

165.   Dai, W.; Jin, W.; Zhang, J.; Wang, X.; Wang, J.; Zhang, X.; Wan, Y.; Zhang, Q., Spatiotemporally Controlled Co-delivery of Anti-vasculature Agent and Cytotoxic Drug by Octreotide-Modified Stealth Liposomes. *Pharm. Res.* **2012,** *29* (10), 2902-2911.

166.   Morton, S. W.; Lee, M. J.; Deng, Z. J.; Dreaden, E. C.; Siouve, E.; Shopsowitz, K. E.; Shah, N.

J.; Yaffe, M. B.; Hammond, P. T., A nanoparticle-based combination chemotherapy delivery system for enhanced tumor killing by dynamic rewiring of signaling pathways. *Sci. Signal.* **2014,** *7* (325), ra44.

167.   Al-Saadi, A.; Yu, C. H.; Khutoryanskiy, V. V.; Shih, S.-J.; Crossley, A.; Tsang, S. C., Layer-by-Layer Electrostatic Entrapment of Protein Molecules on Superparamagnetic Nanoparticle: A New Strategy to Enhance Adsorption Capacity and Maintain Biological Activity. *J. Phys. Chem. C* **2009,** *113* (34), 15260-15265.

168.   Yoshida, K.; Sato, K.; Anzai, J.-i., Layer-by-layer polyelectrolyte films containing insulin for pH-triggered release. *J. Mater. Chem.* **2010,** *20* (8), 1546-1552.

169.   Trimaille, T.; Pichot, C.; Delair, T., Surface functionalization of poly(d,l-lactic acid) nanoparticles with poly(ethylenimine) and plasmid DNA by the layer-by-layer approach. *Colloids Surf., A* **2003,** *221* (1–3), 39-48.

170.   Thierry, B.; Kujawa, P.; Tkaczyk, C.; Winnik, F. M.; Bilodeau, L.; Tabrizian, M., Delivery Platform for Hydrophobic Drugs: Prodrug Approach Combined with Self-Assembled Multilayers. *J. Am. Chem. Soc.* **2005,** *127* (6), 1626-1627.

171.   Wood, K. C.; Chuang, H. F.; Batten, R. D.; Lynn, D. M.; Hammond, P. T., Controlling interlayer diffusion to achieve sustained, multiagent delivery from layer-by-layer thin films. *Proc. Natl. Acad. Sci. USA* **2006,** *103* (27), 10207-10212.

172.   Boudou, T.; Crouzier, T.; Ren, K.; Blin, G.; Picart, C., Multiple Functionalities of Polyelectrolyte Multilayer Films: New Biomedical Applications. *Adv. Mater.* **2010,** *22* (4), 441-467.

173.   Pavlukhina, S.; Sukhishvili, S., Polymer assemblies for controlled delivery of bioactive molecules from surfaces. *Adv. Drug Del. Rev.* **2011,** *63* (9), 822-836.

174.   Hammond, P. T., Engineering Materials Layer-by-Layer: Challenges and Opportunities in Multilayer Assembly. *AICHE J.* **2011,** *57* (11), 2928-2940.

175.   Lvov, Y.; Decher, G.; Sukhorukov, G., Assembly of thin films by means of successive deposition of alternate layers of DNA and poly(allylamine). *Macromolecules* **1993,** *26* (20), 5396-5399.

176.   Schuler, C.; Caruso, F., Decomposable hollow biopolymer-based capsules. *Biomacromolecules* **2001,** *2* (3), 921-926.

177.   Dudnik, V.; Sukhorukov, G. B.; Radtchenko, I. L.; Mohwald, H., Coating of colloidal particles by controlled precipitation of polymers. *Macromolecules* **2001,** *34* (7), 2329-2334.

178.   He, P. G.; Bayachou, M., Layer-by-layer fabrication and characterization of DNA-wrapped single-walled carbon nanotube particles. *Langmuir* **2005,** *21* (13), 6086-6092.

179.   Shchukin, D. G.; Patel, A. A.; Sukhorukov, G. B.; Lvov, Y. M., Nanoassembly of Biodegradable Microcapsules for DNA Encasing. *J. Am. Chem. Soc.* **2004,** *126* (11), 3374-3375.

180.   Reibetanz, U.; Claus, C.; Typlt, E.; Hofmann, J.; Donath, E., Defoliation and Plasmid Delivery with Layer-by-Layer Coated Colloids. *Macromol. Biosci.* **2006,** *6* (2), 153-160.

181.   Elbakry, A.; Zaky, A.; Liebl, R.; Rachel, R.; Goepferich, A.; Breunig, M., Layer-by-Layer Assembled Gold Nanoparticles for siRNA Delivery. *Nano Lett.* **2009,** *9* (5), 2059-2064.

182.   Elbakry, A.; Wurster, E.-C.; Zaky, A.; Liebl, R.; Schindler, E.; Bauer-Kreisel, P.; Blunk, T.; Rachel, R.; Goepferich, A.; Breunig, M., Layer-by-Layer Coated Gold Nanoparticles: Size-Dependent Delivery of DNA into Cells. *Small* **2012,** *8* (24), 3847-3856.

183.   Lee, M.-Y.; Park, S.-J.; Park, K.; Kim, K. S.; Lee, H.; Hahn, S. K., Target-Specific Gene Silencing of Layer-by-Layer Assembled Gold–Cysteamine/siRNA/PEI/HA Nanocomplex. *ACS Nano* **2011,** *5* (8), 6138-6147.

184.   Tan, Y. F.; Mundargi, R. C.; Chen, M. H. A.; Lessig, J.; Neu, B.; Venkatraman, S. S.; Wong, T. T., Layer-by-Layer Nanoparticles as an Efficient siRNA Delivery Vehicle for SPARC Silencing. *Small* **2014,** *10* (9), 1790-1798.

185.   Guo, S.; Huang, Y.; Jiang, Q.; Sun, Y.; Deng, L.; Liang, Z.; Du, Q.; Xing, J.; Zhao, Y.; Wang, P. C.; Dong, A.; Liang, X.-J., Enhanced Gene Delivery and siRNA Silencing by Gold Nanoparticles Coated with

Charge-Reversal Polyelectrolyte. *ACS Nano* **2010**, *4* (9), 5505-5511.

186.   Green, J. J.; Zugates, G. T.; Tedford, N. C.; Huang, Y. H.; Griffith, L. G.; Lauffenburger, D. A.; Sawicki, J. A.; Langer, R.; Anderson, D. G., Combinatorial Modification of Degradable Polymers Enables Transfection of Human Cells Comparable to Adenovirus. *Adv. Mater.* **2007**, *19* (19), 2836-2842.

187.   Bishop, C. J.; Tzeng, S. Y.; Green, J. J., Degradable polymer-coated gold nanoparticles for co-delivery of DNA and siRNA. *Acta Biomater.* **2015**, *11*, 393-403.

188.   Han, L.; Zhao, J.; Liu, J.; Duan, X.-L.; Li, L.-H.; Wei, X.-F.; Wei, Y.; Liang, X.-J., A universal gene carrier platform for treatment of human prostatic carcinoma by p53 transfection. *Biomaterials* **2014**, *35* (9), 3110-3120.

189.   Han, L.; Zhao, J.; Zhang, X.; Cao, W.; Hu, X.; Zou, G.; Duan, X.; Liang, X.-J., Enhanced siRNA Delivery and Silencing Gold–Chitosan Nanosystem with Surface Charge-Reversal Polymer Assembly and Good Biocompatibility. *ACS Nano* **2012**, *6* (8), 7340-7351.

190.   Chen, Z.; Zhang, L.; He, Y.; Shen, Y.; Li, Y., Enhanced shRNA Delivery and ABCG2 Silencing by Charge-Reversible Layered Nanocarriers. *Small* **2015**, *11* (8), 952-962.

191.   Shen, J.; Kim, H.-C.; Mu, C.; Gentile, E.; Mai, J.; Wolfram, J.; Ji, L.-n.; Ferrari, M.; Mao, Z.-w.; Shen, H., Multifunctional Gold Nanorods for siRNA Gene Silencing and Photothermal Therapy. *Adv. Healthcare Mater.* **2014**, *3* (10), 1629-1637.

192.   Yang, Z.; Liu, T.; Xie, Y.; Sun, Z.; Liu, H.; Lin, J.; Liu, C.; Mao, Z.-W.; Nie, S., Chitosan layered gold nanorods as synergistic therapeutics for photothermal ablation and gene silencing in triple-negative breast cancer. *Acta Biomater.* **2015**, *25*, 194-204.

193.   Fisher, E.; Boenink, M.; van der Burg, S.; Woodbury, N., Responsible healthcare innovation: anticipatory governance of nanodiagnostics for theranostics medicine. *Expert Rev. Mol. Diagn.* **2012**, *12* (8), 857-870.

194.   Cheng, L.; Yang, K.; Li, Y.; Zeng, X.; Shao, M.; Lee, S.-T.; Liu, Z., Multifunctional nanoparticles for upconversion luminescence/MR multimodal imaging and magnetically targeted photothermal therapy. *Biomaterials* **2012**, *33* (7), 2215-2222.

195.   Wang, X.; Liu, K.; Yang, G.; Cheng, L.; He, L.; Liu, Y.; Li, Y.; Guo, L.; Liu, Z., Near-infrared light triggered photodynamic therapy in combination with gene therapy using upconversion nanoparticles for effective cancer cell killing. *Nanoscale* **2014**, *6* (15), 9198-9205.

196.   Chen, H.; Chi, X.; Li, B.; Zhang, M.; Ma, Y.; Achilefu, S.; Gu, Y., Drug loaded multilayered gold nanorods for combined photothermal and chemotherapy. *Biomater. Sci.* **2014**, *2* (7), 996-1006.

197.   Dickerson, E. B.; Dreaden, E. C.; Huang, X.; El-Sayed, I. H.; Chu, H.; Pushpanketh, S.; McDonald, J. F.; El-Sayed, M. A., Gold nanorod assisted near-infrared plasmonic photothermal therapy (PPTT) of squamous cell carcinoma in mice. *Cancer Lett.* **2008**, *269* (1), 57-66.

198.   Dreaden, E. C.; Mackey, M. A.; Huang, X.; Kang, B.; El-Sayed, M. A., Beating cancer in multiple ways using nanogold. *Chem. Soc. Rev.* **2011**, *40* (7), 3391-3404.

199.   Dreaden, E. C.; Alkilany, A. M.; Huang, X.; Murphy, C. J.; El-Sayed, M. A., The Golden Age: Gold Nanoparticles for Biomedicine. *Chem. Soc. Rev.* **2012**, *41*, 2740-2779.

200.   Dreaden, E. C.; Austin, L. A.; Mackey, M. A.; El-Sayed, M. A., Size matters: gold nanoparticles in targeted cancer drug delivery. *Therapeutic Delivery* **2012**, *3* (4), 457-478.

201.   Dreaden, E. C.; El-Sayed, M. A., Detecting and Destroying Cancer Cells in More than One Way with Noble Metals and Different Confinement Properties on the Nanoscale. *Acc. Chem. Res.* **2012**, *45* (11), 1854-1865.

202.   Dreaden, E. C.; Mwakwari, S. C.; Austin, L. A.; Kieffer, M. J.; Oyelere, A. K.; El-Sayed, M. A., Small Molecule–Gold Nanorod Conjugates Selectively Target and Induce Macrophage Cytotoxicity towards Breast Cancer Cells. *Small* **2012**, *8* (18), 2819-2822.

203.   Austin, L.; Mackey, M.; Dreaden, E.; El-Sayed, M., The optical, photothermal, and facile surface chemical properties of gold and silver nanoparticles in biodiagnostics, therapy, and drug delivery. *Archives*

Toxicol. **2014**, *88* (7), 1391-1417.

204.   Hong, G.; Zou, Y.; Antaris, A. L.; Diao, S.; Wu, D.; Cheng, K.; Zhang, X.; Chen, C.; Liu, B.; He, Y.; Wu, J. Z.; Yuan, J.; Zhang, B.; Tao, Z.; Fukunaga, C.; Dai, H., Ultrafast fluorescence imaging in vivo with conjugated polymer fluorophores in the second near-infrared window. *Nat Commun* **2014**, *5*.

205.   Hong, G.; Lee, J. C.; Jha, A.; Diao, S.; Nakayama, K. H.; Hou, L.; Doyle, T. C.; Robinson, J. T.; Antaris, A. L.; Dai, H.; Cooke, J. P.; Huang, N. F., Near-Infrared II Fluorescence for Imaging Hindlimb Vessel Regeneration With Dynamic Tissue Perfusion Measurement. *Circ. Cardiovasc. Imaging* **2014**, *7* (3), 517-525.

206.   Hong, G.; Lee, J. C.; Robinson, J. T.; Raaz, U.; Xie, L.; Huang, N. F.; Cooke, J. P.; Dai, H., Multifunctional in vivo vascular imaging using near-infrared II fluorescence. *Nat. Med.* **2012**, *18* (12), 1841-1846.

207.   Hong, G.; Robinson, J. T.; Zhang, Y.; Diao, S.; Antaris, A. L.; Wang, Q.; Dai, H., In vivo fluorescence imaging with Ag2S quantum dots in the second near-infrared region. *Angew. Chem.* **2012**, *51* (39), 9818-21.

208.   Robinson, J. T.; Hong, G.; Liang, Y.; Zhang, B.; Yaghi, O. K.; Dai, H., In Vivo Fluorescence Imaging in the Second Near-Infrared Window with Long Circulating Carbon Nanotubes Capable of Ultrahigh Tumor Uptake. *J. Am. Chem. Soc.* **2012**, *134* (25), 10664-10669.

209.   Hong, G.; Diao, S.; Antaris, A. L.; Dai, H., Carbon Nanomaterials for Biological Imaging and Nanomedicinal Therapy. *Chem. Rev.* **2015**, *115* (19), 10816-10906.

210.   Ghosh, D.; Bagley, A. F.; Na, Y. J.; Birrer, M. J.; Bhatia, S. N.; Belcher, A. M., Deep, noninvasive imaging and surgical guidance of submillimeter tumors using targeted M13-stabilized single-walled carbon nanotubes. *Proc. Natl. Acad. Sci. USA* **2014**, *111* (38), 13948-13953.

211.   Schneider, G.; Decher, G., Functional Core/Shell Nanoparticles via Layer-by-Layer Assembly. Investigation of the Experimental Parameters for Controlling Particle Aggregation and for Enhancing Dispersion Stability. *Langmuir* **2008**, *24* (5), 1778-1789.

212.   Yan, Y.; Björnmalm, M.; Caruso, F., Assembly of Layer-by-Layer Particles and Their Interactions with Biological Systems. *Chem. Mater.* **2014**, *26* (1), 452-460.

213.   Voigt, A.; Lichtenfeld, H.; Sukhorukov, G. B.; Zastrow, H.; Donath, E.; Bäumler, H.; Möhwald, H., Membrane Filtration for Microencapsulation and Microcapsules Fabrication by Layer-by-Layer Polyelectrolyte Adsorption. *Ind. Eng. Chem. Res.* **1999**, *38* (10), 4037-4043.

214.   Shchukin, D. G.; Kommireddy, D. S.; Zhao, Y.; Cui, T.; Sukhorukov, G. B.; Lvov, Y. M., Polyelectrolyte Micropatterning Using a Laminar-Flow Microfluidic Device. *Adv. Mater.* **2004**, *16* (5), 389-393.

215.   Priest, C.; Quinn, A.; Postma, A.; Zelikin, A. N.; Ralston, J.; Caruso, F., Microfluidic polymer multilayer adsorption on liquid crystal droplets for microcapsule synthesis. *Lab Chip* **2008**, *8* (12), 2182-2187.

216.   Kantak, C.; Beyer, S.; Yobas, L.; Bansal, T.; Trau, D., A 'microfluidic pinball' for on-chip generation of Layer-by-Layer polyelectrolyte microcapsules. *Lab Chip* **2011**, *11* (6), 1030-1035.

217.   Richardson, J. J.; Teng, D.; Björnmalm, M.; Gunawan, S. T.; Guo, J.; Cui, J.; Franks, G. V.; Caruso, F., Fluidized Bed Layer-by-Layer Microcapsule Formation. *Langmuir* **2014**, *30* (33), 10028-10034.

218.   Qi, A.; Chan, P.; Ho, J.; Rajapaksa, A.; Friend, J.; Yeo, L., Template-free Synthesis and Encapsulation Technique for Layer-by-Layer Polymer Nanocarrier Fabrication. *ACS Nano* **2011**, *5* (12), 9583-9591.

219.   Richardson, J. J.; Ejima, H.; Lörcher, S. L.; Liang, K.; Senn, P.; Cui, J.; Caruso, F., Preparation of Nano- and Microcapsules by Electrophoretic Polymer Assembly. *Angew. Chem.* **2013**, *52* (25), 6455-6458.

220.   DeVetter, B. M.; Sivapalan, S. T.; Patel, D. D.; Schulmerich, M. V.; Murphy, C. J.; Bhargava, R., Observation of Molecular Diffusion in Polyelectrolyte-Wrapped SERS Nanoprobes. *Langmuir* **2014**, *30* (29), 8931-8937.

Chapter 2. New methods for LbL synthesis

Layer-by-layer (LbL) self-assembly is a versatile technique from which multicomponent and stimuli-responsive nanoscale drug carriers can be constructed. Despite the benefits of LbL assembly, the conventional synthetic approach for fabricating LbL nanoparticles requires numerous purification steps that limit scale, yield, efficiency, and potential for clinical translation. This chapter describes a generalizable method for increasing throughput with LbL assembly by using highly scalable, closed-loop diafiltration to manage intermediate purification steps. This method facilitates highly controlled fabrication of diverse nanoscale LbL formulations smaller than 150 nm composed from solid-polymer, mesoporous silica, and liposomal vesicles. The technique allows for the deposition of a broad range of polyelectrolytes that included native polysaccharides, linear polypeptides, and synthetic polymers. In Section 2.3, we also explore the cytotoxicity, shelf life and long-term storage of LbL nanoparticles produced using this approach. We find that LbL coated systems can be reliably and rapidly produced: specifically, LbL-modified liposomes could be lyophilized, stored at room temperature, and reconstituted without compromising drug encapsulation or particle stability, thereby facilitating large scale applications.

2.1. Introduction to challenges of scale and translation

Multifunctional nanoscale therapies have the capacity to transform modern healthcare by providing greater control over the spatial and temporal release of drugs.[1-3] Formulations sized from 15 to 100 nm exhibit unique properties and functions that promote accumulation in target tissues while minimizing nonspecific clearance from the body.[4] These nanotherapies are by their own nature a complex composite of materials that can simultaneously protect, guide, and release biologically active compounds in a desirable manner. Complex materials, in turn, provide significant challenges from a translational point of view – particularly in terms of their eventual scalable fabrication. Effective nanoscale therapies must further exhibit adequate shelf lives under clinically relevant storage conditions in order to facilitate their eventual translation.

LbL assembly is a well-established technique for the solution-phase synthesis of hierarchical and multifunctional nanoscale therapeutics.[5-7] LbL nanoparticles can possess a range of desirable properties for drug and gene delivery due to the versatility granted by the technique. In its most frequently employed form, LbL assembly is driven by the electrostatic interaction between oppositely charged polyelectrolytes on a charged substrate. Possible substrates include colloids such as gold, polymer, silica, and liposomal nanoparticles, amongst others.[8-13] Along with the flexibility in the choice of a core substrate, any polyelectrolyte with a multivalent charge can be incorporated into an LbL construct, including native polysaccharides, nucleic acids, linear polypeptides, and synthetic polymers.[8, 14-16] The LbL technique has been well characterized and studied by the materials community since the fundamental concept of alternating electrostatic assembly was first described by Iler in 1966.[17-23] In addition to electrostatics, it is well documented that LbL assembly can be driven by a multitude of intermolecular interactions that include hydrogen bonding, covalent bonding, and biologically specific interactions.[24] More recent research into LbL nanomaterials has yielded important developments for a variety of fields including chemical sensing, catalysis, energy storage, optics, and drug delivery.[13, 25-29]

Several advances specifically highlight the promise of LbL nanoparticle systems for drug delivery, including the ability to generate novel hybrid organic-inorganic nanoparticles with tunable cell-particle interactions, and the generation of nanoparticle systems that can release combination drugs and small interfering RNA (siRNA) in a staged and synergistic fashion.[30-32] Importantly, the

thickness of polyelectrolyte multilayers formed by LbL is on the order of nanometers, providing investigators a high degree of control over the final size of an LbL nanoparticle. As generally the polymer film is very thin, the size of an LbL formulation is largely determined by the core substrate, which has been reported to be as small as 10 nm in diameter.[33-36] Using the LbL platform, researchers have been able to preserve the size of a conventional nanoparticle formulation while providing improved stability and environmentally sensitive functionalities that capitalize on cues from the tumor microenvironment to initiate cellular uptake.[15, 37] Additional functionalities provided by the multilayer film allows for tuning of drug release and the incorporation of therapeutics into the polymer film.[13, 31, 38]

Despite their numerous advantages, both basic research and clinical translation of LbL nanoparticles have been impeded by scalability problems associated with their preparation. Traditional preparation of these materials relies on centrifugal purification to eliminate excess polyelectrolyte, but this approach is both time-intensive and prone to causing irreversible aggregation of LbL particles. Unfortunately, centrifugation becomes much more problematic when transitioning from micro- to nanoscale formulations, due to the need to significantly increase the spin speed and time needed to isolate smaller particles. Work to optimize centrifugal protocols rely on meticulous optimization of polymer molecular weight, charge ratios, centrifugal force, and spin times.[39] Efforts to try and resolve problems with scalability have generated creative techniques including vacuum-filtration, atomization, microfluidic, electrophoresis, and fluidized bed-mediated LbL assembly.[40-46] While these innovative approaches do offer advances in efficacy and yield during the preparation of colloidal LbL materials, they place limitations on the types and sizes of materials that can be used, reducing LbL versatility. Our group previously described another LbL preparation method, which relies on PRINT® technology. While this approach is robust, it does not allow for the layering of many nanoparticle cores that are of great interest for drug delivery and theranostics, such as quantum dots, liposomes, and responsive self-assembled polymeric colloids.[47]

To address the need for an accessible, robust, and scalable approach for preparing diverse LbL nanoparticles, we incorporated tangential flow filtration (TFF) into our synthetic workflow. TFF works by a process known as diafiltration, where permeable molecules are removed from a solution while passing through a hollow ultrafiltration membrane. Diafiltration for nanoparticle purification has been well characterized for colloidal solutions.[48-49] When a solution of LbL nanoparticles

is pumped through the fiber membrane, the permeable polyelectrolytes rapidly exit through the pores in the membrane and are removed from the system. Meanwhile, the larger nanoparticles are retained and re-circulated through the system until the desired purity is reached. The sample volume can be held constant by the introduction of replacement buffer at the same rate that waste is removed from the system, allowing the purification to be continued for any desired amount of time. Collected waste (permeate) solution can also be recovered and re-concentrated in order to recycle reagents and reduce synthetic costs. Furthermore, these devices are easily scalable to prepare samples ranging anywhere from a single milliliter to more than a liter.

Lohse and colleagues previously described the use of a TFF-based reactor for the synthesis and functionalization of gold nanoparticles, including LbL modification with poly(acrylic acid) and polyallylamine.[50] This early application of TFF towards LbL modification faced issues of efficient purification, requiring washing nanoparticles with upwards of 20 volume equivalents before achieving sufficient purity to perform the next deposition step. Inefficient polyelectrolyte removal also appeared to cause off-target toxicity due to the carryover of free polycations. Here, we employ high surface-area, porous hollow-fiber filtration cassettes that provide improved flux rates that allow TFF purification to occur more rapidly and completely. Indeed, very recently the work by Björnmalm and coworkers demonstrated the effective preparation of LbL particles with this new class of membrane, with more emphasis on the generation of micrometer- and submicrometer-sized particles and capsules.[51] Here, we specifically describe a generalizable method for using TFF to prepare LbL nanoparticles ranging from 40 to 150 nm, which are within the size range important for systemic drug delivery, tumor targeting, and tissue penetration. We document major improvements in efficiency and yield using this method relative to traditional protocols. Furthermore, we demonstrate the compatibility of this method with a broad range of biomedically relevant materials through the fabrication of LbL nanoparticles composed from a variety of substrates and biocompatible polyelectrolytes, and include several novel LbL formulations. To highlight the clinical relevance of these materials, we go on to demonstrate that LbL nanoparticles fabricated using this new technique are biocompatible, and can be stably stored in both refrigerated and lyophilized states.

2.2. Results: Streamlining LbL nanoparticle synthesis using tangential flow filtration for improved scale and yield

2.2.1. Preparation of filter membranes for LbL assembly

In LbL assembly, the role of salts is well known to promote the generation of thicker films by shielding the Coulombic repulsion between adsorbed polyelectrolytes.[39, 52-54] Extensive discussion relating to salt and bulk conditions in colloidal LbL is provided in Chapter 4, but here we briefly outline some of the challenges associated with working with salts in the context of the interlayer purification steps.

While salts can provide a measure of control over film thickness, they also promote particle flocculation by masking the repulsive forces between distinct particles. The inclusion of salt is particularly problematic in LbL formulations where the researcher must balance the electrostatic repulsion between polyelectrolytes that are also subject to intermolecular attractive forces like hydrogen bonding. Consideration for delicate materials aside, the purification of LbL particles requires the eventual removal of salt to halt the gradual re-organization and decomposition of the LbL film.[54] Normally, salt-removal is accomplished by using pure water during the sequential centrifugal washing steps, where salt-removal actually helps to better stabilize the particles by improving their electrostatic repulsion. Unfortunately, this poses a challenge for efficient purification using filtration, due to the slight negative charge associated with most polymeric filter membranes.[40, 55] For LbL preparations, the sequential exposure of alternatively charged particle-polymer solutions leads to the buildup of an LbL film onto the filter membrane itself, which reduces yields and fouls the membrane.[56]

To overcome this problem, we separate the purification of positively and negatively charged particles to their own filter membranes **(Figure 2.1a)**. To discourage cationic nanoparticles from adhering to the negative membrane walls, dilute solutions of free polycation (10 mg mL⁻¹) are re-circulated through the filter membrane for 10 minutes. This pre-treatment allows free polycation to bind to anionic sites on the membrane via electrostatic attraction, and reduces the membrane's capacity for nonspecific adsorption of cationic nanoparticles during purification. For the membrane that processes negatively charged particles, no modifications were made as its
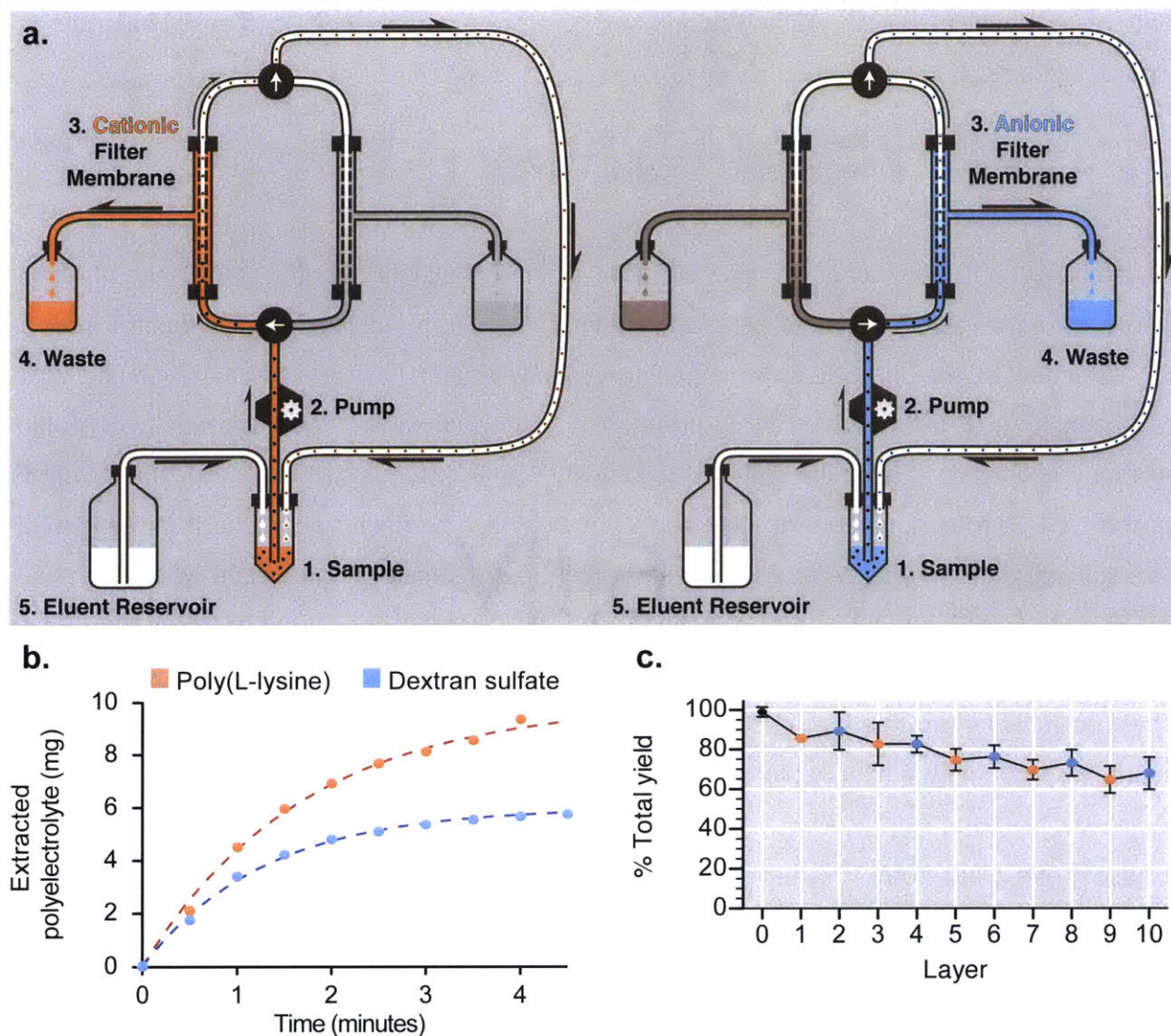
Figure 2.1. Tangential flow filtration (TFF) facilitates the rapid and controlled fabrication of layer-by-layer nanoparticles. (a) TFF purification schematic depicting continuous diafiltration through a porous membrane. A peristaltic pump drives nanoparticle samples through a circuit containing a filter membrane. Polyelectrolytes, driven by a mild pressure gradient, exit the circuit through the pores in the filter membrane and into a waste reservoir. Removal of solution generates a vacuum within the system, which draws replacement buffer from an attached reservoir to hold sample volume constant. To prevent nonspecific adsorption onto the filter membrane, purification of cationic and anionic nanoparticles was separated to different purification loops, each with its own filtration membrane. The left panel denotes the cationic purification loop, and the right panel denotes the anionic purification loop. (b) Purification of excess poly-L-lysine (PLL) or dextran sulfate (DXS) following LbL deposition can be completed in minutes using TFF. The concentration of PLL extracted using TFF was determined using a BCA assay on samples taken sequentially from the waste stream. DXS concentrations were determined by analyzing permeate samples by gel permeation chromatography. Data were fitted using a one-phase exponential decay model. (c) High yields ($68 \pm 5\%$ after 10 layers) are reproducibly obtained using TFF-assisted LbL fabrication. Nanoparticle concentration was quantified using a fluorescence plate reader following each purification step during the fabrication of 100 nm, carboxy-modified latex particles coated with five bilayers of PLL and DXS (CML-[PLL/DXS]$_5$). Error bars represent standard deviation of three independent syntheses.

intrinsic negative charge suitably repels nonspecific adsorption. Separation of charge to specific

67

membranes greatly improved yields with salt-free conditions and allowed us to easily and quickly prepare diverse LbL constructs.

2.2.2. Purification kinetics and product yields

We assessed purification kinetics using 500 kDa molecular weight cut off (MWCO) membranes and observed the rapid removal of excess 15 kDa poly(L-lysine) (PLL) and 10 kDa dextran sulfate (DXS) from an LbL nanoparticle grown on a fluorescently labeled, 100 nm, carboxy-modified latex (CML) substrate **(Figure 2.1b)**. During purification, permeate waste was sequentially collected and then analyzed by either the bicinchoninic acid (BCA) assay or by gel permeation chroma-tography (GPC) to quantify the removal of polyelectrolyte. The results indicated that removal of polyelectrolytes of this size reaches a plateau within four minutes of purification while operating the TFF at a transmembrane pressure between 3-5 PSI. We applied a linear regression analysis to fit the data and calculate the time required to reach a desired purity. The results were similar to the qualitative interpretation of the data, indicating that 95% purity could be expected in 5.1 minutes for PLL and 3.8 minutes for the smaller DXS.

To assess the yield from TFF-assisted LbL synthesis, we repeatedly fabricated ten-layer LbL particles composed of a fluorescently labeled, 100 nm CML core coated with 15 kDa PLL and 10 kDa DXS (100CML-[PLL/DXS]$_5$). After each purification step, a sample was taken to quantify particle recovery. Data from three independent syntheses were combined to determine the typical yield possible using this technique **(Figure 2.1c)**. The results indicated that a total yield of 68 ± 5% could be expected after ten layer depositions. Linear regression analysis of the data suggested that 96.9 ± 0.4% yield could be expected per layer deposition.

One of the major findings of this work was the rapid timescale of nanoparticle purification using TFF, which reduced purification time to 4-6 minutes per layer. Relative to the 30-60 minutes typi-cally required for a single centrifugal spin during traditional synthesis, TFF-assisted LbL assembly is dramatically more efficient. Analysis of recovered permeates during the purification of either 15 kDa PLL or 10 kDa DXS revealed that free polymers were efficiently removed after washing with 5 volume equivalents of the eluent solution, a significant improvement upon the 20 equivalents required by previous TFF-based approaches for nanoparticles.[50]
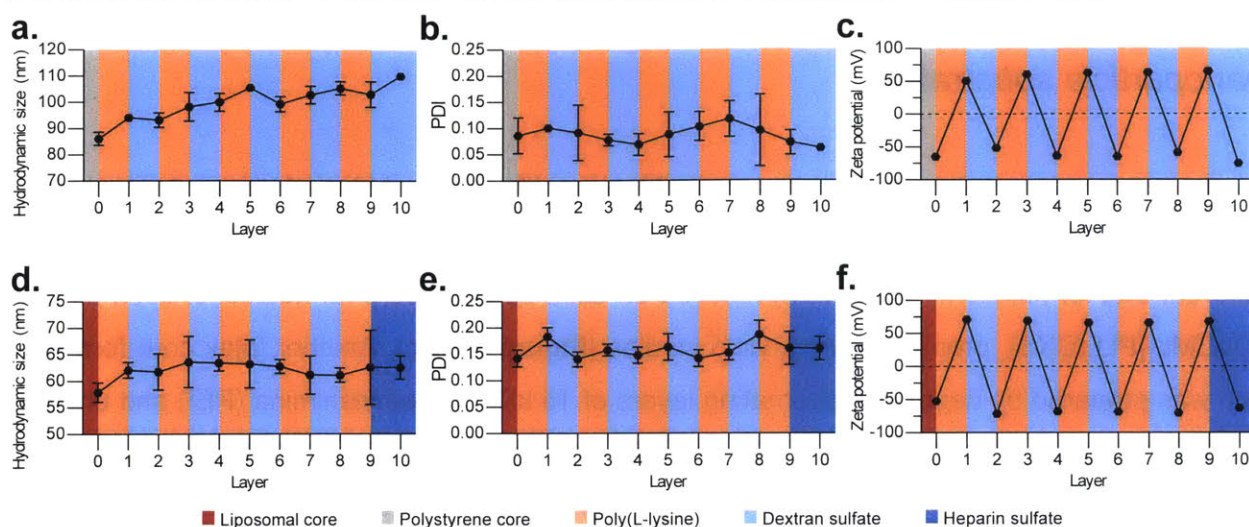
Figure 2.2. Diverse layer-by-layer (LbL) nanoparticles are prepared in a controlled manner using the tangential flow filtration (TFF)-assisted method. (a-c) Solid-core LbL particles were prepared by coating 100 nm, carboxy-modified latex particles with five bilayers of poly(L-lysine) and dextran sulfate (100CML-[PLL/DXS]$_5$). **(d-f)** LbL-modified liposomal particles were prepared by coating negatively charged, doxorubicin-containing liposomes with four bilayers of PLL and DXS followed by a bilayer of PLL and heparin sulfate (Lipo-[PLL/DXS]$_4$-PLL-HS). **(a, d)** These particles exhibited controlled size increase during layer deposition. **(b, e)** Nanoparticle uniformity was maintained throughout the layering process as indicated by the low polydispersity index (PDI). **(c, f)** Complete charge reversal was observed after each layer deposition indicating successful LbL modification. Size and polydispersity data were acquired by dynamic light scattering, and zeta potential data was measured using laser Doppler electrophoresis. Error bars represent standard deviation of three technical replicates. For population-based data see Supplemental Appendix A Figure 5.

Using our diafiltration-based system, rapid purification times are complimented by a reliable, high degree of product yield of 96.9 ± 0.4% per layer, leading to 68 ± 5% yield after ten layer depositions on 100 nm latex cores. This provides 83 ± 2% yield after four layer depositions, which is the number of layers in the formulations we have previously described for applications involving targeted drug delivery to tumors.[31] These results are a marked improvement over previously published optimized centrifugal protocols that report a 54.1% yield after the deposition of ten layers.[39] Improved yields will facilitate the exploration of LbL drug-carriers that incorporate useful but costly materials, such as siRNA, into the multilayer film. Similarly, recovery of the polyelectrolytes from the permeate solution, as was examined in this study to quantify purification kinetics, could lead to recycling of excess polymer to further reduce costs. Overall, our system allows for faster synthesis of LbL nanoparticles, with a higher yield as compared to previously described methods.

2.2.3. LbL modification of solid carboxy-modified latex and drug-loadable nanoparticle substrates

To confirm that our method retains the desirable versatility of the LbL technique, the hydrodynamic size, uniformity, and surface charge were monitored throughout the preparation of several different LbL formulations. Initial work focused on solid polymer core formulations, such as the 100CML-[PLL/DXS]$_5$ prepared during yield studies **(Figure 2.2a-c)**. Another latex core formulation was prepared by depositing alternating layers of 15 kDa polyethylenimine (PEI) and unfractionated heparin sulfate (HS) onto a 100 nm CML substrate (100CML-[PEI/HS]$_3$, see **Appendix A Figure 1**). Finally, to demonstrate the capacity to prepare smaller sized products, a formulation using 40 nm CML coated with PLL and DXS was prepared, reaching a final hydrodynamic size of 58 ± 3 nm, a low polydispersity index of 0.12 ± 0.01, and a surface charge of -71.6 ± 0.9 mV (40CML-[PLL/DXS]$_3$, **Appendix A Figure 2**).

To demonstrate the fabrication of clinically relevant LbL nanoparticles, focus was shifted to the LbL modification of two drug-loadable nanoscale templates, mesoporous silica and liposomal vesicles. We successfully prepared LbL nanoparticles from 30 nm mesoporous silica coated with poly(L-arginine) (PLA) and poly(L-glutamic acid) (PG) (MSN-[PLA/PG]$_3$, **Appendix A Figure 3**). The final LbL silica particles possessed a hydrodynamic size of 41 ± 4 nm, a polydispersity index of 0.22 ± 0.02, and a surface charge of -58 ± 2 mV.

Subsequent efforts focused on the LbL modification of colloidal liposomal cores, where PLL, DXS, and HS-containing multilayers were formed on the negatively charged surfaces of doxorubicin-loaded liposomes (Lipo-[PLL/DXS]$_4$-PLL/HS, **Figure 2.2d-f**). An additional LbL liposome formulation was prepared using PLA and DXS and later used for freeze-dried storage experiments (Lipo-[PLA/DXS]$_2$, **Appendix A Figure 4**). Notably, the TFF-assisted method did not need to be altered with any of these formulations, with the exception of changing the MWCO of the filter membrane when working with smaller or more flexible formulations. For particles 100 nm or larger in diameter, 500 kDa MWCO membranes were suitable. For smaller formulations, or liposomal formulations, 100 kDa MWCO membranes were more appropriate. In general, the optimal MWCO was determined by assessing changes in filter flux, where if the MWCO was large enough to permit nanoparticle penetration, then a decay of flux was observed. If flux decay was observed, the

MWCO was decreased until stable flux rates were achieved. When changing MWCO of the membrane, the feed flow rate of the peristaltic pump was adjusted to keep the transmembrane pressure between 3-5 PSI and the shear rate below 6,000 s^{-1}.

Hydrodynamic diameter was tracked using dynamic light scattering (DLS) after each purification, and revealed the steady growth from 86 ± 3 nm to a final size of 110 ± 1 nm **(Figure 2.2a)** for the case of 100CML-[PLL/DXS]$_5$. The Lipo-[PLL/DXS]$_4$-PLL/HS formulation exhibited thinner film formation, but nonetheless grew steadily from 58 ± 2 nm to 63 ± 2 nm **(Figure 2.2d)**. The difference between film thicknesses on these two cores

Figure 2.3. Cryogenic TEM images of core particles before and after layering confirm the presence of a thin film. Cryogenic TEM of (a) uncoated, carboxy-modified latex particles; (b) purified, LbL-coated carboxy-modified latex (CML-[PLL/DXS]5); (c) uncoated, doxorubicin-loaded liposome; (d) purified, LbL-coated, doxorubicin-loaded liposome (Lipo-[PLL/DXS]4-PLL-HS).

was anticipated, given previous experience with these substrates.[31, 57-59] In addition to size measurements, successful layering was confirmed by tracking the complete charge reversal of LbL particles throughout the synthesis. Both 100CML-[PLL/DXS]$_5$ and Lipo-[PLL/DXS]$_4$-PLL/HS alternated between zeta potentials of roughly +60 mV and -60 mV during alternate deposition steps, in accordance to the deposited polyelectrolyte's charge **(Figure 2.2c,f)**. Nanoparticle uniformity was well preserved throughout the synthesis, as indicated by the low polydispersity index (PDI) measured by DLS − 0.06 ± 0.01 for 100CML-[PLL/DXS]$_5$ and 0.16 ± 0.02 for Lipo-[PLL/DXS]$_4$-PLL/ HS **(Figure 2.2b,c)**. The other LbL formulations discussed exhibited similar characteristics, and that data can be seen in Appendix A. Further, population based, documentation on the ten-layer formulation's size and charge can also be seen in **Appendix A Figure 5**.

To further validate the successful LbL assembly of the two principle formulations, cryogenic transmission electron microscopy (Cryo-TEM) was used to evaluate changes in particle morphology after LbL modification **(Figure 2.3)**. Comparison of the electron micrographs showed the presence of thin films on the LbL nanoparticles that are not visible on the unmodified substrates. These
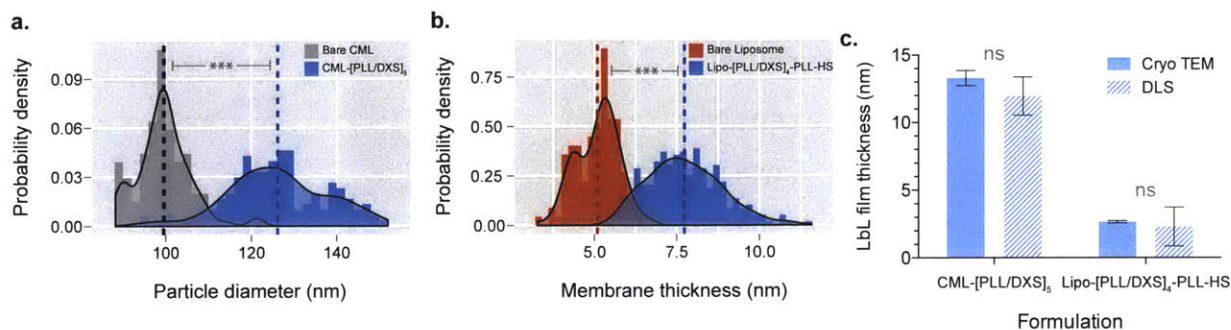
Figure 2.4. The quantification of Cryo-TEM images confirm statistically significant increases in size consistent with LbL modification. (a) Comparison of the diameters of bare, carboxy-modified latex (CML) particles and LbL-modified CMLs indicate a statistically significant (P<0.0001) shift in the size distribution. Dashed line denotes the mean size. N = 103 for bare and 153 for LbL CML. **(b)** Similarly, comparison of the liposome membrane thickness reveals statistically significant (P<0.0001) increase in thickness after LbL modification. Dashed lines denote the mean thickness. N = 113 for bare and 298 for LbL liposomes. **(c)** Calculation of LbL film thickness from either Cryo-TEM data or dynamic light scattering data give statistically consistent results for both CML (13.3 ± 0.6 nm by Cryo-TEM and 12 ± 1 nm by DLS) and liposomal (2.65 ± 0.09 nm by Cryo-TEM and 2 ± 1 nm by DLS) substrates. Error bars represent SEM. These data highlight important changes in LbL film thickness due to substrate selection. Individual particle measurements were plotted as a histogram and the kernel density function was estimated using R Statistical Software. All statistical tests were performed using one-way ANOVA (alpha = 0.01), with the Bonferroni post-test, on PRISM graphing software.

images were further analyzed using ImageJ to quantify size changes from the unmodified and layered formulations. The data reveal statistically significant (P<0.0001) increases in nanoparticle diameter (for 100CML-[PLL/DXS]$_5$) and membrane thickness (for Lipo-[PLL/DXS]$_4$-PLL/HS) relative to the unmodified substrate **(Figure 2.4a-b)**. Furthermore, comparison of LbL film thickness calculated from either Cryo-TEM or DLS produced statistically consistent estimates for particles formed on CML (13.3 ± 0.6 nm by Cryo-TEM and 12 ± 1 nm by DLS) and liposomal (2.65 ± 0.09 nm by Cryo-TEM and 2 ± 1 nm by DLS) substrates **(Figure 2.4c)**.

These results indicate the highly efficient and scalable fabrication of LbL nanoparticles smaller than 150 nm using TFF. Another major finding of this study was that the TFF-assisted method could be generalized to a diverse number of nanoscale formulations including solid latex, mesoporous silica, and liposomal cores. The breadth of polyelectrolytes used to construct LbL nanoparticles shows that TFF-assisted LbL assembly is compatible with many different material systems. Careful tracking of the nanoparticle size, surface charge, and uniformity during synthesis indicated that this method provided a great deal of control over these important nanomaterial characteristics. The results from Cryo-TEM validated the presence of intact and uniform films on LbL-modified latex nanoparticles and liposomes. Furthermore, the agreement between film thicknesses calculated from Cryo-TEM or DLS measurements further support the presence of a thin,

but measurable, film on the nanoparticle surface. These small changes in size are representative of the highly controllable growth of the polyelectrolyte multilayer afforded by the LbL technique. The generalizable nature and excellent quality control of this method has important implications for the future of basic research into LbL nanomedicines, as TFF is a highly accessible technology that could be employed by most laboratories.

2.2.4. Generation of an LbL small library

The generation of a small library of LbL nanoparticles demonstrated the potential of TFF-assisted LbL assembly to increase experimental throughput, allowing researchers to better evaluate the contribution of different variables in their nanoparticle formulations. Since one of the greatest strengths of the LbL platform is its ability to generate diverse material systems, there is a large parameter space to be explored. It has been well documented that nanoparticle surface chemistry plays an important role in particle-cell interactions.[60-61] The work by Murphy and colleagues

Table 1. Ten formulations of LbL nanoparticles with unique terminal polymer layers were fabricated using the TFF method. Each particle is a bilayer formed on carboxy-modified polystyrene substrates (CML-[poly(L-arginine)/ polymer X], where polymer X is one of the terminal layers described below). The size, uniformity and zeta potential of each nanoparticle formulation was determined by dynamic light scattering and laser Doppler electrophoresis. Error represents the standard deviation of three technical replicates.

Terminal Layer	Average Hydrodynamic Size [nm]	Polydispersity Index	Zeta Potential [mV]
Carboxy-modified latex	95 ± 5	0.10 ± 0.03	-63 ± 1
Poly(L-arginine)	105 ± 2	0.03 ± 0.01	66 ± 1
Poly(L-aspartic acid)	101 ± 9	0.08 ± 0.02	-63 ± 1
Poly(L-glutamic acid)	106 ± 3	0.04 ± 0.04	-61 ± 1
Poly(L-glutamic acid)-b-polyethylene glycol	105 ± 9	0.08 ± 0.01	-51 ± 3
Poly(acrylic acid)	99 ± 7	0.05 ± 0.03	-68 ± 2
Hyaluronic acid	153 ± 8	0.05 ± 0.02	-56 ± 2
Dextran sulfate	109 ± 9	0.13 ± 0.04	-75 ± 1
Heparin-folate conjugate[a]	120 ± 9	0.07 ± 0.03	-61 ± 2
Sulfated beta cyclodextrin polymer	110 ± 8	0.05 ± 0.06	-50 ± 2
Heparin sulfate	107 ± 4	0.11 ± 0.04	-73 ± 2
Fucoidan	126 ± 4	0.12 ± 0.05	-61 ± 1

[a] Heparin sulfate was conjugated to folic acid using NHS addition chemistry. See supplemental information for more detail.

has highlighted several biological effects of LbL nanoparticles that depend on surface chemistry, demonstrating the importance of broadly studying different terminal coatings.[30, 62] To this end, ten unique LbL nanoparticle formulations were generated from 100 nm CML cores. Each particle was coated with PLA and then terminated with one of ten polyanions described in **Table 1**. These terminal coats include a variety of polysaccharides, linear polypeptides, and synthetic or modified polymers. In particular, the hyaluronic acid and heparin-folate conjugate coated formulations possess known targeting properties.[63-64] Of note, the inclusion of hyaluronic acid into LbL particles can be challenging due to the polymer's propensity to form secondary and tertiary structures that can drive aggregation.[65-67] However, hyaluronic acid is a highly desirable material that benefits biomedical applications with its unique biological behaviors such as mucoadhesion, receptor targeting, and antifouling.[8, 37, 68] Use of the TFF-assisted method greatly increased the throughput of nanoparticles functionalized with hyaluronic acid (ca. 10-fold per particle). Each particle prepared for the library exhibited excellent size, uniformity, and surface charge, consistent with the descriptions of the more highly layered formulations.

Importantly, this work describes the manufacture of several novel LbL formulations that incorporated sulfated beta-cyclodextrin polymer, the algae-derived polysaccharide fucoidan, and a heparin sulfate-folate conjugate. The fabrication of stable LbL particles composed of a cyclodextrin polymer opens the door to generating LbL films with drug-loaded polyelectrolytes for the inclusion of hydrophobic small molecules. LbL nanoparticles coated with fucoidan present opportunities to investigate emergent reports of this molecule's involvement in cellular differentiation and immune modulation.[69-70] The inclusion of a heparin-folate conjugate also raises opportunities to leverage both molecules' biological interactions towards an effective targeted therapy. Furthermore, given the success of this technique with a variety of material systems, it is likely that this approach could be adapted to prepare LbL formulations that utilize alternative attractive forces such as hydrogen bonding and hydrophobic interactions.

2.3. Results: Characterization of the safety and the long-term stability of drug-loaded LbL liposomes

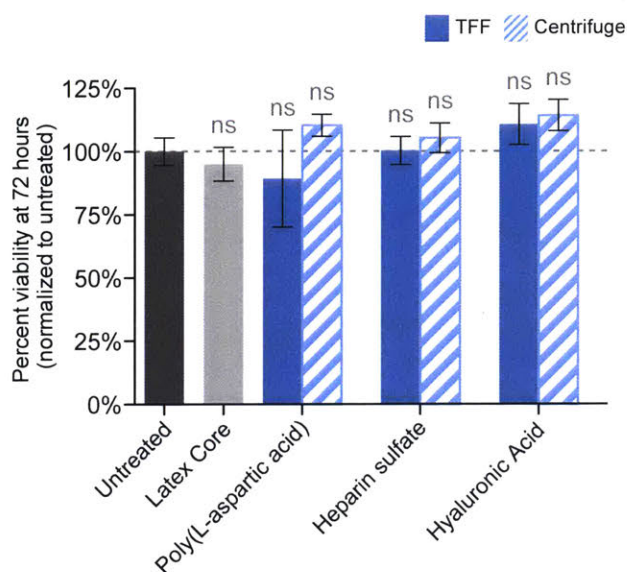### 2.3.1. Evaluation of LbL nanoparticle toxicity

Figure 2.5. LbL nanoparticles prepared using the TFF-assisted method do not exhibit nonspecific cytotoxic effects in vitro. SKOV3 cells were incubated with poly(L-aspartic acid), herparin sulfate, and hyaluronic acid terminated LbL nanoparticles that were prepared by either the TFF method (solid, blue bars) or the conventional centrifugal method (striped bars). After 72 hours, the cellular viability was determined using the Cell-Titer Glo luminescence assay. The results were normalized relative to untreated controls, and subsequent analysis by one-way ANOVA failed to find any statistically significant changes in cellular viability for any formulation, regardless of preparation method.

To address the concern that TFF-made LbL nanoparticles may have unintended cytotoxic effects due to the carryover of excess polycation, a viability assay was performed on SKOV3 cells with three LbL formulations. Poly(L-aspartic acid), hyaluronic acid, and heparin sulfate terminated nanoparticles were prepared by either the TFF-method or the conventional centrifugal method and incubated with SKOV3 cells over the course of 72 hours. Cell viability was measured at 24, 48, and 72 hours and compared to the viability of untreated cells and cells exposed to the bare latex core (**Figure 2.5** and **Appendix A Figure 6**). None of the nanoparticle formulations exhibited statistically significant changes in viability compared to untreated controls, indicating that TFF-made LbL nanoparticles show low toxicity *in vitro*.

These results provide evidence that LbL nanoparticles prepared using the TFF method are cell-compatible by performing a head-to-head comparison of toxicities between several formulations. The results further prove that TFF purification provides highly pure LbL nanoparticles free of cytotoxic contaminants such as free polyelectrolytes.
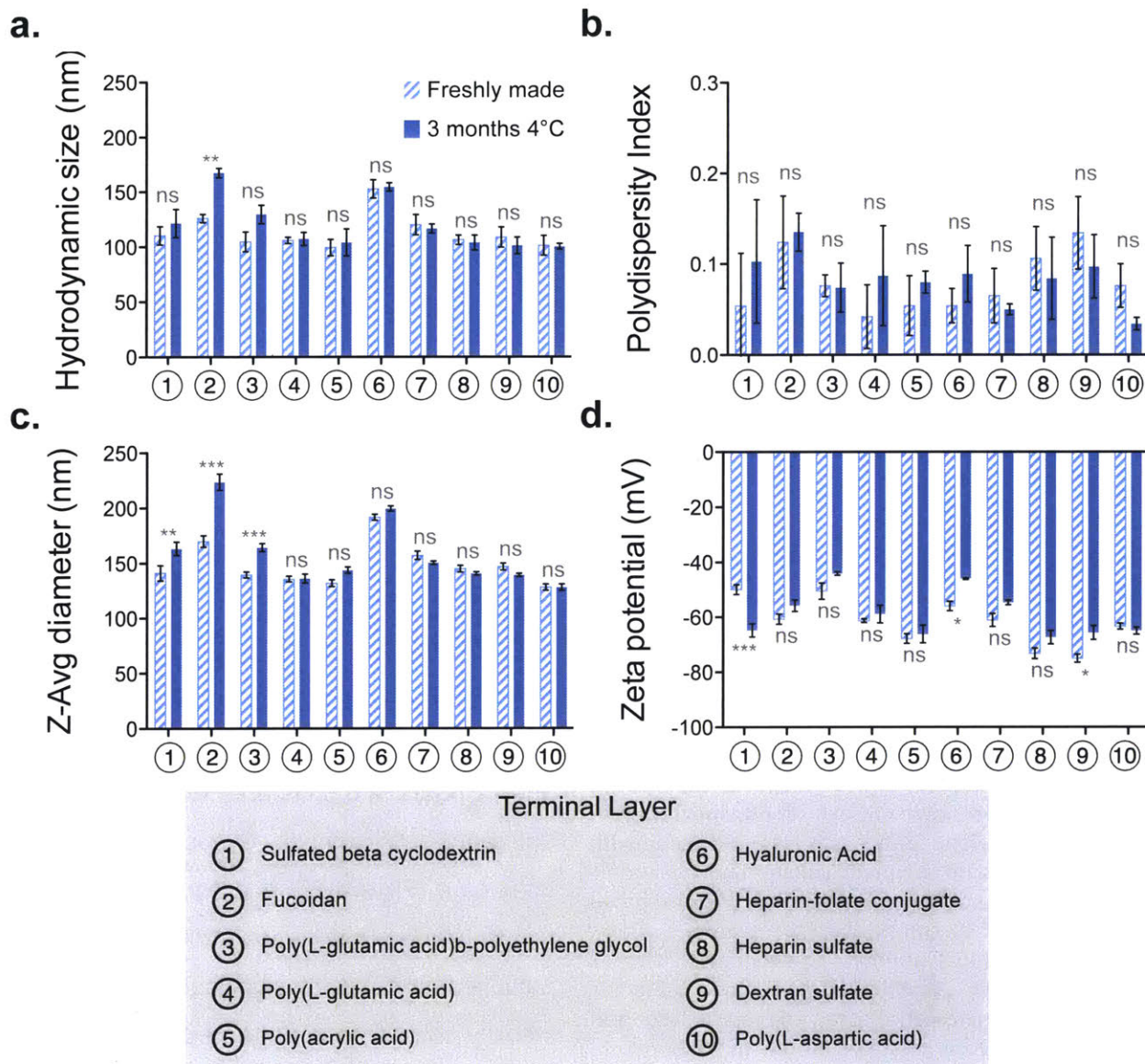
Figure 2.6. LbL nanoparticles have long refrigerated shelf lives as indicated by the preservation of their size, uniformity and charge characteristics. Ten different LbL nanoparticle formulations consisting of a carboxy-modified latex core and a bilayer of poly(L-arginine) and a unique polyanion were stored for three months at 4 degrees Celsius. **(a)** We compared the hydrodynamic number average size for the particles after storage and compared them to the particle's original size. With the exception of the Fucoidan-coated particle, all others maintained statistically consistent sizes during storage. **(b)** These particles likewise exhibited statistically consistent polydispersity index, suggesting that particle uniformity is maintained during storage. **(c)** The z-average size measurement, which is more sensitive to aggregates, demonstrated that 7 out 10 formulations exhibited statistically consistent sizes during storage. **(d)** Generally, the zeta potential of the nanoparticles was conserved during storage with a few exceptions. Sulfated beta cyclodextrin-coated particles exhibited a significant charge increase during storage. On the other hand, hyaluronic acid and dextran sulfate-coated particles exhibited a small, but statistically significant decrease in zeta potential. Overall these data indicate that LbL particles would be amenable to months-long refrigerated storage without concern of loss of colloidal stability. One-way ANOVA with the Bonferroni post-test (alpha = 0.01) was used to determine statistical significance between the indicated samples.

2.3.2. LbL nanoparticle refrigerated shelf-life

The capability to increase the scale, yield and throughput of LbL preparations is an important step towards realizing clinical translation. Another important factor for translation, which to our knowledge has not been addressed previously for LbL nanoparticles, is their shelf life. We evaluated whether appreciable destabilization would occur with nanoparticles from our small library during a three-month storage period in pure water at 4°C. We found that LbL nanoparticles broadly retained their number-average and z-average sizes, as well as their low PDI and high zeta potentials **(Figure 2.6)**. Relative to the freshly prepared nanoparticles, nine out of ten formulations exhibited statistically consistent hydrodynamic sizes. Using the more aggregate-sensitive size determinant, z-average size, seven out of ten formulations retain their original size. Interestingly, the PDI of all formulations remained statistically consistent during storage, which may indicate that size changes are due more to swelling of the film than to aggregation events. Furthermore, the zeta potential of the LbL nanoparticles remained very high during storage, although some statistically significant changes were noted. Two formulations (HA and DXS-terminated) exhibited minor but significant (P<0.05) loss of charge. On the other hand, sulfated beta-cyclodextrin-terminated particles exhibited a modest (14.9 mV) and significant (P<0.001) increase in magnitude of surface charge during storage. Overall, these data suggest that LbL formulations are stable on the order of at least 3 months when stored under refrigerated, aqueous salt-free conditions. Stability is important because it indicates that these formulations could be kept at-the-ready in clinical settings, and furthermore, could facilitate use in clinical settings by minimizing the need for constant reconstitution prior to administration.

2.3.3. Freeze-dried, room temperature storage of drug-loaded LbL liposomes

Refrigerated storage can pose its own problems for clinical translation in terms of transportation and accessibility. Moreover, storing LbL nanoparticles in an aqueous state can allow for the slow release of encapsulated small molecule drugs. With this in mind, lyophilization and room temperature storage of freeze-dried powders is ultimately a far more convenient and manageable option for clinical and industrial scale operations.[71] To determine if LbL nanoparticles can survive such storage conditions, the doxorubicin-loaded Lipo-[PLA/DXS]$_2$ formulation was used
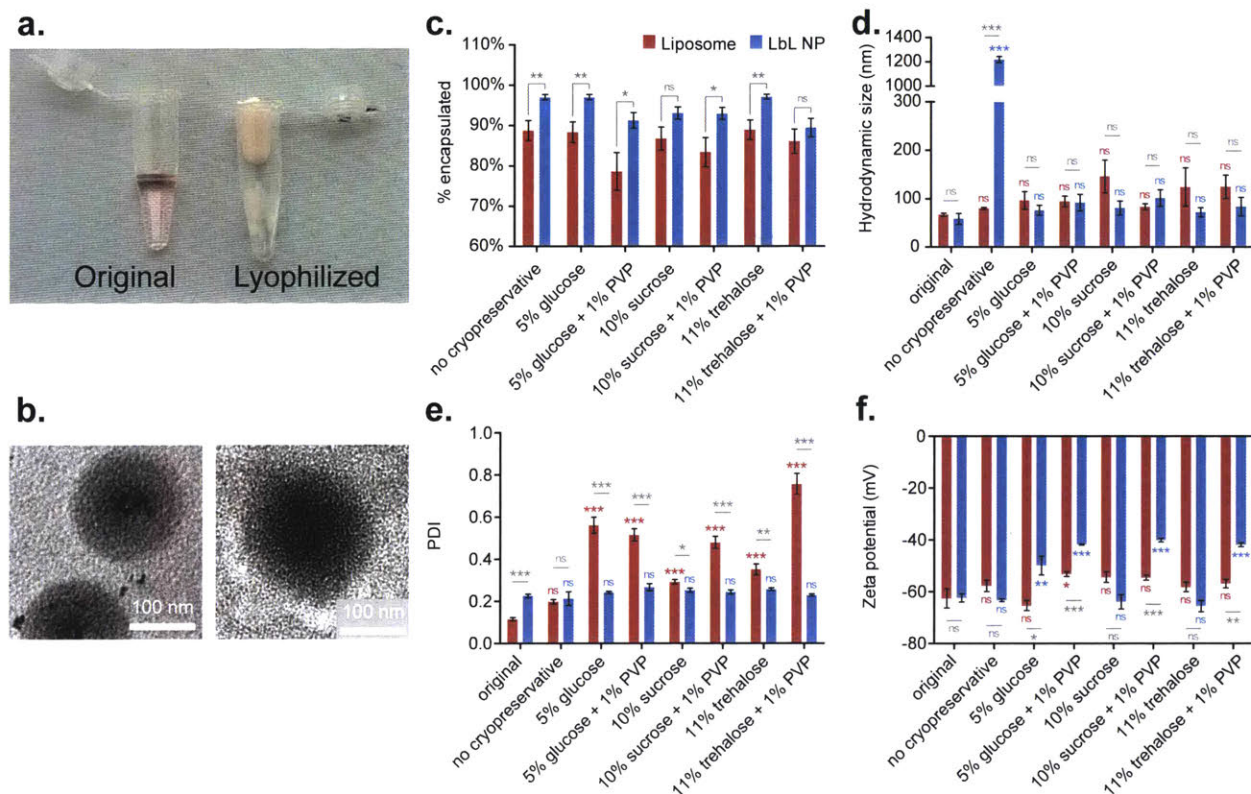
Figure 2.7. Layer-by-layer (LbL) modified liposomes can be lyophilized and reconstituted for long-term storage. Doxorubicin-loaded liposomes were coated with two bilayers of poly(L-arginine) and dextran sulfate (Lipo-[PLA/DXS]$_2$), using the TFF-method. **(a)** Lipo-[PLA/DXS]$_2$ nanoparticles were lyophilized with different cryo-preservatives. **(b)** TEM of particles before lyophilization (left panel) and after being reconstituted from freeze-dried powder (right panel). **(c)** LbL modified liposomes (blue data) retained more drug than bare liposomes (red data) regardless of choice of cryoprotectant, though several protectants facilitate nearly 100% drug retention during storage and reconstitution. **(d)** The presence of cryoprotectants prevents aggregation upon LbL liposome recon-stitution. **(e)** Reconstituted LbL liposomes exhibit lower polydispersity index than reconstituted bare liposomes, indicating improved uniformity. **(f)** Cryopreservation with 10% sucrose or 11% trehalose prevented decreases in the zeta potential of LbL liposomes. Size and polydispersity data were acquired by dynamic light scattering, and zeta potential data was measured using laser Doppler electrophoresis. Error bars represent standard deviation of three technical replicates.

as a model system for cryogenic storage. LbL liposomes were combined with several different cryoprotectants (5% glucose, 10% sucrose, 11% trehalose), and with or without a poly(vinyl alcohol) preservative (PVP). LbL-modified and bare liposomes were flash-frozen in liquid nitrogen and lyophilized to produce a fluffy, cotton-like powder **(Figure 2.7a)**. The powder was kept at room temperature for a week prior to being reconstituted in pure water.[72] The reconstituted particles were dialyzed overnight and then analyzed to determine if particle integrity or drug encapsulation had been compromised.

The results indicated that LbL liposomes protected their drug payload better than bare liposomes

under these storage conditions **(Figure 2.7c)**. In five out of seven conditions, including the cryo-preservative-free control, statistically significant (P<0.05 or P<0.01) improvements in retention relative to bare liposomes were observed. Notably, preservation by 5% glucose or 11% trehalose led to virtually no drug loss in LbL liposomes (97 ± 3% and 97 ± 2% encapsulation, respectively). The rest of the formulations retained at least 89% of the drug payload, whereas the liposomes only retained 79-89% of their encapsulated drug after reconstitution.

Generally, we observed that inclusion of PVP was detrimental to overall stability of these nanoparticles. These results are consistent with previous work, which demonstrated that poly(vinyl acid)-based preservatives fail to adequately stabilize liposomes unless modified.[73] In contrast, it has been seen that PVP is sufficient for protection of polymeric nanoparticles, such as those composed of poly(dl-lactide-co-glycolide), poly (D,L-lactic acid), and poly(lactic acid-co-ethylene oxide).[74-76] Therefore, the presence of a polymeric film on the LbL-coated liposomes may help to explain their better stability relative to bare liposomes when lyophilized in the presence of PVP.

Cryoprotectants were found to be essential for LbL nanoparticle survival under long-term storage conditions. Without cryoprotectants, LbL particles undergo irreversible aggregation into micron-sized particles. With protectants, there is no statistically significant impact on LbL nanoparticle size after freeze-dried storage **(Figure 2.7d, Appendix A Figure 7)**. On the other hand, the use of cryoprotectants led to statistically significant (P<0.001) increases in the z-average diameter of bare liposomes **(Appendix A Figure 7)**. Inclusion of PVP partially rescued liposomes protected with either glucose or sucrose, but the resulting z-average size was still significantly larger than the original formulation. Bare liposomes also undergo statistically significant (P=0.001) increases in PDI after reconstitution, in contrast to LbL liposomes, which retain low PDIs that are statistically consistent with their original PDI **(Figure 2.7e)**.

Zeta potential measurements of the reconstituted particles indicated that the choice of cryoprotectant was important in preserving the original surface charge on LbL nanoparticles **(Figure 2.7f)**. Either 10% sucrose or 11% trehalose managed to prevent any decrease in zeta potential for LbL particles. These results are consistent with prior work, which demonstrated that disaccharides are more suitable cryoprotectants for lipid-based nanoparticles than monosaccharides.[77] Overall this choice of cryoprotectant is an important characteristic to optimize, as loss of surface charge may

79

compromise the reconstituted particle's shelf life or further *in vivo* stability.

Overall, these results strongly indicate that LbL liposomes can be stably stored under freeze-dried, room-temperature conditions. This finding has major implications for the clinical and industrial translatability of this technology, as it would facilitate the stockpiling, shipping and distribution of future nanomedicines. Our work compared the efficacy of several cryoprotectants head-to-head, and revealed that 11% trehalose was the most consistent protectant and maintained the size, uniformity, and charge of our LbL liposomes. Furthermore, preservation by trehalose facilitated high drug payload retention, with a 97 ± 2% encapsulation of doxorubicin. Notably, LbL liposomes exhibited superior drug cargo retention compared to bare doxorubicin-containing liposomes, and could represent a safe and straightforward means towards the improvement of already clinically approved nanotherapies that may suffer from suboptimal drug-retention under storage.

2.4. Conclusions and future work

LbL nanoparticles represent a desirable class of materials that are modular, hierarchical, and multifunctional. These characteristics are critical for the advancement of potent next-generation nanomedicines. Until now, these materials were difficult to prepare, despite their straightforward assembly behavior. So far, intermediate purification steps between layer depositions presented the greatest barrier for both lab scale research and clinical translation. Here we described a solution to this bottleneck by using tangential flow filtration to handle the cumbersome and time-consuming washing steps. This approach did not restrict the hallmark versatility of LbL assembly, allowing us to prepare nanoparticles ranging from 40 to 150 nm from solid polymer, mesoporous silica, and liposomal substrates. Furthermore, this technique was compatible with several distinct LbL formulations composed of over a dozen biologically relevant polyelectrolytes. This versatility was accompanied by rapid purification/processing times, excellent product yields, and control over important nanoparticle characteristics (e.g., size, uniformity, and surface charge). This approach has the potential to become fully automated, which would benefit the colloidal LbL community in a similar way that robotic dipping machines have enhanced research into the LbL modification of macroscopic substrates. In particular, future work that focuses on incorporating programmable, robotic operation of TFF devices would provide hands-off synthesis of LbL nanomaterials.

This report also highlights that LbL materials can be stored in aqueous, refrigerated conditions on the order of months. Additionally, we demonstrate that LbL liposomes loaded with small molecule drugs, namely doxorubicin, can be stored under freeze-dried, room temperature conditions without compromising drug encapsulation or nanoparticle characteristics. Overall, this work provides a new path towards ramping up basic research into this important class of drug-delivery vehicles, as well as a means to scale-up existing and future technologies to the clinic.

2.5. Methods

Colloidal Substrate And Polyelectrolyte Preparation: The polyelectrolytes poly(L-lysine) HBr (PLL, 4-15 kDa; Sigma Aldrich), dextran sulfate sodium salt (DXS, 6.5-10 kDa; Sigma Aldrich), poly(acrylic acid) (PAA, 15 kDa; Sigma Aldrich), poly(L-arginine) (PLA, 9.6 kDa; Alamanda Polymers), poly(L-glutamic acid) (PG, 15 kDa; Alamanda Polymers), poly(L-aspartic acid) (PD, 14 kDa; Alamanda Polymers), poly(L-glutamic acid)-b-polyethylene glycol (PG-b-PEG, 30 kDa PG, 5 kDa PEG; Alamanda Polymers), linear polyethylenimine (PEI, 25 kDa, Polysciences), hyaluronic acid (HA, 40 kDa; LifeCore Biomedical), sulfated beta-cyclodextrin polymer (18kDa; Cyclodextrin Technologies), and fucoidan (57 kDa; Santa Cruz Biotechnology) were used without modifications. Heparin sodium salt (HS, unfractionated; Celsus Labs) was used both unmodified and as a conjugate with folic acid (Sigma Aldrich) as described previously.[78] For additional detail on the synthesis see Appendix A.

The fluorescent, carboxylate-modified latex nanoparticles (100 nm, blue fluorescent (350/440) and 40 nm yellow-green fluorescent (505/515); Life Technologies) were used without modification.

Mesoporous silica nanoparticles were prepared according to the protocol for 40 nm particles described by Zhang and coworkers.[79] The procedure was as follows: (i) 1.52 g of hexadecyl-trimethylammonium bromide (CTAB, Sigma Aldrich), 0.35 g triethanolamine (0.311 mL, Sigma Aldrich), and 100 mL Millipore water were mixed and heated at 80°C for 1 hour, until dissolved. (ii) 14.6 g of tetraethyl orthosilicate (Sigma Aldrich) was added quickly to the solution, which was left stirring for another 2 hours. (iii) Particles were isolated by high-speed centrifugation (30,000 x g for 1 hour) and washed once with water and then once more with methanol. Particles were resuspended in methanol for CTAB extraction (iv) Template removal was accomplished by first adding 1 mL of 12 M HCl followed by refluxing the solution at 80 °C for 14 hours. (v) The silica particles were recovered by centrifugation and washed twice with methanol prior to being dried under vacuum. For LbL preparations, dried silica was reconstituted in Millipore water. The size of these particles was measured to be 30 ± 10 nm by dynamic light scattering. For the porosity of these nanoparticles, the reader is referred to the original paper describing this protocol.[79]

Doxorubicin-loaded liposomes were prepared as follows: (i) 1,2-distearoyl-sn-glycero-3-phospho-

choline (DSPC; Avanti Polar Lipids), 1-palmitoyl-2-oleoyl-sn-glycero-3-phospho-(1'-rac-glycerol) sodium salt (POPG; Avanti Polar Lipids), and cholesterol (Sigma Aldrich) prepared at a 56:5:39 weight ratio were dissolved in a cosolvent of cholesterol and methanol (2:1 volume ratio). (ii) The solution was evaporated using a rotary evaporator at 40°C at 150 mbar to make a thin lipid film. (iii) The film was hydrated in 300 mM citric acid buffer (pH 4) under sonication at 65°C until uniform liposomes are generated. (iv) 300 mM sodium carbonate buffer was added into the liposome solution to adjust the pH of the solution to 6.5, which generated a pH gradient between the buffer solution outside liposomes and the internal environment of liposomes. (v) Doxorubicin HCl salt (Dox; LC Laboratories) was dissolved at 3 mg mL^{-1} in sodium chloride solution (154 mM, 0.9 wt/vol %), and the Dox solution was added into the liposome solution under sonication at 65°C for 5 min. Dox-loaded liposomes were purified using the TFF system (500 kDa MWCO filter module; Spectrum Labs) as described below.

Tangential Flow Filtration Assisted LbL Fabrication: Colloidal substrates (CS) and polyelectrolytes (PE) were dissolved in equal volumes of purified water at a 1:5 mass ratio of CS to PE. Prior to the first layer deposition, the CS solution was sonicated for 5 minutes and the PE solution for 15 minutes to disrupt any pre-existing aggregates. The CS solution was added to the PE solution under sonication to generate the PE film. Once mixed, the CS-PE mixture was sonicated for 5 more seconds and incubated on an orbital shaker for 15 minutes. The CS-PE mixture was then transferred to a 50 mL conical flask (Corning) and connected to a tangential flow filtration (TFF) device (KrosFlo Research IIi; Spectrum Labs). All connections were made using MasterFlex size 14 Pharma-Pure tubing, with the exception of the tubing that runs through the peristaltic pump, which is size 16. The TFF was connected to a suitable filtration membrane composed of modified polyethersulfone, either a 100 kDa MWCO or a 500 kDa MWCO membrane (Spectrum Labs, MidiKros Class) depending on the size of the CS being used. Refer to the supplemental information for a video showing the experimental set up.

The filter membranes were used exclusively with one charge type to prevent product loss and membrane fouling. The membrane used to process positively charged nanoparticles is pre-processed by recirculating salt-free, cationic PE solution for 10 minutes to mask anionic sites. The negative-particle membrane is used without further modification.

83

The CS-PS mixture was pumped with a constant feed rate (190 mL min^{-1} for 500 kDa membrane and 170 mL min^{-1} for 100 kDa membranes) through the appropriate TFF membrane using a peristaltic pump. Feed rate was chosen to maintain a transmembrane pressure between 3-5 PSI and a shear rate below 6,000 s^{-1}. These values were calculated using the provided software and sensors within the TFF device.

To maintain a constant sample volume during purification, a 2 L buffer reservoir filled with Millipore water was connected to the sample container. The CS-PE mixture was washed until 5 complete volumes were eluted (for a 40 mL sample that would be 200 mL of permeate) when using a 500 kDa membrane. With the 100 kDa membrane, 7 complete volumes were eluted. Permeate solution was collected in sequential 20 mL aliquots to determine purification kinetics as described below.

After adequate purification, the nanoparticle sample was disconnected from the buffer reservoir in order to concentrate the pure product down to 20 mL in anticipation for the next layer deposition. At this stage, samples were taken for characterization of the nanoparticles as described below.

After removing the pure CS sample from the TFF device, another layer was deposited as before, with an oppositely charged PE solution. During this incubation, filter membranes were briefly rinsed with water and switched to the appropriate charge-specific membrane for the next purification. This process was repeated until reaching the desired number of layers.

Note that the mass ratio of 1:5 for substrate to polyelectrolyte generally yielded stable layer depositions, but for certain polyelectrolytes the ratio was shifted until a zeta potential measurement with a magnitude of at least 40 mV was observed in the unpurified mixture. For example, our CML cores were used at a 1:5 mass ratio with PLL, whereas we used a 1:3 mass ratio with DXS, which equates to 10 mg of PLL and 6 mg of DXS being used per layer deposition during the modification of 2 mg of CML substrates.

Characterizing Purification Kinetics and Yield: Permeate samples were taken from purifications involving PLL and DXS. To quantify the amount of PLL extracted using the TFF, we directly analyzed the PLL permeate samples as well as PLL standards using the bicinchoninic assay (BCA;

Pierce). Absorbance measurements were taken with a TECAN Infinite M200 Pro plate reader and used to calculate the mass of PLL removed from the system.

The concentration of DXS in the permeate was determined by gel permeation chromatography (GPC). DXS permeate samples and standards were lyophilized and re-dissolved in the appropriate GPC eluent. The measurements of DXS was performed on an Viscotek GPCmax system (Malvern) equipped with Agilent PL aquagel-OH columns (PL aquagel-OH Guard 8 μm (50 mm x 7.5 mm), and PL aquagel-OH MIXED-M 8 μm (300 mm x 7.5 mm, exclusion limit > 6×10^5 g mol^{-1})) thermostated to 35°C and a refractive index detector maintained at 35°C. 100 mM $NaNO_3$ and 10 mM NaH_2PO_4 in aqueous solution at pH 7.4 containing 4:1 (v/v) MeOH was used as mobile phase with a flow rate of 1.0 mL min^{-1}. The refractive index area (mVmL) of each sample (injection volume constant at 50 μL) was measured and calibrated against a DXS standard curve.

To determine nanoparticle yields, purified product was weighed in tared conical flasks to determine recovered sample volume. Then, 10 μL samples of the product were taken and diluted to 100 μL in pure water and analyzed using the Infinite M200 plate reader. Sample fluorescence measurements (350 nm excitation, 440 nm emission) were compared to standards of known CML concentration in order to calculate the product yield.

For LbL nanoparticles prepared by centrifugation, instead of processing with the TFF the nanoparticle solution was centrifuged at 15,000 rcf for 15 minutes. Supernatant was removed and spun again until no nanoparticle pellet was formed, about 6 spins total per layer. Recovered pellets were gently resuspended in pure water, to avoid dislodging any insoluble aggregates from the tube wall. HA terminated nanoparticles was spun at 10,000 rcf for 5 minutes to minimize product loss.

Lbl Liposome Lyophilization And Storage: Samples were prepared with cryoprotectant (5% glucose, 10% sucrose or 11% trehalose; Sigma Aldrich), cryoprotectant plus poly(vinyl alcohol) preservative (PVP, Mowiol 4-88; Sigma Aldrich), or without any stabilizer. Samples were flash frozen in liquid nitrogen for 15 minutes and lyophilized for 48 hours. The freeze-dried powders were backfilled with N_2 and stored at room temperature on the bench top for a week prior to reconstitution in pure water (reverse osmosis, MilliQ) followed by an overnight equilibrium dialysis (8 kDa

MWCO, 4C).

Nanoparticle Characterization: Hydrodynamic size and polydispersity index were measured using dynamic light scattering (Malvern ZS90 particle analyzer, λ = 633 nm, material/dispersant RI 1.590/1.330). Zeta potential measurements were made using laser Doppler electrophoresis with the Malvern ZS90 as well. All measurements were conducted in water (reverse osmosis, MilliQ). Cryo-TEM was performed with a JEOL 2100 FEG instrument, and quantitative image analysis was performed using ImageJ software. For Cryo-TEM, 3 uL of the sample solution was dropped onto a lacey copper grid coated with a continuous carbon film. The sample was blotted to remove excess liquid by Gatan Cryo Plunge III. The grid was mounted on a Gatan 626 cryo-holder, and then the specimen and holder tip were cooled using liquid nitrogen. Imaging was performed using the minimum dose method to prevent damage to the sample by the electron beam. The microscope was operated at 200 kV with a magnification setting of 10,000-30,000 for assessing particle size and distribution. All images were then recorded on a Gatan 2kx2k UltraScan CCD camera. Conventional TEM was conducted using either a FEI Tecnai Multipurpose TEM (120 kV) or JEOL 2011 High Contrast Digital TEM (120 kV). Specimens for conventional TEM were prepared by drop-casting nanoparticle solutions onto mesh copper grid coated with a continuous carbon film.

Drug encapsulation was determined for Dox-loaded nanoparticles by measuring Dox fluorescence (500 nm excitation, 600 nm emission) from particle and diafiltrate solutions (50% DMSO) following an overnight equilibrium dialysis (8 kDa MWCO, 4C) against lyophilization solutions. Fluorescence measurements were made using the Infinite M200 plate reader.

Cytotoxicity Characterization: SKOV3 (ATTC) ovarian cancer cells were maintained in regular Dulbecco's modified Eagle medium (DMEM, Corning) supplemented with 10% fetal bovine serum (Seradigm) and 1% penicillin-streptomycin (Corning). Cells were seeded in tissue-culture grade 96-well plates (Greiner) at a density of 5,000 cells per well the night before treatment with LbL nanoparticles. The next day, the cells were incubated in media containing a 20 pM concentration of LbL nanoparticles. At the reported time points, the cellular viability was determined using the Cell-Titer Glo luminescence assay (Promega).

Data Processing And Statistical Analysis:

Purification kinetics data were fit to a one-phase exponential decay model with PRISM software. The model constrained y0 (set to 0), plateau (set to known amount introduced into the system), and K (must be greater than 0). PRISM was also used to fit a basic linear model to yield data.

One-way ANOVA with the Bonferroni post-test was used to determine statistically significant differences in most cases (results from this test are annotated in gray on all plots). To assess statistically significant changes between original nanoparticles and the various cryogenic storage conditions, one-way ANOVA with the Dunnet post-test was performed. Determinations from this particular test are denoted in blue (for LbL particles) and red (for bare liposomes) in Figure 7. Unless noted otherwise, alpha was set to 0.01 (99% confidence). All tests were conducted in PRISM software.

Size measurements taken from ImageJ were imported and analyzed in R studio. The data were visualized as probability density histograms, and overlaid with their kernel density distribution estimate using the ggplot2 package. Size and charge distribution data exported from the Malvern Zetasizer software were processed in Microsoft excel to convert the raw data into a frequency table for import into R studio. The distributions were then plotted using the violinplot functionality of the ggplot2 package to produce the figures seen in the supplemental documentation.

2.6. References

1. Peer, D.; Karp, J. M.; Hong, S.; Farokhzad, O. C.; Margalit, R.; Langer, R., Nanocarriers as an emerging platform for cancer therapy. *Nat. Nanotechnol.* **2007,** *2* (12), 751-60.

2. Torchilin, V. P., Multifunctional nanocarriers. *Adv. Drug Deliv. Rev.* **2012,** *64* (SUPPL.), 302-315.

3. Bao, G.; Mitragotri, S.; Tong, S., Multifunctional nanoparticles for drug delivery and molecular imaging. *Annu. Rev. Biomed. Eng.* **2013,** *15,* 253-82.

4. Schroeder, A.; Heller, D. A.; Winslow, M. M.; Dahlman, J. E.; Pratt, G. W.; Langer, R.; Jacks, T.; Anderson, D. G., Treating metastatic cancer with nanotechnology. *Nat. Rev. Cancer* **2012,** *12* (1), 39-50.

5. Caruso, F., Nanoengineering of particle surfaces. *Adv. Mater.* **2001,** *13* (1).

6. Hammond, P. T., Form and Function in Multilayer Assembly: New Applications at the Nanoscale. *Adv. Mater.* **2004,** *16* (15), 1271-1293.

7. Hammond, P. T., Polyelectrolyte multilayered nanoparticles: using nanolayers for controlled and targeted systemic release. *Nanomedicine* **2012,** *7* (5), 619-22.

8. Poon, Z.; Lee, J. B.; Morton, S. W.; Hammond, P. T., Controlling in vivo stability and biodistribution in electrostatically assembled nanoparticles for systemic delivery. *Nano Lett.* **2011,** *11* (5), 2096-103.

9. Morton, S. W.; Shah, N. J.; Quadir, M. A.; Deng, Z. J.; Poon, Z.; Hammond, P. T., Osteotropic therapy via targeted layer-by-layer nanoparticles. *Adv. Healthcare Mater.* **2014,** *3* (6), 867-75.

10. Wang, Y.; Yan, Y.; Cui, J.; Hosta-Rigau, L.; Heath, J. K.; Nice, E. C.; Caruso, F., Encapsulation of water-insoluble drugs in polymer capsules prepared using mesoporous silica templates for intracellular drug delivery. *Adv. Mater.* **2010,** *22* (38), 4293-7.

11. Fujimoto, K.; Toyoda, T.; Fukui, Y., Preparation of Bionanocapsules by the Layer-by-Layer Deposition of Polypeptides onto a Liposome. *Macromolecules* **2007,** *40* (14), 5122-5128.

12. Gittins, D. I.; Caruso, F., Tailoring the Polyelectrolyte Coating of Metal Nanoparticles. *J. Phys. Chem. B* **2001,** *105* (29), 6846-6852.

13. Morton, S. W.; Poon, Z.; Hammond, P. T., The architecture and biological performance of drug-loaded LbL nanoparticles. *Biomaterials* **2013,** *34* (21), 5328-35.

14. Elbakry, A.; Zaky, A.; Liebl, R.; Rachel, R.; Goepferich, A.; Breunig, M., Layer-by-layer assembled gold nanoparticles for siRNA delivery. *Nano Lett.* **2009,** *9* (5), 2059-64.

15. Poon, Z.; Chang, D.; Zhao, X.; Hammond, P. T., Layer-by-layer nanoparticles with a pH-sheddable layer for in vivo targeting of tumor hypoxia. *ACS Nano* **2011,** *5* (6), 4284-92.

16. Shutava, T. G.; Balkundi, S. S.; Vangala, P.; Steffan, J. J.; Bigelow, R. L.; Cardelli, J. A.; O'Neal, D. P.; Lvov, Y. M., Layer-by-Layer-Coated Gelatin Nanoparticles as a Vehicle for Delivery of Natural Polyphenols. *ACS Nano* **2009,** *3* (7), 1877-85.

17. Iler, R. K., Multilayers of colloidal particles. *J. Colloid Interface Sci.* **1966,** *21* (6), 569-594.

18. Decher, G.; Hong, J.-D., Buildup of ultrathin multilayer films by a self-assembly process, 1 consecutive adsorption of anionic and cationic bipolar amphiphiles on charged surfaces. *Makromol. Chem., Macromol. Symp.* **1991,** *46* (1), 321-327.

19. Decher, G.; Hong, J. D.; Schmitt, J., Buildup of ultrathin multilayer films by a self-assembly process: III. Consecutively alternating adsorption of anionic and cationic polyelectrolytes on charged surfaces. *Thin Solid Films* **1992,** *210,* 831-835.

20. Keller, S. W.; Johnson, S. A.; Brigham, E. S.; Yonemoto, E. H.; Mallouk, T. E., Photoinduced Charge Separation in Multilayer Thin Films Grown by Sequential Adsorption of Polyelectrolytes. *J. Am. Chem. Soc.* **1995,** *117* (51), 12879-12880.

21. Donath, E.; Sukhorukov, G. B.; Caruso, F.; Davis, S. A.; Möhwald, H., Novel Hollow Polymer Shells by Colloid-Templated Assembly of Polyelectrolytes. *Angew. Chem. Int. Ed.* **1998,** *37* (16), 2201-2205.

22. Sukhorukov, G. B.; Donath, E.; Davis, S.; Lichtenfeld, H.; Caruso, F.; Popov, V. I.; Möhwald, H.,

Stepwise polyelectrolyte assembly on particle surfaces: a novel approach to colloid design. *Polym. Adv. Technol.* **1998,** *9* (10-11), 759-767.

23.   Caruso, F.; Caruso, R. A.; Mohwald, H., Nanoengineering of Inorganic and Hybrid Hollow Spheres by Colloidal Templating. *Science* **1998,** *282* (5391), 1111-4.

24.   Borges, J.; Mano, J. F., Molecular interactions driving the layer-by-layer assembly of multilayers. *Chem Rev* **2014,** *114* (18), 8883-942.

25.   Del Mercato, L. L.; Abbasi, A. Z.; Ochs, M.; Parak, W. J., Multiplexed sensing of ions with bar-coded polyelectrolyte capsules. *ACS Nano* **2011,** *5* (12), 9668-74.

26.   Del Mercato, L. L.; Abbasi, A. Z.; Parak, W. J., Synthesis and characterization of ratiometric ion-sensitive polyelectrolyte capsules. *Small* **2011,** *7* (3), 351-63.

27.   Kazakova, L. I.; Shabarchina, L. I.; Sukhorukov, G. B., Co-encapsulation of enzyme and sensitive dye as a tool for fabrication of microcapsule based sensor for urea measuring. *Phys. Chem. Chem. Phys.* **2011,** *13* (23), 11110-7.

28.   Shchukin, D. G.; Sukhorukov, G. B., Nanoparticle Synthesis in Engineered Organic Nanoscale Reactors. *Adv. Mater.* **2004,** *16* (8), 671-682.

29.   Ariga, K.; Hill, J. P.; Ji, Q., Layer-by-layer assembly as a versatile bottom-up nanofabrication technique for exploratory research and realistic application. *Phys. Chem. Chem. Phys.* **2007,** *9* (19), 2319-40.

30.   Alkilany, A. M.; Boulos, S. P.; Lohse, S. E.; Thompson, L. B.; Murphy, C. J., Homing peptide-conjugated gold nanorods: the effect of amino acid sequence display on nanorod uptake and cellular proliferation. *Bioconjug. Chem.* **2014,** *25* (6), 1162-71.

31.   Deng, Z. J.; Morton, S. W.; Ben-Akiva, E.; Dreaden, E. C.; Shopsowitz, K. E.; Hammond, P. T., Layer-by-layer nanoparticles for systemic codelivery of an anticancer drug and siRNA for potential triple-negative breast cancer treatment. *ACS Nano* **2013,** *7* (11), 9571-84.

32.   Dreaden, E. C.; Kong, Y. W.; Morton, S. W.; Correa, S.; Choi, K. Y.; Shopsowitz, K. E.; Renggli, K.; Drapkin, R.; Yaffe, M. B.; Hammond, P. T., Tumor-Targeted Synergistic Blockade of MAPK and PI3K from a Layer-by-Layer Nanoparticle. *Clin. Cancer Res.* **2015,** *21* (19), 4410-9.

33.   Chanana, M.; Gliozzi, A.; Diaspro, A.; Chodnevskaja, I.; Huewel, S.; Moskalenko, V.; Ulrichs, K.; Galla, H. J.; Krol, S., Interaction of polyelectrolytes and their composites with living cells. *Nano Lett.* **2005,** *5* (12), 2605-12.

34.   Schneider, G.; Decher, G., From Functional Core/Shell Nanoparticles Prepared via Layer-by-Layer Deposition to Empty Nanospheres. *Nano Lett.* **2004,** *4* (10), 1833-1839.

35.   Schneider, G.; Decher, G.; Nerambourg, N.; Praho, R.; Werts, M. H.; Blanchard-Desce, M., Distance-dependent fluorescence quenching on gold nanoparticles ensheathed with layer-by-layer assembled polyelectrolytes. *Nano Lett.* **2006,** *6* (3), 530-6.

36.   Hong, X.; Li, J.; Wang, M.; Xu, J.; Guo, W.; Li, J.; Bai, Y.; Li, T., Fabrication of Magnetic Luminescent Nanocomposites by a Layer-by-Layer Self-assembly Approach. *Chem. Mater.* **2004,** *16* (21), 4022-4027.

37.   Dreaden, E. C.; Morton, S. W.; Shopsowitz, K. E.; Choi, J. H.; Deng, Z. J.; Cho, N. J.; Hammond, P. T., Bimodal tumor-targeting from microenvironment responsive hyaluronan layer-by-layer (LbL) nanoparticles. *ACS Nano* **2014,** *8* (8), 8374-82.

38.   Schneider, G. F.; Subr, V.; Ulbrich, K.; Decher, G., Multifunctional cytotoxic stealth nanoparticles. A model approach with potential for cancer therapy. *Nano Lett.* **2009,** *9* (2), 636-42.

39.   Schneider, G.; Decher, G., Functional core/shell nanoparticles via layer-by-layer assembly. investigation of the experimental parameters for controlling particle aggregation and for enhancing dispersion stability. *Langmuir* **2008,** *24* (5), 1778-89.

40.   Voigt, A.; Lichtenfeld, H.; Sukhorukov, G. B.; Zastrow, H.; Donath, E.; Bäumler, H.; Möhwald, H., Membrane Filtration for Microencapsulation and Microcapsules Fabrication by Layer-by-Layer Polyelectrolyte Adsorption. *Ind. Eng. Chem. Res.* **1999,** *38* (10), 4037-4043.

41.   Qi, A.; Chan, P.; Ho, J.; Rajapaksa, A.; Friend, J.; Yeo, L., Template-free synthesis and encapsulation technique for layer-by-layer polymer nanocarrier fabrication. *ACS Nano* **2011,** *5* (12), 9583-91.

42.   Shchukin, D. G.; Kommireddy, D. S.; Zhao, Y.; Cui, T.; Sukhorukov, G. B.; Lvov, Y. M., Polyelectrolyte Micropatterning Using a Laminar-Flow Microfluidic Device. *Adv. Mater.* **2004,** *16* (5), 389-393.

43.   Kantak, C.; Beyer, S.; Yobas, L.; Bansal, T.; Trau, D., A 'microfluidic pinball' for on-chip generation of Layer-by-Layer polyelectrolyte microcapsules. *Lab Chip* **2011,** *11* (6), 1030-5.

44.   Priest, C.; Quinn, A.; Postma, A.; Zelikin, A. N.; Ralston, J.; Caruso, F., Microfluidic polymer multilayer adsorption on liquid crystal droplets for microcapsule synthesis. *Lab Chip* **2008,** *8* (12), 2182-7.

45.   Richardson, J. J.; Ejima, H.; Lorcher, S. L.; Liang, K.; Senn, P.; Cui, J.; Caruso, F., Preparation of nano- and microcapsules by electrophoretic polymer assembly. *Angew. Chem. Int. Ed.* **2013,** *52* (25), 6455-8.

46.   Richardson, J. J.; Teng, D.; Bjornmalm, M.; Gunawan, S. T.; Guo, J.; Cui, J.; Franks, G. V.; Caruso, F., Fluidized bed layer-by-layer microcapsule formation. *Langmuir* **2014,** *30* (33), 10028-34.

47.   Morton, S. W.; Herlihy, K. P.; Shopsowitz, K. E.; Deng, Z. J.; Chu, K. S.; Bowerman, C. J.; Desimone, J. M.; Hammond, P. T., Scalable manufacture of built-to-order nanomedicine: spray-assisted layer-by-layer functionalization of PRINT nanoparticles. *Adv. Mater.* **2013,** *25* (34), 4707-13.

48.   Dalwadi, G.; Benson, H. A.; Chen, Y., Comparison of diafiltration and tangential flow filtration for purification of nanoparticle suspensions. *Pharm. Res.* **2005,** *22* (12), 2152-62.

49.   Sweeney, S. F.; Woehrle, G. H.; Hutchison, J. E., Rapid purification and size separation of gold nanoparticles via diafiltration. *J. Am. Chem. Soc.* **2006,** *128* (10), 3190-7.

50.   Lohse, S. E.; Eller, J. R.; Sivapalan, S. T.; Plews, M. R.; Murphy, C. J., A simple millifluidic benchtop reactor system for the high-throughput synthesis and functionalization of gold nanoparticles with different sizes and shapes. *ACS Nano* **2013,** *7* (5), 4135-50.

51.   Bjornmalm, M.; Roozmand, A.; Noi, K. F.; Guo, J.; Cui, J.; Richardson, J. J.; Caruso, F., Flow-Based Assembly of Layer-by-Layer Capsules through Tangential Flow Filtration. *Langmuir* **2015,** *31* (33), 9054-60.

52.   Dubas, S. T.; Schlenoff, J. B., Swelling and smoothing of polyelectrolyte multilayers by salt. *Langmuir* **2001,** *17* (25), 7725-7727.

53.   Burke, S. E.; Barrett, C. J., Acid-base equilibria of weak polyelectrolytes in multilayer thin films. *Langmuir* **2003,** *19* (8), 3297-3303.

54.   Parveen, N.; Schonhoff, M., Swelling and Stability of Polyelectrolyte Multilayers in Ionic Liquid Solutions. *Macromolecules* **2013,** *46* (19), 7880-7888.

55.   Shields, P. A.; Farrah, S. R., Influence of Salts on Electrostatic Interactions between Poliovirus and Membrane Filters. *Appl Environ Microb* **1983,** *45* (2), 526-531.

56.   Zhang, G. J.; Yan, H. H.; Ji, S. L.; Liu, Z. Z., Self-assembly of polyelectrolyte multilayer pervaporation membranes by a dynamic layer-by-layer technique on a hydrolyzed polyacrylonitrile ultrafiltration membrane. *J Membrane Sci* **2007,** *292* (1-2), 1-8.

57.   Petrache, H. I.; Dodd, S. W.; Brown, M. F., Area per Lipid and Acyl Length Distributions in Fluid Phosphatidylcholines Determined by 2H NMR Spectroscopy. *Biophys. J.* **2000,** *79* (6), 3172-3192.

58.   Henin, J.; Shinoda, W.; Klein, M. L., Models for phosphatidylglycerol lipids put to a structural test. *J Phys Chem B* **2009,** *113* (19), 6958-63.

59.   Hermanson, G. T., *Bioconjugate Techniques*. 2nd ed.; Academic Press: Amsterdam, 2008.

60.   Grabinski, C.; Schaeublin, N.; Wijaya, A.; D'Couto, H.; Baxamusa, S. H.; Hamad-Schifferli, K.; Hussain, S. M., Effect of gold nanorod surface chemistry on cellular response. *ACS Nano* **2011,** *5* (4), 2870-9.

61.   Hauck, T. S.; Ghazani, A. A.; Chan, W. C., Assessing the effect of surface chemistry on gold nanorod uptake, toxicity, and gene expression in mammalian cells. *Small* **2008,** *4* (1), 153-9.

62.   Alkilany, A. M.; Lohse, S. E.; Murphy, C. J., The gold standard: gold nanoparticle libraries to

understand the nano-bio interface. *Acc. Chem. Res.* **2013,** *46* (3), 650-61.

63.   Choi, K. Y.; Yoon, H. Y.; Kim, J. H.; Bae, S. M.; Park, R. W.; Kang, Y. M.; Kim, I. S.; Kwon, I. C.; Choi, K.; Jeong, S. Y.; Kim, K.; Park, J. H., Smart nanocarrier based on PEGylated hyaluronic acid for cancer therapy. *ACS Nano* **2011,** *5* (11), 8591-9.

64.   Salazar, M. D.; Ratnam, M., The folate receptor: what does it promise in tissue-targeted therapeutics? *Cancer Metastasis Rev.* **2007,** *26* (1), 141-52.

65.   Scott, J. E.; Cummings, C.; Brass, A.; Chen, Y., Secondary and tertiary structures of hyaluronan in aqueous solution, investigated by rotary shadowing-electron microscopy and computer simulation. Hyaluronan is a very efficient network-forming polymer. *Biochem. J.* **1991,** *274,* 699-705.

66.   Scott, J. E.; Heatley, F., Hyaluronan forms specific stable tertiary structures in aqueous solution: a 13C NMR study. *Proc. Natl. Acad. Sci. USA* **1999,** *96* (9), 4850-5.

67.   Scott, J. E.; Heatley, F., Biological properties of hyaluronan in aqueous solution are controlled and sequestered by reversible tertiary structures, defined by NMR spectroscopy. *Biomacromolecules* **2002,** *3* (3), 547-53.

68.   Lim, S. T.; Martin, G. P.; Berry, D. J.; Brown, M. B., Preparation and evaluation of the in vitro drug release properties and mucoadhesion of novel microspheres of hyaluronic acid and chitosan. *J. Control Release* **2000,** *66* (2-3), 281-92.

69.   Kim, B. S.; Kang, H. J.; Park, J. Y.; Lee, J., Fucoidan promotes osteoblast differentiation via JNK- and ERK-dependent BMP2-Smad 1/5/8 signaling in human mesenchymal stem cells. *Exp. Mol. Med.* **2015,** *47* (1), e128.

70.   Sharma, G.; Kar, S.; Basu Ball, W.; Ghosh, K.; Das, P. K., The curative effect of fucoidan on visceral leishmaniasis is mediated by activation of MAP kinases through specific protein kinase C isoforms. *Cellular & molecular immunology* **2014,** *11* (3), 263-74.

71.   Abdelwahed, W.; Degobert, G.; Stainmesse, S.; Fessi, H., Freeze-drying of nanoparticles: formulation, process and storage considerations. *Adv. Drug Delivery Rev.* **2006,** *58* (15), 1688-713.

72.   Because the lyophilization and reconstitution stages of the freeze-dried storage process are most likely to destabilize the nanoparticles, we expect that these particles could be stored for longer periods than demonstrated here. Nonetheless, a full week was chosen so as to demonstrate compatibility with timeframes common to shipping needs.

73.   Takeuchi, H.; Yamamoto, H.; Toyoda, T.; Toyobuku, H.; Hino, T.; Kawashima, Y., Physical stability of size controlled small unilameller liposomes coated with a modified polyvinyl alcohol. *Int J Pharm* **1998,** *164* (1-2), 103-111.

74.   Murakami, H.; Kobayashi, M.; Takeuchi, H.; Kawashima, Y., Preparation of poly(DL-lactide-co-glycolide) nanoparticles by modified spontaneous emulsification solvent diffusion method. *Int J Pharm* **1999,** *187* (2), 143-52.

75.   Berton, M.; Allémann, E.; Stein, C. A.; Gurny, R., Highly loaded nanoparticulate carrier using an hydrophobic antisense oligonucleotide complex. *Eur J Pharm Sci* **1999,** *9* (2), 163-170.

76.   De Jaeghere, F.; Allemann, E.; Leroux, J. C.; Stevels, W.; Feijen, J.; Doelker, E.; Gurny, R., Formulation and lyoprotection of poly(lactic acid-co-ethylene oxide) nanoparticles: influence on physical stability and in vitro cell uptake. *Pharm Res* **1999,** *16* (6), 859-66.

77.   Kamiya, S.; Nozawa, Y.; Miyagishima, A.; Kurita, T.; Sadzuka, Y.; Sonobe, T., Physical characteristics of freeze-dried griseofulvin-lipids nanoparticles. *Chem. Pharm. Bull.* **2006,** *54* (2), 181-4.

78.   Li, L.; Bae, B. C.; Tran, T. H.; Yoon, K. H.; Na, K.; Huh, K. M., Self-quenchable biofunctional nanoparticles of heparin-folate-photosensitizer conjugates for photodynamic therapy. *Carbohyd Polym* **2011,** *86* (2), 708-715.

79.   Zhang, K.; Xu, L. L.; Jiang, J. G.; Calin, N.; Lam, K. F.; Zhang, S. J.; Wu, H. H.; Wu, G. D.; Albela, B.; Bonneviot, L.; Wu, P., Facile large-scale synthesis of monodisperse mesoporous silica nanospheres with tunable pore structure. *J Am Chem Soc* **2013,** *135* (7), 2427-30.

Chapter 3. Discovery of ovarian cancer targeting surface chemistries through a library approach

Surface chemistry plays a crucial role in determining tumor-targeting abilities of nanoparticle drug carriers, but this role remains poorly understood. Notably, there are few studies that systematically inspect diverse and complex surface chemistries. In light of this, we report a methodical study of colloidal surface chemistry and its role in targeting ovarian cancer both in vitro and in a metastatic murine model. Using the layer-by-layer (LbL) assembly method, we varied the surface chemistry of 100 nm polystyrene nanoparticles in order to study ten different sulfated or carboxylated surfaces that span native polypeptides and polysaccharides. We report that carboxylated LbL nanoparticles shared an intrinsic affinity toward ovarian cancer cells, whereas sulfated LbL and non-LbL carboxylated formulations mediated poor binding. Despite this shared affinity, the various carboxylated LbL nanoparticles maintained distinct subcellular fates. These insights led to the discovery of several promising tumor-targeting LbL coatings as well as principles to guide the future design of therapeutic nanoparticles.

92

3.1. Introduction

Nanoparticle (NP) drug delivery vehicles can preferentially steer drugs to neoplastic tissue[1] and deliver therapeutic cargos that were previously undeliverable[2]. The advantages that nanoparticles bring to the table ought to lead to meaningful improvements for cancer therapy, where these capabilities can directly translate to improved efficacy, safety and the development of next-generation therapies, like combined RNAi and chemotherapy[3-4]. But the clinical success of nanomedicines has been frustrated by their inability to improve efficacy over free-drug formulations – although meaningfully reduced toxicities are often noted[5-7]. Clinical studies do indicate that nanoparticles improve drug accumulation in neoplastic tissue relative to surrounding healthy tissue[8-9], but it also appears that the overreliance on passive targeting strategies and the enhanced permeability and retention (EPR) effect has contributed to lackluster drug delivery in humans[10-11]. The next steps for nanomedicine require exploration of alternative targeting strategies, including new approaches for active targeting tailored to the unique challenges and opportunities posed by specific cancers.

Active targeting has been a topic of extensive research, largely focused on chemical conjugation of targeting ligands onto colloids[12]. More often than not, the surfaces of these particles are PEGylated to improve EPR-mediated passive targeting. It is not surprising, then, that systematic studies of NP surface chemistry - and the role surface chemistry plays in tumor targeting - have primarily focused on varying ligand and PEG brush density[13-17]. But there is a much broader parameter space beyond this to consider.

The surface of a nanoparticle ultimately interfaces with soluble factors, cellular membranes and extracellular matrix, all of which form sophisticated interactions with one another. But the rich physiochemical diversity in biological systems is not reflected in the surface chemistries used by most NPs. Part of the problem is that we do not know how to deploy complex surface chemistries to achieve a particular outcome, because there are few systematic studies that compare truly different surface chemistries[18-20].

One reason for the dearth of studies into this area may be the difficulty of installing complex biopolymers onto colloids using covalent conjugation techniques. To overcome this issue, we use the layer-by-layer (LbL) assembly method to systematically study nanoparticles bearing diverse surface chemistries. The LbL technique allows traditional colloidal substrates as small as 10 nm

(e.g., liposomes, mesoporous silica nanoparticles, and poly(lactic-co-glycolic acid) nanoparticles) to be functionalized with multilayered, nanoscale polymeric films through the sequential adsorption of polyelectrolytes of alternating charge[21-22]. The process is mediated by electrostatic interactions, making it compatible with an extensive list of bioactive and biocompatible polyelectrolytes (e.g., polysaccharides, polypeptides, nucleic acids). As a result, the technique is able to incorporate materials of significant chemical complexity without the need to develop similarly complex chemical conjugation techniques. And recent advances in the scale and throughput of LbL NPs now make it possible to study many more formulations than was previously feasible[23-24].

The modular nature of the LbL platform allows us to de-couple the role of different elements of the nanoparticle. This makes the LbL-NPs an ideal tool for systematic appraisal of the numerous parameters that influence nanoparticle engagement with cells and the body. In a previous study, we used the LbL technique to homogenize the surface chemistries of several disparate core substrates to better discern the effects of size and shape on the biodistribution of NPs in models of ovarian cancer[25]. Here, we shift our focus toward surface chemistry by functionalizing fluorescent, 100 nm carboxylate-modified latex (CML) nanoparticles with ten distinct LbL films. We used this panel of LbL NPs to disentangle the role of surface chemistry in mediating binding and internalization across a panel of ovarian cancer cells, normal stromal cells, and normal immune cells.

We focus this study on ovarian cancer (OvCa) because it presents particular drug delivery challenges. OvCa is characterized by the rampant spread of smaller tumors throughout the intraperitoneal (IP) space. Free-floating tumor spheroids often form that can subsist from nutrients available in the IP fluid, making some tumors difficult to access via systemic delivery routes — essentially establishing a protected reservoir of cancer cells[26]. However, the confinement of metastasis to the IP cavity also provides a unique opportunity to explore IP-administration routes of NPs, an approach that is already showing clinical benefits in the administration of free-drugs[27-29]{Wright, 2015 #251;van Driel, 2018 #252;Narod, 2016 #253}.

Our results reveal a fascinating capability for carboxylated LbL nanoparticles to bind preferentially to ovarian cancer cells in vitro and in vivo, a capability not shared with non-LbL carboxylated NPs and sulfated LbL formulations. In this work, we explore both systemic and IP routes, and report significantly higher NP accumulation in neoplastic tissue following IP-administration. Our

94

approach identified several surface chemistries with no known ligand-binding capabilities that have cancer cell affinities comparable to NPs with well-documented active targeting mechanisms. Notably, we also document the subcellular trafficking of these NPs and ovarian cancer cells' impressive ability to distinguish between even highly similar surface chemistries. Overall, this work provides a framework for future studies that leverage the versatility and compatibility of the LbL platform toward more systematic assessment of critical nanoparticle parameters.

3.2. Results: Surface chemistry dictates LbL nanoparticle affinity for ovarian cancer cells

LbL NPs were synthesized to explore the role of different sulfated and carboxylated surfaces on nanoparticle-ovarian cancer cell interactions. CML cores were first coated with poly(L-arginine) to establish a cationic polymer film suitable for subsequent layering of polyanions (**Figure 3.1a**). The two chemistry families were then fabricated through the electrostatic adsorption of a variety of natural and synthetic polyelectrolytes (**Figure 3.1a, right panel**). The carboxylate (COOH) family includes LbL nanoparticles terminated with the polysaccharide hyaluronic acid (HA), which binds to several known ligands overexpressed on ovarian cancer including the CD44 protein[30]. The sulfated (SO_3) family includes the polysaccharide heparin sulfate (HS), which has a variety of biological binding partners that include growth hormones and differentiation factors enriched in certain cancers[31]. The sulfated family also contains a derivative of HS that bears folic acid pendant groups (HF) to target folic acid receptor, also known to be overexpressed on ovarian cancer[32]. The LbL-NPs prepared for this study possess average hydrodynamic diameters ranging from 100 to 155 nm and average polydispersity indices between 0.04 and 0.13 (**Figure 3.1b**). And consistent with successful layering, we observe charge reversal during the deposition of the first PLR layer (-61±1 mV to +63±2 mV) followed by another charge reversal (ranging from -51 mV to -75 mV) after deposition of the final anionic layer (**Figure 3.1c**). The nanoparticle morphology was assessed using TEM, where all formulations appeared well dispersed and within the size ranges predicted by light scattering techniques (**Appendix B Figure 1**).

The surface chemistry family (e.g., COOH or SO_3) had an outsize role in determining binding affinity between the various LbL NP formulations and ovarian cancer cells, where COOH-LbL-NPs exhibited an intriguing OvCa-targeting behavior. The binding affinity of the LbL NPs was determined using flow cytometry to measure increases in NP-associated fluorescence for cells incubated with the NPs for 4 or 24 hours (**Figure 3.1d-e**). A panel of ten human ovarian cancer cell lines (Caov3, COV318, COV362, Fuov1, JHOS2, JHOS4, OVCAR3, OVCAR4, OVCAR8, and SKOV3) were tested, as well as a subset of healthy cells consisting of induced pluripotent stem cell (iPSC)-derived endothelial cells and primary immune and stromal cells isolated from fresh murine spleens. The median NP-associated fluorescence intensity (MFI) for each cell was normalized by the MFI of untreated cells to obtain a MFI ratio (MFR), which corresponds to the ex-

Discovery of ovarian cancer targeting surface chemistries through a library approach
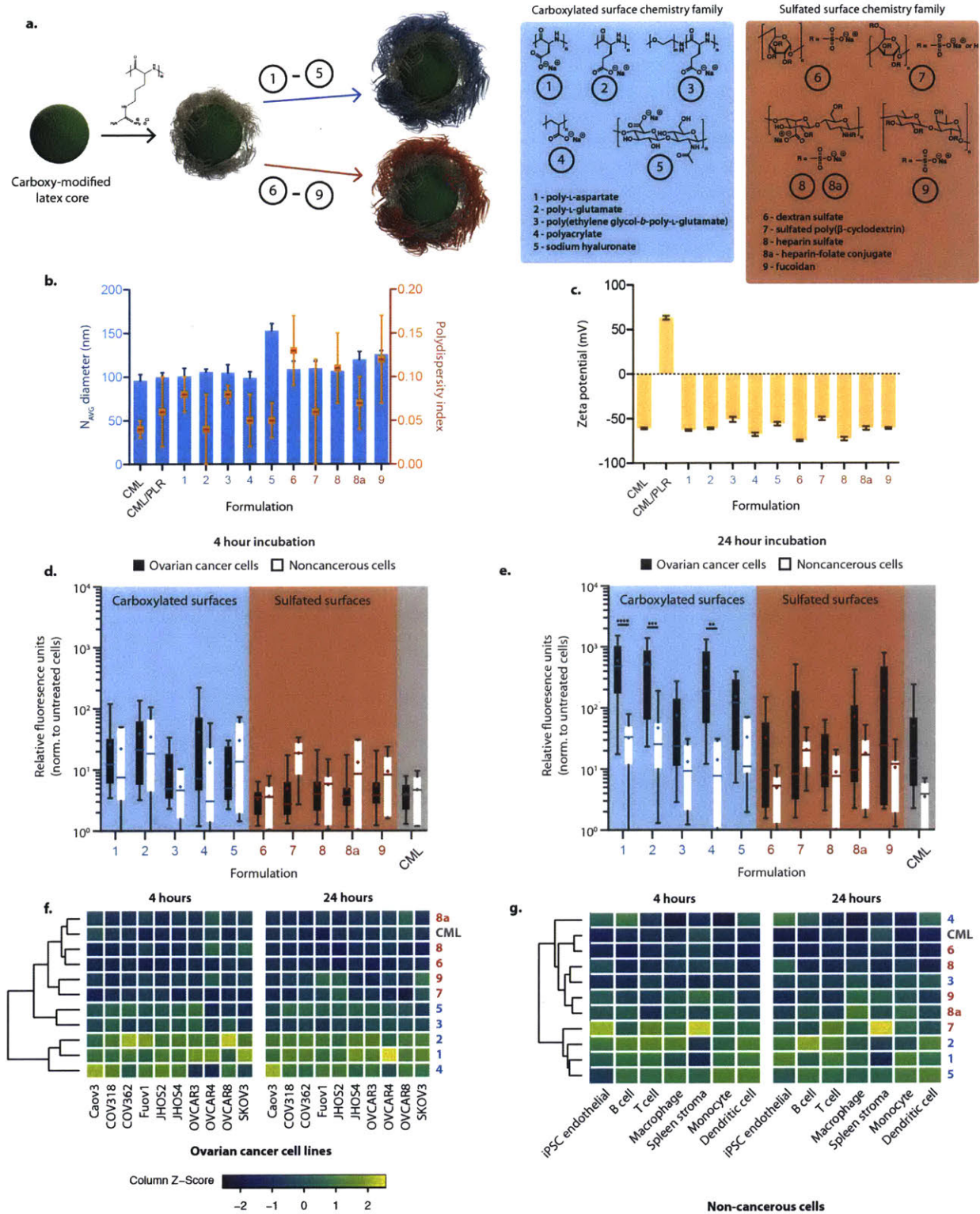
Figure 3.1. Layer-by-layer nanoparticles (LbL-NPs) with carboxylated terminal layers interact preferentially with ovarian cancer cells, in contrast to LbL-NPs with sulfated terminal layers and carboxy-modified latex (CML) nanoparticles. a) LbL-NPs were prepared from a fluorescent 100 nm CML core template by adsorbing a cationic layer of poly-L-arginine followed by adsorption of one of ten different terminal anionic polymers.

Figure 3.1 continued: b) LbL-NPs retain similar size and monodispersity relative to the CML template, and **c)** exhibit charge reversal upon adsorption of each layer as expected with the LbL technique. Size and polydispersity data were acquired by dynamic light scattering, and zeta potential data were measured using laser Doppler electrophoresis. Error bars represent standard deviation of three technical replicates. To determine the role of LbL-NP surface chemistry on cell-binding, LbL-NPs were incubated with a panel of ten human ovarian cancer cell lines and seven noncancerous primary cells and analyzed using flow cytometry to quantify increases in nanoparticle-associated fluorescence after **d)** 4 hours and **e)** 24 hours. Sulfated LbL-NPs bound less to cancer cells at 4 hours, and showed a highly variable binding by 24 hours. On the other hand, carboxylated LbL-NPs bind more efficiently to cancer cells by 24 hours and exhibit significantly higher enrichment in cancer cells relative to noncancerous cells. **f)** Hierarchical clustering of LbL-NP binding data leads to a grouping of formulations by their surface chemistry, with the exception of the core CML template that behaves more similarly to sulfated LbL-NPs. **g)** Clustering of NP-binding data in noncancerous cells does not lead to surface chemistry-based groupings.

tent of nanoparticle bound to the cells. The results shown group all OvCa lines and healthy cells. After 4 hours, COOH-LbL-NPs bind well to both OvCa (average MFR of 10 to 42) and healthy (average MFR of 6 to 49) cells. On the other hand, at 4 hours SO_3-LbL-NPs have low overall binding in OvCa cells (average MFR of 3 to 6) and a higher but more variable uptake in healthy cells (average MFR of 4 to 22) (**Figure 3.1d**). The unmodified CML cores, which are simply decorated with carboxylate groups, behaved very differently from the COOH-LbL-NPs, and accumulate to a lesser extent with an average MFR of only 4 for OvCa cells and 5 for healthy cells.

By 24 hours, the COOH-LbL-NPs are enriched in OvCa cells (average MFR of 76 to 595) relative to healthy cells (average MFR of 13 to 71), and despite the variability amongst the different OvCa and healthy cell lines this finding was significant with a p value <0.0001 (one-way ANOVA, Bonferonni post hoc test, **Figure 3.1e**). This behavior does not extend to SO_3-LbL-NPs, where uptake is highly variable among OvCa cells, and while these NPs accumulate more in OvCa cells (average MFR of 18 to 191) relative to healthy cells (average MFR of 5 to 22) the difference was not statistically significant. Surprisingly, HA and HF-coated NPs did not bind to OvCa cells as efficiently as formulations with no known receptor-binding abilities. For example, HA-coated NPs on average exhibited a 154-fold increase in MFI, but poly(L-aspartate) (PLD)-coated NPs had an average MFI increase of 595-fold. HF-coated NPs (average MFR of 72) improved their uptake relative to HS-coated NPs (average MFR of 19), but were outperformed by sulfated beta cyclodextrin (SBC)-coated and fucoidan-coated NPs (average MFR of 107 and 192, respectively). Interesting results involving the SBC-coated NPs and endothelial cells were noted, and are discussed in **Appendix B**. These results suggest that while inclusion of a targeting ligand can improve tumor targeting, their contribution to binding affinity may be overshadowed by the contribution from the surface chemistry of the terminal layer (e.g., COOH or SO_3). Importantly, unmodified CML cores

behave more like SO_3-LbL-NPs even at 24 hours, with an average MFR of 50 for OvCa and 29 for healthy cells. This result indicates a special role for the LbL film in mediating the interactions observed with COOH-LbL-NPs, which may explain why prior studies of carboxylated inorganic cores do not observe elevated cell-binding properties. It is also possible that the affinity towards COOH-LbL-NPs is based on biology particular to ovarian cancer cells.

Hierarchical clustering of the uptake data provides additional confirmation of a surface chemistry effect on NP-binding for OvCa cells (**Figure 3.1f**), but not healthy cells (**Figure 3.1g**). The MFR data for both time points were used to generate a clustered heatmap using the heatmap.2 function in the gplot package on RStudio. Clusters were calculated using the default function settings. For the OvCa cells, the NP formulations primarily cluster together in an order that corresponds to their surface chemistry. The exception to this is the CML core, which clusters along with the SO_3-LbL-NPs. The clusters generated for the healthy cells do not order the formulations based on their surface chemistry, supporting the notion that ovarian cancer cells may possess an affinity for certain surface chemistries that are not shared by the healthy cells assayed here.

3.3. Results: Carboxylated LbL nanoparticles mediate distinct subcellular trafficking routes

Subcellular localization of NPs determines the types of drugs that can be delivered with a given formulation. And while our flow cytometry study indicated NP-association with cells, it did not provide insight into the role that surface chemistry plays in determining the subcellular fate of the different formulations tested. To answer that question, we performed live cell confocal microscopy on JHOS4 ovarian cancer cells that had been incubated with 20 pM NP concentrations for 24 hours. The findings from this study generally confirmed the observations from flow cytometry (e.g., improved accumulation with COOH-LbL-NPs relative to CML and SO_3-LbL-NPs), but also revealed distinct subcellular fates particular to the two surface chemistry families.

At 24 hours, COOH-coated LbL NPs without a targeting ligand (PLD, poly(L-glutamate) (PLE), poly(ethylene glycol-b-poly-L-glutamate) (PEG-PLE), and polyacrylate (PAA)) were often associated with the cell membrane (**Appendix B Figure 2a**). PEG-PLE and PAA-coated NPs were almost entirely surface-bound, whereas PLD and PLE-coated NPs were both internal and external. HA, on the other hand, is generally internalized at this time point, which we hypothesize is due to its CD44-binding capabilities. In contrast, the unmodified CML core is much less abundant but also generally internalized. The SO_3-LbL-NPs are not bound to all cells, consistent with the high variability seen by flow cytometry (**Appendix B Figure 2b**). But when they are bound, they are generally internalized – with the exception of fucoidan-coated particles which appear primarily on the surface of JHOS4 cells.

Of note, the PLD and PLE-coated NPs exhibited a remarkable affinity for ovarian cancer cells, leading to 4.5 to 5.5-fold more nanoparticles per cell than the HA-coated particles (**Appendix B Figure 2c**). Flow cytometry results of other ovarian cancer cell lines consistently recapitulated this trend (**Figure 3.2a**). The reproducibility and magnitude of this observation led us to hypothesize that some unknown specific binding interaction may be occurring between these polypeptide-coated systems and ovarian cancer cells. Efforts to determine apparent dissociation constants (Kd_{app}) through a saturation binding isotherm confirmed that PLD, PLE, and HA-coated NPs possess a high binding affinity for OVCAR8 ovarian cancer cells, whereas unmodified CML core, dextran sulfate (DXS)-coated and PEGylated NP controls exhibit binding curves typical to

100

Dextran sulfate (DXS)   Sodium hyaluronate (HA)   Poly-L-glutamate (PLE)   Poly-L-aspartate (PLD)
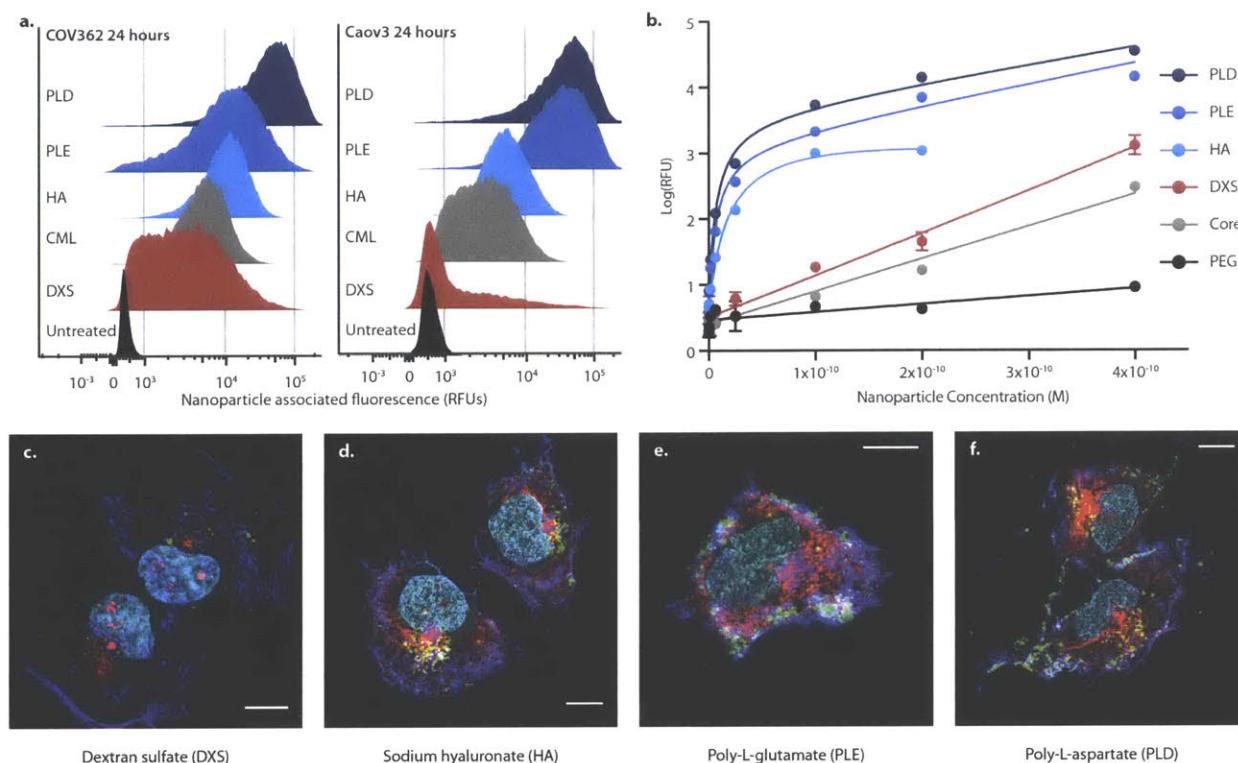
Figure 3.2. Carboxylated LbL-NPs have improved binding to ovarian cancer cells, but possess distinct sub-cellular localization despite their similar surface chemistries. Flow cytometry analysis indicates that LbL-NPs terminated with the carboxylated polymers poly-L-aspartate (PLD), pol-L-glutamate (PLE) and sodium hyaluronate (HA) bound to **a)** COV362 and Caov3 ovarian cancer cells to a much greater extent than dextran sulfate (DXS)-terminated LbL-NPs and the unmodified carboxylated latex core. **b)** A binding saturation isotherm experiment was conducted to estimate apparent K_d values for these nanoparticles. The results indicate a strong specific interaction for the PLD and PLE-coated systems with respective K_d values of 6.8±1.6 and 6.2±2.2 pM. HA-coated NPs had a K_d value of 18.7±18.4 pM. DXS-coated, PEGylated and unmodified CML cores could not be fit to the model, but the shape of their curve suggests a nonspecific binding interaction. **c)** Confocal microscopy of OVCAR8 ovarian cancer cells demonstrate a minimal accumulation of DXS-terminated LbL-NPs, which are internalized at 24 hours. Nuclei are psuedocolored cyan, lysosomes are red, actin is blue, and nanoparticles are in green. **d)** HA-terminated LbL-NPs accumulate to a much greater extent, and are mostly internalized at 24 hours. **c)** In contrast, PLE- coated LbL-NPs have a significant fraction of bound nanoparticle retained on the surface of the cell at 24 hours. **d)** PLD-coated systems presented a distinct subcellular trafficking pattern relative to the highly similar PLE-coated particle, resulting in a sizeable fraction of internalized and surface-bound nanoparticles at 24 hours. Scale bars indicate 10 micrometers. Error bars in b) represent SEM, error on the apparent K_d value are SEM.

nonspecific interactions (**Figure 3.2b**). Further study is needed to determine the binding mechanisms between PLE/PLD and OvCa cells, but a potential clue may come from prior studies that indicate carboxylated polymers are mucoadhesive[33-34], and since OvCa cells have been found to overexpress a variety of mucins[35] it warrants further study.

While PLE and PLD-coated NPs bind to OvCa cells with a high affinity, their subcellular fates were distinct from HA, and even from one another. We confirmed that the unique morphologi-
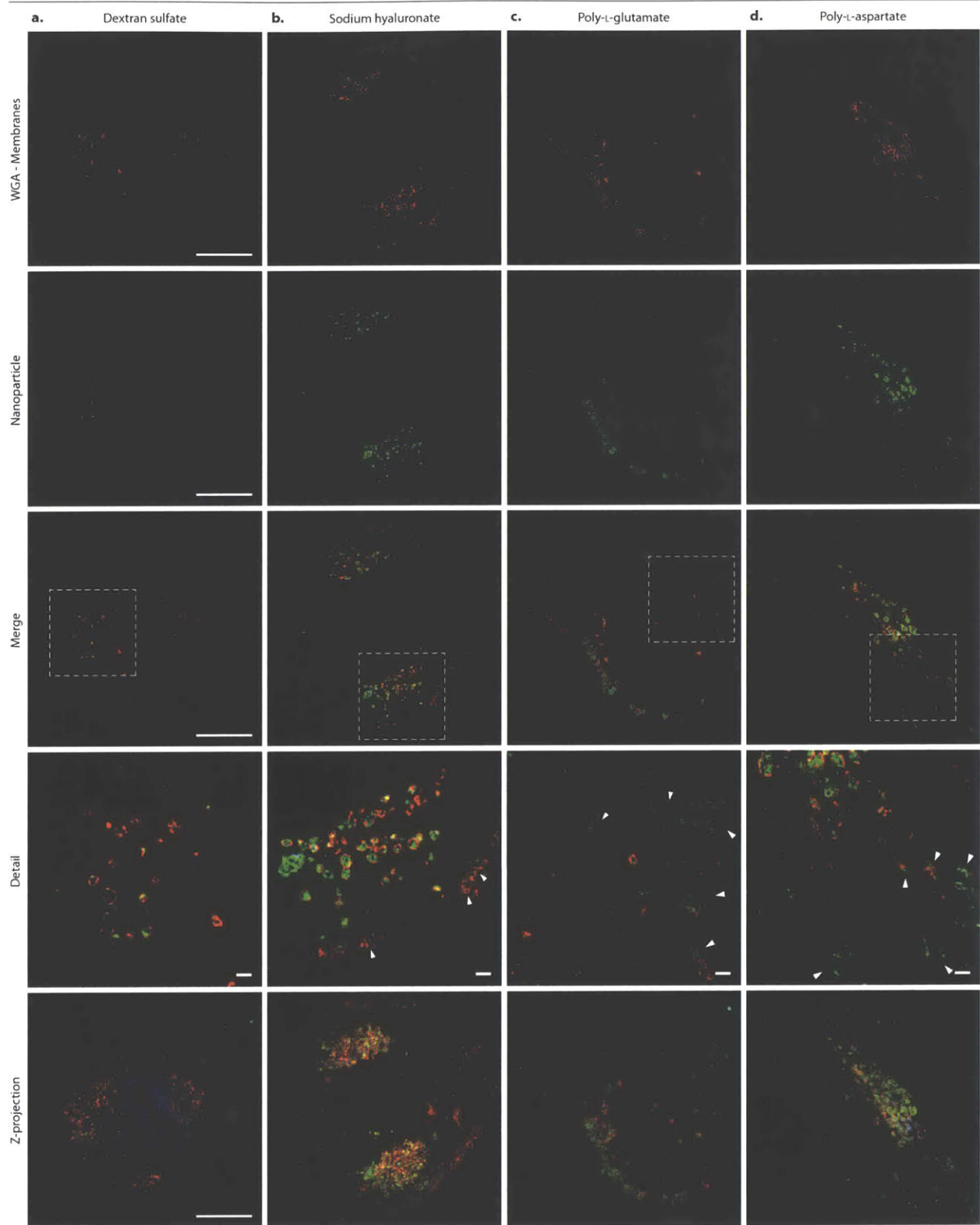
Figure 3.3. Surface chemistry on LbL NPs shapes subcellular fate and influences the partitioning of NPs on the membrane and on the interior of OVCAR8 cells. Cells were treated with 20 pM LbL NP for 24 hours and then fixed and processed for super resolution microscopy. Wheat germ agglutinin (WGA) was used to stain membranes (including outer membrane, vesicular membranes and the nuclear membrane) and is shown in red.

Figure 3.3 continued: Nanoparticles are shown in green and nuclei in blue. Scale bars denote 10 microns, with the exception of the scale bar for the detail panels, where they denote 1 micron. **a)** Dextran sulfate (DXS)-coated NPs are observed on the interior of the cell within vesicular structures. **b)** Sodium hyaluronate (HA)-coated NPs are found in enlarged vesicles within the cell, but also in small punctate spots on the membrane surface as indicated with white arrows. **c)** Poly-L-glutamate (PLE)-coated NPs are observed inside enlarged vesicles, but with a considerable fraction on the membrane with a seemingly diffuse morphology as indicated by the arrows. **d)** Poly-L-aspartate (PLD)-NPs are found both inside enlarged vesicles and on the membrane. However, PLD-NPs on the membrane appear more as punctate structures as indicated by arrows in the detail row.

cal features observed in the JHOS4 cell line could be reproduced in COV362 and Caov3 cells through additional live cell imaging studies (**Appendix B Figures 3-4**). And we also confirmed the unique surface-bound morphology in fixed cell confocal imaging studies using the OVCAR8 cell line (**Figure 3.2c-f**). In general, HA-coated NPs are mostly internalized in these cells, PLD-coated NPs exhibit punctate localization both inside and on the cell membrane, and PLE presents with a seemingly fibrous surface coating as well as some punctate internalization.

We continued to study the subcellular trafficking of these NPs in OVCAR8 cells through a systematic confocal microsopy study to inspect co-localization of NPs with key organelles such as early endosome (EEA1 or RAB5+), caveolae (CAV1+), clathrin-coated vesicles, late endosomes (Rab7+), lysosomes (Lamp1+), and trans golgi (RCAS1+) (**Appendix B Figures 5 and 6**). These initial studies indicated that NPs that are internalized by 24 hours are almost entirely in the late endolysosomal compartment (**Appendix B Figure 5i-p**). However, for the PLE and PLD-coated NPs we observed frequent co-localization with caveolae for surface-bound NPs (**Appendix B Figure 5c-d**). Intriguing but inconclusive data demonstrating NPs near the trans golgi stacks for COOH-LbL-NPs were also noted (**Appendix B Figure 5r-t**).

To improve the conclusiveness of these studies, a similar set of co-localization experiments was repeated using super resolution microscopy (**Figure 3.3, Appendix B Figures 7-10**). The improved dynamic range of this approach revealed a previously undetected, smaller subset of HA-coated particles that were surface-bound (**Figure 3.3b**) and associated to caveolae (**Appendix B Figure 8b**). Super resolution microscopy also further confirmed an enriched surface-bound fraction for PLD and PLE-coated particles (**Figure 3.3c-d**). However, while this fraction was typically associated to caveolae for PLD (**Appendix B Figure 8d**), the membrane-bound PLE-NPs did not necessarily always co-localized with caveolae (**Appendix B Figure 8c**). And while trans-golgi co-localization was ultimately not observed, the vesicles containing COOH-NPs were often found very near or between trans golgi stacks (**Appendix B Figure 10**).
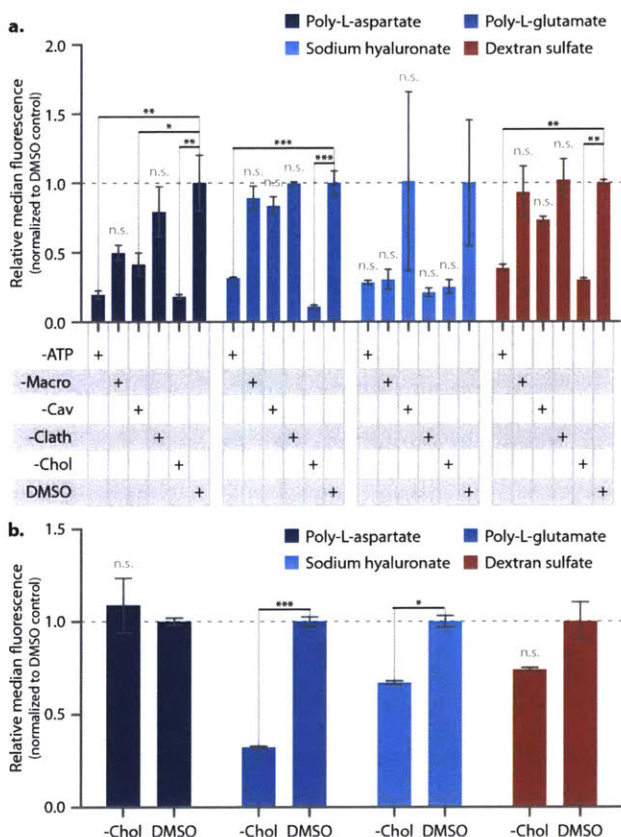
Figure 3.4. LbL-NP surface chemistry determines uptake pathways in OVCAR8 cells, indicating a shared role for ATP and lipid-raft mediated internalization as well as pathways unique to each formulation. a) OVCAR8 cells were pretreated with endocytosis inhibitors prior to a 4-hour incubation with LbL-NPs, followed by flow cytometry analysis. Poly-L-aspartate (PLD)-coated NPs depended upon caveolar uptake, and may be involved in macropinocytosis and clathrin-mediated processes, although those trends were not statistically significant. Notably, none of these pathways impact uptake of PLE. And while not statistically significant, HA appears to be impacted by most inhibitors except for caveolar inhibition. **b)** OVCAR8 cells incubated with LbL-NPs for 24 hours were depleted of cholesterol using methyl beta cyclodextrin prior to analysis by flow cytometry. Removal of cholesterol causes a significant decrease in nanoparticle-associated fluorescence in cells incubated with PLE-coated LbL-NPs. Error bars represent SEM, and statistical analysis was performed using one-way ANOVA test with a Dunnett post-hoc test and an alpha of 0.5.

These LbL-NPs were then tested on patient-derived xenograft (PDX) spheroids grown briefly (2 days) in culture. Flow cytometry on the dissociated spheroids and confocal microscopy of the intact spheroids provide evidence consistent with what we observed with the established cell lines (**Appendix B Figure 11**). Namely, that the COOH-LbL NPs possess a strong affinity for ovarian cancer cells, whereas sulfated LbL-NPs do not. However, even the COOH-LbL NPs do not penetrate into the spheroids, as indicated by a nanoparticle-negative population in the flow cytometry results.

During the microscopy studies, it was noted that PLE-treated cells permeabilized with saponin (all intracellular stains except caveolar) exhibited less membrane-bound nanoparticles than prior experiments that used triton-based permeabilization. This difference indicated a potential role for lipid rafts in the binding and trafficking of the COOH-LbL-NPs, because saponin acts to specifically remove cholesterol from the membrane[36-37]. To investigate this, as well as other uptake mechanisms, we performed an uptake-inhibition study to probe the relative roles of ATP, caveo-

lar, clatherin, macropinocytosis, and cholesterol-mediated uptake in OVCAR8 cells (**Figure 3.4**). Cells were pre-treated with inhibitor and then co-treated with LbL-NPs for 4 hours prior to flow cytometry analysis (**Figure 3.4a**). We observed that ATP and cholesterol-mediated processes were critical for the uptake of all NPs tested. But interestingly, only PLD-coated NPs were dependent on caveolar uptake – potentially indicating their role in internalizing these particles but not in the internalization of HA or PLE.

In a similar experiment, OVCAR8 cells were incubated with LbL-NPs for 24 hours and then treated with methyl-beta cyclodextrin to deplete cholesterol, in order to determine if at later time points the NPs associate with cholesterol-rich portions of the cell membrane. Notably, the PLE-treated cells bear significantly fewer nanoparticles after cholesterol depletion. Surprisingly, HA-treated cells see a smaller but statistically significant impact, whereas PLD-treated cells are unaffected (**Figure 3.4b**). These results suggest an early role for cholesterol in the uptake of PLD, where the NP may be associated with cholesterol-rich regions of the cell membrane. But at later time points, that association appears to fade. On the other hand, PLE appears to be highly associated with cholesterol throughout the time points studied. These differences among COOH-LbL-NPs are remarkable, particularly in the context of the PLE and PLD formulations, which differ by a single methylene group.

These results suggest an exquisite sensitivity to surface chemistry among ovarian cancer cells, which translates to unique subcellular fates for even highly similar formulations. Each of these formulations presents interesting opportunities from a drug delivery standpoint. PLE, for example, has applications for presenting therapeutic compounds on the surface of cancer cells, such as immunostimulatory cytokines and polymers. PLD-coated systems, on the other hand, present opportunities for nanoparticles to perform both intracellular and extracellular functions. HA-coated systems have clear benefits for drugs that require internalization, like siRNA and mRNA. Overall, this indicates how a systematic study of surface chemistry using the LbL platform can supply researchers with useful new formulations and nanoparticle design insights.

3.4. Results: Carboxylated LbL nanoparticles improve biodistribution in a orthotopic model of ovarian cancer

Ovarian cancer presents particular challenges and opportunities from a drug delivery perspective. The ability for OvCa spheroids to form and subsist from the nutrient-rich IP fluid creates a protected population of tumor cells, and evidence suggests these cells possess the stemlike properties needed to regenerate tumors[26]. But although OvCa metastasizes widely through the IP cavity, it rarely spreads outside of this space[38]. It also has the unique characteristic of growing superficially on organs rather than penetrating the mesothelial lining to invade those tissues[26]. As a result, OvCa may benefit from IP-administration of therapeutics moreso than other malignancies, and in fact clinical trials with free-drug therapies have found benefits to this approach. Nanoparticles 50-720 nm administered IP are known to be readily cleared into the lymphatic drainage, driving NPs directly into the thoracic lymph duct where they can be readily scavenged[39]. But recent work demonstrates that NPs with avid binding to the mesothelium are able to coat the lining of the IP space and serve as local drug depots[40]. Given the avidity of our NPs to OvCa cells in vitro, we set out to compare how IV and IP administration alters the biodistribution of COOH-LbL-NPs, control sulfated LbL NPs (DXS), PEGylated NPs, and unmodified CML cores.

We observed that IP administration confers a significant improvement in NP association with neoplastic tissues in an orthotopic model of metastatic ovarian cancer (luciferized/mCherry expressing OVCAR8 cells). Tumor-bearing mice were injected IP or IV with infrared-fluroescent LbL NPs, PEGylated NPs or unmodified CML NPs. After 24 hours, the mice were sacrificed and the bioluminescence and infrared fluroescence of each organ was measured using an IVIS imaging device. Systemically administered NPs were present in most metastatic nodules and in parts of the primary tumor masses (**Appendix B Figures 12-17**), and of note the PLD-coated NPs appeared to co-localize particularly well. But after IV administration, the bulk of the NP dosage was observed in the liver for LbL-NPs and CML cores, and in the liver and spleen for the PEGylated NPs. On the other hand, the IP-administered NPs co-localize with neoplastic tissues but also accumulate to a much greater extent for all NPs tested (**Appendix B Figure 18**). PEGylated and unmodified CML NPs accumulate to a lesser extent than all the LbL-NPs, and notably PEGylated NPs are detected diffusely throughout the liver and spleen, suggesting they are being cleared into the lymphatics and are penetrating the blood compartment where they can be scavenged by
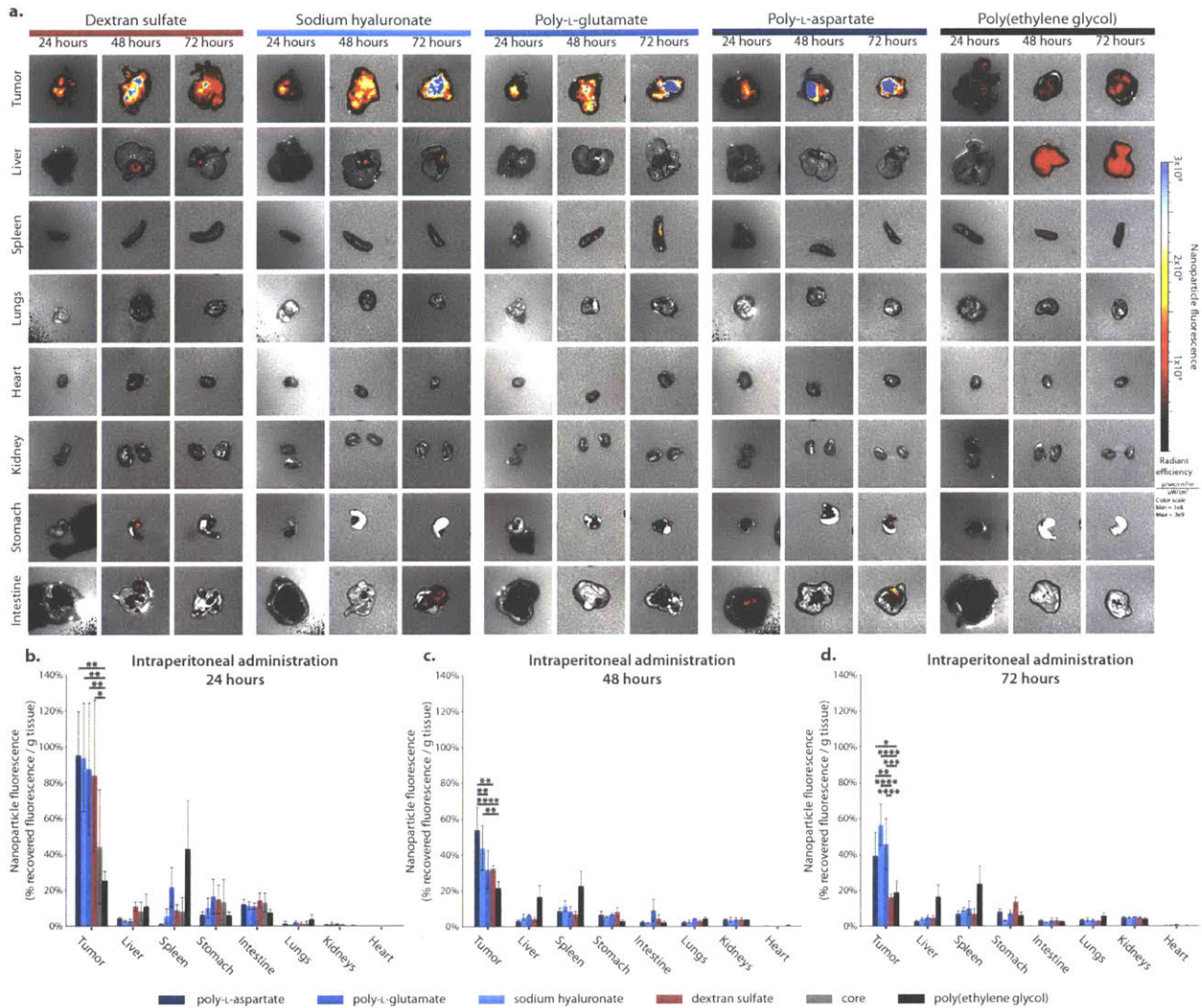
Figure 3.5. Tracking biodistribution over 72 hours shows a durable enrichment of COOH LbL-NPs in neoplastic tissue relative to dextran sulfate-coated and PEGylated NPs. NPs were administered IP to murine models of metastatic ovarian cancer, and **a)** infrared fluorescence from the nanoparticles were measured for each organ using an IVIS imaging device at the indicated time points. For CML core images, reference Appendix B Figure 12. **b)** Quantification of percent recovered NP fluorescence per gram of tissue indicated that LbL NPs had significant and improved accumulation in neoplastic tissue relative to PEGylated control NPs. Notably, unmodified CML cores did not significantly differ from PEG controls. **c)** At 48 hours, NP enrichment decreases for all NPs, but PLD and HA-NPs retain significant improvements over PEGylated controls. Notably, PLD-coated NPs are also significantly improved relative to PLE and DXS-coated systems at this time point. **d)** At 72 hours, all the COOH LbL-NPs demonstrate significantly improved tumor accumulation relative to both DXS and PEGylated controls. While not statistically significant in these data, it is interesting to note that the PEGylated control NP accumulates more in the liver and spleen than any LbL-NP, especially after 24 hours.

phagocytic cells. Unexpectedly, the DXS-coated NPs associate well with tumors at this time point, in contrast to our in vitro observations.

Although surface chemistry did not appear to shape LbL-NPs interactions with tumor tissues at 24

107

hours, the contribution from surface chemistry becomes more apparent at later time points. LbL-NP and PEGylated NP biodistribution was measured at 48 and 72 hours after IP administration in tumor bearing mice, using the same approach as in our IV and IP comparison study (**Figure 3.5**). We noted a less variable biodistribution profile emerged beginning at 48 hours, around which time we also note that PEGylated NPs begin to spill significantly into the liver and spleen compartments. It is likely that the antifouling properties of the PEG NPs prevents binding and internalization into tumors, and thus the NPs are eventually cleared into the lymphatics where they can be efficiently scavenged by the phagocytic cells of the liver and spleen. We also note that at these later time points the results fall in line with our earlier in vitro observations on the role of surface chemistry, with COOH-LbL-NPs systems providing improved tumor localization relative to the DXS-coated control particle (**Figure 3.5c-d**). By 72 hours, the COOH-LbL-NPs were broadly retained in the tumor tissue, whereas DXS-coated NPs and PEGylated NPs are cleared. Promisingly, LbL-NPs administered IP do not accumulate in off-target tissues even at later times, which would suggest that these NPs avoid lymphatic drainage into the blood compartment. The extent to which NP signal is observed in off-target organs is almost always co-localized to a metastatic lesion (**Appendix B Figures 19-23**). On the other hand, PEGylated nanoparticles clear into the liver and spleen by 48 and 72 hours. This leads to a ca. 4 and 3-fold increase in recovered nanoparticle signal from liver and spleen of PEG NP-treated mice relative to the liver and spleens from LbL NP-treated mice (average of all COOH-LbL-NPs) by 72 hours. This biodistribution profile indicates that the COOH-LbL-NPs may provide a highly selective delivery of drugs to tumor tissue when administered IP, potentially allowing for the delivery of drugs with narrow therapeutics windows.

Histological and whole-tissue imaging modalities were used to determine if LbL-NPs are able to penetrate tumor tissue when administered IP, and in general indicate that while these NPs are enriched on the tumor surface, they do penetrate as far as 100-300 microns. Histological samples obtained from these biodistribution experiment indicate that IP-injected NPs accumulate on the surface of tumors at 24 hours (**Figure 3.6a**). It was also noted that extensive handling and processing steps used to prepare histological samples from formalin-fixed tissue led to significant loss of NP in the tissue, leaving many surface regions of the tumors bare. Cryohistology of PLE-NP treated mice indicates a more uniform coating exists on pristine tissues, but cryohistology was not carried out for all other conditions and time points (**Appendix B Figure 24**). Nonetheless, the
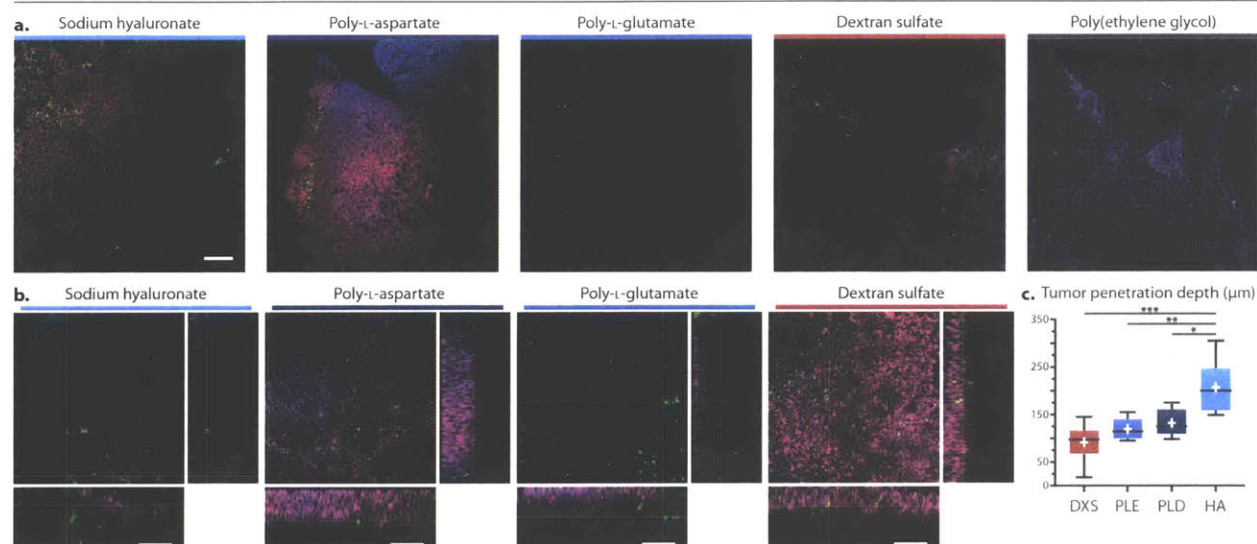
Figure 3.6. LbL-NPs penetrate into tumor tissue and may be aided by receptor-ligand interactions. Tumors from the prior biodistribution study were fixed and preserved for histology or for multi-photon whole-tissue imaging. **a)** Tissue sections 24 hours after IP-administration of nanoparticles shows enrichment of nanoparticles on the periphery of the tumor, with some penetration into the tissue. Red and blue signal are psuedocolored auto fluorescence from H&E staining, green signal indicates nanoparticle. Scale bar on the first image indicates 100 microns for all histological images. **b)** Representative slices and orthogonal views of z-stacks acquired from whole-tumor imaging using multi-photon microscopy. Blue signal corresponds to the second harmonic autofluorescence from collagen, red corresponds to the mCherry signal from tumor cells, and green signal is from nanoparticles. **c)** The z-stacks from multi-photon imaging were quantified to measure the deepest NP penetration into tumor tissues. HA-coated NPs penetrated the deepest into tissue with an average depth of 200.0±23.4 microns. While DXS-coated NPs had more variable penetration, their penetration was not significantly different from the PLE or PLD-NPs. Because HA-NPs have a known receptor ligand interaction, it is possible that this is mediating deeper distribution into the tumor.

remaining particles in the more complete formalin-fixed dataset indicate what we believe to be a reliable representation of nanoparticle distribution within the tumor. Additional studies on intact formalin-fixed tumors from the 72 hour timepoint were performed using multi-photon microscopy to more accurately assess tissue penetration depth (**Figure 3.6b**). The LbL-NPs were detectable on the multi-photon microscope at both a normal fluorescence channel catching the tail-end of the NP emission spectra (Cy5.5) and more clearly at a shorter wavelength channel (DAPI) capturing a multi-photon event from these NPs. In the z-sections examined, the LbL NP average penetration depth ranged from 97.5 to 200 microns, with HA-coated NPs managing to mediate deeper penetration. Quantification of these images indicated that PLD, PLE, HA, and DXS-coated NPs achieved average penetration depths of 125.0±12.1, 114.5±9.6, 97.5±17.5, and 200.0±23.4 microns, respectively (**Figure 3.6c**). Notably, the PEGylated nanoparticles were not detectable on the multi-photon at laser powers that avoided significant tissue autofluorescence, and thus could not be quantified. The results from whole-tissue imaging provide a more complete picture of NP

penetration, indicating the ability for LbL-NPs to navigate into tumor tissue after IP-administration. They also suggest a potentially important role in the ligand-binding capabilities of HA-coated NPs, which perhaps help to mediate the improved tissue penetration depths observed here. Overall, this indicates LbL-NPs, particularly ones with carboxylated terminal layers, can selectively coat and to an extent penetrate OvCa tumors following IP administration. This strategy could be used to develop new nanomedicines that leverage both the relatively high dose achieved on the tumor surface and the ability to minimize spillover to other organs and tissues.

3.5. Conclusions and future work

This work demonstrated the potential of using the LbL self-assembly method to systematically screen surface chemistries for affinity towards ovarian cancer. Ten unique surface chemistries were studied that consisted of either sulfated or carboxylated species, including a variety of natural polymers such as polysaccharides and polypeptides. Notably, this study identified a unique affinity between carboxylated LbL nanoparticles and ovarian cancer cells, an affinity that was not recapitulated with polystyrene nanoparticles simply functionalized with carboxylates. Carboxylated LbL nanoparticles also stood apart from their sulfated counterparts, which generally mediated relatively poor and nonspecific binding interactions with ovarian cancer cells. Interestingly, the binding of carboxylated LbL nanoparticles to healthy cells was not significantly enhanced relative to sulfated systems, indicating that biology particular to ovarian cancer cells might mediate this improved uptake. Notably, while carboxylated LbL nanoparticles exhibited improved binding as a family, the subcellular trafficking patterns of the individual formulations differed. Hyaluronic acid-coated systems mediated efficient internalization, likely due to their ability to bind surface receptors like CD44. On the other hand, poly(L-aspartate) and poly(L-glutamate)-coated particles exhibited membrane-bound morphologies and possessed even greater affinity towards ovarian cancer cells than HA-coated systems. Even between these two highly similar surface chemistries, meaningful differences in their uptake mechanism demonstrated the exquisite ability for ovarian cancer cells to differentiate between nanoparticle formulations.

The observations made in vitro were recapitulated in vivo using an orthotopic model of ovarian cancer. Given the difficulties inherent to metastatic ovarian cancer and its relative confinement to organs of the intraperitoneal space, we also performed a head-to-head assessment of four of our LbL formulations administered both systemically and intraperitoneally. We found that while systemically injected nanoparticles do co-localize to the tumor, the majority of the dose is lost to the liver and spleen. However, if given intraperitoneally, the majority of LbL nanoparticles localize to neoplastic tissues, with minimal spillage into the liver and spleen. Carboxylated LbL NPs perform best, providing a persistent elevated association with tumor tissue over 3 days. The sulfated LbL control particle, in contrast, clears away from the tissue and has a similar tumor-association seen with PEGylated controls. Notably PEGylated controls not only clear from the tumor over this period of time, but also spill over into the liver and spleen. Whole-tissue imaging also confirms

that the LbL nanoparticles are able to penetrate into the tumor tissue, and not remain relegated on the tumor's surface. These findings suggest that these LbL surface chemistries may be able to mediate a specific interaction with ovarian tumors if injected intraperitoneally, and could be used to functionalize colloidal drug carriers. Because the LbL films explored can be applied to a diverse number of core substrates, this approach provides flexibility towards the development of a multitude of novel therapeutic interventions for ovarian cancer.

The systematic appraisal of nanoparticle surface chemistry using the LbL platform is a path towards a more rigorous mapping of the parameter space available to colloidal drug carriers. Our results indicate that LbL films may provide novel and unexpected interactions between nanoparticles and particular cell types. Excitingly, this observation combined with the diversity and modularity of LbL films means that there are significant opportunities for future work to identify new biomedically-relevant surface chemistries. Mapping out this landscape could begin to unlock a deeper understanding of structure-function relationships, allowing researchers to better design nanoparticles suited for particular goals and tasks. We intend to continue studying the role of surface chemistry on biodistribution with a more thorough assessment of tumor and clearance organ histological sections, to better understand the penetration of NPs into tissues and other organs. We also plan to perform a flow cytometry assay that will provide insight into the specific cell types involved in LbL-NP uptake in vivo.

Beyond surface chemistry, the field should look to additional parameters for LbL NPs can also begin to be explored more systematically, including the role of intermediary layers on important behaviors like swelling, drug release, and transfection efficiency. Of course, simultaneous work to understand how core size, shape and rigidity impact the observations described here are also needed. The field has focused enormous efforts in the development of unique and fascinating formulations to achieve particular drug delivery goals, but the next stages of nanomedicine will benefit primarily from efforts that begin to tie all these disparate efforts together through deliberate and methodological studies aimed at disentangling the roles played by key material properties.

3.6. Methods

Materials and reagents: The polyelectrolytes dextran sulfate sodium salt (DXS, 6.5-10 kDa; Sigma Aldrich), poly(acrylic acid) (PAA, 15 kDa; Sigma Aldrich), poly(L-arginine) (PLR, 9.6 kDa; Alamanda Polymers), poly(L-glutamic acid) (PLE, 15 kDa; Alamanda Polymers), poly(L-aspartic acid) (PLD, 14 kDa; Alamanda Polymers), poly(ethylene glycol-b-poly-L-glutamic acid) (PEG-PLE) (30 kDa PLD, 5 kDa PEG; Alamanda Polymers), hyaluronic acid (HA, 20 kDa; LifeCore Biomedical), sulfated beta-cyclodextrin polymer (18kDa; Cyclodextrin Technologies), and fucoidan (57 kDa; Santa Cruz Biotechnology) were used without modifications. Heparin sodium salt (HS, unfractionated; Celsus Labs) was used both unmodified and as a conjugate with folic acid (Sigma Aldrich) as described previously.

The fluorescent, carboxylate-modified latex nanoparticles (100 nm, blue fluorescent (350/440), 100 nm yellow-green fluorescent (505/515), 100 nm infrared (715/760); Life Technologies) were used without modification for LbL-NP assembly. For PEGylated control NPs, the latex particles were modified with 3 kDa PEG according to the manufacturer's instructions.

Cell lines: Caov3, OVCAR3 and SKOV3 cell lines were purchased from ATCC (catalog numbers HTB-75, DSMZ ACC 444, HTB-161, and HTB-77). Fuov1 cells were purchased from DSMZ (catalog number ACC 444). COV362, COV318, JHOS2 and JHOS4 cell lines were donated to us by the Drapkin Lab. OVCAR4 and OVCAR8 cell lines were donated by the Bhatia lab. Caov3, COV362, OVCAR3, OVCAR4, OVCAR8, cell lines have been authenticated using STR profiling. All cell lines were tested for mycoplasma contamination periodically, including immediately upon thawing, and over time when in culture, using the Lonza MycoAlert kit (Catalog #: LT07-318). Results were always negative for mycoplasma contamination.

Synthesis of layer-by-layer nanoparticles: LbL nanoparticles were prepared as described previously. Briefly, carboxylate-modified latex nanoparticles (Thermo Fisher) were coated with poly(L-arginine) in milli-Q water, with no added salts. The deposition step was carried out by adding an equal volume of 1 mg/mL CML core to 4 mg/mL PLR while under sonication (Branson bath sonicator). The mixture was allowed to sonicate for 5 seconds, then left to incubate at RT for 1 hour. The particle was then purified using tangential flow filtration (Spectrum Labs, KrosFlo

II system) with a 100 kDa molecular weight cut-off filter (Spectrum Labs, D02-E100-05-N). The filter was pre-treated with a 4 mg/mL solution (10 minutes, continuous flow with permeate valve closed) of PLR. The nanoparticle was washed until five volume equivalents were collected in the permeate, using milli-Q water as the exchange buffer. The CML/PLR particles were then split into different batches to be coated with the various polyanions, using the same steps outlined above for PLR but using a different filter cassette. The filter cassette for anionic layers was not pre-treated with polymer solution. The core-to-polymer mass ratios for each polyanion were determined from polyelectrolyte titrations that identified optimal ratios that provided complete charge conversion. The ratios used were 1:6 for heparin sulfate folate conjugate; 1:10 for heparin sulfate and fucoidan; 1:8 for dextran sulfate; 1:24 for randomly sulfated beta cyclodextrin; 1:6 for poly(ethylene glycol-b-poly-L-glutamate); 1:4 for hyaluronic acid, poly(L-aspartate) and poly(L-glutamate); and 1:3 for polyacrylate. No salts were added during the deposition or purification steps for the polyanion layers.

Nanoparticle characterization: Nanoparticle hydrodynamic size and polydispersity were measured using dynamic light scattering (Malvern ZS90 Particle Analyzer, λ = 633 nm, material/dispersant RI 1.590/1.330). Zeta potential measurements were also acquired with the Malvern ZS90, using laser Doppler electrophoresis. Nanoparticle solutions were diluted in milli-Q water in polystyrene semi-micro cuvettes (VWR) or DTS1070 folded capillary cuvettes (Malvern) to produce samples for characterization. TEM was performed with a JEOL 2011 High Contrast Digital TEM (120 kV). Nanoparticle solutions were drop casted onto mesh copper grids coated with continuous carbon films to produce specimens for TEM.

Binding assay for ovarian cancer and healthy cells: The ovarian cancer cell lines and iPSC-derived endothelial cells were seeded onto 96-well plates (Nunc) at a density of 15,000 cells per well in 100 uL of the serum supplemented media corresponding to each cell line. Caov3, COV318, and COV362 were grown in DMEM media (Corning) supplemented with 10% FBS and 2 mM of L-glutamine (Gibco). Fuov1, JHOS2, and JHOS4 cells were grown in DMEM:Ham's F-12 (1:1) (Corning) supplemented with 10% FBS. Media for the JHOS lines was further supplemented with 0.1 mM MEM non-essential amino acids (Gibco). OVCAR3, OVCAR4, and OVCAR8 lines were grown in RPMI-1640 media (Corning) supplemented with 10% FBS. OVCAR3 cells were further supplemented with 0.01 mg/mL bovine insulin (MilliporeSigma). SKOV3 cells

were grown in McCoy's 5A media (Corning) supplemented with 10% FBS. Induced-pluripotent stem cell-derived endothelial cells (iPSC-ECs; Cellular Dynamics International) were grown in Lifeline, Vasculife VEGF Medium Kit, substituting FBS with media supplement obtained from CDI, according to the manufacturer's instructions. Splenocytes were harvested from homogenized whole mouse (Balb/C female) spleens and seeded at a 500,000 cell per well density. Splenocytes were grown in RPMI-1060 media supplemented with 10% FBS, 0.1 mM MEM non-essential amino acids, 1% sodium pyruvate and 50 uM 2-mercaptoethanol. All media was supplemented with 1% penicillin streptomycin. All cells were allowed to adhere/grow for 24 hours before treatment with nanoparticles in a Heracell Incubator (Thermo Fisher) at 37C and 5% CO_2.

Green fluorescent nanoparticle compound plates were prepared in a polystyrene v-bottom 96 well plates (Corning) and standardized to a concentration of 130 ug polystyrene/mL milli-Q water. A TECAN Freedom Evo 150 with an MCA96 head was used to mix the nanoparticles in the compound plate, transfer 5 uL of and gently mix the nanoparticle solution in the cell assay plate. Cells were allowed to incubate with nanoparticles for 4 and 24 hours, and then the plates were washed 3 times with PBS and 20 ul of trypsin-EDTA was added to the cells using a BioTek EL406 plate washer. The cells were incubated for 5 minutes at 37C to dissociate them from the tissue culture plastic. The TECAN Freedom Evo 150 was then used to add 80 uL of DMEM supplemented with 10% FBS to each well, and to mix the cells into a single cell suspension. Resuspended cells were then analyzed using an iQue high throughput flow cytometer and nanoparticle fluorescence data was collected in the FL1-A channel.

For splenocytes, the protocol differed in order to identify specific cell populations. Splenocyte plates were spun down at 500 RCF for 5 minutes to pellet suspension cells. The supernatant was removed using the BioTek EL406 Plate Washer, and 20 uL of trypsin EDTA was added to each well to dissociate any adherent cells from the plate surface. 80 uL of complete DMEM was added as described above, and then the cells were spun again at 500 RCF for 5 minutes and washed with PBS. Dead cells were labeled using live/dead aqua stain (BioLegend), according to the manufacturer's protocols. Cells were pelleted again as described above and then resuspended in 80 uL PBS supplemented with 3% BSA. 2x antibody master with Fc block (BioLegend, 101302) mix was prepared to label specific cell types and then added to each well using a multichannel

repeater pipette (Integra). The cells were incubated in the antibody mix for 30 minutes at 4C and then washed twice with 3% BSA PBS prior to analysis on a BD Fortessa cytometer. The antibodies used were APC CD45 (hematopoietic marker, BD, clone 30-F11), APC-Cy7 B220 (B cell marker, eBioscience, clone RA3-6B21), PE CD3 (T cell marker, BioLegend, clone 17A2), PE-Cy7 CD11b (leukocyte marker, BioLegend, clone M1/70), PerCP-Cy5.5 F4/80 (macrophage marker, Biolegend, clone BM8), and BV605 CD11c (dendritic cell marker, Biolegend, clone N418).

All data were analyzed using FlowJo software. Single-color flow was analyzed without compensation. The splenocytes were analyzed using appropriate compensation matrix generated from single color controls. Populations were gated such that only single cells (and live cells in the case of the splenocytes) were quantified for nanoparticle-associated fluorescence. The median nanoparticle-associated fluorescence was determined for each population, and imported into an R workspace for further analysis. Triplicates for each treatment condition for each cell type were averaged and then normalized to the average median fluorescence value acquired for corresponding cells that were not treated with nanoparticles to generate a median fluorescence intensity ratio (MFR). The MFR of the different ovarian cancer cells were combined to visualize uptake in Figure 1, as were the data for healthy cells. The data for both time points were used to generate a clustered heatmap using the heatmap.2 function in the gplot package. Clusters were calculated using the built-in Euclidean distance function.

Saturation binding isotherm: OVCAR8 cells were trypsinized and washed in complete RPMI media to generate a cell suspension at 500,000 cells/mL in 4C media. 50,000 cells were added to each well (100uL) of a v-bottom 96 well plate. Serial dilutions of nanoparticles were prepared in a deep v-bottom 96 well compound plate. Both plates were chilled to 4C. A TECAN Freedom Evo 150 was used to premix the nanoparticle compound plate, transfer 100 uL of 2x nanoparticle solution and mixed into each well of the OVCAR8 suspension plate, which was then kept on ice for 1 hour. Afterwards, the treatment plate was spun at 500 RCF and the supernatant was removed using a BioTek EL406 Plate Washer. Cells were washed with 200 uL of PBS and re-centrifuged. The cells were then resuspended in live/dead far-red stain (BioLegend) at 4C for 15 minutes. The cells were recentrifuged and then resuspended in 100 uL 1 ug/mL hoescht in PBS for 5 minutes. Finally the cells were recentrifuged one last time and resuspended in 80 uL of ice cold PBS. The plates were then analyzed using a BD LSR2 cytometer. All data was analyzed

on FlowJo, and the populations were gated such that only single cells that were hoescht+ and red- cells were analyzed. The hoescht stain eliminated the chance for any nanoparticle aggregates from the highest concentration conditions might be mistaken for cells on the cytometer. Median fluorescence intensity data was exported to Prism GraphPab software, where it was log-transformed and fit using the one site-total binding model without any constraints.

Live cell confocal imaging: COV362, and Caov3 cells were seeded on 35mm MatTek glass bottom dishes and allowed to adhere for 24 hours. JHOS4 cells were seeded onto black glass-bottom 96-well plates and also allowed to adhere for 24 hours. Cells were treated with 20 pM concentrations of blue-fluorescent nanoparticles and analyzed after a 24-hour incubation. Prior to imaging, cells were stained for using AlexaFluor 555 wheat germ agglutinin at 10 ug/mL in serum-free imaging media to label the cell membrane. Lysotracker red was also added and used to label lysosomes following the manufacturer's protocol. Nuclei were labeled using the NucRed dye, also according to the manufacturer's protocols. The cells were imaged using a 20x or 60x objective on a Nikon A1R confocal microscope using the 405 , 488, 561, and 640 laser lines. The filters cubes used were 450/50, 525/50, and 595/50. Images were linearly adjusted to improve contrast, and then psuedocolored to represent the cell membrane in magenta, nucleus in blue, lysosomes in red, and nanoparticles in green.

Fixed cell confocal imaging of nanoparticle subcellular trafficking: LabTek chambered glass slides were coated with rat tail collagen (300 uL of 50ug/mL in 0.02N acetic acid). After 1 hour, the wells were washed with PBS and OVCAR8 cells were seeded at 15,000 cells per well. The cells were allowed to adhere for 24 hours prior to treatment with 20 pM concentration of green fluorescent LbL nanoparticles. Cells were incubated until 4 or 24 hours, depending on the desired time point, at which time the cells were washed three times with PBS and fixed in 4% methanol-free formaldehyde prepared in PBS (15 minutes, room temperature). The cells were then washed in ice cold PBS three times (5 minutes per wash). For all intracellular stains except for CAV1, cells were treated with blocking buffer (0.025% saponin and 5% goat serum in 1x PBS) for one hour. Blocking buffer was removed and replaced with a primary antibody diluted in antibody diluent buffer (0.025% saponin and 1% BSA in 1xPBS). The antibody dilutions used were as follows: EEA1 (CST) 1:200; RAB5 (CST) 1:100; RAB7 (CST) 1:400; Clathrin (CST) 1:100; LAMP1 (Abcam) 1:400; and RCAS1 (CST) 1:400. Cells were incubated in the primary

antibody stain overnight at 4C, then washed three times in PBS (5 minutes per wash). The anti-rabbit AF647 Fab fragment (CST) was diluted 1:1000 in antibody diluent buffer and added to the cells. After 1 hour at room temperature, the cells were once again washed three times with PBS (5 minutes per wash) and then stained with DyLight 554 phalloidin, according to the manufacturer's protocols. Afterwards, the phalloidin solution is discarded and replaced with a 1 ug/mL hoescht PBS solution (2-minute incubation). Finally, the cells are washed three more times in PBS (5 minutes per wash) and the chamber walls are removed following the manufacturer's instructions. A no 1.5 glass coverslip is then mounted using ProLong Antifade Diamond. Nail polish is used to seal the coverslip and the slide is allowed to cure for 24 hours prior to imaging. For CAV1 staining, a Triton-X based permeabolization technique is used instead. The permeabolization step occurs after fixation, and uses a 0.2% Tritron X100 in 1x PBS solution. Afterwards, blocking is performed using a 1x PBS solution supplemented with 10% goat serum and 0.1% Tween 20 (30 minutes, room temperature). The antibody diluent buffer used in the Triton-X protocol is 1% BSA 0.1% Tween 20 in PBS. The CAV1 antibody is used at a 1:1600 dilution.

Specimens were imaged using an FV1200 Olympus Laser Scanning Confocal Microscope using a 60x silicon oil objective, 1.30 N.A. and the 405, 473, 559 and 635 laser lines. Hoescht and nanoparticle signals were captured using the standard PMT detectors with filter cubes 430-455 nm and 490-540 nm, respectively. The phalloidin and organelle signals were collected using the high sensitivity detectors with filter cubes 575-620 nm and 575-675 nm respectively. Image LUTs were linearly adjusted to improve contrast on FIJI, and were psuedocolored to represent nuclei in cyan and phalloidin in blue.

3D-Super resolution microscopy of nanoparticle subcellular trafficking: The protocol used above for fixed cell imaging was modified to suit the requirements of the Applied Precision DeltaVision-OMX Super Resolution Microscope. Namely, instead of LabTek chambered glass slides, chambered coverlglass was used. Also, after fixation, cells were washed three times with Hank's Buffered Saline Solution (5 minutes per wash) and stained with AlexaFluor 647 wheat germ agglutinin (WGA, 10ug/mL in Hank's Buffered Saline Solution, 10 minutes). The cells were washed three times with PBS (5 minutes per wash) and then re-fixed using 4% formaldehyde for 2 minutes at room temperature. The phalloidin staining step is omitted on the super resolution samples, and the hoescht stain is increased to a 1.25 ug/mL stain. After all staining is complete,

118

the cells are re-fixed using 1% formaldehyde solution for 5 minutes at room temperature. Following three more rounds of washing with PBS, the wells are filled with 5 drops of VectaShield (H-1000) and stored in the dark at 4C until imaged. The cells in Figure 3 were only stained with WGA and hoescht, and were not processed further with any permeabilization agents, which is why the vesicular stain is more intact in those images.

The cells were imaged with the Delta OMX- V4 Blaze 3D structured illumination microscope (Applied Precision, now GE), equipped with 405 nm, 488 nm, 563 nm and 647 nm lasers and three sCMOS cameras. Images were acquired with a 60X, NA 1.43 oil objective, at 0.125 micron z step, using 1.518 immersion oil at RT. All images were acquired under the same illumination settings and then processed with OMX softWoRx software (Applied Precison/GE). Images were saved as tiff. Image LUTs were linearly adjusted to improve contrast on FIJI, and were psuedocolored in 4-color samples to represent the wheat germ membrane stain in magenta.

Uptake inhibitor study: OVCAR8 cells were seeded at 20,000 cell/well in 96 well plates 24 hours prior to any further treatment. Drug compound plates were prepared in deep well v-bottom 96 well plates containing complete media containing inhibitors for specific uptake processes. Sodium azide (0.65 mg/mL) and 2-deoxy-D-glucose (8.2 mg/mL) were used to inhibit ATP-mediated processes. Wortmannin (4.3 ug/mL) was used to inhibited macropinocytosis. Genistein (54 ug/mL) was used to inhibit caveolar uptake. Chlorpromazine (3.6 ug/mL) was used to inhibit clathrin mediated uptake. Methyl-beta cyclodextrin (6.6 mg/mL) was used to deplete cholesterol and thereby inhibit cholesterol-mediated uptake. Wortmannin, genistein and chlorpromazine were prepared using 200x DMSO master stocks. An equivalent amount of DMSO was added to the water soluble inhibitor solutions to eliminate DMSO as a variable. DMSO-only and untreated controls were used as well. Nanoparticle master plates were prepared in v-bottom 96 well plates at 130 ug polystyrene/mL milli-Q water.

Cell assay plates were washed three times with PBS using a BioTek EL406 plate washer and a TECAN Freedom Evo 150 transferred 100 uL of inhibitor-containing media to each well. Cells were incubated at 37C 5% CO2 for one hour, and then the TECAN was used to transfer 5 uL of nanoparticle solution to each well. The cells were incubated with nanoparticles for 4 hours and then the BioTek plate washer was used to wash the plates three times with PBS and to add 20 uL

of trypsin EDTA to each well. After a 5 minute incubated at 37C 5% CO2, the 80 uL of complete media supplemented with propidium iodide was added to each well. The cells were then analyzed using a BD LSR2 cytometer.

For the 24-hour cholesterol depletion experiment, cells were seeded at the same density and allowed to adhere for 24 hours. The cells were then treated with nanoparticles in the same way as above, but incubated for 24 hours. After 24 hours, the cells were washed three times with PBS and 100 uL of methyl-beta cyclodextrin-containing media was added to each well. The cells were incubated for 4 hours and then washed three times with PBS and processed as described above for analysis by flow cytometry. All data were analyzed using FlowJo software, where live single cell populations were quantified for nanoparticle-associated fluorescence. Fluorescence quantification was exported for visualization and statistical analysis on GraphPad PRISM.

Animal studies: All animal experiments were approved by the Massachusetts Institute of Technology Committee on Animal Care (CAC) and were conducted under the oversight of the Division of Comparative Medicine (DCM).

Biodistribution studies: Female NCR nude sp/sp mice were purchased from Taconic and kept on AIN-93 imaging diet for at least 1 week prior to biodistribution experiments. Mice were injected intraperitoneally with 100,000 OVCAR8 mCherry/luciferase cells in PBS, and allowed to develop metastatic disease over the course of 4-8 weeks. Mice were randomly assigned to a nanoparticle treatment, and were then dosed with 8.3×10^{12} nanoparticles / kg formulated in 5% dextrose in milli-Q water. All nanoparticles prepared for animal experiments were generated from infrared fluorescent CML cores (ThermoFisher). Dosing was performed either systemically (by retro-orbital injection or tail-vein injection) or intraperitoneally via an IP-injection. Mice were sacrificed at 24, 48, and 72 hours depending on the randomly assigned time point. Immediately following, full necropsies were performed to harvest tumors, lungs, heart, spleen, liver, intestines, kidneys, and stomach from each mouse. The organs were immersed in 12-well plates containing 300 ug/ mL d-luciferin PBS solution. The organs were allowed to incubate for at least 15 minutes in the d-luciferin solution prior to imaging on a Xenogen IVIS Imaging System (PerkinElmer). Organs were imaged using the bioluminescence imaging functionality to identify signal from OVCAR8 cells in the primary tumor masses and from metastatic nodules that could not be removed from

the other organs. The organs were also imaged to detect nanoparticle signal using the fluorescence imaging function, using a 710 excitation and 760 emission filter. After imaging, all organs were placed into tared tubes and weighed to record organ masses into Excel spreadsheets. IVIS data was analyzed using the LivingImage software, where total radiant efficiency (TRE) for each organ was measured and exported to Excel spreadsheets. A python script was then used to extract the data from spreadsheets and sort it into a database for subsequent processing. Nanoparticle signal was baseline-corrected using the values measured for empty wells, and then a total recovered fluorescence value was generated from the sum of the total radiant efficiency (STRE) measured for each organ of a given mouse. The TRE of each organ was normalized by the STRE to generate a % recovered fluorescence value (%RFV) for each organ. The %RFV was then normalized to organ mass in grams to generate the final metric used to quantify biodistribution. The processed data was then exported to GraphPad PRISM for additional statistical analysis.

After imaging and weighing all the organs from the biodistribution studies, the tissues were transferred to 10% formalin for 72 hours. Afterwards, the tissues were rinsed thoroughly in milli-Q water and then transferred to 70% ethanol for long term storage. Some of the tumor tissues were used for histology and for whole-tissue imaging described below.

Histology and immunofluorescence: Because the CML cores are destroyed by the xylenes employed for most histological procedures involving formalin-fixed tissue, the tissue for these studies were processed through alternative means. The fixed tissue (prepared as described above) was taken and sucrose-infiltrated by immersion in 15% sucrose milli-Q water for 4 hours at 4C. Tissues were then transferred to 30% sucrose solutions and held overnight at 4C. Next, the tissues were blotted dry using kimwipes and washed three times using OCT medium. Finally, the tissue was cryomolded in OCT using a snap-freezing method. Briefly, the technique floats the cryomold on a petri dish over liquid nitrogen for 10 minutes or until the top of the OCT mold becomes opaque. The molds were maintained at -80C until they could be cryosectioned by the Koch Institute's histology core facility. Afterwards, the samples were stained with DAPI and coverslipped using vectashield mountant. The slides were then imaged using a Pannoramic Fluorescent Slide Scanner, using the DAPI, TRITC, and Cy7 channels to detect nuclei, mCherry, and nanoparticle signal, respectively. Detailed images were obtained using an FV1200 Laser

Scanning Confocal Microscope.

Multi-photon imaging of whole tissues: Fixed whole tumor tissue was imaged using an Olympus FV1000 Multiphoton Laser Scanning Confocal Microscope. The 25x, 1.05 N.A. objective was used to image two tumor z-stacks for each mouse analyzed, following 10 um steps. The 690-1040 nm laser was used at 710 to excite the nanoparticle, and regular fluorescence data was acquired in the red filter (572-642 nm) due to the broad emission spectrum from the fluorescent core. Multi-photon events from the nanoparticle were captured by the UV filter (410-440 nm). The laser was then set to 840 nm to capture the second harmonic from tissue collagen and to obtain two-photon event data from the mCherry expressed by OVCAR8 cells. To quantify the data, the deepest tissue penetration observed for each z-stack was averaged together for each treatment condition.

Statistical analysis: GraphPad PRISM was used to perform statistical analyses. Unless otherwise noted, statistical comparisons were performed using a two-way ANOVA with a Tukey post-hoc test, alpha = 0.05. The analysis for the uptake inhibitor study uses a one-way ANOVA and Dunnett post-hoc test between treatment groups and DMSO-only controls, alpha = 0.05.

3.7. References

1.   Wang, A. Z.; Langer, R.; Farokhzad, O. C., Nanoparticle Delivery of Cancer Drugs. In *Annual Review of Medicine, Vol 63*, Caskey, C. T.; Austin, C. P.; Hoxie, J. A., Eds. Annual Reviews: Palo Alto, 2012; Vol. 63, pp 185-198.

2.   de Fougerolles, A. R., Delivery vehicles for small interfering RNA in vivo. *Hum Gene Ther* **2008,** *19* (2), 125-32.

3.   Deng, Z. J.; Morton, S. W.; Ben-Akiva, E.; Dreaden, E. C.; Shopsowitz, K. E.; Hammond, P. T., Layer-by-layer nanoparticles for systemic codelivery of an anticancer drug and siRNA for potential triple-negative breast cancer treatment. *ACS Nano* **2013,** *7* (11), 9571-84.

4.   Gu, L.; Deng, Z. J.; Roy, S.; Hammond, P. T., A Combination RNAi-Chemotherapy Layer-by-Layer Nanoparticle for Systemic Targeting of KRAS/P53 with Cisplatin to Treat Non-Small Cell Lung Cancer. *Clin Cancer Res* **2017,** *23* (23), 7312-7323.

5.   Park, K., Facing the truth about nanotechnology in drug delivery. *ACS Nano* **2013,** *7* (9), 7442-7.

6.   Barenholz, Y., Doxil(R)--the first FDA-approved nano-drug: lessons learned. *J Control Release* **2012,** *160* (2), 117-34.

7.   Leonard, R. C.; Williams, S.; Tulpule, A.; Levine, A. M.; Oliveros, S., Improving the therapeutic index of anthracycline chemotherapy: focus on liposomal doxorubicin (Myocet). *Breast* **2009,** *18* (4), 218-24.

8.   Boulikas, T., Clinical overview on Lipoplatin: a successful liposomal formulation of cisplatin. *Expert Opin Investig Drugs* **2009,** *18* (8), 1197-218.

9.   Harrington, K. J.; Mohammadtaghi, S.; Uster, P. S.; Glass, D.; Peters, A. M.; Vile, R. G.; Stewart, J. S., Effective targeting of solid tumors in patients with locally advanced cancers by radiolabeled pegylated liposomes. *Clin Cancer Res* **2001,** *7* (2), 243-54.

10.   Jain, R. K.; Stylianopoulos, T., Delivering nanomedicine to solid tumors. *Nat Rev Clin Oncol* **2010,** *7* (11), 653-64.

11.   Chen, H.; Zhang, W.; Zhu, G.; Xie, J.; Chen, X., Rethinking cancer nanotheranostics. *Nat Rev Mater* **2017,** *2*, 17024.

12.   Verma, A.; Stellacci, F., Effect of surface properties on nanoparticle-cell interactions. *Small* **2010,** *6* (1), 12-21.

13.   Walkey, C. D.; Olsen, J. B.; Guo, H.; Emili, A.; Chan, W. C., Nanoparticle size and surface chemistry determine serum protein adsorption and macrophage uptake. *J Am Chem Soc* **2012,** *134* (4), 2139-47.

14.   Zhao, F.; Zhao, Y.; Liu, Y.; Chang, X.; Chen, C.; Zhao, Y., Cellular uptake, intracellular trafficking, and cytotoxicity of nanomaterials. *Small* **2011,** *7* (10), 1322-37.

15.   Davis, M. E., The first targeted delivery of siRNA in humans via a self-assembling, cyclodextrin polymer-based nanoparticle: from concept to clinic. *Mol Pharm* **2009,** *6* (3), 659-68.

16.   Wang, J.; Byrne, J. D.; Napier, M. E.; DeSimone, J. M., More effective nanomedicines through particle design. *Small* **2011,** *7* (14), 1919-31.

17.   Bertrand, N.; Grenier, P.; Mahmoudi, M.; Lima, E. M.; Appel, E. A.; Dormont, F.; Lim, J. M.; Karnik, R.; Langer, R.; Farokhzad, O. C., Mechanistic understanding of in vivo protein corona formation on polymeric nanoparticles and impact on pharmacokinetics. *Nat Commun* **2017,** *8* (1), 777.

18.   Hauck, T. S.; Ghazani, A. A.; Chan, W. C., Assessing the effect of surface chemistry on gold nanorod uptake, toxicity, and gene expression in mammalian cells. *Small* **2008,** *4* (1), 153-9.

19.   Alkilany, A. M.; Nagaria, P. K.; Hexel, C. R.; Shaw, T. J.; Murphy, C. J.; Wyatt, M. D., Cellular uptake and cytotoxicity of gold nanorods: molecular origin of cytotoxicity and surface effects. *Small* **2009,** *5* (6), 701-8.

20.   de Castro, C. E.; Ribeiro, C. A. S.; Alavarse, A. C.; Albuquerque, L. J. C.; da Silva, M. C. C.;

Jager, E.; Surman, F.; Schmidt, V.; Giacomelli, C.; Giacomelli, F. C., Nanoparticle-Cell Interactions: Surface Chemistry Effects on the Cellular Uptake of Biocompatible Block Copolymer Assemblies. *Langmuir* **2018**, *34* (5), 2180-2188.

21.   Wang, Y.; Angelatos, A. S.; Caruso, F., Template synthesis of nanostructured materials via layer-by-layer assembly. *Chem Mater* **2008**, *20* (3), 848-858.

22.   Hammond, P. T., Polyelectrolyte multilayered nanoparticles: using nanolayers for controlled and targeted systemic release. *Nanomedicine (Lond)* **2012**, *7* (5), 619-22.

23.   Correa, S.; Choi, K. Y.; Dreaden, E. C.; Renggli, K.; Shi, A.; Gu, L.; Shopsowitz, K. E.; Quadir, M. A.; Ben-Akiva, E.; Hammond, P. T., Highly scalable, closed-loop synthesis of drug-loaded, layer-by-layer nanoparticles. *Adv Funct Mater* **2016**, *26* (7), 991-1003.

24.   Bjornmalm, M.; Roozmand, A.; Noi, K. F.; Guo, J.; Cui, J.; Richardson, J. J.; Caruso, F., Flow-Based Assembly of Layer-by-Layer Capsules through Tangential Flow Filtration. *Langmuir* **2015**, *31* (33), 9054-60.

25.   Dang, X.; Gu, L.; Qi, J.; Correa, S.; Zhang, G.; Belcher, A. M.; Hammond, P. T., Layer-by-layer assembled fluorescent probes in the second near-infrared window for systemic delivery and detection of ovarian cancer. *Proc Natl Acad Sci U S A* **2016**, *113* (19), 5179-84.

26.   Lengyel, E., Ovarian cancer development and metastasis. *Am J Pathol* **2010**, *177* (3), 1053-64.

27.   Alberts, D. S.; Liu, P. Y.; Hannigan, E. V.; O'Toole, R.; Williams, S. D.; Young, J. A.; Franklin, E. W.; Clarke-Pearson, D. L.; Malviya, V. K.; DuBeshter, B., Intraperitoneal cisplatin plus intravenous cyclophosphamide versus intravenous cisplatin plus intravenous cyclophosphamide for stage III ovarian cancer. *N Engl J Med* **1996**, *335* (26), 1950-5.

28.   Markman, M.; Bundy, B. N.; Alberts, D. S.; Fowler, J. M.; Clark-Pearson, D. L.; Carson, L. F.; Wadler, S.; Sickel, J., Phase III trial of standard-dose intravenous cisplatin plus paclitaxel versus moderately high-dose carboplatin followed by intravenous paclitaxel and intraperitoneal cisplatin in small-volume stage III ovarian carcinoma: an intergroup study of the Gynecologic Oncology Group, Southwestern Oncology Group, and Eastern Cooperative Oncology Group. *J Clin Oncol* **2001**, *19* (4), 1001-7.

29.   Armstrong, D. K.; Bundy, B.; Wenzel, L.; Huang, H. Q.; Baergen, R.; Lele, S.; Copeland, L. J.; Walker, J. L.; Burger, R. A.; Gynecologic Oncology, G., Intraperitoneal cisplatin and paclitaxel in ovarian cancer. *N Engl J Med* **2006**, *354* (1), 34-43.

30.   Dreaden, E. C.; Morton, S. W.; Shopsowitz, K. E.; Choi, J. H.; Deng, Z. J.; Cho, N. J.; Hammond, P. T., Bimodal tumor-targeting from microenvironment responsive hyaluronan layer-by-layer (LbL) nanoparticles. *ACS Nano* **2014**, *8* (8), 8374-82.

31.   Tsutsui, J.; Kadomatsu, K.; Matsubara, S.; Nakagawara, A.; Hamanoue, M.; Takao, S.; Shimazu, H.; Ohi, Y.; Muramatsu, T., A new family of heparin-binding growth/differentiation factors: increased midkine expression in Wilms' tumor and other human carcinomas. *Cancer Res* **1993**, *53* (6), 1281-5.

32.   van Dam, G. M.; Themelis, G.; Crane, L. M.; Harlaar, N. J.; Pleijhuis, R. G.; Kelder, W.; Sarantopoulos, A.; de Jong, J. S.; Arts, H. J.; van der Zee, A. G.; Bart, J.; Low, P. S.; Ntziachristos, V., Intraoperative tumor-specific fluorescence imaging in ovarian cancer by folate receptor-alpha targeting: first in-human results. *Nat Med* **2011**, *17* (10), 1315-9.

33.   Patel, M. M.; Smart, J. D.; Nevell, T. G.; Ewen, R. J.; Eaton, P. J.; Tsibouklis, J., Mucin/poly(acrylic acid) interactions: A spectroscopic investigation of mucoadhesion. *Biomacromolecules* **2003**, *4* (5), 1184-1190.

34.   Solomonidou, D.; Cremer, K.; Krumme, M.; Kreuter, J., Effect of carbomer concentration and degree of neutralization on the mucoadhesive properties of polymer films. *J Biomater Sci Polym Ed* **2001**, *12* (11), 1191-205.

35.   Chauhan, S. C.; Kumar, D.; Jaggi, M., Mucins in ovarian cancer diagnosis and therapy. *J Ovarian Res* **2009**, *2* (1), 21.

36.   Bangham, A. D.; Glauert, A. M.; Horne, R. W.; Dingle, J. T.; Lucy, J. A., Action of Saponin on

Biological Cell Membranes. *Nature* **1962,** *196* (4858), 952-&.

37.   Jamur, M. C.; Oliver, C., Permeabilization of Cell Membranes. In *Immunocytochemical Methods and Protocols*, Oliver, C.; Jamur, M. C., Eds. Humana Press: Totowa, NJ, 2010; pp 63-66.

38.   Tarin, D.; Price, J. E.; Kettlewell, M. G. W.; Souter, R. G.; Vass, A. C. R.; Crossley, B., Mechanisms off Human Tumor Metastasis Studied in Patients with Peritoneovenous Shunts. *Cancer Res.* **1984,** *44* (8), 3584-3592.

39.   Bajaj, G.; Yeo, Y., Drug delivery systems for intraperitoneal therapy. *Pharm Res* **2010,** *27* (5), 735-8.

40.   Deng, Y.; Yang, F.; Cocco, E.; Song, E.; Zhang, J.; Cui, J.; Mohideen, M.; Bellone, S.; Santin, A. D.; Saltzman, W. M., Improved i.p. drug delivery with bioadhesive nanoparticles. *Proc Natl Acad Sci U S A* **2016,** *113* (41), 11453-11458.

Chapter 4. The role of solution conditions in the robust synthesis of layer-by-layer liposomes

Layer-by-layer (LbL) nanoparticles offer great potential to the field of drug delivery, where these nanocomposites have been studied for their ability to deliver chemotherapy, small molecule inhibitors, and nucleic acids. Most exciting is their ability to encapsulate multiple functional elements, which allows nanocarriers to deliver complex combination therapies with staged release and to act as theranostic devices. However, relative to planar LbL constructs, the colloidal LbL systems have not undergone extensive systematic studies that outline critical synthetic solution conditions needed to develop robust and efficient assembly. The multistaged process of adsorbing a series of materials onto a nanoscopic template is inherently complex, and facilitating the self-assembly of these materials depends on identifying proper solution conditions for each synthetic step and each adsorbed material. Here, we focus on the fundamental questions that must be answered in order to obtain a reliable and robust synthesis of siRNA-containing LbL liposomes. This includes a study of solution conditions such as pH, ionic strength, salt composition and valency, and their impact on the preparation of LbL nanoparticles. Our results provide insight into the selection of solution conditions to control degree of ionization and electrostatic screening length to suit the adsorption of siRNA, native polypeptides, and polysaccharides. The optimization of these parameters led to a roughly 8-fold improvement in siRNA loading in LbL liposomes, indicating the importance of optimizing solution conditions in the preparation of therapeutic LbL nanoparticles.

4.1. Introduction

Layer-by-layer (LbL) self-assembly is a well-established means for the development of hierarchically organized nanocomposites[1-5], materials with applications for catalysis[6-8], sensing[9-11], electronics[12-14], and drug delivery[15-17]. Within the realm of biomedical applications, the LbL platform provides the unparalleled ability to incorporate numerous functional materials into discrete nanoparticles, thereby creating multifunctional drug delivery vehicles. To form LbL nanoparticles (NPs), polyelectrolytes of alternating charge are sequentially adsorbed onto an appropriately charged colloidal template. Such templates include nanoparticles with well-documented biomedical applications, such as drug-loaded PLGA[18-19] and liposomal cores[20-21]. LbL modification grants these nanoparticle cores a multilayered polyelectrolyte film coating, and when the polyelectrolytes in the film are carefully chosen, the resulting LbL nanoparticles gain added functionality beyond that of the core template. Such functionalities include the introduction of stimuli-responsive drug release characteristics[22-24] and extended systemic circulation times[18, 25]. Even active targeting functionality can be incorporated via adsorption of terminal polyelectrolyte layers that are natural binding partners to surface receptors expressed on target cells, such as the CD44-binding polysaccharide hyaluronic acid[26].

One of the most exciting capabilities of LbL nanoparticles is that nucleic acids can be incorporated directly into the LbL film and independently of drugs loaded into the NP core[27]. This allows the delivery of promising therapeutics like small interfering RNA (siRNA) that silence expression of specific genes. Despite its potential, siRNA has yet to be translated to the clinic due to intrinsic difficulties in the delivery of this delicate molecule[28]. Free administration of siRNA fails due to ubiquitous serum nucleases that rapidly degrade extracellular RNA. Additionally, due to its size and high charge density, RNA is unable to pass through the lipid bilayer of target cells. When incorporated into an LbL film, siRNA is protected from premature degradation[29-30]; furthermore, a terminal layer that targets cancer cells allows LbL siRNA-carriers to deliver cargo intracellularly[20]. Once within the target cell, the cationic elements of the LbL film, such as polyethylenimine[31], poly(beta-amino ester)[32], or cationic polypeptides[33-34] (e.g., poly(L-arginine) (PLR) and poly(L-lysine)), can mediate escape from the endolysosomal system to deliver the siRNA to the cytoplasm, where the siRNA can exert its therapeutic function. This capability is currently being leveraged to develop nanocarriers that deliver potent chemotherapy alongside siRNA. These combination nanotherapies use

the siRNA component to silence genes vital for drug resistance, thereby improving the efficacy of the co-encapsulated chemotherapeutic.

The clinical potential of LbL nanoparticles is being actively explored by studies that describe increasingly impactful and novel therapeutic formulations[16]. While this important work continues to identify promising new avenues for LbL nanomedicine, there is an outstanding need to further explore the fundamental parameters that underlie the robust synthesis of nanoscale LbL drug delivery vehicles. The parameter space for LbL nanoparticles is very broad, and includes a host of variables that include purification methods, mixing conditions, physiochemical properties of the polymer and colloidal species, and synthetic solution conditions. This parameter space provides the LbL platform with its rich diversity and versatility, but requires thorough study into the means of production in order to guarantee reproducible and high quality end products. The role of solution conditions on nanoscale LbL self-assembly is especially poorly understood, and this deficit translates into obstacles, such as batch-to-batch variability and drug loading limitations, that must be overcome to continue advancing these promising nanomaterials towards the clinic.

Separate batches of LbL nanoparticles can be prepared following the identical sequence of material deposition steps, yet yield end products that differ from one another, for example, by using different interlayer purification techniques. Some techniques, such as Caruso and coworkers' gel electrophoresis method[35], cause re-arrangement of the film as evidenced by zeta potential measurements. Centrifugation-based approaches can cause a decrease in zeta potential, possibly due to the LbL film rearranging in the pellet. On the other hand, tangential flow filtration approaches can enhance the charge of the terminal layer after purification[36]. Essentially, these techniques can all produce LbL nanoparticles using the same substrate and layer deposition steps but yield end products that are inherently distinct from one another. While it is straightforward to keep purification methods consistent from batch-to-batch, other, subtler, conditions may shift and compromise the consistency of the end product. These conditions include the solution conditions during self-assembly, which impact the electrostatic forces that both drive LbL assembly and provide colloidal stability to LbL nanoparticles.

One way to observe how slight shifts in solution conditions impacts LbL assembly is to track changes to the core-to-polymer (C:P) mass ratio used to generate layered particles. Optimizing

128

the C:P ratio is critical for successful layering, because the core substrate must be exposed to sufficient polyelectrolyte in order to generate an oppositely charged particle with a surface potential strong enough to electrostatically stabilize the colloid[37]. Empirically, and in consensus with prior work[38], we have noted that LbL nanoparticles require a zeta potential with a magnitude of at least |30 mV| to yield a stable species. But beyond this threshold, varying the amount of excess polyelectrolyte influences how subsequent layers are adsorbed[39]. This cascading effect highlights the need to maintain consistent C:P ratios in order to achieve batch-to-batch consistency, especially with regards to the amount of adsorbed materials in the LbL film. And since the individual constituents of the LbL film play important roles in these systems, keeping the adsorbed amount of each consistent is critical for their safe and efficacious use.

Extensive work on macroscale, planar LbL films indicates the importance of solution conditions in mediating efficient LbL assembly, where high concentrations of buffers and salts are routinely used[40]. In contrast, very limited work has been done on solution conditions for colloidal LbL systems, in part due to the sensitivity of electro-sterically stabilized colloids to salts. A few studies on colloidal LbL systems have been reported, including work by Caruso and coworkers[41], wherein they demonstrated that colloidal gold was layered more efficiently in the presence of sodium chloride (NaCl), but that the particles flocculate at NaCl concentration greater than 30 mM. Similarly, Decher and colleagues[37] found that NaCl could induce thicker film formation on colloidal gold, but also cause aggregation at some point between 10 mM and 100 mM due to electrostatic shielding that can compromise colloidal suspension stability. On the other hand, Huang et al.[42] observed that carbon nanotubes could only template LbL assembly at very high salt concentrations (0.4-1.0 M NaCl), demonstrating that even highly flexible polymers like poly(allylamine hydro- chloride) and poly(styrenesulfonate) struggle to wrap around the extreme curvature of this substrate without proper electrostatic screening. Outside of these systematic studies, the field largely relies on individual reports of novel formulations for insight into synthetic solution conditions, and many reports of LbL colloid syntheses do not explicitly mention solution conditions. For those that do, the conditions can vary significantly: the absence of salt[36, 43-47]; the absence of salt but with a specified pH (presumably via titration)[48-50]; salt for some layers but not for others[20, 39, 51-55]; salt only during layer deposition but not rinse/purification steps[37, 41, 56-65]; salt only during interlayer purification[66]; or salt throughout the synthesis[26, 42, 67-71]. Even when solution conditions are specified, it is rare for there to be discussion or justification for those conditions. Fortunately, future experimental work

can be guided by prior computational work that has modeled the role of salts in the wrapping of polyelectrolytes around charged nanospheres[72]. For example, work by Netz et al.[73] determine a key role in the charge density on the colloidal substrate in mediating tightly bound polymer coatings. Work by Chai et al.[74] predict that ion valency can impact polyelectrolyte wrapping, with bulky multivalent species destabilizing the layering process. And additional studies by Netz and coworkers[75] predicts advantage to using salt for the complexation of nucleic acids with nanospheres.

The following is a comprehensive study of the solution conditions that influence the synthesis of siRNA-carrying LbL liposomes, a type of LbL nanoparticle with applications towards the development of functional gene therapies and multi-drug delivery vehicles. This study first evaluates the impact of the liposomal substrate's charge density on LbL synthesis, and identifies some criteria for selecting a liposomal formulation appropriate for LbL-functionalization. Afterwards, the impact of salts of differing size and valency on the preparation of LbL liposomes (with an LbL film composed of natural polypeptides and siRNA) is systematically studied to assess how salt impacts colloidal stability and C:P mass ratios during synthesis. During this investigation, the role of pH in shifting C:P ratios is noted and leveraged towards mitigating rearrangement of the LbL film during the final layer deposition step, thereby preventing loss of siRNA. The salt screen ultimately identified HEPES, Tris-HCl, and NaCl as compatible salts for the preparation of LbL liposomes. We later determine that using HEPES and NaCl in combination provides excellent means to tune the degree of ionization and electrostatic screening length during LbL synthesis via controlling the pH and ionic strength of solution. The role of solution conditions during the interlayer purification step is also investigated, and reveals a significant advantage to removing salts during purification using the tangential flow filtration method. With optimized synthetic solution conditions in place, the weight percent loading of siRNA to lipid is improved 8-fold from 3.7% to 30.8%, indicating the significance of these conditions for the end product. Furthermore, LbL liposomes prepared using the HEPES and NaCl method demonstrate superior gene silencing in ovarian cancer cells both in vitro and in vivo. These techniques were then extended to the optimization of solution conditions for layering the native polysaccharide hyaluronic acid, which can introduce active targeting capabilities and prolong the circulation of LbL nanoparticles. We report that HA requires specific solution conditions for successful incorporation, indicating that different polyions may demand distinct solution conditions in accordance to the particular intermolecular forces at play during the relevant stage of self-assembly. Finally, we briefly note how the identity of the colloidal substrate

can lead to surprising differences from the approaches optimized for LbL liposomes. Overall, this study represents a major contribution towards a more comprehensive understanding of solution conditions in the context of colloidal LbL self-assembly, and how they can be leveraged towards the robust synthesis of LbL liposomes with high weight percent loading of siRNA.

4.2. Results: Optimization of solution conditions improves LbL NP reproducibility and siRNA loading

Salts and buffers play an invaluable role in the optimization of macroscale LbL-modification of planar and microparticle substrates[40, 76-81], where they provide control over critical factors like degree of polyelectrolyte ionization, electrostatic screening length, and the thermodynamics of self-assembly. The same holds true in nanoscale colloidal LbL[37, 41, 82], but these benefits must be carefully weighed against the risks that even weak ionic strengths pose in terms of colloidal flocculation, film rearrangement and even destabilization and erosion. On the other hand, to avoid salts altogether risks developing protocols where slight salt contamination or day-to-day changes in water pH and purity lead to unpredictable effects on LbL synthetic outcomes. Even slight contamination with salts has a significant impact with regards to which core-to-polymer (C:P) mass ratio will yield a stable layered nanoparticle. We demonstrate this effect by performing a polymer titration to determine the C:P ratio for the adsorption of 9.6 kDa PLR onto an anionic liposome (58:18:24 mole ratio of DSPC:POPG:Cholesterol) in either deionized water (dH$_2$O) or
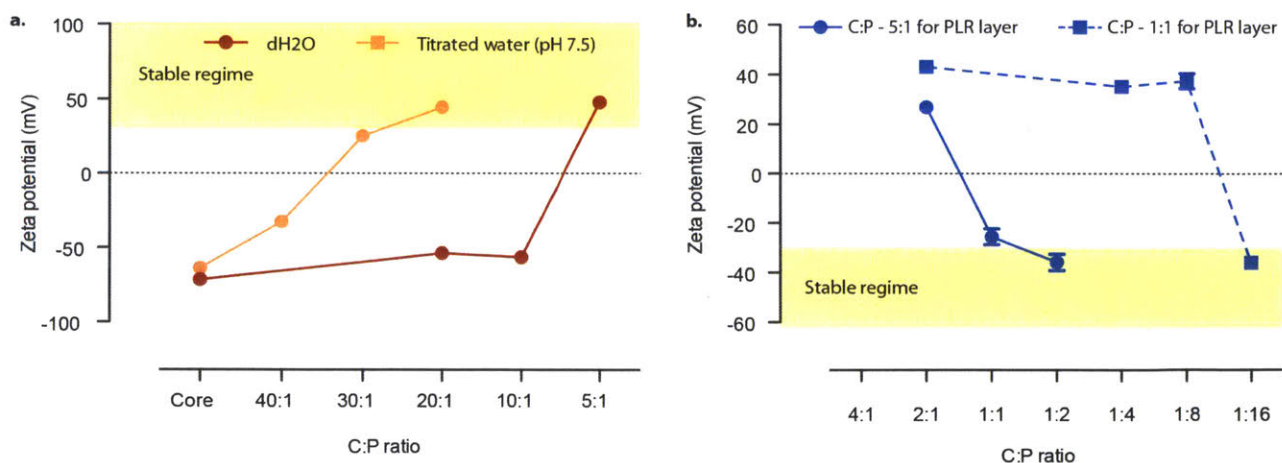
Figure 4.1. The presence of even dilute salt can significantly change the amount of polymer needed to produce a stable, layered nanoparticle. Layers are deposited onto a core substrate by mixing the substrate with oppositely charged polyelectrolytes at a core-to-polymer (C:P) mass ratio. At the optimal ratio, the nanoparticle reverses its charge, and possesses a zeta potential with a magnitude of at least |30 mV| to be electrosterically stabilized. **a)** Anionic liposomes (58:18:24 mole ratio DSPC:POPG:cholesterol) were mixed with poly(L-arginine) (PLR) at various C:P ratios to identify ratios that yield charge conversion within the stable regime. Depending on if the titration is carried out in dH$_2$O or pH 7.5 titrated water (20 μM Na$_2$HPO$_4$), the optimal C:P ratio varies 4-fold - from 20:1 in 20 μM Na$_2$HPO$_4$ or 5:1 in dH$_2$O. **b)** Changes in the C:P ratio in the initial layer have downstream effects on the subsequent layer. PLR-coated liposomes were formed using C:P ratios of 5:1 or 1:1 in dH$_2$O, yielding two PLR-coated species with zeta potentials of roughly +30 mV and +40 mV, respectively. To successfully add the subsequent siRNA layer on the +40 mV substrate, we require an 8-fold increase in the amount of siRNA added to the system, relative to the +30 mV substrate.

dH_2O titrated to pH 7.5 using 20 μM Na_2HPO_4 (**Figure 4.1a**). In dH_2O (pH 5.5-6), a C:P ratio of 5:1 is sufficient for charge conversion into the stable regime (e.g., zeta potential > 30 mV), whereas with a pH of 7.5, a C:P ratio of 20:1 is required to yield a stable colloid - a four-fold decrease in polyelectrolyte. At such a dilute salt concentration, the change in the optimal C:P for layering reflects the influence of pH on the system.

Changes in C:P ratios for one of the underlying layers of an LbL film can have a cascading effect on the adsorption of the subsequent layers. To illustrate this, we coated liposomes with PLR in dH_2O using the 5:1 C:P ratio, but also at a 1:1 C:P ratio that yields a greater charge conversion. Both species are stable, with the liposomes coated with PLR at a 5:1 or 1:1 C:P ratio generating layered nanoparticles with approximate zeta potentials of +30 and +40 mV, respectively (**Figure 4.1b**). To adsorb the next layer, composed of a 21-base pair siRNA, drastically different C:P ratios must be used to generate a stable colloid. The 5:1 liposome-PLR system produced a stable siRNA-coated particle at a C:P ratio of 1:2, but the 1:1 liposome-PLR system requires a C:P ratio of 1:16 to achieve charge conversion. Given the cost of siRNA, such a ratio would be prohibitive for routine manufacturing. To preserve continuity between batches of LbL NPs, keeping track of the C:P ratio becomes essential – and given the significant variation of this value due to shifts in pH it becomes imperative to develop means that robustly control pH while maintaining colloidal stability.

The ability for dilute salt concentrations and small shifts in pH to meaningfully impact the optimal C:P ratio for generating stable layered particles prompted us to look further into the effects of various salts and buffers. Different research groups have developed divergent practices for solution conditions during colloidal LbL assembly, and while some systematic studies have been performed, to our knowledge, a study comparing a variety of salts at different concentrations has not yet been reported. There has also been especially little investigation into the solution conditions that facilitate the LbL-modification of liposomal cores or the considerations required to make liposomal cores appropriate substrates for LbL. To begin addressing this outstanding need, we performed an assessment of liposome formulations of differing charge density in order to optimize the liposomal substrate for LbL-modification.

This study focuses on a liposomal formulation composed of 33.3 mol% cholesterol (CHOL) and

Mole percent: —●— 3.3% DSPG —●— 16.7 DSPG —●— 33.3% DSPG —●— 66.7% DSPG
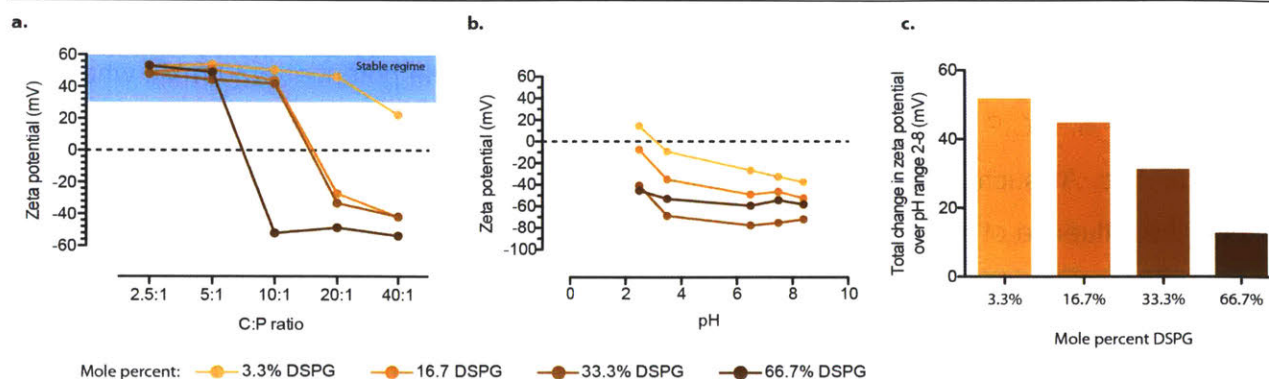
Figure 4.2. The ratio of anionic to zwitterionic phospholipid determines the final liposomes' charge density, sensitivity to pH, and ability to adsorb polyelectrolytes. Liposomes were formulated using a 2:1 phospholipid/cholesterol mole ratio, where the phospholipid compartment was composed of zwitterionic DSPC and/or anionic DSPG. **a)** Liposomes with DSPG mol% of 3.3%,16.7%, 33.3% and 66.7% were prepared to test the impact of charge density on PLR adsorption. As charge density increases, the optimal C:P ratio shifts towards favoring more polymer, intuitively indicating that a more charged substrate requires more oppositely charged polyelectrolyte to reverse its charge. **b)** Liposomes possessing different DSPG content also differ in their surface charge's sensitivity to pH, and liposomes with less than 33.3 mol% DSPG become neutral (e.g.,±10 mV) at pH 2.4 (25 mM HEPES). **c)** The total change in zeta potential over pH 8 to 2 was calculated, and indicated that as DSPG content increases, the degree of surface charge "elasticity" is reduced. Size and polydispersity data were acquired by dynamic light scattering, and zeta potential data was measured using laser Doppler electrophoresis.

66.7 mol% phospholipid, in light of studies[83-84] that find such a composition is ideal for stable drug encapsulation. The phospholipid content is composed of either the zwitterionic DSPC or the anionic DSPG, which were chosen for their high melting temperature (ca. 55C) to improve drug-retention of future formulations[84]. By varying the anionic content of the liposome between 3.3, 16.7, 33.3 and 66.7 mol% DSPG, we observe changes in the optimal C:P ratio needed to layer PLR in pH 7.5 titrated water (**Figure 4.2a**). Intuitively, greater anionic content on the substrate translated to optimal C:P ratios favoring greater polymer concentrations, with 3.3% DSPG converting charge at 40:1, 16.7% and 33.3% DSPG converting charge at 10:1 and 66.7% DSPG converting charge at 5:1. The charge stability of the core substrate was also investigated with a pH range from 2.4 to 8.4 (**Figure 4.2b**), which showed that the liposomal cores with less DSPG content are more sensitive to pH and become more neutral at acidic pH. As expected, the total zeta potential shift going from pH 8 to pH 2 (**Figure 4.2c**) indicated that the amount of DSPG in the liposome determines the extent in the shift in zeta potential. Because retaining a stable surface charge is a desirable quality for LbL synthesis, we determined that 33.3% and 66.7% DSPG systems would be appropriate substrates for LbL-modification as they retain a strong negative charge throughout the pH ranges studied and are able to adsorb more polyelectrolyte. In addition, both empirical and computational studies have found that greater charge density benefits LbL by
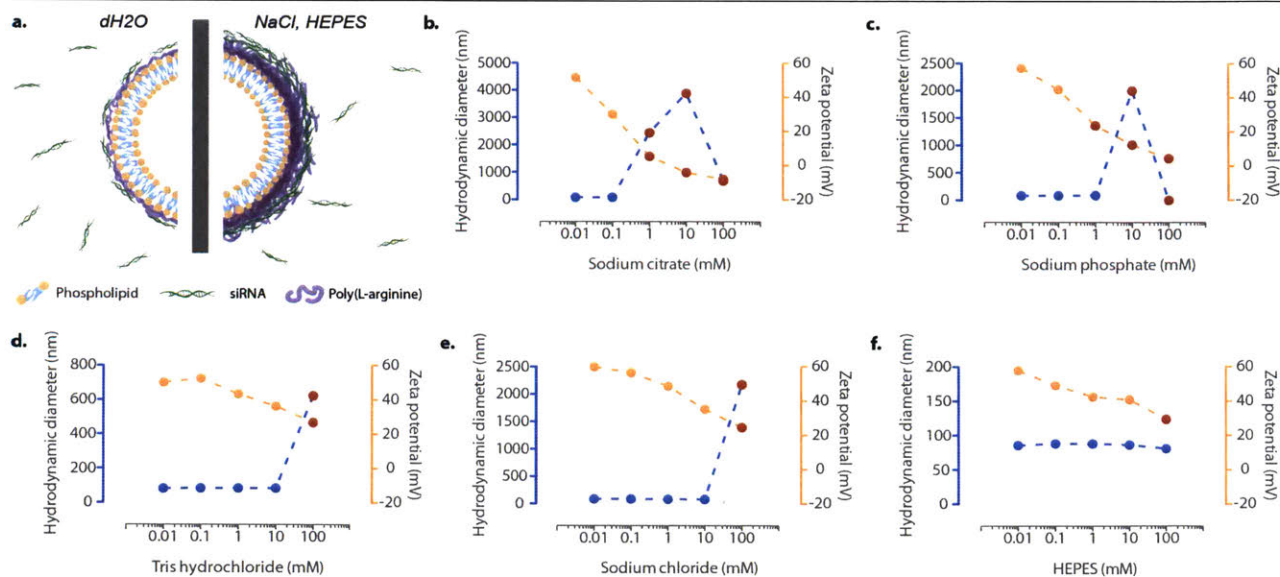
Figure 4.3. Layer-by-layer assembly onto liposomal substrates is affected by both salt concentration and salt identity, with notable differences in colloidal stability noted based on salt valency and size. a) Schematic of the LbL process on liposomes in the absence of salt (using deionized water, dH$_2$O) and in the presence of salts compatible with the LbL process (NaCl and HEPES). Anionic liposomes (1:1:1 DSPC/DSPG/CHOL) were coated with 9.6 kDA PLR using a 1:4 core-to-polymer (C:P) ratio. Solution conditions were varied during this layering step by introducing distinct salt species at concentrations ranging from 0.01 mM to 100 mM. We assess colloidal stability under each of these conditions by measuring hydrodynamic diameter (left axis, blue curve) and zeta potential (orange axis, yellow curve) of the resulting LbL particle. Results that indicate particle instability are denoted using red data points. We demonstrate that multivalent ions like **(b)** sodium citrate and **(c)** sodium phosphate are especially destabilizing to PLR adsorption, even at low concentrations. The monovalent species **(d)** tris hydrochloride and **(e)** NaCl are less destabilizing, but do cause flocculation at moderate concentrations (100 mM). The zwitterionic species **(f)** HEPES was very well tolerated at all concentrations used, with only a slight dip in the zeta potential at 100 mM. Size and polydispersity data were acquired by dynamic light scattering, and zeta potential data was measured using laser Doppler electrophoresis.

preventing film delamination[41], (layers desorb because subsequent layers out-compete the core) and promoting full wrapping of nucleic acids around substrates at moderate salt concentrations[73].

We then performed a screen of different salts at a range of concentrations and determined their impact on the adsorption of PLR onto these anionic liposomal cores (**Figure 4.3**). In selecting the salts used in this study, we were motivated by prior computational studies[74] that modeled the role of salt valency and size in the wrapping of nucleic acids on histones and charged spheres. We chose to study the multivalent salts trisodium phosphate and trisodium citrate, the monovalent salts tris(hydroxymethyl)aminomethane (tris) hydrochloride and NaCl, and the zwitterionic salt 4-(2-hydroxyethyl)-1-piperazineethanesulfonic acid (HEPES). Consistent with computational models, multivalent species were more destabilizing to LbL self-assembly, with sodium citrate (**Figure 4.3b**) causing major flocculation at just 1 mM. Flocculation of this system leads to micron-

sized aggregates, and at the highest salt concentration the aggregates precipitate from solution and are no longer detected by dynamic light scattering. It is noteworthy that when zeta potential drops below 30 mV (indicated by red dots on the orange curve), it generally coincides or closely precedes flocculation as indicated by a sharp increase in hydrodynamic diameter (indicated by red dots on the blue curve). Sodium phosphate, another multivalent species, caused significant flocculation, but only starting at 10 mM in this system (**Figure 4.3c**). We hypothesize that this difference in stability can be attributed to sodium citrate's ability to chelate with polycations in the layers, potentially resulting in NP aggregation.

Relative to multivalent species, the monovalent salts allowed for a much more stable PLR adsorption (**Figure 4.3d-e**). This improvement in stability may stem from multivalent salts being able to form ionic crosslinks with PLR[34] that can interfere with adsorption and promote aggregation, whereas this type of ionic crosslinking is not observed for monovalent salts. In both tris hydrochloride and NaCl, the LbL nanoparticles possess good size and charge until 100 mM. These results are consistent with prior work by Caruso and coworkers[41] that defined an upper limit of 30 mM for NaCl in LbL-gold nanoparticle synthesis, but now we extend that observation to liposomal cores and to the monovalent salt tris hydrochloride.

The zwitterionic salt HEPES was the sole salt that avoided flocculation for the entire range of concentrations tested (**Figure 4.3f**). Notably, only at 100 mM does the zeta potential slightly dip below 30 mV, indicating that we are approaching the upper limit for stability in HEPES. This result, while initially somewhat surprising, is consistent with the underlying molecular forces that mediate flocculation in LbL synthesis. The primary reason that salts can destabilize LbL systems is because they decrease the Debye length of the system, the length scale over which electrostatic forces dominate. For electrosterically stabilized colloids, the Debye length must be long enough to allow for charge-charge repulsion to occur before attractive short-range van der Waals forces take effect. The Debye length is dependent not on salt concentration per se, but rather on ionic strength, which depends also on the valency and dissociation state of the salt in question. However, zwitterionic salts have a complex contribution to electrostatic screening; empirical studies indicate that zwitterions contribute negligibly to the ionic strength of solution [85], and by extension, the electrostatic screening length. This unique trait may grant LbL nanoparticles increased stability in solutions with moderately high HEPES concentrations. Interestingly, these data also point

at deeper mechanisms at play in the discrepancy between colloidal stability in the presence of multivalent and monovalent ions, because when these data are replotted using ionic strength in place of salt concentration the results do not fully converge (**Appendix C Figure 1**). This observation supports the arguments advanced by computational models that ion valency can interfere with the complexation of polyions with a charged nanosphere.

We then turned our attention to the impact of salt on the formation of more sophisticated LbL-liposomes, namely the synthesis of siRNA-containing LbL liposomes. In this study, we aimed to resolve a challenge particular to LbL films which incorporate polyelectrolyte species that compete for incorporation into the LbL film. Specifically, parameters were explored to determine whether or not siRNA remains stably incorporated in the LbL architecture after addition of subsequent layers, both cationic and anionic. The formulation studied consists of the sequential deposition of PLR, siRNA, PLR and a propargyl-modified poly-L-aspartic acid (pPLD) onto a 1:1:1 DSPG:DSPC:Cholesterol liposomal core. Upon addition of the third layer, PLR, on top of the siRNA-coated substrate, no displacement of nucleic acid was observed via agarose gel (**Appendix C Figure 2**). However, when the final pPLD layer was added in deionized water, we observe a displacement of the siRNA from the particle at C:P ratios that yield stable colloidal solutions (**Figure 4.4a**, asterisks denote stable species generated). It is likely that this occurs through competition between pPLD – a more densely charged and flexible polyelectrolyte - and the siRNA that is interpenetrated with the outermost PLR layer. The displacement of siRNA can account for a loss of up to 50% of the encapsulated cargo, prompting us to investigate whether different solution conditions might prevent or mitigate this phenomenon.

Based on the results from our initial salt screen, we fixed the salt concentrations at 10 mM and performed a pPLD titration on the liposome/PLR/siRNA/PLR substrate to determine stable C:P ratios (**Figure 4.4b**). All conditions yielded an appropriate charge conversion at a C:P ratio of 1:4, though the multivalent species produce a visible precipitate. However, regardless of the salt used, all formulations using a 1:4 C:P ratio exhibit a significant displacement of siRNA from the particle. But stable formulations (denoted by an asterisk on the figure) revealed that several of the buffered conditions do yield a stable particle at a C:P ratio of 1:2 where minimal siRNA displacement occurs. We hypothesized that the concentration of pPLD is the primary driver of siRNA displacement, and thus when the absolute concentration of the species is reduced we also reduce
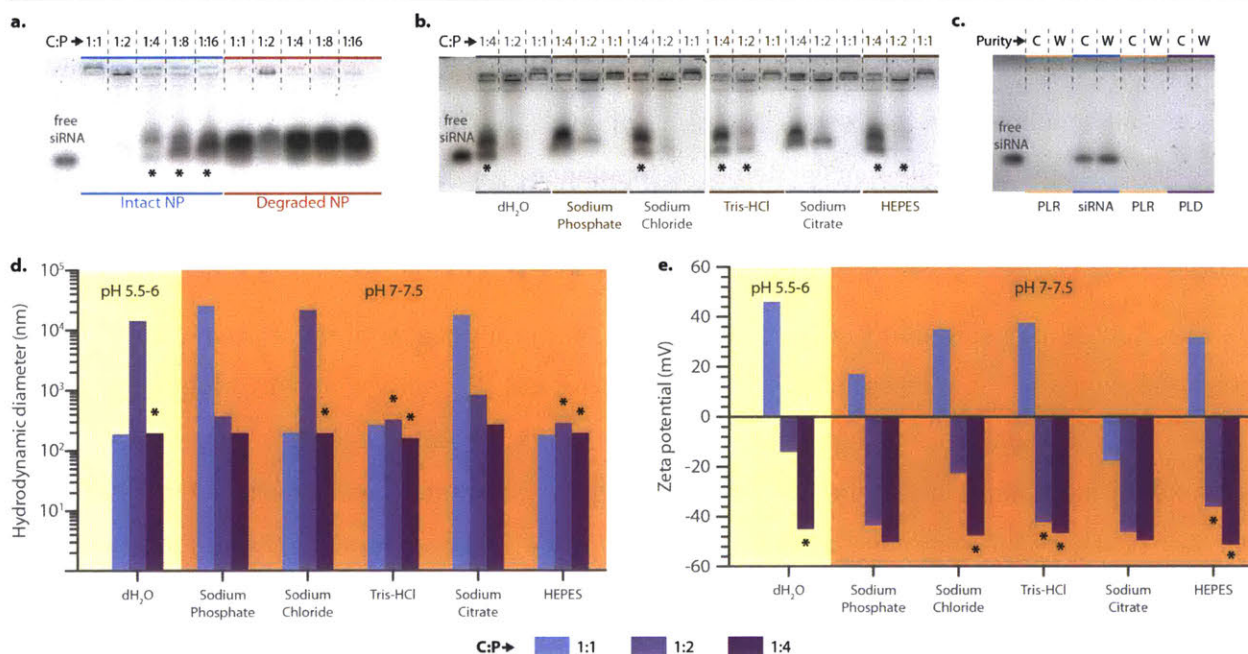
Figure 4.4. Tuning the solution conditions allows for stable nanoparticles to be generated at C:P ratios that prevent rearrangement of the LbL film, which can lead to loss of siRNA after deposition of the terminal polyanion propargyl poly(L-aspartate) (pPLD). a) In dH_2O, the synthesis of an siRNA-containing LbL nanoparticle (liposome/PLR/siRNA/PLR/pPLD) is complicated by the addition of the final pPLD layer, which causes displacement of siRNA as observed by agarose gel. C:P ratios that yield a stable formulation are denoted with an asterisk, and all C:P ratios tested in dH_2O led to considerable siRNA loss. Heparin-degraded nanoparticles show the entire encapsulated siRNA fraction. b) C:P ratio titrations were performed for the final pPLD layer in 10 mM concentrations of each salt species shown. Notably the different salt conditions cannot abate the siRNA loss at the 1:4 ratio, but certain solution conditions lead to stable particle at a C:P ratio of 1:2 where minimal siRNA is displaced. d) Size data of the nanoparticles formulated during the C:P titration of the final pPLD layer indicate stable sizes for particles prepared in HEPES and Tris-HCl at the 1:2 ratio that minimized siRNA loss. e) Zeta data for the same titration series confirms stable charge conversion occurs at a C:P ratio of 1:2 in nearly all salt conditions. This includes some solution conditions that fail to yield stable sizes like sodium phosphate and sodium citrate. Notably, the commonality between all the solution conditions was a neutral pH of 7-7.5. c) The importance of pH is confirmed through the synthesis of the LbL nanoparticle in pH 7.5 titrated water (20 μM Na_2HPO_4), which is sufficient to prevent siRNA displacement during the final layer deposition step. Size and polydispersity data were acquired by dynamic light scattering, and zeta potential data was measured using laser Doppler electrophoresis.

the opportunity for film rearrangement. Additionally, siRNA-containing LbL-NPs synthesized in the presence of salts might be less susceptible to this displacement by pPLD, perhaps due the generation of thicker layers.

When assessing the data in terms of pH during assembly (**Figure 4.4d-e**) it is evident that pH between 7-7.5 shifts the C:P towards lower polymer concentrations to achieve charge conversion, suggesting that pH mediates an optimal C:P ratio that prevents siRNA displacement. To confirm this hypothesis, we demonstrate the complete synthesis of the liposome/PLR/siRNA/PLR/pPLD system using pH 7.5 titrated water (20 μM Na_2HPO_4), where we are also able to eliminate the dis-

a.

Condition	Bulk conditions	
	Layer deposition	Interlayer purification
1	pH 7.5 titrated H_2O (20 µM Na_2HPO_4)	pH 7.5 titrated H_2O (20 µM Na_2HPO_4)
2	25 mM HEPES	25 mM HEPES
3	25 mM HEPES 20 mM NaCl	25 mM HEPES 20 mM NaCl
4	25 mM HEPES 20 mM NaCl	dH_2O

b.

c.
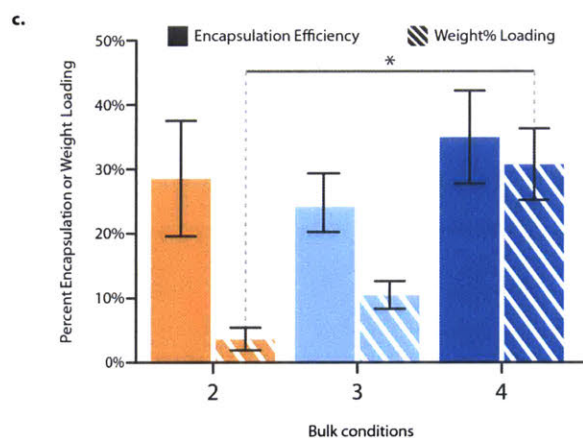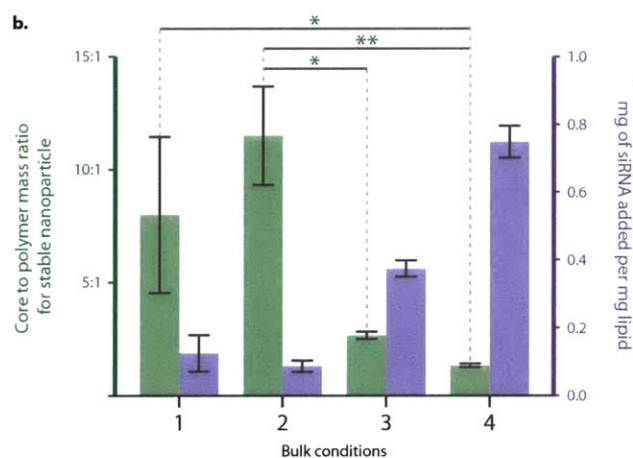
Figure 4.5. Synthetic solution conditions influence the layer deposition and interlayer purification steps differently, and judicious application of optimal conditions facilitates significant improvement in the weight percent loading of siRNA in LbL liposomes. We compare the impact of preparing LbL liposomes (liposome/PLR/siRNA) under different synthetic solution conditions to handle the layer deposition and interlayer purification steps. **a)** The synthetic solution conditions tested in these experiments are defined. **b)** LbL liposomes were prepared under the defined solution conditions and changes in the optimal core-to-polymer (C:P) mass ratio needed to achieve a stable colloid were recorded and averaged (green bars). For ease of interpretation, we also convert the C:P ratio to a mg of siRNA added per mg of lipid (purple bars) to directly visualize siRNA content differences across these conditions. Without the inclusion of NaCl, we observe more variability in the C:P ratio (conditions 1 and 2), and require much less siRNA to convert charge. On the other hand, layering in the presence of NaCl requires more siRNA for charge conversion but reduced variation in C:P from batch-to-batch (conditions 3 and 4). Layering in the presence of NaCl but purifying with dH_2O (condition 4) generated a particle that required roughly double the siRNA to convert charge. **c)** The encapsulation efficiency across solution conditions did not vary significantly, but meaningful improvement in the weight percent of siRNA to lipid was noted. Performing the synthesis in the presence of NaCl triples the average weight percent load to roughly 10%. Notably, purifying LbL liposomes in dH_2O instead of buffered solution further improved loading, yielding an average weight percent loading of 30%. Data is representative of at least three independent syntheses for each condition. Error bars represent SEM. All statistical tests were performed using one-way ANOVA (alpha = 0.05), with the Tukey post-test, on PRISM graphing software.

placement of siRNA from the LbL film (**Figure 4.4c**, **Appendix C Figure 3**). These results highlight the critical role of pH during LbL assembly, where it determines the ionization state of the polymer chains and the colloidal substrate. Tuning the pH with the pKa of the polymer and substrate in mind will maximize the number of charged groups and intensify the electrostatic interactions that drive polymer layering, allowing for more efficient C:P ratios. With the importance of pH in mind, HEPES becomes a natural tool in LbL synthesis to control pH thanks to its broad buffering range

(2.5-3.5 or 6.8-8.2) and, as we demonstrated above, the ability to use concentrations as high as 100 mM without impacting colloidal stability.

We then evaluated whether HEPES alone is sufficient for optimal layering of the siRNA onto the liposome/PLR substrate. Because siRNA is essentially a stiff charged rod[86-88], the adsorption of this species onto the curved nanoparticle surface can be challenging. Computational work indicates that efficient deposition of a nucleic acid onto a colloidal substrate requires careful tuning the Debye-Huckel screening length of the solution[73, 75]. Since HEPES has a complex contribution to the screening length[85], we hypothesized that additional screening would be required to optimally layer siRNA. Because NaCl has a straightforward relationship to the Debye length, and is tolerable in LbL synthesis up to the tens of millimolar range, we turn to it as a tool to tune the electrostatic screening length during LbL synthesis. In the following study, we perform the entire LbL synthesis in either:

1) pH 7.5 titrated water (20 μM Na_2HPO_4),

2) 25 mM HEPES,

3) or 25 mM HEPES 20 mM NaCl.

And while these conditions assess the appropriate solution conditions for the layer deposition step, they do not take into account whether special solution conditions are needed during the purification step that occurs between each layer. Limited prior literature suggests that removal of salt is important for preventing further rearrangement of the LbL film[89], but there are also empirical reports from groups that specifically use salt only during the purification step[66]. Therefore, to also determine the role that salts may play in the interlayer purification steps, we include a fourth condition:

4) where particles layered in the presence of 25 mM HEPES 20 mM NaCl are buffer exchanged to dH_2O during purification.

We first evaluate how these four solution conditions influence the optimal C:P ratio for siRNA loading into the LbL film (**Figure 4.5b**). Syntheses were carried out at least three times for each condition, and the results indicated that titrated water and 25 mM HEPES-buffered systems exhibited highly variable C:P ratios (green bars), with the average ratio being 8:1 and 11.5:1, respectively. On the other hand, layering in 25 mM HEPES 20 mM NaCl increased the uniformity of inter-batch C:P ratio considerably, and also shifts it to more polymer-heavy ratios of 2.66:1 and

140

1.33:1 for both salt-purified and dH_2O-purified conditions. For ease of interpretation, the C:P ratio is translated to mg of siRNA added per mg of lipid in the same figure, as the purple bars. Overall, inclusion of NaCl provides an immediate benefit by stabilizing C:P ratio across batches, and also leads to more siRNA needing to be added to generate a stable particle.

To determine whether this additional siRNA contributes towards the end product, or is simply lost during purification, we measured the encapsulation efficiency (EE) and weight percent loading for the buffered conditions (**Figure 4.5c**). Overall, EE varies little across the tested conditions, ranging from 20-40%. However, given the significantly different C:P ratios used in the different conditions, this translates to meaningful changes in the weight percent loading of siRNA to lipid. Notably, the HEPES-only condition leads to 3.7%±3.1% weight percent loadings that are in line with our prior published siRNA-based LbL nanoparticles (5.5%±0.5%), which were prepared entirely in dH_2O. However, the EE efficiency is improved in HEPES, where we see 28.6%±15.5% of siRNA encapsulated, up from our prior work where we reported an EE of 7.5%±2.5%. These results suggest perhaps more efficient layering (e.g., less siRNA needed to convert charge) but not improved weight percent loading.

In contrast, inclusion of 20 mM NaCl tripled the weight percent loading of siRNA from an average loading of 10.5%±3.7% for particles that are exposed to NaCl and HEPES throughout the entire synthesis. We propose that this is because 20 mM NaCl decreases the electrostatic screening length to 2.1 nm, and according to prior computational work[90-91], the screening length of solutions can alter the flexibility of polyelectrolytes. There are also empirical studies that confirm a relationship between nucleic acid flexibility and ionic strength[92]. This improved flexibility may allow better adsorption onto the nanoparticle substrate, as well as help to form a more densely packed siRNA layer. Computational models also predict that the layering of nucleic acids requires exceeding a critical screening length, and that layering efficiency continues to improve with greater salt concentrations[73, 75]. In real world situations, the salt concentration must be limited to prevent aggregation, but until that point it appears that LbL systems aiming to incorporate siRNA will benefit from higher salt concentrations.

While including NaCl during the layering stage improved loading of siRNA, purification in the presence of NaCl and HEPES had a negative impact on loading. The introduction of the nanoparticles

to high salt concentrations without free siRNA leads to conditions in which siRNA can diffuse back into solution. On the other hand, layering in HEPES and NaCl and then switching to dH_2O for the subsequent purification step yielded an siRNA weight percent loading of 30.8%±15.7% - a roughly 8–fold improvement over HEPES alone. This significant improvement in loading could indicate that when LbL nanoparticles are purified using the TFF technique in the presence of salt, the thicker LbL film may be able to rearrange and disassemble. This notion of film deconstruction is supported by the observation that at most stages, the salt-purified samples required less polymer to convert their charge relative to their dH_2O-purified counterparts. This shift in C:P ratio could be indicative of a partial loss of adsorbed material when the particles are purified in salt. To an extent, this observation is consistent with a prior study[93] that demonstrated that planar LbL constructs can be eroded after exposure to continuous flow of polymer and salt.

These results suggest that NaCl in conjunction with HEPES provide a straightforward means to tune solution conditions for optimal loading of siRNA into LbL liposomes. We also provide evidence that the resulting particles are of good size and charge throughout the synthesis of 2:1 DSPG:Cholesterol liposomes coated with PLR/siRNA/PLR/pPLD using either deionized water, titrated water or 25 mM HEPES and 20 mM NaCl in **Appendix C Figure 4**. The results indicate similar monodispersity and charge is achieved (**Appendix C Figure 4c-d**) albeit using different C:P ratios (**Appendix C Figure 4e**). Notably, in non-ionic or low ionic strength conditions, the size of the LbL liposome appears more or less unchanged throughout the synthesis, within the range of error for dynamic light scattering (+/- a few nanometers). This observation corresponds well with past theoretical work in planar LbL films that predicts very thin layer deposition (ca. 1-2 nm) under such solution conditions[94]. But with the inclusion of HEPES and NaCl for shielding, we observe a steady growth in particle size that is measurable with DLS, and is more consistent with prior LbL colloid literature and our experience with other core substrates. We expect that this is in part due to the deposition of thicker layers in the presence of salts as described in the literature, which may also explain the improved loading of siRNA into liposomes prepared in the presence of salt.

We also directly compare the size and charge of particles purified in salt or in water. Overall, the nanoparticles generated from both methods were of acceptable uniformity, with salt-purified and water-purified particles yielding polydispersity indexes of 0.23±0.04 and 0.26±0.02, respectively.

142

The role of solution conditions in the robust synthesis of layer-by-layer liposomes
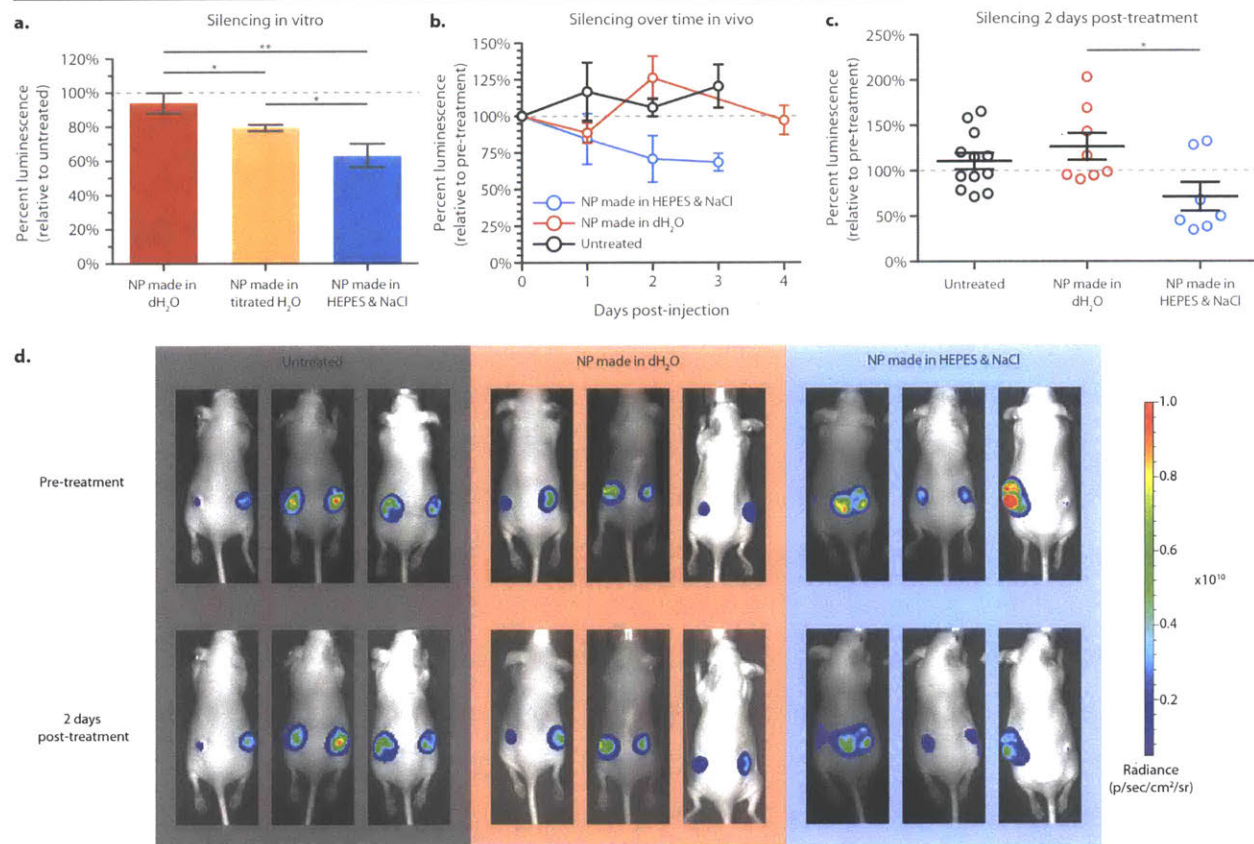
Figure 4.6. Optimized solution conditions produce LbL siRNA-carriers that mediate improved transfection of model genes in ovarian cancer in vitro and in vivo. LbL nanoparticles (liposome/PLR/siLuciferase/PLR/PLD) were prepared either in dH_2O, pH 7.5 titrated water (20 μM Na_2HPO_4), or using the optimized HEPES/NaCl conditions (layered in 25 mM HEPES 20 mM NaCl and purified in dH_2O). **a)** Luciferized OVCAR8 human ovarian cancer cell lines were treated with nanoparticles at doses that exposed the cells to 30 nM siRNA, and then luciferase expression was assessed after 1 day. LbL liposomes prepared using HEPES/NaCl conditions showed statistically significant improvement over NPs made either dH_2O or titrated water. **b)** NCR nude mice bearing subcutaneous flank tumor xenografts were intravenously injected with nanoparticles to provide a 0.5 mg/kg dose of siRNA. Luciferase signal was determined using IVIS whole-animal imaging, and indicates a brief knockdown is achieved 1 day post-treatment for particles prepared in dH_2O. In contrast, particles prepared using the optimized HEPES/NaCl method mediate a prolonged knockdown over the course of three days post-injection. **c)** The data from 2 days post-treatment indicates the particles prepared in HEPES/NaCl outperform particles made in water. Notably, two outliers in the HEPES/NaCl group deviate from the mean – but data from the third day indicates continued silencing for these outliers (see Appendix C Figure 9). **d)** Representative whole-animal luminescence images of mice treated with LbL liposomes prior to treatment and 2 days post-treatment. Error bars represent SD of triplicates in panel a and SEM of at least n=6 in panels b and c. All statistical tests were performed using one-way ANOVA (alpha = 0.05), with the Tukey post-test, on PRISM graphing software.

But the particles prepared in salt begin to diverge in size during the final (fourth) layer, which involves adsorption of the anionic polypeptide PLD. This step yields much larger particles with a Z-average hydrodynamic diameter of 245±7 nm, relative to the 173±4 nm diameter of the water-purified system (**Appendix C Figure 5a**). This is perhaps due to the weaker zeta potential (-26±3 mV) of the salt-purified system relative to the water-purified particles (-42±2 mV). Particles that

143

were purified in the presence of salt required less polymer in subsequent layers to achieve charge conversion, ca. 2:1 C:P for the siRNA layer in salt-purified vs ca. 1:1 C:P ratio for deionized water purified particles. Therefore, for both conditions, separate C:P ratios were chosen at each layering step in an effort to keep resulting zeta potentials as similar as possible prior to purification (**Appendix C Figure 5b**). Nonetheless, the need to shift the C:P ratios potentially indicates rearrangement or erosion of the film.

The practical consequences for optimizing siRNA loading become apparent in the ability of the final siRNA LbL liposomes to transfect cells. We demonstrate that LbL liposomes prepared following our optimized solution condition method (layered in 25mM NaCl and 20mM HEPES, purified in dH_2O) are able to mediate improved gene silencing in the human ovarian cancer cell line OVCAR8, compared to particles prepared in suboptimal solution conditions (**Figure 4.6a**). In our experience, this cell line is especially challenging to transfect using nanoparticle constructs, whereas for easier to transfect human ovarian cancer cells like COV362, each of these formulations fares well in vitro (**Appendix C Figure 6**). Because the OVCAR8 cell line can provide a more realistic model of ovarian cancer than prior models[95], the ability to transfect this line is interesting for advancing preclinical studies. Here we show that LbL liposomes (2:1 DSPG:cholesterol liposome/PLR/siLuciferase/PLR/PLD) prepared with optimal solution conditions are able to mediate prolonged silencing compared to LbL liposomes prepared in dH_2O in a subcutaneous flank xenograft of OVCAR8 (**Figure 4.6b**). After a single 0.5 mg siRNA/kg injection, the nanoparticle prepared in dH_2O is able to mediate some knockdown of luciferase signal 1 day after treatment (88%±6.8% expression relative to pre-treatment), but this effect dissipates 2 days after treatment. On the other hand, the gene silencing effect of the solution condition-optimized formulation becomes more intense out to 3 days post-treatment, with luciferase expression (relative to pre-treatment) decreasing from 84.6%±17.3% at day 1, to 70.9%±15.8% at day 2, and finally to 68.5%±6% at day 3. Notably, at day 2 (**Figure 4.6c**), two outliers deviate from the mean for the nanoparticles made in HEPES and NaCl, but by day 3 luciferase expression for those outliers dips back down in line with the other subjects (**Appendix C Figure 7**). The ability to mediate prolonged silencing following a single dose at 0.5 mg/kg in this model of ovarian cancer indicates these particles have immediate utility in the development of therapeutics for this difficult-to-treat malignancy.

The conditions studied so far have improved the preparation of LbL liposomes composed of poly-
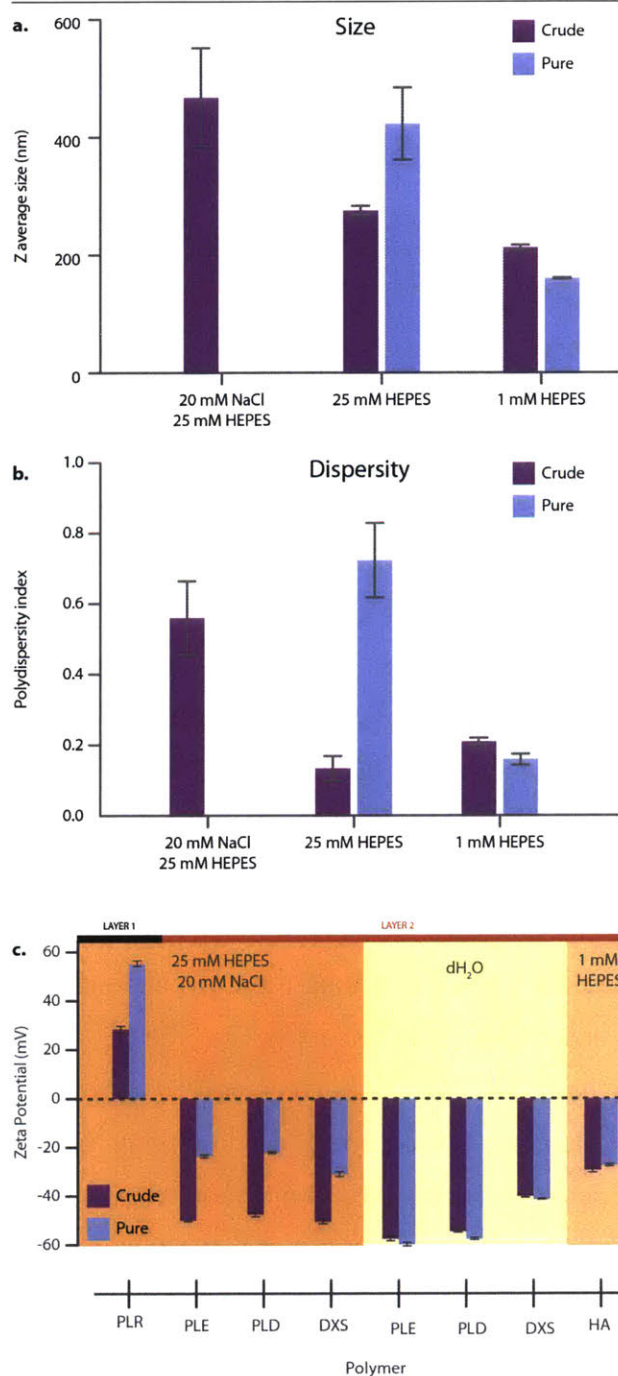
Figure 4.7. Figure 5. Ideal solution conditions vary based on the polymer being layered and the colloidal substrate being used. The hyaluronic acid (HA) layer requires specific solution conditions, and latex core substrates behave differently from liposomal-core formulations after the first layer deposition. **a)** HA deposition onto LbL liposomes is highly sensitive to ionic strength, and leads to immediate aggregation in the presence of 20 mM NaCl. Layering in 25 mM HEPES yields an unstable species of approximately 250 nm that aggregates during purification (buffer exchanged to water). HA layers successfully in 1 mM HEPES, producing a 215±7 nm particle that survives purification. **b)** Polydispersity data for the same syntheses supporting the observations made in panel a. **c)** Layering onto a carboxy-modified latex core leads to loss of charge using the 25 mM HEPES 20 mM NaCl conditions optimized for liposomal cores. While the initial PLR layer deposits in a manner consistent with observations for liposomal systems, the second anionic layer diverges. Poly(L-glutamate) (PLE), poly(L-aspartate) (PLD), and dextran sulfate (DXS) were deposited as second layers in salt, yielding highly charged species. These nanoparticles lost roughly half their surface charge upon purification, in contrast to systems where the second layer was deposited in the absence of any salt. Layering of HA using 1 mM HEPES still yields consistent results with liposomal systems. Size and polydispersity data were acquired by dynamic light scattering, and zeta potential data was measured using laser Doppler electrophoresis. Error bars represent standard deviation of three technical replicates.

peptides and siRNA, but there is also interest in working with more challenging materials such as hyaluronic acid (HA). This polysaccharide is a native constituent of the extracellular matrix, and provides LbL nanoparticles with unique capabilities that include pH-dependent swelling, hydrophilic characteristics that prolong circulation, and specific binding to the CD44 receptor that is overexpressed by a host of cancers[18, 26]. Taking advantage of these traits is complicated by the synthetic challenges that HA presents in LbL synthesis, due to its ability to form intramolecular hydrogen bonds and significantly change solution viscosity[96-99]. In general, we note that HA mediates the formation of much thicker layers and introduce the risk of flocculation. The extensive hydrogen bonding available to

145

HA also provides HA-coated nanoparticles with a very hydrophilic surface, which likely helps to mediate some of its resistance to opsonization and monocyte clearance.

We set out to determine if the solution conditions determined for our prior formulation, consisting of PLD as the outer layer, were compatible with incorporation of HA into an LbL nanoparticle. Because of the inter and intramolecular forces that complicate working with HA{Suh, 2005 #187, we hypothesized that the shorter electrostatic screening lengths provided by the salts that were optimal for siRNA layering would be destabilizing to HA. To assess this, we layered HA at 25 mM HEPES and 20 mM NaCl, 25 mM HEPES, and 1 mM HEPES (**Figure 4.7a-b**). Inclusion of NaCl led to the immediate aggregation of the colloid upon mixing with HA. Interestingly, when using 25 mM HEPES the nanoparticle formed is initially monodisperse and of acceptable size (0.17±0.05 PDI and 189±3 nm z-average diameter), but continues to grow in size over time without becoming more polydisperse (0.13±0.06 PDI and 276±14 nm z-average diameter). This trend might suggest continual growth of a thick HA film over time, but the resulting system appears to be unstable because purification leads to irreversible aggregation as indicated by size and PDI changes in Figure 4a-b. On the other hand, 1 mM HEPES yielded smaller monodisperse particles (Z-average diameter of 215±7 nm and PDI of 0.21±0.02) that reduced in size and remained stable after purification (Z-average diameter of 160±2 nm and PDI of 0.16±0.03). We propose that this trend suggests that HA is likely more sensitive to electrostatic screening than the polypeptides and siRNA we tested previously. Even the effects of low ionic strength salt species, like HEPES, alone may be sufficient to tip the system into an unstable state. We found that dilute HEPES allows for moderate control of pH for this layer with minimal electrostatic screening, which creates a high degree of ionization along the HA chain that may promote a stable HA layer and maximize charge-repulsion between chains to minimize the intermolecular hydrogen bonds[98] characteristic of HA.

These results indicate that the solution conditions for LbL nanoparticles are also dependent on the structure of the polymers being deposited, highlighting how different layers may require specific solution conditions for a successful synthesis. Along a similar line of inquiry, we also pose the question of whether the colloidal substrate might impact considerations for optimal solution conditions. To test this, we performed parallel syntheses of bilayered LbL nanoparticles on carboxy-modified latex (CML) templates (**Figure 4.7c**). CML/PLR particles were all prepared using 25 mM HEPES 20 mM NaCl for layering, and purified in water (as optimized above).

146

We observe an increase in zeta potential after purification of the CML/PLR particle, a typical occurrence that can be explained by the removal of excess salts during buffer exchange to deionized water. Surprisingly, we observed a different trend after layering and purifying the second, anionic layer. A significant loss of surface charge occurred after purification, from ca. -40 mV to ca. -20 mV. This trend was noted for several terminal layers (e.g., poly(L-glutamate) (PLE), poly(L-aspartate) (PLD), and dextran sulfate (DXS)) that were deposited in the presence of HEPES/NaCl and purified with deionized water. The initial charge of the crude products is in line with expected charge conversion. However, all conditions wherein the layer was deposited in the presence of salt lose significant surface charge upon purification. Despite the loss of charge, the resulting particles were monodisperse and of acceptable size (PDI ranging from 0.05 to 0.07 and Z-average size from 120-130 nm). In contrast, if the second layer is deposited in the absence of salts, the charge of crude and pure particles remain constant before and after purification.

Interestingly, deposition of HA, using the 1 mM HEPES condition, also provides stable particles using the CML core, and they do not exhibit a loss of charge upon purification. We also note that the synthetic solution conditions during LbL may have implications for the fully formed particle. LbL nanoparticles possess pH-sensitive functionalities, that can mediate charge-shifting and film swelling. These features of the LbL platform can be used to develop pH-triggered drug release or cellular uptake[26]. We observed that LbL nanoparticles (CML/PLR/HA) prepared at pH 7.4 or pH 6 can initiate swelling characteristics at slightly different pHs (**Appendix C Figure 8**). While the shift is modest, it is possible that swelling behavior could be tuned via the synthetic pH.

These intriguing results indicate that the core template may be an important consideration, as it may alter the ideal solution conditions for LbL synthesis. Further investigation into this phenomenon should be performed to understand the underlying mechanisms that mediate this discrepancy between liposomal and CML-core LbL systems, and if those principles extend to other biomedically relevant substrates like PLGA or mesoporous silica nanoparticles.

4.3. Conclusions and future work

This work describes a comprehensive and systematic study of the role of solution conditions in the preparation of LbL-functionalized liposomes for the delivery of siRNA. Our findings demonstrate important lessons for the continued development of this novel class of therapeutic nanoparticle, namely through the identification of strategies to independently tailor the degree of polyelectrolyte ionization and electrostatic screening length using HEPES to control pH and NaCl to control ionic strength, respectively. We demonstrate that LbL synthesis is tolerant to certain salts but not to others, exploring the effects of multivalent, monovalent, and zwitterionic salts. This finding confirms predictions from prior computational work on the destabilizing nature of larger and more multi-valent ions on the wrapping of polyelectrolytes around charged spheres. While we demonstrate that LbL synthesis is relatively tolerant to the presence of monovalent salts like NaCl and tris hydrochloride, we report that the zwitterionic species HEPES provides outstanding compatibility with LbL self-assembly. The HEPES buffer provides researchers with an excellent tool for controlling pH, and in turn the degree of polymer ionization, for a particular layer deposition step. We suggest that the compatibility of HEPES with LbL assembly stems from the negligible contribution of zwitterionic species to electrostatic screening. Meanwhile, the moderate compatibility of LbL liposomes with NaCl provides the ability to tailor the electrostatic screening length of the solution to permit more efficient layering of rigid molecules like siRNA. The judicious application of these conditions ultimately allows for an 8-fold improvement in the weight percent loading of siRNA in LbL liposomes, from 3.7% to 30%. Notably, the LbL liposomes prepared using the optimized solution conditions reported here are able to mediate improved gene silencing in human ovarian cancer cells, both in vitro and in vivo.

Our findings also draw attention to the role of pH in the determination of core-to-polymer mass ratios that yield stable, layered colloids. Tailoring this condition to maximize the ionization of the polyelectrolytes and corresponding substrate allow for more efficient mass ratios that call for less polymer to generate a stable particle. This provides benefits from a materials cost perspective, but it also has implications for preventing rearrangement of the LbL film. We demonstrate in this work that polyelectrolytes can compete for incorporation into the LbL film, leading to displacement of siRNA when the more flexible and charge-dense poly(L-aspartate) is incorporated as the fourth layer. Shifting pH allows the deposition of PLD to occur using less polymer, which eliminated the

issue of siRNA displacement on the final layer deposition step.

We extended our studies to analyze the role of salts during the purification process, and determined that it is beneficial to remove salts from the LbL system during interlayer purification. Using tangential flow filtration-based methods, we found that purification using salt-containing exchange buffer led to undesirable increases in particle size and potentially mediates rearrangement or erosion of the LbL film. This hypothesis is supported by the observation that particles that were purified in salt required less polymer to achieve charge conversion relative to formulations where layers are deposited in salt but purified in water. We also report that 3-fold less siRNA incorporation occurs when LbL liposomes are purified in salt, further suggesting that the film may be eroding or otherwise rearranging during this stage. Using water for the purification allows for improved encapsulation efficiency and ultimately high weight percent loading of siRNA in the resulting LbL nanoparticle.

Our study also briefly examines the impact of changing the colloidal substrate for LbL, and we observe that switching from an anionic liposome to a carboxy-modified latex core has consequences for LbL synthesis. While the initial PLR layer behaves similarly across CML and liposomes, if the second layer is deposited in the presence of salts then there is a systematic loss of zeta potential in the purified LbL CML particle. This observation suggests the need for deeper study into the role of the colloidal template and how it influences the development of optimal solution conditions for LbL systems.

Finally, we demonstrated that solution conditions ought to be considered independently for each polymer being incorporated into the LbL nanoparticle. The polysaccharide hyaluronic acid provides a breadth of advantages as a terminal layer for the targeted delivery of drugs to cancer, but also poses considerable challenges during synthesis due to its ability to form inter and intramolecular hydrogen bonds. Deposition of this valuable layer is incompatible with the NaCl and HEPES conditions that improve siRNA loading, likely because HA must repel other HA molecules from itself to prevent crosslinking and aggregation of the LbL particle. Consistent with that hypothesis, we show that by increasing the electrostatic screening length via the removal of NaCl altogether, we are able to successfully generate thinner films of HA onto LbL liposomes and achieve a stable colloidal suspension.

This study demonstrates the importance of carefully optimizing solution conditions for the self-assembly of LbL nanoparticles, especially for systems designed for drug delivery. Consideration of the various intermolecular forces and the physical processes that mediate efficient layering can be used to design solution conditions to optimize the loading of functional biopolymers into this emerging class of nanocarrier. The work described here offers a useful template for optimization of similar systems, and aims to promote greater investigation into the role of solution conditions in the development of these systems.

4.4. Methods

Chemical and biological reagents: NaCl powder was purchased from (). 1 M Tris-HCl solution was purchased from (). HEPES, sodium citrate, Na_2HPO_4 and NaH_2PO_4 powders were purchased from MilliporeSigma. 1,2-distearoyl-sn-glycero-3-phosphocholine (DSPC), 1-palmitoyl-2-oleoyl-sn-glycero-3-phospho-(1'-rac-glycerol) (sodium salt) (POPG), 1,2-distearoyl-sn-glycero-3-phospho-(1'-rac-glycerol) (sodium salt) (DSPG), and cholesterol were purchased from Avanti. Chloroform and methanol were purchased from TCI and Sigma, respectively. Whatman nuclepore polycarbonate hydrophilic membranes (400, 200, 100 and 50 nm sizes) were purchased from GE. All glassware was obtained from Chemglass. 50/15 mL Falcon tubes and 50/5/2 mL DNA loBind Eppendorf tubes were purchased from VWR. Polysytrene latex microspheres (Fluospheres), locked nucleic acid siRNAs (Silencer Select), 5 M bioreagent grade NaCl solution, and pre-cast EX 2% agarose E-gels were obtained from Thermo Fisher Scientific. 1 M bioreagent-grade HEPES was purchased from Fisher Scientific. D02-E100-05-N and C02-E100-05-N tangential flow filtration filters were purchased from Spectrum Labs. Poly(L-arginine hydrochloride) (9.6 kDa, 38.5 kDa), poly(L-glutamic acid sodium salt) (15 kDa), and poly(L-aspartic acid sodium salt) (14 kDa) were purchased from Alamanda Polymers. Dextran sulfate sodium salt (15 kDa) was purchased from MilliporeSigma. Hyaluronic acid (20 kDa) was purchased from LifeCore. Heparin sulfate was a generous gift from the Sasisekharan Lab. Propargyl-modified PLD was synthesized according to prior methods{Wang, 2018 #245}{Li, 2017 #244}. Polystyrene semi-micro cuvettes for the Malvern Zetasizer were purchased from VWR and DTS1070 folded capillary cells were purchased directly from Malvern. Black 364 well plates for the Wyatt DLS were purchased directly from the Peterson (1957) Nanotechnology Core Facility.

OVCAR8 and COV362 human ovarian cancer cell lines were gifts from the Bhatia Lab at MIT and the Elias Lab at Brigham and Women's Hospital, respectively. Tissue culture plasticware (T75, T25, clear and white 96 well plates), trypsin EDTA, penicillin streptomycin and RPMI 1640 media was purchased from Corning. Fetal bovine serum was purchased from Gibco. Steady-Glo luciferase expression assay and CellTiter-Fluor viability assay were purchased from Promega.

Preparation of liposomal cores: DSPC, POPG, and cholesterol were dissolved in chloroform and DSPG was dissolved in a 65:35:8 mixture of chloroform, methanol and deionized water (milli-

Q). Lipid mixtures composed of 66.7 mol% phospholipid and 33.3% cholesterol were prepared in round bottom flasks (RBFs) (10 or 50 mL depending on scale), and for DSPG-formulations methanol was added dropwise until the solution cleared. The lipid solution was evaporated using a BUCHI RotoVap system under heat (60C, water bath) until completely dry (<15 mBarr). A Branson sonicator bath was filled with reverse-osmosis water and heated until >70C, at which point the RBF with the lipid film was partially submerged in the bath and a volume of dH_2O was added to resuspend the lipid film to a 1 mg lipid/mL solution. The liposome solution was sonicated for roughly 1 minute and then transferred to an Avestin LiposoFast LF-50 liposome extruder. The extruder was connected to a Cole-Parmer Polystat Heated Recirculator Bath to maintain a temperature > 65C. The liposome solution was extruded through successively smaller nucle-pore membranes until a 50-100 nm liposome was obtained. Generally, this required 1 pass through a stack of 2-3 400, 200, 100 and 50 nm membranes. Liposomes were characterized for size and zeta using the techniques outlined below.

Buffer preparation: For the initial PLR layering screen, all buffers were prepared as 200 mM stock solutions in milli-Q water, and serially diluted to generate 2x strength solutions for each concentration to be tested. Solution pH was measured using both pH paper and a Hanna electronic pH-meter. Tris-HCl and sodium citrate were titrated with HCl to obtain pH 7-7.6. Sodium phosphate was titrated with NaOH to a pH 7-7.6. For the pH-sensitivity experiment in Supplementary Figure 2, liposomes were diluted in 25 mM HEPES buffer titrated to the desired pH using either HCl or NaOH. For experiments using the optimized solution conditions, a 50 mM HEPES 40 mM NaCl solution was prepared in milli-Q water and titrated to pH 7.5.

Layer by layer assembly: Nanoparticles were layered by adding an equal volume of nanopar-ticle solution (not exceeding 1 mg/mL) to an equal volume of polyelectrolyte solution under sonication (Branson bath sonicator, room temperature). The mixture was sonicated for roughly 5 seconds. Optimal C:P ratios for each layer were determined prior to the deposition step via a polyelectrolyte titration using 25-50uL samples of the nanoparticle solution for each tested C:P ratio. The test ratios were mixed as above, but only incubated for 5-10 minutes before char-acterization. If the resulting particle had a zeta potential greater than 30 mV (either positive or negative) and an appropriate size, it was chosen as the optimal ratio.

For conditions involving a buffer or salt throughout the entire synthesis, the polyelectrolyte solution is prepared in 2x strength buffer for the initial layer, and then in 1x strength buffer for subsequent layers. For conditions that remove the salt during purification steps, the polyelectrolyte solution is prepared in 2x strength buffer for all deposition steps. Bioreagent-grade NaCl and HEPES were used for syntheses involving siRNA. DNA loBind tubes are used as the mixing vessels for all experiments, to prevent nonspecific adsorption of siRNA and other polymers to the plasticware.

The layered particle is allowed to incubate at room temperature for 1 hour and is then purified using the tangential flow filtration method, as described previously[36]. Briefly, crude nanoparticle solution is connected to a Spectrum Labs KrosFlo II system using masterflex, Teflon-coated tubing. D02-E100-05-N (batch volume > 5 mL) or C02-E100-05-N (batch volume < 1 mL) 100 kDa filters were used to purify the particles until 5 volume-equivalents were collected in the permeate. For cationic layers, the TFF filter was pre-treated with a solution of free polycation (same concentration used for layering) in order to minimize nonspecific adsorption of particles to the membrane walls. Samples were run at 80 mL/min (size 16 tubing, used with D02-series filters) or 13 mL/min (size 13 tubing, used with C02-series filters). Once pure, the sample was either concentrated (by disconnecting the buffer reservoir) or recovered via reversing the direction of the peristaltic pump. For more complete yields, 1-3 mL of the appropriate buffer was run backwards through the tubing to recover any remaining particles. This process was repeated until the desired LbL formulation was obtained. Exchange buffer is chosen to be consistent with the intended synthetic solution conditions.

Characterization of LbL nanoparticles: Nanoparticles were characterized using dynamic light scattering. The Wyatt Dyna Pro was used for high throughput experiments shown in Figure 1 and 2 and the Malvern ZS90 Particle Analyzer for all other size measurements reported. Zeta potential measurements were made using laser Doppler electrophoresis on the Malvern ZS90. Samples were diluted in milli-Q water for all measurements. Results from the Malvern are reported using the SD of three measurements.

Determination of siRNA loading and retention (agarose gel and NanoDrop): Agarose gels were used to determine the complexation state and loading of siRNA. To determine complexation state, nanoparticles were diluted and 20uL of the diluted particle were added to the wells of a

153

pre-cast EX 2% agarose E-gel. To determine loading, the LbL nanoparticles were dissociated by addition of excess heparin, e.g., the particles were diluted in a solution of 5 mg/mL heparin and heated (37C) for fifteen minutes. The gel was run using the E-gel system (Thermo Fisher) for 5 minutes and then visualized using a Typhoon laser scanning imager (GE). To quantify encapsulation efficiency, permeate fractions were collected during tangential flow filtration of the siRNA-coated nanoparticles. Fractions were analyzed for siRNA concentration using the Nano-Drop system (Thermo Fisher), and used to determine total amount of siRNA removed from the system. The encapsulation efficiency was used in conjunction with the known amount of siRNA introduced into the system and the yield-adjusted mg of lipid in the system to determine weight percent loading.

Cell culture and transfection: OVCAR8 and COV362 cells were seeded at a density of 20,000 cells per well in a 96 well plate in complete RPMI 1640 media (10% FBS, 1% pen-strep). Cells were allowed to adhere to the plate for 24 hours prior to treatment with nanoparticles. Nanoparticles were dosed to provide equivalent siRNA concentrations across conditions (30 nM). After 24 hours, cell viability and luciferase expression were measured using the multiplexed CellTiter-Fluor and Steady-Glo assay kits according the manufacturer's protocols. Luciferase expression was normalized to the well viability and then normalized to expression from untreated cells.

In vivo transfection: Female NCR *nu/nu* mice were purchased from Taconic and subcutaneously injected with mCherry/Luciferase expressing OVCAR8 cells (1 million cells per flank, 200 uL injections in 1:1 PBS:MatriGel). Tumors were allowed to establish over the course of one month, and then randomized into treatment groups. Mice were then injected (tailvein injection, 200 uL bolus) with nanoparticles to provide a 0.5 mg/kg dose of siRNA against the luciferase gene. Whole animal imaging was performed using the Xenogen IVIS Imaging System (PerkinElmer) following an intraperitoneal injection of d-luciferin (200 uL, 15 mg/mL, 10 minute incubation prior to imaging). These experiments were approved by the Massachusetts Institute of Technology Committee on Animal Care (CAC).

Calculations and statistics: All statistics were performed using the GraphPad PRISM software, using the one-way ANOVA test for significance with a Tuker post-hoc test (alpha set to 0.05). Ionic strengths are calculated as follows:

154

$$pH = pK_a + \log_{10}(\frac{\alpha}{1-\alpha})$$

Where I is the ionic strength, summed over n ionizable species in solution, c is the molar concentration of the ith ionized species, and z is the charge number (valency) of the ith species

As there is an inherent relationship for dissociation of acids and bases, Henderson-Hasselbach was used to calculate the degree of dissociation as follows:

$$pH = pK_a + \log_{10}(\frac{\alpha}{1-\alpha})$$

Where α is the degree of dissociation. Note that for salts, such as NaCl, it is assumed that they are completely dissociated.

The Debye length κ^{-1} (meters) is calculated as follows:

$$\kappa^{-1} = \left[\frac{N_A e^2}{\varepsilon \varepsilon_0 k_B T} * 2I\right]^{-\frac{1}{2}}$$

Where N_A is Avogadro's number, e is the elementary charge of an electron, ε is the dielectric constant of water (assumed to be 80), ε_0 is the permittivity of free space, k_B is the Boltzmann constant, T is the temperature (298K), and I is the ionic strength.

4.5. References

1.   Lvov, Y.; Decher, G.; Mohwald, H., Assembly, Structural Characterization, and Thermal-Behavior of Layer-by-Layer Deposited Ultrathin Films of Poly(Vinyl Sulfate) and Poly(Allylamine). *Langmuir* **1993,** *9* (2), 481-486.

2.   Hammond, P. T., Form and function in multilayer assembly: New applications at the nanoscale. *Adv Mater* **2004,** *16* (15), 1271-1293.

3.   Iler, R. K., Multilayers of Colloidal Particles. *J Colloid Interf Sci* **1966,** *21* (6), 569-+.

4.   Wang, Y.; Angelatos, A. S.; Caruso, F., Template synthesis of nanostructured materials via layer-by-layer assembly. *Chem Mater* **2008,** *20* (3), 848-858.

5.   Ariga, K.; Yamauchi, Y.; Rydzek, G.; Ji, Q. M.; Yonamine, Y.; Wu, K. C. W.; Hill, J. P., Layer-by-layer Nanoarchitectonics: Invention, Innovation, and Evolution. *Chem. Lett.* **2014,** *43* (1), 36-68.

6.   Zacher, D.; Shekhah, O.; Woll, C.; Fischer, R. A., Thin films of metal-organic frameworks. *Chem Soc Rev* **2009,** *38* (5), 1418-29.

7.   Ren, N.; Yang, Y. H.; Zhang, Y. H.; Wang, Q. R.; Tang, Y., Heck coupling in zeolitic microcapsular reactor: A test for encaged quasi-homogeneous catalysis. *J Catal* **2007,** *246* (1), 215-222.

8.   Wang, B.; Vyas, R. N.; Shaik, S., Preparation parameter development for layer-by-layer assembly of Keggin-type polyoxometalates. *Langmuir* **2007,** *23* (22), 11120-6.

9.   Ji, Q.; Honma, I.; Paek, S. M.; Akada, M.; Hill, J. P.; Vinu, A.; Ariga, K., Layer-by-layer films of graphene and ionic liquids for highly selective gas sensing. *Angew Chem Int Ed Engl* **2010,** *49* (50), 9737-9.

10.   Bae, W. K.; Kwak, J.; Lim, J.; Lee, D.; Nam, M. K.; Char, K.; Lee, C.; Lee, S., Multicolored light-emitting diodes based on all-quantum-dot multilayer films using layer-by-layer assembly method. *Nano Lett* **2010,** *10* (7), 2368-73.

11.   Zhang, X.; Li, S.; Jin, X.; Zhang, S., A new photoelectrochemical aptasensor for the detection of thrombin based on functionalized graphene and CdSe nanoparticles multilayers. *Chem Commun (Camb)* **2011,** *47* (17), 4929-31.

12.   Whang, D.; Jin, S.; Wu, Y.; Lieber, C. M., Large-scale hierarchical organization of nanowire arrays for integrated nanosystems. *Nano Lett* **2003,** *3* (9), 1255-1259.

13.   Ho, P. K.; Kim, J. S.; Burroughes, J. H.; Becker, H.; Li, S. F.; Brown, T. M.; Cacialli, F.; Friend, R. H., Molecular-scale interface engineering for polymer light-emitting diodes. *Nature* **2000,** *404* (6777), 481-4.

14.   Kotov, N. A.; Dekany, I.; Fendler, J. H., Layer-by-Layer Self-Assembly of Polyelectrolyte-Semiconductor Nanoparticle Composite Films. *J. Phys. Chem.* **1995,** *99* (35), 13065-13069.

15.   Tang, Z. Y.; Wang, Y.; Podsiadlo, P.; Kotov, N. A., Biomedical applications of layer-by-layer assembly: From biomimetics to tissue engineering. *Adv Mater* **2006,** *18* (24), 3203-3224.

16.   Correa, S.; Dreaden, E. C.; Gu, L.; Hammond, P. T., Engineering nanolayered particles for modular drug delivery. *J Control Release* **2016,** *240,* 364-386.

17.   Johnston, A. P. R.; Cortez, C.; Angelatos, A. S.; Caruso, F., Layer-by-layer engineered capsules and their applications. *Current Opinion in Colloid & Interface Science* **2006,** *11* (4), 203-209.

18.   Morton, S. W.; Poon, Z.; Hammond, P. T., The architecture and biological performance of drug-loaded LbL nanoparticles. *Biomaterials* **2013,** *34* (21), 5328-35.

19.   Luo, R.; Neu, B.; Venkatraman, S. S., Surface functionalization of nanoparticles to control cell interactions and drug release. *Small* **2012,** *8* (16), 2585-94.

20.   Deng, Z. J.; Morton, S. W.; Ben-Akiva, E.; Dreaden, E. C.; Shopsowitz, K. E.; Hammond, P. T., Layer-by-layer nanoparticles for systemic codelivery of an anticancer drug and siRNA for potential triple-negative breast cancer treatment. *ACS Nano* **2013,** *7* (11), 9571-84.

21.   Dreaden, E. C.; Kong, Y. W.; Morton, S. W.; Correa, S.; Choi, K. Y.; Shopsowitz, K. E.; Renggli, K.; Drapkin, R.; Yaffe, M. B.; Hammond, P. T., Tumor-Targeted Synergistic Blockade of MAPK and PI3K from a Layer-by-Layer Nanoparticle. *Clin Cancer Res* **2015,** *21* (19), 4410-9.

22.   Shu, S.; Sun, C.; Zhang, X.; Wu, Z.; Wang, Z.; Li, C., Hollow and degradable polyelectrolyte nanocapsules for protein drug delivery. *Acta Biomater* **2010,** *6* (1), 210-7.

23.   Li, P.; Liu, D.; Miao, L.; Liu, C.; Sun, X.; Liu, Y.; Zhang, N., A pH-sensitive multifunctional gene carrier assembled via layer-by-layer technique for efficient gene delivery. *Int J Nanomedicine* **2012,** 7, 925-39.

24.   Yang, X. Z.; Du, J. Z.; Dou, S.; Mao, C. Q.; Long, H. Y.; Wang, J., Sheddable ternary nanoparticles for tumor acidity-targeted siRNA delivery. *ACS Nano* **2012,** *6* (1), 771-81.

25.   Ramasamy, T.; Haidar, Z. S.; Tran, T. H.; Choi, J. Y.; Jeong, J. H.; Shin, B. S.; Choi, H. G.; Yong, C. S.; Kim, J. O., Layer-by-layer assembly of liposomal nanoparticles with PEGylated polyelectrolytes enhances systemic delivery of multiple anticancer drugs. *Acta Biomater* **2014,** *10* (12), 5116-5127.

26.   Dreaden, E. C.; Morton, S. W.; Shopsowitz, K. E.; Choi, J. H.; Deng, Z. J.; Cho, N. J.; Hammond, P. T., Bimodal tumor-targeting from microenvironment responsive hyaluronan layer-by-layer (LbL) nanoparticles. *ACS Nano* **2014,** *8* (8), 8374-82.

27.   Gu, L.; Deng, Z. J.; Roy, S.; Hammond, P. T., A Combination RNAi-Chemotherapy Layer-by-Layer Nanoparticle for Systemic Targeting of KRAS/P53 with Cisplatin to Treat Non-Small Cell Lung Cancer. *Clin Cancer Res* **2017,** *23* (23), 7312-7323.

28.   Pecot, C. V.; Calin, G. A.; Coleman, R. L.; Lopez-Berestein, G.; Sood, A. K., RNA interference in the clinic: challenges and future directions. *Nat Rev Cancer* **2011,** *11* (1), 59-67.

29.   Morry, J.; Ngamcherdtrakul, W.; Gu, S.; Reda, M.; Castro, D. J.; Sangvanich, T.; Gray, J. W.; Yantasee, W., Targeted Treatment of Metastatic Breast Cancer by PLK1 siRNA Delivered by an Antioxidant Nanoparticle Platform. *Molecular Cancer Therapeutics* **2017,** *16* (4), 763-772.

30.   Yao, Y.; Su, Z.; Liang, Y.; Zhang, N., pH-Sensitive carboxymethyl chitosan-modified cationic liposomes for sorafenib and siRNA co-delivery. *Int J Nanomedicine* **2015,** *10,* 6185-97.

31.   Elbakry, A.; Zaky, A.; Liebl, R.; Rachel, R.; Goepferich, A.; Breunig, M., Layer-by-layer assembled gold nanoparticles for siRNA delivery. *Nano Lett* **2009,** *9* (5), 2059-64.

32.   Bishop, C. J.; Tzeng, S. Y.; Green, J. J., Degradable polymer-coated gold nanoparticles for co-delivery of DNA and siRNA. *Acta Biomaterialia* **2015,** *11,* 393-403.

33.   Deng, Z. J.; Morton, S. W.; Bonner, D. K.; Gu, L.; Ow, H.; Hammond, P. T., A plug-and-play ratiometric pH-sensing nanoprobe for high-throughput investigation of endosomal escape. *Biomaterials* **2015,** *51,* 250-256.

34.   Mogaki, R.; Hashim, P. K.; Okuro, K.; Aida, T., Guanidinium-based "molecular glues" for modulation of biomolecular functions. *Chem Soc Rev* **2017,** *46* (21), 6480-6491.

35.   Richardson, J. J.; Ejima, H.; Lorcher, S. L.; Liang, K.; Senn, P.; Cui, J.; Caruso, F., Preparation of nano- and microcapsules by electrophoretic polymer assembly. *Angew Chem Int Ed Engl* **2013,** *52* (25), 6455-8.

36.   Correa, S.; Choi, K. Y.; Dreaden, E. C.; Renggli, K.; Shi, A.; Gu, L.; Shopsowitz, K. E.; Quadir, M. A.; Ben-Akiva, E.; Hammond, P. T., Highly scalable, closed-loop synthesis of drug-loaded, layer-by-layer nanoparticles. *Adv Funct Mater* **2016,** *26* (7), 991-1003.

37.   Schneider, G.; Decher, G., Functional core/shell nanoparticles via layer-by-layer assembly. investigation of the experimental parameters for controlling particle aggregation and for enhancing dispersion stability. *Langmuir* **2008,** *24* (5), 1778-89.

38.   Hanaor, D.; Michelazzi, M.; Leonelli, C.; Sorrell, C. C., The effects of carboxylic acids on the aqueous dispersion and electrophoretic deposition of ZrO2. *J Eur Ceram Soc* **2012,** *32* (1), 235-244.

39.   Bishop, C. J.; Tzeng, S. Y.; Green, J. J., Degradable polymer-coated gold nanoparticles for co-delivery of DNA and siRNA. *Acta Biomater* **2015,** *11,* 393-403.

40.   Bertrand, P.; Jonas, A.; Laschewsky, A.; Legras, R., Ultrathin polymer coatings by complexation of polyelectrolytes at interfaces: suitable materials, structure and properties. *Macromol. Rapid Commun.* **2000,** *21* (7), 319-348.

41.   Gittins, D. I.; Caruso, F., Tailoring the polyelectrolyte coating of metal nanoparticles. *J Phys Chem B* **2001,** *105* (29), 6846-6852.

42.   Huang, S. C.; Artyukhin, A. B.; Wang, Y.; Ju, J. W.; Stroeve, P.; Noy, A., Persistence length control of the polyelectrolyte layer-by-layer self-assembly on carbon nanotubes. *J Am Chem Soc* **2005,** *127* (41), 14176-7.

43.   Dang, X.; Gu, L.; Qi, J.; Correa, S.; Zhang, G.; Belcher, A. M.; Hammond, P. T., Layer-by-layer assembled fluorescent probes in the second near-infrared window for systemic delivery and detection of ovarian cancer. *Proc Natl Acad Sci U S A* **2016,** *113* (19), 5179-84.

44.   Bjornmalm, M.; Roozmand, A.; Noi, K. F.; Guo, J.; Cui, J.; Richardson, J. J.; Caruso, F., Flow-Based Assembly of Layer-by-Layer Capsules through Tangential Flow Filtration. *Langmuir* **2015,** *31* (33), 9054-60.

45.   Zhang, P.; Chiu, Y. C.; Tostanoski, L. H.; Jewell, C. M., Polyelectrolyte Multilayers Assembled Entirely from Immune Signals on Gold Nanoparticle Templates Promote Antigen-Specific T Cell Response. *ACS Nano* **2015,** *9* (6), 6465-77.

46.   Schneider, G.; Decher, G., From functional core/shell nanoparticles prepared via layer-by-layer deposition to empty nanospheres. *Nano Lett* **2004,** *4* (10), 1833-1839.

47.   Lee, S. K.; Tung, C. H., A fabricated siRNA nanoparticle for ultra-long gene silencing in vivo. *Adv Funct Mater* **2013,** *23* (28), 3488-3493.

48.   Poon, Z.; Lee, J. B.; Morton, S. W.; Hammond, P. T., Controlling in vivo stability and biodistribution in electrostatically assembled nanoparticles for systemic delivery. *Nano Lett* **2011,** *11* (5), 2096-103.

49.   Cui, W.; Wang, A.; Zhao, J.; Yang, X.; Cai, P.; Li, J., Layer by layer assembly of albumin nanoparticles with selective recognition of tumor necrosis factor-related apoptosis-inducing ligand (TRAIL). *J Colloid Interface Sci* **2016,** *465,* 11-7.

50.   Shutava, T. G.; Balkundi, S. S.; Vangala, P.; Steffan, J. J.; Bigelow, R. L.; Cardelli, J. A.; O'Neal, D. P.; Lvov, Y. M., Layer-by-Layer-Coated Gelatin Nanoparticles as a Vehicle for Delivery of Natural Polyphenols. *ACS Nano* **2009,** *3* (7), 1877-85.

51.   Tian, L.; Yang, J.; Ji, F.; Liu, Y.; Yao, F., Drug co-loading and pH-sensitive release core-shell nanoparticles via layer-by-layer assembly. *J Biomater Sci Polym Ed* **2014,** *25* (14-15), 1573-89.

52.   Zhu, Y. F.; Meng, W. J.; Gao, H.; Hanagata, N., Hollow Mesoporous Silica/Poly(L-lysine) Particles for Codelivery of Drug and Gene with Enzyme-Triggered Release Property. *J Phys Chem C* **2011,** *115* (28), 13630-13636.

53.   Guo, S.; Huang, Y.; Jiang, Q.; Sun, Y.; Deng, L.; Liang, Z.; Du, Q.; Xing, J.; Zhao, Y.; Wang, P. C.; Dong, A.; Liang, X. J., Enhanced gene delivery and siRNA silencing by gold nanoparticles coated with charge-reversal polyelectrolyte. *ACS Nano* **2010,** *4* (9), 5505-11.

54.   Han, L.; Zhao, J.; Zhang, X.; Cao, W.; Hu, X.; Zou, G.; Duan, X.; Liang, X. J., Enhanced siRNA delivery and silencing gold-chitosan nanosystem with surface charge-reversal polymer assembly and good biocompatibility. *ACS Nano* **2012,** *6* (8), 7340-51.

55.   Labala, S.; Jose, A.; Chawla, S. R.; Khan, M. S.; Bhatnagar, S.; Kulkarni, O. P.; Venuganti, V. V. K., Effective melanoma cancer suppression by iontophoretic co-delivery of STAT3 siRNA and imatinib using gold nanoparticles. *Int J Pharmaceut* **2017,** *525* (2), 407-417.

56.   Pavlov, A. M.; Sukhorukov, G. B.; Gould, D. J., Location of molecules in layer-by-layer assembled microcapsules influences activity, cell delivery and susceptibility to enzyme degradation. *J Control Release* **2013,** *172* (1), 22-29.

57.   Son, K. J.; Yoon, H. J.; Kim, J. H.; Jang, W. D.; Lee, Y.; Koh, W. G., Photosensitizing hollow nanocapsules for combination cancer therapy. *Angew Chem Int Ed Engl* **2011,** *50* (50), 11968-71.

58.   Shen, J.; Kim, H. C.; Mu, C.; Gentile, E.; Mai, J.; Wolfram, J.; Ji, L. N.; Ferrari, M.; Mao, Z. W.; Shen, H., Multifunctional gold nanorods for siRNA gene silencing and photothermal therapy. *Adv Healthc Mater* **2014,** *3* (10), 1629-37.

59.   Caruso, R. A.; Susha, A.; Caruso, F., Multilayered titania, silica, and Laponite nanoparticle coatings on polystyrene colloidal templates and resulting inorganic hollow spheres. *Chem Mater* **2001,** *13* (2), 400-409.

60.   Caruso, F.; Lichtenfeld, H.; Giersig, M.; Mohwald, H., Electrostatic self-assembly of silica nanoparticle - Polyelectrolyte multilayers on polystyrene latex particles. *J. Am. Chem. Soc.* **1998,** *120* (33), 8523-8524.

61.   Park, M. K.; Onishi, K.; Locklin, J.; Caruso, F.; Advincula, R. C., Self-assembly and characterization of polyaniline and sulfonated polystyrene multilayer-coated colloidal particles and hollow shells. *Langmuir* **2003,** *19* (20), 8550-8554.

62.   Gittins, D. I.; Caruso, F., Multilayered polymer nanocapsules derived from gold nanoparticle templates. *Adv Mater* **2000,** *12* (24), 1947-+.

63.   Burke, S. E.; Barrett, C. J., Acid-base equilibria of weak polyelectrolytes in multilayer thin films. *Langmuir* **2003,** *19* (8), 3297-3303.

64.   Melby, E. S.; Lohse, S. E.; Park, J. E.; Vartanian, A. M.; Putans, R. A.; Abbott, H. B.; Hamers, R. J.; Murphy, C. J.; Pedersen, J. A., Cascading Effects of Nanoparticle Coatings: Surface Functionalization Dictates the Assemblage of Complexed Proteins and Subsequent Interaction with Model Cell Membranes. *ACS Nano* **2017,** *11* (6), 5489-5499.

65.   Ai, H.; Pink, J. J.; Shuai, X.; Boothman, D. A.; Gao, J., Interactions between self-assembled polyelectrolyte shells and tumor cells. *J Biomed Mater Res A* **2005,** *73* (3), 303-12.

66.   Elbakry, A.; Zaky, A.; Liebkl, R.; Rachel, R.; Goepferich, A.; Breunig, M., Layer-by-Layer Assembled Gold Nanoparticles for siRNA Delivery. *Nano Lett* **2009,** *9* (5), 2059-2064.

67.   Hong, X.; Li, J.; Wang, M. J.; Xu, J. J.; Guo, W.; Li, J. H.; Bai, Y. B.; Li, T. J., Fabrication of magnetic luminescent nanocomposites by a layer-by-layer self-assembly approach. *Chem Mater* **2004,** *16* (21), 4022-4027.

68.   Mayya, K. S.; Schoeler, B.; Caruso, F., Preparation and organization of nanoscale polyelectrolyte-coated gold nanoparticles. *Advanced Functional Materials* **2003,** *13* (3), 183-188.

69.   Gole, A.; Murphy, C. J., Polyelectrolyte-coated gold nanorods: Synthesis, characterization and immobilization. *Chem Mater* **2005,** *17* (6), 1325-1330.

70.   Lohse, S. E.; Eller, J. R.; Sivapalan, S. T.; Plews, M. R.; Murphy, C. J., A simple millifluidic benchtop reactor system for the high-throughput synthesis and functionalization of gold nanoparticles with different sizes and shapes. *ACS Nano* **2013,** *7* (5), 4135-50.

71.   Chen, Z.; Zhang, L.; He, Y.; Shen, Y.; Li, Y., Enhanced shRNA delivery and ABCG2 silencing by charge-reversible layered nanocarriers. *Small* **2015,** *11* (8), 952-62.

72.   Carnal, F.; Stoll, S., Adsorption of weak polyelectrolytes on charged nanoparticles. Impact of salt valency, pH, and nanoparticle charge density. Monte Carlo simulations. *J Phys Chem B* **2011,** *115* (42), 12007-18.

73.   Netz, R. R.; Joanny, J. F., Complexation between a semiflexible polyelectrolyte and an oppositely charged sphere. *Macromolecules* **1999,** *32* (26), 9026-9040.

74.   Chai, A.; Jiang, Y.; Zhang, Y.; He, L.; Zhang, D.; Zhang, L., Wrapping/unwrapping transition of double-stranded DNA in DNA-nanosphere complexes induced by multivalent anions. *Soft Matter* **2014,** *10* (27), 4875-84.

75.   Kunze, K. K.; Netz, R. R., Salt-induced DNA-histone complexation. *Phys Rev Lett* **2000,** *85* (20), 4389-92.

76.   Sukhishvili, S. A., Responsive polymer films and capsules via layer-by-layer assembly. *Current Opinion in Colloid & Interface Science* **2005,** *10* (1-2), 37-44.

77.   Ferreira, M.; Rubner, M. F., Molecular-Level Processing of Conjugated Polymers .1. Layer-by-Layer Manipulation of Conjugated Polyions. *Macromolecules* **1995,** *28* (21), 7107-7114.

78.   de Villiers, M. M.; Otto, D. P.; Strydom, S. J.; Lvov, Y. M., Introduction to nanocoatings produced by layer-by-layer (LbL) self-assembly. *Adv Drug Deliv Rev* **2011,** *63* (9), 701-15.

79.   Clark, S. L.; Montague, M. F.; Hammond, P. T., Ionic effects of sodium chloride on the templated deposition of polyelectrolytes using layer-by-layer ionic assembly. *Macromolecules* **1997,** *30* (23), 7237-7244.

80.   Chen, W.; McCarthy, T. J., Layer-by-layer deposition: A tool for polymer surface modification. *Macromolecules* **1997,** *30* (1), 78-86.

81.   Lee, L.; Cavalieri, F.; Johnston, A. P.; Caruso, F., Influence of salt concentration on the assembly of DNA multilayer films. *Langmuir* **2010,** *26* (5), 3415-22.

82.   Schneider, G. F.; Decher, G., From "nano-bags" to "micro-pouches". Understanding and tweaking flocculation-based processes for the preparation of new nanoparticle-composites. *Nano Lett* **2008,** *8* (11), 3598-604.

83.   Sercombe, L.; Veerati, T.; Moheimani, F.; Wu, S. Y.; Sood, A. K.; Hua, S., Advances and Challenges of Liposome Assisted Drug Delivery. *Front Pharmacol* **2015,** *6*, 286.

84.   Briuglia, M. L.; Rotella, C.; McFarlane, A.; Lamprou, D. A., Influence of cholesterol on liposome stability and on in vitro drug release. *Drug Deliv Transl Res* **2015,** *5* (3), 231-42.

85.   Stellwagen, E.; Prantner, J. D.; Stellwagen, N. C., Do zwitterions contribute to the ionic strength of a solution? *Anal Biochem* **2008,** *373* (2), 407-9.

86.   Hagerman, P. J., Flexibility of RNA. *Annu Rev Biophys Biomol Struct* **1997,** *26*, 139-56.

87.   Kebbekus, P.; Draper, D. E.; Hagerman, P., Persistence length of RNA. *Biochemistry-Us* **1995,** *34* (13), 4354-7.

88.   Gary, D. J.; Puri, N.; Won, Y. Y., Polymer-based siRNA delivery: perspectives on the fundamental and phenomenological distinctions from polymer-based DNA delivery. *J Control Release* **2007,** *121* (1-2), 64-73.

89.   Parveen, N.; Schonhoff, M., Swelling and Stability of Polyelectrolyte Multilayers in Ionic Liquid Solutions. *Macromolecules* **2013,** *46* (19), 7880-7888.

90.   Dobrynin, A. V., Electrostatic persistence length of semiflexible and flexible polyelectrolytes. *Macromolecules* **2005,** *38* (22), 9304-9314.

91.   Skolnick, J.; Fixman, M., Electrostatic Persistence Length of a Wormlike Polyelectrolyte. *Macromolecules* **1977,** *10* (5), 944-948.

92.   Chen, H.; Meisburger, S. P.; Pabit, S. A.; Sutton, J. L.; Webb, W. W.; Pollack, L., Ionic strength-dependent persistence lengths of single-stranded RNA and DNA. *Proc Natl Acad Sci U S A* **2012,** *109* (3), 799-804.

93.   Kovacevic, D.; van der Burgh, S.; de Keizer, A.; Stuart, M. A. C., Kinetics of formation and dissolution of weak polyelectrolyte multilayers: Role of salt and free polyions. *Langmuir* **2002,** *18* (14), 5607-5612.

94.   Netz, R. R.; Joanny, J. F., Adsorption of semiflexible polyelectrolytes on charged planar surfaces: Charge compensation, charge reversal, and multilayer formation. *Macromolecules* **1999,** *32* (26), 9013-9025.

95.   Mitra, A. K.; Davis, D. A.; Tomar, S.; Roy, L.; Gurler, H.; Xie, J.; Lantvit, D. D.; Cardenas, H.; Fang, F.; Liu, Y.; Loughran, E.; Yang, J.; Sharon Stack, M.; Emerson, R. E.; Cowden Dahl, K. D.; M, V. B.; Nephew, K. P.; Matei, D.; Burdette, J. E., In vivo tumor growth of high-grade serous ovarian cancer cell lines. *Gynecol Oncol* **2015,** *138* (2), 372-7.

96.   Day, A. J.; Sheehan, J. K., Hyaluronan: polysaccharide chaos to protein organisation. *Curr Opin Struct Biol* **2001,** *11* (5), 617-22.

97.   Atkins, E. D. T.; Meader, D.; Scott, J. E., Model for Hyaluronic-Acid Incorporating 4 Intramolecular

Hydrogen-Bonds. *Int J Biol Macromol* **1980,** *2* (5), 318-319.

98.   Morris, E. R.; Rees, D. A.; Welsh, E. J., Conformation and dynamic interactions in hyaluronate solutions. *J Mol Biol* **1980,** *138* (2), 383-400.

99.   Park, J. W.; Chakrabarti, B., Optical-Properties and Viscosity of Hyaluronic-Acid in Mixed-Solvents - Evidence of Conformational Transition. *Biopolymers* **1978,** *17* (5), 1323-1333.

Chapter 5. Developing theranostic layer-by-layer nanoparticles through clickable terminal layers

Layer-by-layer (LbL) nanoparticles (NPs) are hierarchically organized nanocomposites capable of incorporating multiple functional materials through sequential deposition steps. While the LbL process readily integrates charged functional polyelectrolytes, such as siRNA, there are limited options for materials that are neutral or poorly charged. Here, we describe the covalent attachment of functional biosensing and targeting peptides that would otherwise be incompatible with LbL assembly, thereby adding new diagnostic capabilities to pre-formed LbL NPs. We report the preparation of NPs that encapsulate a high weight percentage of siRNA to silence specific genes, but also carry a biosensing peptide on their surface that is cleaved into a synthetic urinary biomarker upon exposure to specific metalloproteases overexpressed by tumors. We show this nanotheranostic is able to mediate simultaneous gene therapy and noninvasive urinary-based diagnostics in vivo. Importantly, this biosensor reports back on a molecular signature characteristics to metastatic tumors and associated with poor prognosis – MMP9 protease overexpression. This work provides a modular nanotheranostic platform to both perturb and characterize tumors at the molecular level.

162

5.1. Introduction

Nanotheranostics refers to multifunctional nanotechnology capable of interweaving diagnostic and therapeutic utilities[1]. In addition to bulk tumor imaging, emerging nanotheranostics now aim to provide molecular and cellular information about the tumor, information that would allow for patient stratification and treatment personalization. LbL assembly provides a natural route towards multifunctional nanotheranostics because it introduces functional nanoscale polymer films onto colloidal substrates, such as drug-loadable and imaging nanoparticles[2]. It is no wonder that the LbL technique has already been extended towards the development of nanotheranostics that combine imaging with various therapies[3-5].

Nevertheless, the development of more advanced LbL nanotheranostics for the molecular or cellular characterization of tumors will require more sophisticated approaches. Beyond imaging, biosensing peptides have been developed that allow for urinary-based detection of molecular signatures of metastatic disease when attached to NPs[4, 6]. These peptides contain cleavage motifs specific to particular proteases, and when cleaved by the right protease a synthetic biomarker is released from the NP, which can later be detected in the urine. Such an approach provides both tumor detection and high-level molecular information about the protease environment, which is known to correlate with patient prognosis[7-9].

Integrating this biosensor peptide technology into the LbL platform would be a significant development towards advanced nanotheranostics. The LbL platform would be distinctly capable of incorporating small molecule drugs[10], therapeutic nucleic acids[11], imaging modalities[5], and molecular probes all within a discrete nanoparticle. The modularity of the approach also lends itself towards personalization to specific clinical contexts, which could themselves be inferred from the diagnostic/prognostic functionalities of these nanotheranostic devices.

However, integrating this class of functional peptides into LbL assemblies is not possible through standard LbL-adsorption techniques, due to a general insufficiency of charged groups on these peptides. Unfortunately, LbL NPs are not compatible with some of the reaction conditions needed for typical conjugation chemistries, such as N-hydroxysulfosuccinimide (sulfo-NHS) coupling. And because many LbL NPs take advantage of facile biopolymer incorporation, such as poly-

163

saccharides[12-14] and native polypeptides[15], their complex surface chemistries present additional challenges for conjugation techniques. To overcome this issue, we describe the optimization of copper(I)-catalyzed "click" conjugation of functional macromolecules onto pre-formed LbL liposomes. It is worth noting that pre-functionalizing the pPLD polymer prior to LbL assembly could be another approach towards developing these NPs. We opted against this approach for several reasons. First, the LbL method works best when layering using an excess of free polypeptide, so pre-functionalizing the pPLD would lead to significant losses in peptide and excessive materials costs. Second, it is unclear how the pre-functionalized pPLD would self-assemble onto the LbL particle. For example, it could layer in a way that buries at least some of the biosensor peptide in the film, making some peptides inaccessible to protease cleavage. Lastly, pre-functionalization of the pPLD would limit downstream modularity of the LbL-NP, which could be conjugated to additional biosensors and molecules depending on the particular biomedical application. Indeed, we demonstrate this modularity by also exploring a formulation that click-conjugates the cyclic tumor-targeting peptide iRGD, which has been shown to improve the functionality of this class of nanosensor[16].

While click chemistry techniques have been used in the past to build multilayered assemblies on planar[17-19] and microparticle substrates[20], or to later crosslink hydrogen-bonded assembled LbL films[21-22], limited efforts have been made to introduce this key technique to LbL NPs. By adopting click-conjugation to modify LbL-NPs, we provide a means to begin introducing functional macromolecules that are otherwise inaccessible via traditional LbL assembly. We demonstrate that this approach yields stable LbL NPs constructed from liposomal cores, siRNA and polypeptides. Using a model siRNA, we have shown that the resulting nanoparticles can silence gene expression in vivo to demonstrate their therapeutic utility, and can detect the MMP9 protease signature characteristic to a variety of metastatic diseases to demonstrate their diagnostic utility.

5.2. Results: Covalent attachment of biosensing peptides onto LbL NPs yields stable colloidal species

We use the biorthogonal copper-catalyzed azide alkyne cycloaddition to conjugate azide substrates onto propargyl-modified poly(L-aspartate) (pPLD) coated LbL-NPs. Because LbL-NPs are easily aggregated by the presence of salts[23], this method has the advantage over tradition amide bond formation reactions of requiring minimal buffering and higher reactivity at low reagent and catalyst concentrations, all of which reduce the ionic strength of reaction medium. The synthetic bulk conditions for LbL assembly were also optimized to generate particles in the presence of low ionic strength, as described in Chapter 4. While those studies were aimed at improving siRNA loading into the LbL-NP, we anticipated that LbL-NPs synthesized in the presence of salts would have improved compatibility with the solution conditions involved during downstream conjugation reactions.

To produce biosensor LbL NPs, we first synthesized click-compatible LbL-NPs through the sequential adsorption of poly(L-arginine), siRNA, poly(L-arginine) (PLR), and propargyl-modified poly(L-aspartate) (pPLD) onto an anionic liposomal core. We chose a liposomal

Figure 5.1. Click-chemistry compatible LbL nanoparticles were formed from liposomal cores, poly-L-arginine (PLR), siRNA, and propargyl-modified poly-L-aspartate (pPLD). The anionic liposomal core was sequentially coated with the charged polyelectrolytes. **a)** The steady growth of nanoparticle hydrodynamic diameter was observed during synthesis while maintaining a low polydispersity index. Z-average size (which is more sensitive to aggregates) and number average size (which is more representative of the NP population) are both included to provide a complete assessment of the NP size. **b)** The zeta potential conversion at each stage of the synthesis corresponds to the successful layering of each oppositely charged polyelectrolyte. **c)** Purification kinetics of the siRNA layer were used to determine overall siRNA loading. Dashed line represents siRNA introduced into the synthesis. **d)** Encapsulation efficiency of the siRNA was determined to be 37.4% and used to calculate a siRNA to lipid weight percent loading of 41%. Error bars represent standard deviation of triplicate measurements. Where error bars are shorter than the height of the data point symbol, they are omitted.

substrate due to their clinical precedence, ability to encapsulate both hydrophobic and hydrophilic drugs, tunable surface charge density, and compatibility with extrusion techniques that can

yield monodisperse particles of specific sizes[24-27]. The PLR coatings were used due to their well-documented ability to mediate transfection while avoiding nonspecific cytotoxicity[28-29]. The PLD outer layer was chosen to provide a strongly anionic surface that promotes colloidal stability and repels negatively charged serum proteins. Additionally, approximately 12% of the carboxylic side chains of the PLD were converted to propargyl groups to yield propargyl-modified PLD (pPLD) to allow for the downstream click-conjugation with biosensor peptides and other neutral macromolecules (synthetic details available in Appendix D). The nanoparticle size, uniformity and charge were tracked during the LbL synthesis (**Figure 5.1a-b**), and the collective data demonstrated the controlled growth (Z-average diameter of 95±1 nm to 124±3 nm, polydispersity index (PDI) below 0.2 throughout) and sequential charge reversal typical to successful LbL assembly.

The therapeutic capabilities of this nanotheranostic stem from the gene silencing capabilities of the incorporated siRNA, and the ability for the LbL NP to potently mediate gene silencing depends in part on the siRNA loading efficiency. We quantified the purification kinetics in order to determine the encapsulation efficiency of siRNA (**Figure 5.1c-d**). After siRNA deposition, permeate fractions were collected during tangential flow filtration and analyzed using a UV-spectrophotometer, indicating an encapsulation efficiency of 37.4%. The weight percent loading of siRNA to lipid was calculated to be 41%, and we attribute this high loading to judicious application of salts during LbL assembly as described in Chapter 4.

Having confirmed that the LbL-NPs possessed good size, charge, and siRNA loading, we used our modified conjugation conditions to click on various combinations of the MMP9 biosensor peptide, iRGD targeting peptide, and poly(ethylene glycol) (PEG) pendants (**Figure 5.2**). We initially use the PEG pendants in case the biosensor peptides, which are relatively hydrophobic, might destabilize the colloid. However, size and zeta characterization of the various formulations indicate the PEG is not necessary for stability (**Figure 5.2a-b**). As expected with the addition of a hydrophilic polymer brush layer, inclusion of PEG causes an increase in the hydrodynamic diameter (from 124±3 nm to 184±15 nm for the PEG/Sensor conjugated LbL NP and 175±4 nm for the PEG/Sensor/iRGD conjugated NP) and a moderate but statistically significant neutralization of zeta potential (from -50±6 mV to -30±1 mV for PEG/Sensor and -24±1 mV for PEG/Sensor/iRGD, p<0.0001 one-way ANOVA with the Dunnett post-hoc test).

Using our optimized solution conditions, LbL-NPs tolerated the click conjugation of the biosensor, iRGD, and PEG, yielding nanoparticles with mean Z-average hydrodynamic diameters ranging from 121 to 184 nm, PDIs ranging from 0.139 to 0.232, and zeta potentials ranging from -24 to -43 mV. To confirm the diagnostic utility is preserved in these NPs, biosensor-functionalized LbL-NPs were exposed to recombinant MMP9 to test the ability for the protease to cleave the reporter fragment off of the nanoparticle. The MMP9-digested particles were pelleted via centrifugation and the supernatant was analyzed for the peptide reporter fragment using enzyme-linked immunosorbent assay (ELISA) (**Figure 5.2c**). The results indicated that the biosensor is still accessible to the MMP9 protein, providing detectable peptide signal in the supernatant for both Sensor and Sensor/iRGD-functionalized LbL NPs.
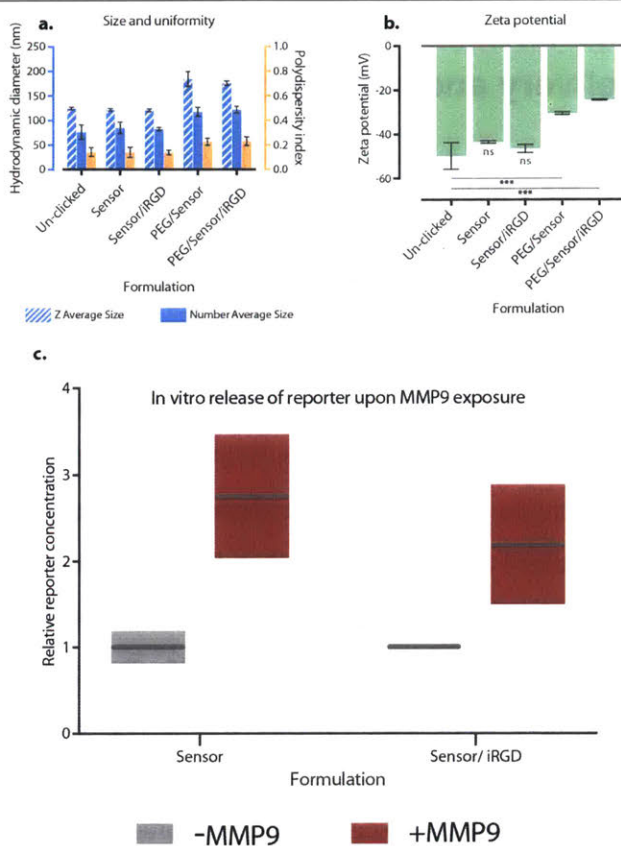
Figure 5.2. Click-functionalized LbL NPs remain stable and exhibit protease-responsive behavior. Various formulations of LbL NP were generated via covalent attachment of MMP9 biosensing peptide, iRGD targeting peptide, and PEG. **a)** The size an uniformity of all the click-functionalized LbL NP formulations were consistent with the un-clicked NP. PEGylated formulations exhibit a larger hydrodynamic diameter, potentially due to the increased hydrophilicity of these NPs. **b)** The zeta potential of the clicked LbL NPs remains strong enough to mediate electrosteric stability for the Sensor and Sensor/iRGD formulations. PEGylation causes a moderate but significant loss of charge. **c)** Biosensor LbL NPs were incubated in the preserve or absence of recombinant MMP9 protease, and afterwards were pelleted via centrifugation. The supernatant was collected and analyzed for the biomarker cleavage product using ELISA which indicated elevated peptide fragment in the MMP9-treated NPs. Error bars represent standard deviation, and statistical analysis of panel b uses one-way ANOVA with a Dunnett post-hoc test and alpha of 0.05.

5.3. Results: Peptide-functionalized LbL liposomes mediate gene delivery and urinary based diagnostics in vivo

We then assess the diagnostic capabilities of the biosensor LbL-NP across models of colorectal, pancreatic and ovarian cancer. After each model formed tumors, we systemically injected Sensor/PEG functionalized LbL-NPs (Lipo/PLR/siRNA/PLR/pPLD) to provide a dosage of biosensor peptide equivalent to 0.03 mg/kg. One hour after injection, the urine from the individual mice was collected and analyzed using ELISA. Tumor-free mice were also injected with biosensor LbL-NP as a control, and their urine was used to determine baseline peptide reporter fragment (PRF) concentrations in the urine. The results indicated a broad capability to detect significantly enriched PRF concentration in the urine of tumor-bearing mice relative to tumor-free mice (**Figure 5.3a-c**). These results indicate the in vivo diagnostic capabilities of the peptide biosensor are preserved after conjugation to LbL-NPs. Click conjugation of these reporter peptides can therefore facilitate the development of advanced LbL nanotheranostics capable of sensing molecular signatures, and potentially characterizing the tumor microenvironment at the molecular level all without the need of cumbersome imaging infrastructure.
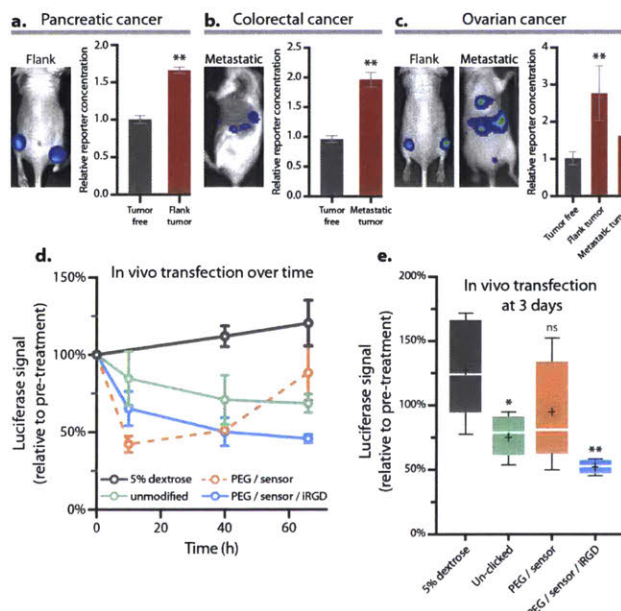
Figure 5.3. Addition of the biosensing peptide onto siRNA-loaded LbL liposomes yields a NP capable of simultaneous tumor detection and gene silencing. PEG/Sensor functionalized LbL liposomes were systemically administered to several models of cancer. Analysis of the urine of the mice one hour after injection indicates that the theranostic LbL NP yields significantly elevated levels of the peptide reporter fragment in the urine in **a)** pancreatic cancer flank model, **b)** a metastatic model of colorectal cancer, and **c)** a model of ovarian cancer. Significantly elevated marker levels were detects in the flank ovarian model, and report levels were elevated in the metastatic model. **d)** Theranostic LbL NPs were administered to the flank ovarian cancer model to provide a siRNA dosage of 0.5 mg/kg to silence the model gene luciferase in vivo. Bioluminescence levels were monitored over three days using an IVIS imaging device. **e)** All LbL NPs tested mediated gene silencing but the duration and intensity of the silencing differed based on the surface chemistry of the NP. Inclusion of the iRGD ligand improved silencing efficacy out to three days. On the other hand, PEGylation without a targeting ligand causes a more transient transfection, which by day 3 trends lower than controls but is not statistically significant (p=0.27). Error bars represent SEM, and statistical analysis of panels a and b use students t-tests, while panel c uses a one-way ANOVA with a Dunnett post-hoc test and alpha of 0.05. Panel e uses a one-way ANOVA with a Tukey post-hoc test and alpha of 0.05.

Having confirmed the diagnostic capabilities of the biosensor LbL-NP, we then demonstrate that these NPs retain their ability to deliver siRNA in a flank xenograft of ovarian cancer (**Figure 5.3e**). Biosensor LbL-NPs were prepared using siRNA against the luciferase reporter gene and click-conjugated with PEG/Sensor or PEG/Sensor/iRGD, and systemically administered to mice to provide an siRNA dosage of 0.5 mg/kg. Notably, under these conditions, the PEG/Sensor NP mediated good knockdown after a single dose, decreasing luciferase signal to 51±2% at day 2, comparable to the 50±9% signal observed from mice treated with the PEG/Sensor/iRGD formulation (**Appendix D Figure 2**). However, the effects of the PEG/Sensor NP dissipate quickly, leading to a rise in expression by the third day (88±17% luciferase signal, relative to pre-treatment). On the other hand, the iRGD NP is able to mediate a consistent and more durable knockdown – maintaining a decreasing luciferase expression of 50±9% and 46±3% at 2 and 3 days, respectively. We also compare the transfection ability of the non-clicked particle, and find that while it is able to mediate knockdown of the luciferase gene with a duration similar to the iRGD-formulation, it is an overall weaker transfection with a peak effect at 3 days with a 68±6% luciferase signal.

5.4. Results:Click-modification impacts LbL NP interaction with ovarian cancer cells and biodistribution in a metastatic model

To begin to address the potential contribution of iRGD to the in vivo transfection efficiency, we performed additional in vitro experiments to probe the impact of this ligand on NP-cell binding (**Figure 5.4**). Fluorescent biosensor LbL-NPs were generated using 100 nm polystyrene cores labeled with an infrared dye. These formulations did not involve an siRNA layer, but rather a PLR/pPLD bilayer that allowed us to probe the impact of the NP surface chemistry on its interaction with ovarian cancer cells. We explored the impact of Sensor, PEG/Sensor, iRGD/Sensor, and PEG/iRGD/Sensor conjugation on LbL-NPs using flow cytometry. OVCAR8 cells were incubated with NPs for 4 or 24 hours prior to analysis via flow cytometry, where shifts in the nanoparticle-associated fluorescence channel were quantified (**Figure 5.4a-b**).

PEGylation of the NPs appeared to correlate with increased percentage of cells gated as nanoparticle-positive at 4 hours, but this effect dissipates by 24 hours. Notably, quantification of NP-associated fluorescence in the nanoparticle-positive population indicates that PEGylation depressed NP uptake at both 4 and 24 hours (**Figure 5.4c-d**). However, this trend was only statistically significant at 24 hours in the absence of iRGD. Inclusion of the iRGD ligand in general led to moderate but significant increases in mean NP-associated fluorescence intensity at both 4 and 24 hours, with the most potent trends occurring in the non-PEGylated formulation. Interestingly, inclusion of the sensor appears to improve uptake of NPs compared to un-clicked LbL NP, though the effect is significantly depressed by 24 hours by inclusion of PEG. Overall, these results indicate moderate improvement in NP binding to ovarian cancer cells after inclusion of either the Sensor or iRGD, as well as a negative effect on binding due to PEGylation.

The biodistribution profile of the biosensor LbL-NP was then assessed after intraperitoneal (IP) administration in an orthotopic model of metastatic ovarian cancer, 72 hours after administration (**Figure 5**). We evaluated the IP administration route specifically for its emerging relevance in the management of ovarian cancer patients in the clinic[30-32]. The LbL-NPs for this study were constructed from Cy7-labeled liposomal cores coated with PLR/siRNA/PLR/pPLD, and the NPs were then further modified via inclusion of the Sensor or Sensor/iRGD. The mice were injected with dosages equivalent to 0.5mg siRNA/kg, and 72 hours later were sacrificed to determine

170
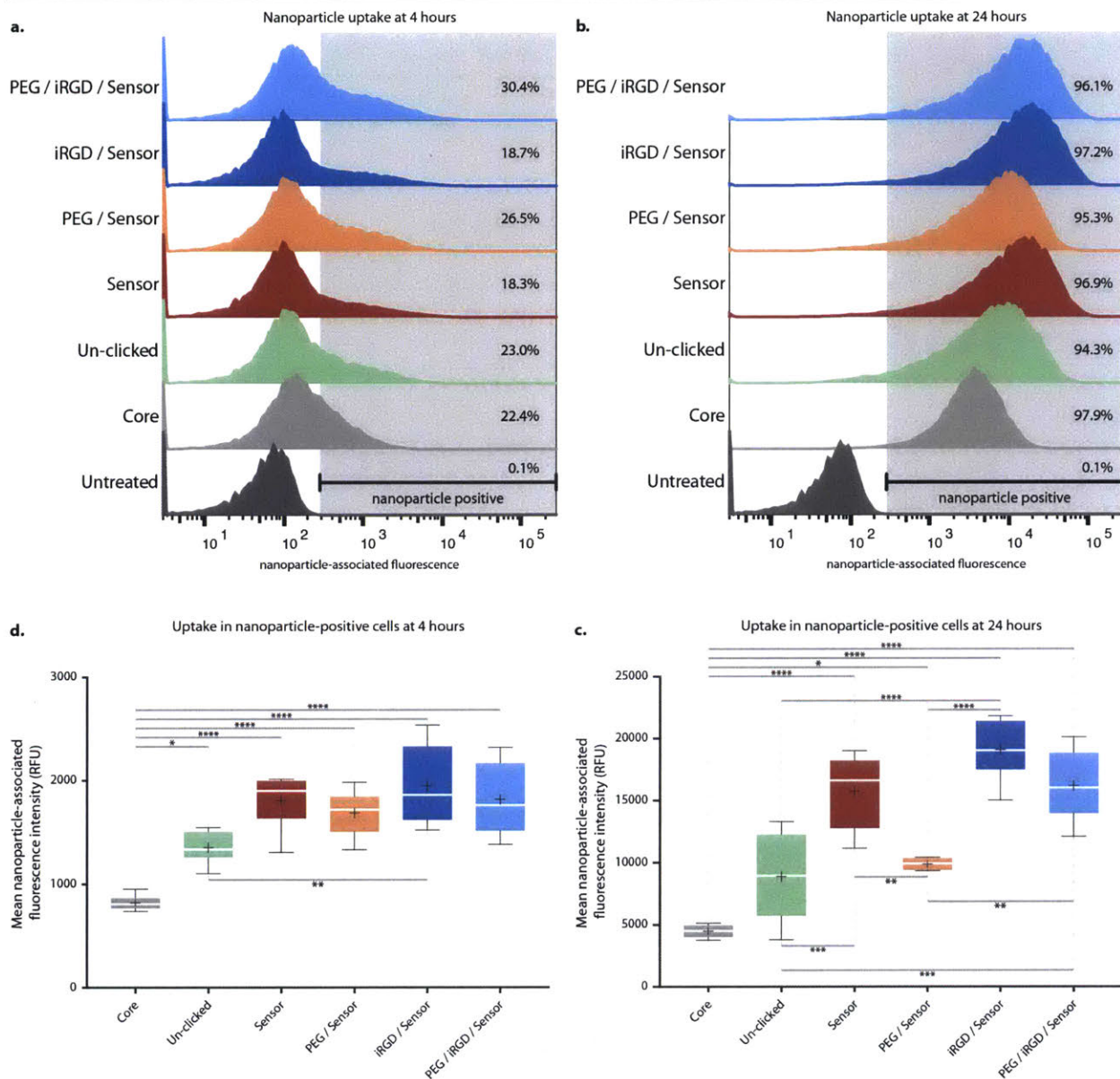
Figure 5.4. Addition of targeting ligands and biosensor peptides improves LbL NP binding to ovarian cancer cells. OVCAR8 ovarian cancer cells were incubated with the indicated formulations of LbL NP or unmodified core substrate and then analyzed using flow cytometry. **a)** At four hours, LbL NPs have bound to a portion of the cells. PEGylation appears to increase the fraction of cells identified as nanoparticle positive. **b)** But by 24 hours, there is little difference across the formulations in terms of the fraction of cells that are nanoparticle positive. **c)** Analysis of the mean nanoparticle-associated fluorescence intensity of the nanoparticle-positive cell population reveals differences in the amount of NP associated to OVCAR8 cells at 4 hours. All LbL NPs mediate significantly improved NP-cell binding relative to unmodified core particle. And inclusion of the iRGD peptide significantly improved uptake over the un-clicked formulation. PEGylation appears to depress uptake, and inclusion of the biosensing peptide appears to improve it, although these trends are not statistically significant. **d)** By 24 hours, these differences are magnified, and the negative influence of PEG on binding affinity becomes apparent with the significant decrease in RFU with the PEG/Sensor over the Sensor formulation. While it also depresses uptake of the iRGD formulation, the trend is not significant. Whiskers represent maximum and minimum values, and statistical analysis was carried out using a one-way ANOVA with Tukey's post-hoc test and an alpha of 0.05.

171
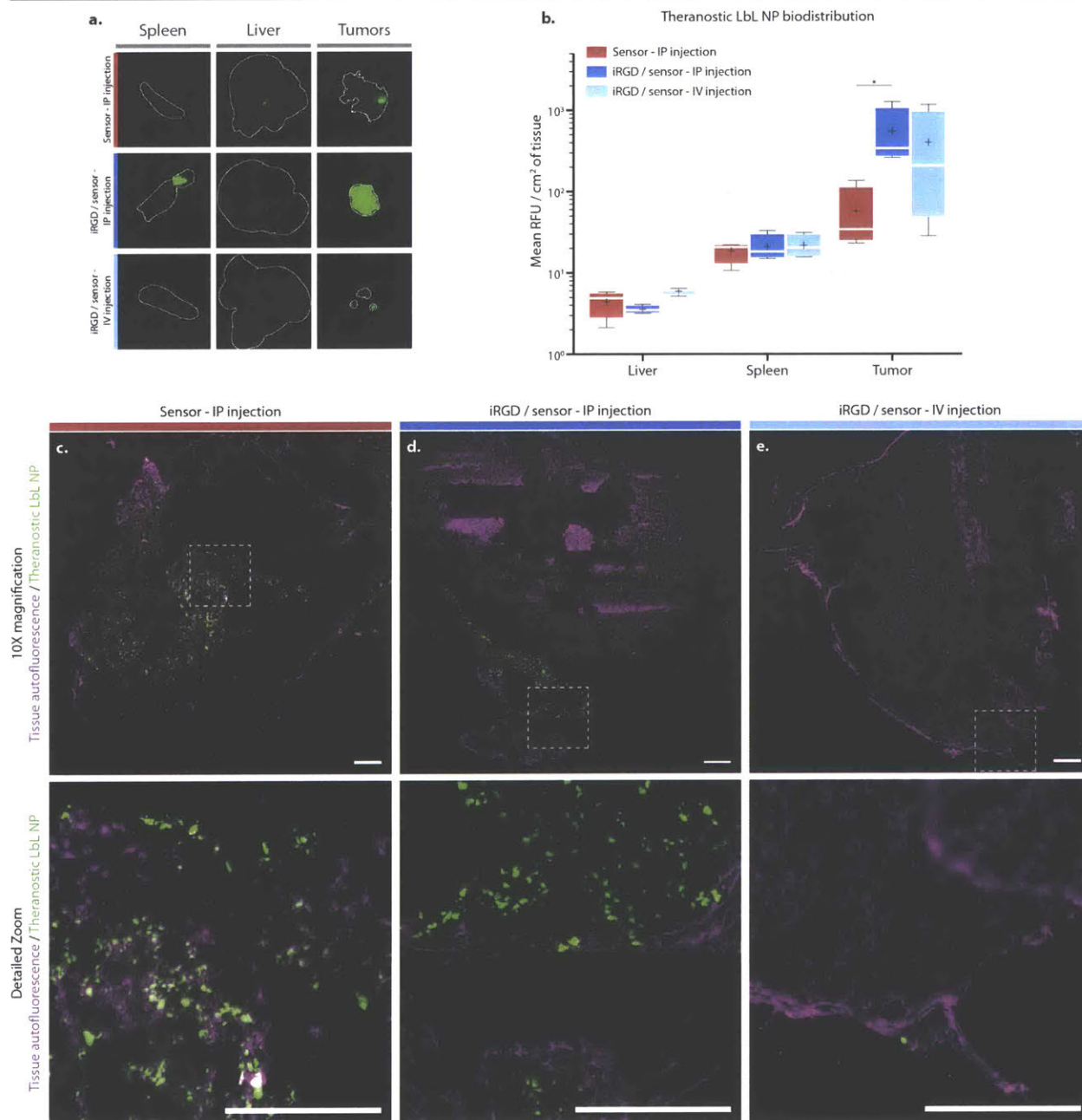
Figure 5.5. Theranostic LbL NP biodistribution in a metastatic model of ovarian cancer indicates good tumor targeting capabilities, especially using intraperitoneal (IP) administration. Mice bearing metastatic ovarian cancer were treated with either Sensor or iRGD/Sensor-functionalized LbL liposomes (Cy7-labeled liposome/PLR/siRNA/PLR/pPLD). **a)** Three days following administration of the NPs, the mice were sacrificed and their liver, spleen, and tumors were isolated for analysis using a fluorescent flatbed scanner (LiCor Odyssey). Tissue autofluorescence was used to generate a region-of-interest (indicated by the white outline) in which to quantify signal from the Cy7-labeled NPs. **b)** NP-associated RFU were normalized by the scanned tissue surface area. Liver and spleen accumulated fewer NPs relative to tumors in all cases. Inclusion of iRGD appears to positively impact accumulation. Intravenous administration of the NP leads to significant heterogeneity in biodistribution. Cryohistology was performed on tumor tissue and imaged using a fluorescent slide scanner to detect tissue autofluorescence (psuedocolored magenta) and nanoparticle signal (psuedocolored green). These representative images show good distribution of LbL liposomes through tumors when administered IP **(c-d)**, but considerably fewer NPs could be found in tumors from mice treated intravenously with LbL NPs **(e)**. Whiskers represent maximum and minimum values, and statistical analysis was carried out using a one-way ANOVA with Tukey's post-hoc test and an alpha of 0.05.

relative nanoparticle levels in the tumor, liver and spleen. The nanoparticle-associated fluorescence of the tissues was measured using a LiCor flatbed scanner, and we observed a significant partitioning of LbL NP into tumor tissue for IP-administered NPs (**Figure 5.5a-b, Appendix D Figure 3**). Relative to the NP signal in the tumor, very little was detected in the liver or the spleen for either Sensor or iRGD/Sensor NPs. Inclusion of the iRGD targeting ligand appears to have a beneficial effect on tumor accumulation, though the method of quantification used here is based on tissue surface area, and could be skewed by differences in tumor burden between the two treatment groups. But based on the qualitative results from the LiCor and histological analyses, it does appear that the two formulations accumulate in neoplastic tissue preferentially when administered IP. We also assessed the ability for the Sensor/iRGD formulation to traffic to the tumor following a systemic administration, and found that these particles do target tumor tissue but very heterogeneously, and do not accumulate to the extent observed in the IP-injected mice. Notably, the IV-administered LbL-NPs do not appear in the liver or spleen by this time, which we propose may indicate the particle is easily degraded and cleared from these organs. Cryohistology of the tumors indicates a good distribution of nanoparticles throughout the outer surface of the tumors for the IP-injected mice (**Figure 5.5c-d**), but very little NP signal could be found in the tumors from IV-injected mice (**Figure 5.5e**). Overall, these results indicate a good tumor-homing ability for these NPs, especially if administered IP, and that these NPs are likely biodegradable and easily cleared from filtration organs.

5.5. Conclusions and future work

Nanotheranostics provide the capability to monitor and characterize tumors and their response to therapies. This approach has tremendous potential for nanomedicine, as it can be used to identify patients who may benefit the most from particular treatments. Here, we described a method for incorporating an advanced diagnostic utility into the LbL nanoparticle platform using click chemistry conjugation techniques, specifically by demonstrating a 54±3% knockdown of a model gene and a sensitive detection of tumor burden in three models of cancer. This approach provides a highly modular system to which biosensing molecules, antifouling agents, and targeting ligands can be readily incorporated on top of an already highly-sophisticated drug carrier. The versatility of the base LbL nanoparticle also provides further layers of modularity in this system, such as the ability to use different siRNAs for a particular application as well as the option to include drugs or imaging modalities into the liposomal core. Importantly, this approach provides LbL nanoparticles the ability to characterize tumors at the molecular level, a functionality which could be employed to detect changes in specific protease levels in the future. Importantly, this platform demonstrated an ability to detect various forms of highly metastatic disease, including colorectal, pancreatic and ovarian cancer. These diseases are so deadly, in part, due to the inability to detect them at early stages, and thus biosensor-functionalized LbL-NPs may provide a route towards early diagnostic testing for these challenging malignancies.

Future work on this project aims to incorporate a therapeutic siRNA into the LbL NP design, specifically siRNA against the transcriptional regulator SMARCE1. This regulator governs the expression of a host of proteases, and correlates with poor prognosis for patients. Preliminary findings suggest that loss of SMARCE1 inhibits the metastatic potential of OVCAR8 cells in our model of metastatic disease, and thus the next steps in this project aim to target SMARCE1 using the theranostic LbL NP. Of interest is whether the loss of SMARCE1 leads to a decrease in protease levels, which would logically lead to a loss of biosensor activity. In this way, the theranostic LbL NP may be able to inform us of the success of siRNA delivery through noninvasive means, a major advancement in the development of devices that can simultaneously mediate and monitor a therapy.

5.6. Methods

Reagents: 1,2-distearoyl-sn-glycero-3-phospho-(1'-rac-glycerol) (sodium salt) (DSPG), 1,2-dio-leoyl-sn-glycero-3-phosphoethanolamine (DOPE) and cholesterol were purchased from Avanti. Sulfo-cyanine 3 and 7 NHS esters were purchased from Lumiprobe. Chloroform and methanol were purchased from TCI and Sigma, respectively. Whatman nuclepore polycarbonate hydrophilic membranes (400, 200, 100 and 50 nm sizes) were purchased from GE. All glassware was obtained from Chemglass. 50/15 mL Falcon tubes and 50/5/2 mL DNA loBind Eppendorf tubes were purchased from VWR. Infrared polysytrene latex microspheres (Fluospheres), locked nucleic acid siRNAs (Silencer Select), and 5 M bioreagent grade NaCl solution were obtained from Thermo Fisher Scientific. 1 M bioreagent-grade HEPES was purchased from Fisher Scientific. D02-E100-05-N and C02-E100-05-N tangential flow filtration filters were purchased from Spectrum Labs. Poly(L-arginine hydrochloride) (38.5 kDa) was purchased from Alamanda Polymers. Polystyrene semi-micro cuvettes for the Malvern Zetasizer were purchased from VWR and DTS1070 folded capillary cells were purchased directly from Malvern. Black 364 well plates for the Wyatt DLS were purchased directly from the Peterson (1957) Nanotechnology Core Facility.

OVCAR8 human ovarian cancer cells were obtained from ATCC. Luciferized and mCherry expressing lines were transfected with Cignal Lenti Reporter Control (Qiagen). Luciferized MC26 murine colorectal cancer cells were a kind gift from Kenneth Tanabe's lab at MGH. And D8-175 pancreatic cancer cells were derived from murine KPC tumors harvested in the lab of Tyler Jacks. Tissue culture plasticware (T75, T25, clear and white 96 well plates), trypsin EDTA, penicillin streptomycin, DMEM and RPMI 1640 media were purchased from Corning. Fetal bovine serum was purchased from Gibco. D-luciferin was purchased from Fisher Scientific.

All peptides were synthesized by CPC Scientific, Inc, with a purity of 90%. In vivo protease sensitive substrates were synthesized to contain a urinary reporter comprised of a protease resistant D-stereoisomer of Glutamate-Fibrinopeptide B with a fluorophore for urinary detection (Biotin-eGvndneeGffsarK(FAM)-gGPLGVRGKK(N3), smaller case indicates D-amino acids).
Tumor targeting and penetrating peptides (iRGD) were synthesized and cyclized iRGD: CRGD-KGPDC .

Polymer synthesis: β-benzyl-L-aspartate N-carboxyanhydride (BLD NCA) was prepared as de-

scribed previously[33]. Briefly, a suspension of β-benzyl-L-aspartate (25.0 g, 112 mmol), THF (200 mL), and triphosgene (30.0 g, 100 mmol) was stirred and sparged with a steady stream of argon under reflux for 2 h. Hexanes (700 mL) were added and the resulting precipitate was collected by vacuum filtration, washed 4 times with hexanes, dissolved in anhydrous THF (300 mL), and recrystallized under a layer of hexanes (700 mL). The solids were collected by vacuum filtration, washed 4 times with hexanes, and dried *in vacuo* to give white crystals (25.7 g, 103 mmol, 92%).

^{1}H NMR (400 MHz, $CDCl_3$) δ 7.47 – 7.30 (m, 5H), 6.13 (s, 1H), 5.19 (s, 2H), 4.60 (dd, J = 9.5, 2.4 Hz, 1H), 3.09 (dd, J = 17.7, 3.1 Hz, 1H), 2.84 (dd, J = 17.7, 9.6 Hz, 1H)

^{13}C{^{1}H} NMR (101 MHz, $CDCl_3$) δ 169.55 (s), 168.31 (s), 151.32 (s), 134.76 (s), 129.03 (s), 128.95 (s), 128.71 (s), 67.98 (s), 53.98 (s), 36.22 (s)

poly(β-benzyl-L-aspartate) (PBLD) was prepared as described previously[33]. Briefly, to a solution of BLD NCA (4.99 g, 20.1 mmol) and DMF (50 mL) was added hexylamine (26.5 µL, 0.201 mmol). The reaction was sparged with a steady stream of argon at RT for 48 h. The polymer was precipitated by addition of water and the resulting precipitate was collected by centrifugation, washed with water, and dried *in vacuo* to give a white powder (3.25 g, 15.8 mmol repeat units, 78.8%).

^{1}H NMR (400 MHz, DMSO): δ 8.37 – 7.98 (m, 1H), 7.51 – 7.08 (m, 5H), 5.21 – 4.92 (m, 2H), 4.74 – 4.48 (m, 1H), 2.98 – 2.54 (m, 2H).

poly(L-aspartate) (PLD) was prepared as described previously[34]. Briefly, to a solution of PBLD (2.42 g, 11.8 mmol repeat units) in trifluoroacetic acid (14.5 mL) was added dropwise 33 wt% HBr in AcOH (6.0 mL). The reaction was stirred for 1 hour after which diethyl ether was added. The precipitate was collected by filtration, washed with diethyl ether, and dried *in vacuo* to yield an off white powder (1.05 g, 9.12 mmol repeat units, 77.3%).

Poly(propargyl-L-asparate-*co*-L-aspartate) (pPLD)

PLD (1.05 g, 9.12 mmol) was added to a round bottom flask equipped with a stir bar and DMF (15 mL), water (2 mL), HOBt hydrate (ca. 20% water) (184 mg, 1.09 mmol), and propargylamine (130 µL, 3.19 mmol) were added. EDC (216 mg, 1.09 mmol) was added portion wise with stirring. After stirring for 24 h, the DMF was removed by extraction with diethyl ether and the pH of the aqueous phase was adjusted to 7 by addition of saturated sodium bicarbonate solution. The aqueous solution was dialyzed against saturated sodium chloride followed by deionized water (MWCO 1 kDa,

regenerated cellulose) and lyophilized to give a white powder (1.06 g). The degree of substitution was determined to be 12% by the ratio of protons on both sides of the side chain amide group. Signals from the amide protons, α-proton, and propargyl proton were visible, but dimished due to deuterium exchange. ^{1}H NMR (400 MHz, D_2O) δ 4.73 – 4.53 (m, 1H), 3.97 (s, 0.24H), 2.86 – 2.50 (m, 2H). Trace available in Supplemental Figure 1.

Tissue culture: OVCAR8 cells were maintained in RPMI media supplemented with 10% FBS. All other cell lines were kept in DMEM media supplemented with 10% FBS. All media was supplemented with 1% penicillin streptomycin. All cells were allowed to adhere/grow for 24 hours before treatment with nanoparticles in a Heracell Incubator (Thermo Fisher) at 37C and 5% CO_2. All cell lines were tested for mycoplasma contamination periodically, including immediately upon thawing, and over time when in culture, using the Lonza MycoAlert kit (Catalog #: LT07-318). Results were always negative for mycoplasma contamination.

Preparation of liposomes: Cholesterol and DOPE were dissolved in chloroform and DSPG was dissolved in a 65:35:8 mixture of chloroform, methanol and deionized water (milli-Q). Lipid mixtures composed of 66.7 mol% DSPG and 33.3% cholesterol were prepared in round bottom flasks (RBFs) (10 or 50 mL depending on scale), and for DSPG-formulations methanol was added dropwise until the solution cleared. For fluorescent liposomes, the formulation was 61.7% DSPG, 5% DOPE and 33.3% cholesterol. The lipid solution was evaporated using a BUCHI RotoVap system under heat (60C, water bath) until completely dry (<15 mBarr). A Branson sonicator bath was filled with reverse-osmosis water and heated until >70C, at which point the RBF with the lipid film was partially submerged in the bath and a volume of dH_2O was added to resuspend the lipid film to a 1 mg lipid/mL solution. The liposome solution was sonicated for roughly 1 minute and then transferred to an Avestin LiposoFast LF-50 liposome extruder. The extruder was connected to a Cole-Parmer Polystat Heated Recirculator Bath to maintain a temperature > 65C. The liposome solution was extruded through successively smaller nuclepore membranes until a 50-100 nm liposome was obtained. Generally, this required 1 pass through a stack of 2-3 400, 200, 100 and 50 nm membranes. Fluorescently labeled liposomes were prepared via standard NHS-coupling of Sulfo-cyanine NHS ester to DOPE head groups. Liposomes were characterized for size and zeta using the techniques outlined below.

Preparation of layer-by-layer nanoparticles: Nanoparticles were layered by adding an equal volume of nanoparticle solution (not exceeding 1 mg/mL) to an equal volume of polyelectrolyte solution under sonication (Branson bath sonicator, room temperature). The mixture was sonicated for roughly 5 seconds. The liposome to polyelectrolyte mass ratios used for each layer were 4:1 for the first PLR, 1:1 for the siRNA, 3:1 for the second PLR, and 1:1 for the pPLD layer. Polyelectrolyte solutions were always prepared in 50 mM HEPES and 40 mM NaCl. DNA loBind tubes are used as the mixing vessels for all experiments, to prevent nonspecific adsorption of siRNA and other polymers to the plasticware.

The layered particle is allowed to incubate at room temperature for 1 hour and is then purified using the tangential flow filtration method, as described previously[35]. Briefly, crude nanoparticle solution is connected to a Spectrum Labs KrosFlo II system using masterflex, Teflon-coated tubing. D02-E100-05-N (batch volume > 5 mL) or C02-E100-05-N (batch volume < 1 mL) 100 kDa filters were used to purify the particles until 5 volume-equivalents were collected in the permeate. For cationic layers, the TFF filter was pre-treated with a solution of free polycation (same concentration used for layering) in order to minimize nonspecific adsorption of particles to the membrane walls. Samples were run at 80 mL/min (size 16 tubing, used with D02-series filters) or 13 mL/min (size 13 tubing, used with C02-series filters). Once pure, the sample was either concentrated (by disconnecting the buffer reservoir) or recovered via reversing the direction of the peristaltic pump. For more complete yields, 1-3 mL of the appropriate buffer was run backwards through the tubing to recover any remaining particles. This process was repeated until the desired LbL formulation was obtained. Exchange buffer was always distilled water.

Click-chemistry conjugation onto LbL nanoparticles: To a suspension of nanoparticles (0.1-0.5 mg/mL) was added an equal volume of a freshly made solution consisting of copper(II) sulfate (48 µM), tris(3-hydroxypropyltriazolylmethyl)amine (0.75 mM), sensor peptide (11 µM), iRGD peptide (7.5 µM), and azido-PEG (12 µM) in deionized water. The solutions were mixed by pipette and a freshly made solution of sodium ascorbate (3.8 mM) in deionized water equal to the original volume of nanoparticle suspension was added and mixed by pipette. The reaction vessel was sealed and incubated in the dark for 12-24 hours, after which the particles were purified by tangential flow filtration.

Characterization of nanoparticles: Nanoparticle hydrodynamic size and polydispersity were measured using dynamic light scattering (Malvern ZS90 Particle Analyzer, λ = 633 nm, material/dispersant RI 1.590/1.330). Zeta potential measurements were also acquired with the Malvern ZS90, using laser Doppler electrophoresis. Nanoparticle solutions were diluted in milli-Q water in polystyrene semi-micro cuvettes (VWR) or DTS1070 folded capillary cuvettes (Malvern) to produce samples for characterization.

In vitro MMP9 cleavage study: NPs were incubated with recombinant proteases (MMP-9: Enzo Life Sciences) in a final volume of 100 uL in enzyme specific buffers (MMP9 buffer: 50 mM Tris, 150 mM NaCl, 5 mM CaCl2, 1uM ZnCl2, pH 7.5) at 37 °C for 1 hour. Final MMP-9 concentration was 100 nM. Afterwards, NPs were pelleted using centrifugation (30,000 RCF for 60 minutes) and the supernatant was collected.

Urinary reporter was detected using an ELISA. Mouse anti-fluorescein (GeneTex) were adsorbed to 96-well Bactiplates (Thermo) at concentrations of 0.4 µg/mL for 1 h in 1×PBS. Plates were then blocked for 1 h with 1× PBS with 2% (wt/vol) BSA (Sigma). Reporter standards were applied to blocked plates in two fold serial dilutions in 100 µL volume for 1 h to characterize assay linearity. To detect reporters, 100 µL of 0.4 µg/mL NeutrAvidin-HRP (Pierce) was applied for 1 h. Bound HRP was exposed with 50µL of Ultra-TMB (Pierce) for 1-5 min followed by quenching with 50 µL of 1 M HCl. Between each step, plates were washed three times with 1× PBS with 0.5% (vol/vol) Tween 20 (Sigma). Absorbance at 450 nm was measured, plotted against known reporter concentration, and used to generate a linear fit over the assay's linear absorbance region. Results were normalized relative to NPs that were not exposed to MMP9.

Animal Studies: All animal experiments were approved by the Massachusetts Institute of Technology Committee on Animal Care (CAC) and were conducted under the oversight of the Division of Comparative Medicine (DCM). Pancreatic cancer flank models were established with a subcutaneous injection of D5-175 cells to both flanks of Balb/C female mice. Flank ovarian cancer models were established by subcutaneous injection of a 1:1 mixture of OVCAR8 cells and matrigel into both flanks of female NCR nude mice. The metastatic model of ovarian cancer was established via intraperitoneal injection of OVCAR8 cells into female NCR nude mice. The metastatic model of colorectal cancer was established by direct injection of MC26 cells into the subsplenic capsule

of Balb/C female mice. After 90 seconds, the spleen was removed to prevent splenic tumors. For all models, tumor growth was monitored by measuring bioluminescence.

Determination of urinary diagnostic function: Theranostic LbL NPs were injected intravenously via the tailvein to dose tumor bearing or tumor free mice with 0.03 mg biosensor peptide / kg body weight. Mice were then held in specialized containers in order to collect urine. One hour after injection, urine was collected and analyzed via ELISA as described in the MMP9 cleavage study above.

Determination of in vivo gene silencing: Baseline bioluminescent signal was established for flank ovarian cancer cell models by injecting 300 uL of 15 mg/mL d-luciferin subcutaneously. Ten minutes after d-luciferin administration, mice were imaged using an IVIS whole-animal imaging device (PerkinElmer). After the initial imaging, mice were injected intravenously via the tailvein to dose 0.5 mg siRNA / kg body weight. Mice were then imaged for bioluminescent signal each day for three days following the same procedure used to establish the baseline signal. Data was analyzed using the LivingImage software to designate regions of interest over the tumors. Each tumor's luminescent signal was normalized relative to their pre-treatment baseline signal.

Biodistribution study: Metastatic ovarian cancer models were injected intraperitoneally or via the tailvein with Cy-t labeled theranostic LbL NP to dose 0.5 mg siRNA / kg body weight. After three days, mice were euthanized and their spleens, livers and tumors were isolated and imaged using a LiCor Odyssey flatbed fluorescence scanner at both the 700 and 800 nm wavelengths. The tissue autofluorescence image generated by the 700 nm channel was used to identify regions of interest for quantitation using FIJI's analyze particle functionality. Fluorescence intensity in the 800 nm channel was then calculated with regions of interest and normalized by the scanned surface area.

Cryohistology: Following imaging by the LiCor in the biodistribution study, tissues were embedded in OCT compound and flash frozen over liquid nitrogen. The cryomolds were maintained at -80C until they could be sectioned by the Koch Institute's histology core facility. The slides were then imaged using a Pannoramic Fluorescent Slide Scanner, using the TRITC, and Cy7 channels to detect tissue autofluorescence and nanoparticle signal, respectively.

Statistical Analysis: All statistical analysis was performed using GraphPad PRISM 7. For single comparisons, a student's t-test was used. For multiple comparison testing, one-way or two-way ANOVA was used in conjuction with the appropriate post-hoc test. Dunnett's test was used when comparing samples to a shared control group, whereas Tukey's test was used when comparing all groups. When relevant, normality tests were performed using a Shapiro-Wilk test.

5.7. References

1.   Chen, H.; Zhang, W.; Zhu, G.; Xie, J.; Chen, X., Rethinking cancer nanotheranostics. *Nat Rev Mater* **2017,** *2,* 17024.

2.   Correa, S.; Dreaden, E. C.; Gu, L.; Hammond, P. T., Engineering nanolayered particles for modular drug delivery. *J Control Release* **2016,** *240,* 364-386.

3.   Shi, X. Y.; Wang, S. H.; Swanson, S. D.; Ge, S.; Cao, Z. Y.; Van Antwerp, M. E.; Landmark, K. J.; Baker, J. R., Dendrimer-functionalized shell-crosslinked iron oxide nanoparticles for in-vivo magnetic resonance imaging of tumors. *Adv Mater* **2008,** *20* (9), 1671-+.

4.   Kim, J. S.; Rieter, W. J.; Taylor, K. M.; An, H.; Lin, W.; Lin, W., Self-assembled hybrid nanoparticles for cancer-specific multimodal imaging. *J Am Chem Soc* **2007,** *129* (29), 8962-3.

5.   Dang, X.; Gu, L.; Qi, J.; Correa, S.; Zhang, G.; Belcher, A. M.; Hammond, P. T., Layer-by-layer assembled fluorescent probes in the second near-infrared window for systemic delivery and detection of ovarian cancer. *Proc Natl Acad Sci U S A* **2016,** *113* (19), 5179-84.

6.   Warren, A. D.; Kwong, G. A.; Wood, D. K.; Lin, K. Y.; Bhatia, S. N., Point-of-care diagnostics for noncommunicable diseases using synthetic urinary biomarkers and paper microfluidics. *P Natl Acad Sci USA* **2014,** *111* (10), 3671-3676.

7.   Pellikainen, J. M.; Ropponen, K. M.; Kataja, V. V.; Kellokoski, J. K.; Eskelinen, M. J.; Kosma, V.-M., Expression of Matrix Metalloproteinase (MMP)-2 and MMP-9 in Breast Cancer with a Special Reference to Activator Protein-2, HER2, and Prognosis. *Clinical Cancer Research* **2004,** *10* (22), 7621.

8.   Wu, Z. S.; Wu, Q.; Yang, J. H.; Wang, H. Q.; Ding, X. D.; Yang, F.; Xu, X. C., Prognostic significance of MMP-9 and TIMP-1 serum and tissue expression in breast cancer. *Int J Cancer* **2008,** *122* (9), 2050-6.

9.   Sier, C. F. M.; Kubben, F. J. G. M.; Ganesh, S.; Heerding, M. M.; Griffioen, G.; Hanemaaijer, R.; vanKrieken, J. H. J. M.; Lamers, C. B. H. W.; Verspaget, H. W., Tissue levels of matrix metalloproteinases MMP-2 and MMP-9 are related to the overall survival of patients with gastric carcinoma. *British Journal of Cancer* **1996,** *74* (3), 413-417.

10.   Dreaden, E. C.; Kong, Y. W.; Morton, S. W.; Correa, S.; Choi, K. Y.; Shopsowitz, K. E.; Renggli, K.; Drapkin, R.; Yaffe, M. B.; Hammond, P. T., Tumor-Targeted Synergistic Blockade of MAPK and PI3K from a Layer-by-Layer Nanoparticle. *Clin Cancer Res* **2015,** *21* (19), 4410-9.

11.   Gu, L.; Deng, Z. J.; Roy, S.; Hammond, P. T., A Combination RNAi-Chemotherapy Layer-by-Layer Nanoparticle for Systemic Targeting of KRAS/P53 with Cisplatin to Treat Non-Small Cell Lung Cancer. *Clin Cancer Res* **2017,** *23* (23), 7312-7323.

12.   Dreaden, E. C.; Morton, S. W.; Shopsowitz, K. E.; Choi, J. H.; Deng, Z. J.; Cho, N. J.; Hammond, P. T., Bimodal tumor-targeting from microenvironment responsive hyaluronan layer-by-layer (LbL) nanoparticles. *ACS Nano* **2014,** *8* (8), 8374-82.

13.   Lee, M. Y.; Park, S. J.; Park, K.; Kim, K. S.; Lee, H.; Hahn, S. K., Target-specific gene silencing of layer-by-layer assembled gold-cysteamine/siRNA/PEI/HA nanocomplex. *ACS Nano* **2011,** *5* (8), 6138-47.

14.   Poon, Z.; Lee, J. B.; Morton, S. W.; Hammond, P. T., Controlling in vivo stability and biodistribution in electrostatically assembled nanoparticles for systemic delivery. *Nano Lett* **2011,** *11* (5), 2096-103.

15.   Ramasamy, T.; Haidar, Z. S.; Tran, T. H.; Choi, J. Y.; Jeong, J. H.; Shin, B. S.; Choi, H. G.; Yong, C. S.; Kim, J. O., Layer-by-layer assembly of liposomal nanoparticles with PEGylated polyelectrolytes enhances systemic delivery of multiple anticancer drugs. *Acta Biomater* **2014,** *10* (12), 5116-5127.

16.   Kwon, E. J.; Dudani, J. S.; Bhatia, S. N., Ultrasensitive tumour-penetrating nanosensors of protease activity. *Nat Biomed Eng* **2017,** *1* (4).

17.   Bergbreiter, D. E.; Chance, B. S., "Click"-based covalent layer-by-layer assembly on polyethylene using water-soluble polymeric reagents. *Macromolecules* **2007,** *40* (15), 5337-5343.

18.   Such, G. K.; Quinn, J. F.; Quinn, A.; Tjipto, E.; Caruso, F., Assembly of ultrathin polymer multilayer films by click chemistry. *J Am Chem Soc* **2006,** *128* (29), 9318-9.

19.   De Geest, B. G.; Van Camp, W.; Du Prez, F. E.; De Smedt, S. C.; Demeester, J.; Hennink, W. E., Degradable Multilayer Films and Hollow Capsules via a 'Click' Strategy. *Macromol. Rapid Commun.* **2008,** *29* (12–13), 1111-1118.

20.   Such, G. K.; Tjipto, E.; Postma, A.; Johnston, A. P.; Caruso, F., Ultrathin, responsive polymer click capsules. *Nano Lett* **2007,** *7* (6), 1706-10.

21.   Kinnane, C. R.; Such, G. K.; Antequera-Garcia, G.; Yan, Y.; Dodds, S. J.; Liz-Marzan, L. M.; Caruso, F., Low-fouling poly(N-vinyl pyrrolidone) capsules with engineered degradable properties. *Biomacromolecules* **2009,** *10* (10), 2839-46.

22.   Leung, M. K.; Such, G. K.; Johnston, A. P.; Biswas, D. P.; Zhu, Z.; Yan, Y.; Lutz, J. F.; Caruso, F., Assembly and degradation of low-fouling click-functionalized poly(ethylene glycol)-based multilayer films and capsules. *Small* **2011,** *7* (8), 1075-85.

23.   Schneider, G.; Decher, G., Functional core/shell nanoparticles via layer-by-layer assembly. investigation of the experimental parameters for controlling particle aggregation and for enhancing dispersion stability. *Langmuir* **2008,** *24* (5), 1778-89.

24.   Torchilin, V. P., Recent advances with liposomes as pharmaceutical carriers. *Nat Rev Drug Discov* **2005,** *4* (2), 145-60.

25.   Akbarzadeh, A.; Rezaei-Sadabady, R.; Davaran, S.; Joo, S. W.; Zarghami, N.; Hanifehpour, Y.; Samiei, M.; Kouhi, M.; Nejati-Koshki, K., Liposome: classification, preparation, and applications. *Nanoscale Res Lett* **2013,** *8* (1), 102.

26.   Levchenko, T. S.; Rammohan, R.; Lukyanov, A. N.; Whiteman, K. R.; Torchilin, V. P., Liposome clearance in mice: the effect of a separate and combined presence of surface charge and polymer coating. *Int J Pharm* **2002,** *240* (1-2), 95-102.

27.   Miller, C. R.; Bondurant, B.; McLean, S. D.; McGovern, K. A.; O'Brien, D. F., Liposome-cell interactions in vitro: effect of liposome surface charge on the binding and endocytosis of conventional and sterically stabilized liposomes. *Biochemistry-Us* **1998,** *37* (37), 12875-83.

28.   Deng, Z. J.; Morton, S. W.; Bonner, D. K.; Gu, L.; Ow, H.; Hammond, P. T., A plug-and-play ratiometric pH-sensing nanoprobe for high-throughput investigation of endosomal escape. *Biomaterials* **2015,** *51*, 250-256.

29.   Zhang, C.; Tang, N.; Liu, X.; Liang, W.; Xu, W.; Torchilin, V. P., siRNA-containing liposomes modified with polyarginine effectively silence the targeted gene. *J Control Release* **2006,** *112* (2), 229-39.

30.   Wright, A. A.; Cronin, A.; Milne, D. E.; Bookman, M. A.; Burger, R. A.; Cohn, D. E.; Cristea, M. C.; Griggs, J. J.; Keating, N. L.; Levenback, C. F.; Mantia-Smaldone, G.; Matulonis, U. A.; Meyer, L. A.; Niland, J. C.; Weeks, J. C.; O'Malley, D. M., Use and Effectiveness of Intraperitoneal Chemotherapy for Treatment of Ovarian Cancer. *J Clin Oncol* **2015,** *33* (26), 2841-7.

31.   van Driel, W. J.; Koole, S. N.; Sikorska, K.; Schagen van Leeuwen, J. H.; Schreuder, H. W. R.; Hermans, R. H. M.; de Hingh, I.; van der Velden, J.; Arts, H. J.; Massuger, L.; Aalbers, A. G. J.; Verwaal, V. J.; Kieffer, J. M.; Van de Vijver, K. K.; van Tinteren, H.; Aaronson, N. K.; Sonke, G. S., Hyperthermic Intraperitoneal Chemotherapy in Ovarian Cancer. *N Engl J Med* **2018,** *378* (3), 230-240.

32.   Narod, S., Can advanced-stage ovarian cancer be cured? *Nat Rev Clin Oncol* **2016,** *13* (4), 255-61.

33.   Li, J.; Wang, W.; He, Y.; Li, Y.; Yan, E. Z.; Zhang, K.; Irvine, D. J.; Hammond, P. T., Structurally Programmed Assembly of Translation Initiation Nanoplex for Superior mRNA Delivery. *ACS Nano* **2017,** *11* (3), 2531-2544.

34.   Wang, W.; Hammond, P. T., Hydrolysis resistant functional polypeptide scaffold for biomaterials. *Polymer Chemistry* **2018,** *9* (3), 346-351.

35.   Correa, S.; Choi, K. Y.; Dreaden, E. C.; Renggli, K.; Shi, A.; Gu, L.; Shopsowitz, K. E.; Quadir, M. A.; Ben-Akiva, E.; Hammond, P. T., Highly scalable, closed-loop synthesis of drug-loaded, layer-by-layer nanoparticles. *Adv Funct Mater* **2016,** *26* (7), 991-1003.

Chapter 6. Summary and conclusions

Layer-by-layer (LbL) assembly is a flexible and versatile technique for fabricating multifunctional nanomaterials. It is uniquely capable of integrating the benefits of traditional colloidal drug carriers with the properties of numerous functional polymers to create sophisticated nanocomposites. The parameter space available to this technique is expansive, especially since most colloids of interest (e.g., liposomes, gold, mesoporous silica and PLGA cores) can be easily modified to become charged templates for LbL assembly. And beyond the core, there are a tremendous number of polyelectrolytes suitable for adsorption into LbL films. Other critical properties of LbL NPs can also be tuned, including polymer molecular weight, core template size, and synthetic solution conditions. What we are left with is a platform with remarkable potential and an expansive frontier for continued research.

To harness this potential, we optimized the fabrication process for LbL NPs. First, we leveraged modern tangential flow filtration (TFF) techniques to develop a higher throughput synthetic approach. We used TFF to handle the cumbersome interlayer purification steps required to synthesize diverse LbL NPs. This approach was broadly compatible with various colloidal templates as small as 40 nm in size, including liposomes, mesoporous silica, and latex nanoparticles. We fabricated LbL NPs featuring layers of synthetic polymers, native polypeptides, polysaccharides and nucleic acids. And importantly, we reported some of the first systematic studies looking at long-term refrigerated and lyophilized storage of LbL NPs, including the shelf life of LbL-modified doxorubicin liposomes.

These improvements in scale and production made it feasible for us to study the role of diverse surface chemistries on nanoparticle interactions with ovarian cancer cells. Using a library of ten different surface chemistries, we systematically compared LbL NP binding affinity to ovarian cancer cells. The library spanned the gamut from simple synthetic polymers (e.g., polyacrylate) to highly complex biopolymers (e.g., heparin sulfate). LbL nanoparticles terminated with carboxylated layers showed a fascinating ability to bind preferentially to ovarian cancer cells, a trait not shared with LbL NPs terminated with sulfated species. Remarkably, this trait was not even shared with the carboxy-modified latex nanoparticle that served as the template for the LbL library. This suggests a unique role for the LbL film in mediating this high-affinity interaction. These trends persisted in a metastatic model of ovarian cancer. We found that administrating these particles via intraperitoneal injection provided a highly selective trafficking of NPs to ovarian tumors in vivo.

While overall trends in binding affinity and biodistribution corresponded well with surface chemistry family (e.g., carboxylated vs sulfated LbL NPs), follow-up studies with high-performing LbL formulations revealed surprisingly different subcellular trafficking patterns among carboxylated LbL NPs. Depending on the terminal layer, these nanoparticles were either readily internalized or exhibited unique surface-bound

morphologies, even at late time points. Studies into each formulation's engagement with specific uptake mechanisms also revealed diversity in dependence on key pathways, including cholesterol and caveolae-mediated uptake.

These unique trafficking patterns could be leveraged to develop nanoparticles capable of mediating specific functions. We demonstrated this by developing a new kind of nanotheranostic device that takes advantage of a poly-L-aspartate-based LbL coating. This theranostic NP needed to deliver siRNA into the cytoplasm of ovarian cancer cells, and also facilitate interactions with extracellular proteases in order to trigger release of a urinary biomarker. The poly-L-aspartate coating, with its ability to mediate both significant internal and external localization in ovarian cancer cells, was a natural choice for this nanotheranostic. The availability of carboxyl groups also allowed us to modify the polymer to include click-compatible propargyl groups – thus allowing attachment of charge-neutral, protease-sensing and tumor-targeting peptides onto the LbL NP's surface.

The specific biomedical goals of the theranostic NP formulation demanded the development of a rigorous synthetic strategy. In order to mediate gene silencing, we needed to reliably form LbL films containing a high content of siRNA. Our LbL NP also needed to be compatible with ionic strengths used during the click conjugation of functional peptides to particle surface. To optimize our synthesis, we performed a systematic study of the role of solution conditions in the fabrication of these nanoparticles, and obtained some of the most comprehensive experimental data reported concerning the impact of salts on colloidal LbL assembly. We ultimately identified an approach that provided robust synthesis of LbL liposomes loaded with a high weight percentage of siRNA to lipid (on average 30%). This strategy directly facilitated the preparation of our theranostic LbL liposome that could mediate gene delivery in a murine model of ovarian cancer, and also detect tumors in pancreatic, colorectal and ovarian cancer models.

This work begins to map the expansive frontier of layer-by-layer nanotechnology. It lays the groundwork for scaling up production to probe multiple fundamental parameters simultaneously. It begins to define the role and importance of solution conditions in colloidal LbL assembly in a systematic way, and indicates areas where continued research is needed. It shows how a methodical study using library-based approaches can identify promising new LbL NP formulations, and how those formulations can be advanced towards specific innovative biomedical applications, such as nanotheranostics. The introduction of click-chemistry compatible handles on the surface of LbL NPs also opens the door for integrating LbL technology with materials that previously were incompatible with the technique, such as charge-neutral peptides and macromolecules.

Future work in this area will benefit from continued efforts to streamline, and hopefully automate, the fabrication of LbL NPs – potentially even the elaboration of good

185

manufacturing practice (GMP)-compliant synthetic methods. This will improve the throughput and scalability of LbL NPs, and thus facilitate more ambitious library-based biomaterials studies. In this way, more advanced and comprehensive exploration of key parameters such as surface chemistry, film composition, swelling behavior, isoelectric point, size, shape, and stimuli-responsive properties can be evaluated. Continued fundamental studies into the role of solution condition will be vital, not only for maintaining consistent and reproducible methodologies but also for developing techniques to tune loading of therapeutic polyelectrolytes and film composition. Additional studies also are needed to gauge the impact of synthetic solution conditions on downstream properties, such as nanoparticle stability, shelf life, swelling behavior, drug release and interactions with biological interfaces. There remains extensive work and opportunity to explore this exciting frontier in nanotechnology, including areas involving process engineering, fundamental materials science and applications-based research. And as this work demonstrates, improving the manufacturing of these nanomaterials facilitates the design and implementation of systematic studies needed to unlock the structure-function relationships that govern drug delivery.

Chapter 7. Funding

Chapter 8. Appendices

Contents

Appendix A

Appendix A.

Supporting information for Chapter 2: *New Methods for LbL synthesis* is provided here.

Appendix A Figures
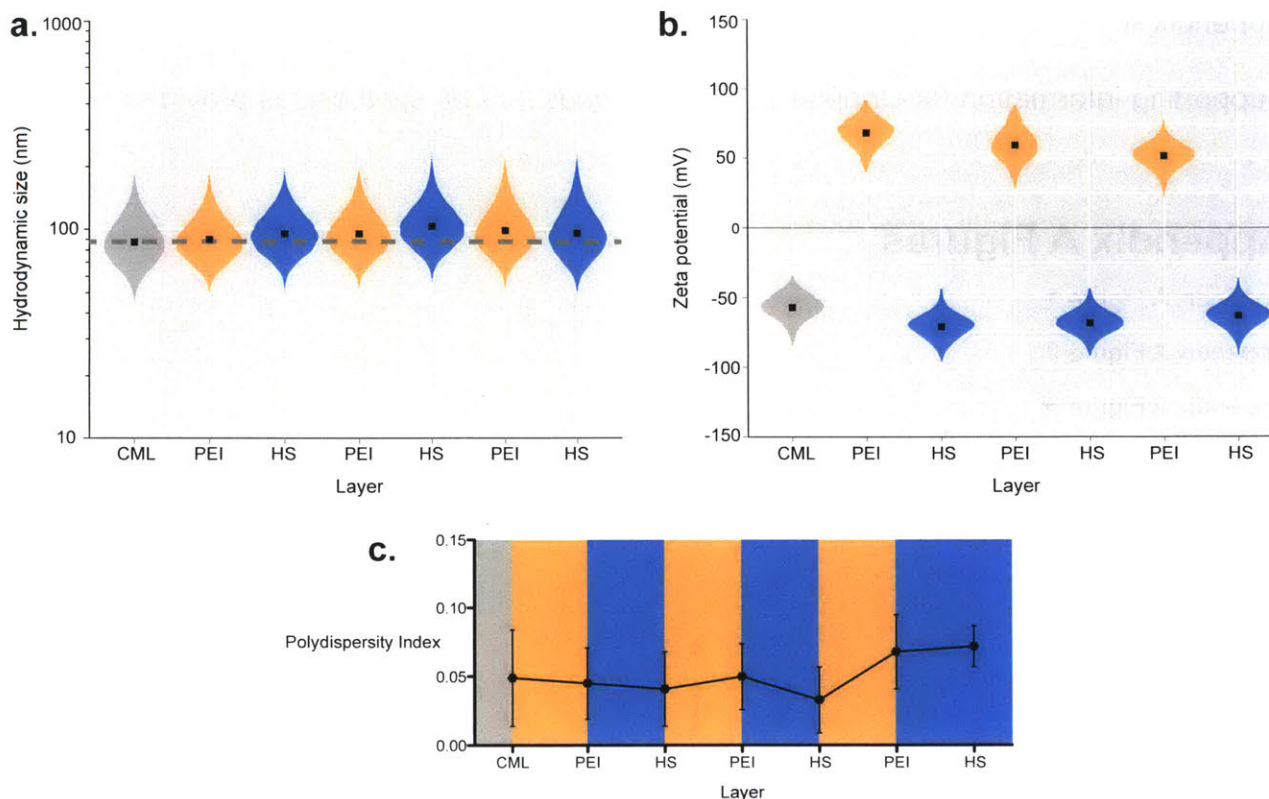
Appendix A Figure 1. Solid-core LbL particles were prepared by coating 100 nm, carboxy-modified latex particles with three bilayers of polyethylenimine and heparin sulfate (100CML-[PEI/HS]$_3$). This formulation was prepared using the TFF-assisted protocol. **(a)** We tracked the hydrodynamic size using dynamic light scattering and plotted the particle size distribution on a violin plot to demonstrate controlled growth. Violin plots display the estimated kernel density of the size or charge distribution, and allow the visualization of population-wide evolution of LbL nanoparticle characteristics during synthesis. The black squares denote the mean hydrodynamic size for each layer. **(b)** The zeta potential reversal at each stage of the layering process confirms successful LbL assembly. This was tracked with laser Doppler electrophoresis, and the charge distributions were plotted as a violin plot. The blacks squares denote the mean zeta potential for each layer. **(c)** The polydispersity index was measured by dynamic light scattering, and remained small throughout LbL assembly indicating good uniformity. Error represents SD of three technical replicates. Gray denotes latex core, orange denotes PEI layers, and dark blue denotes HS layers.
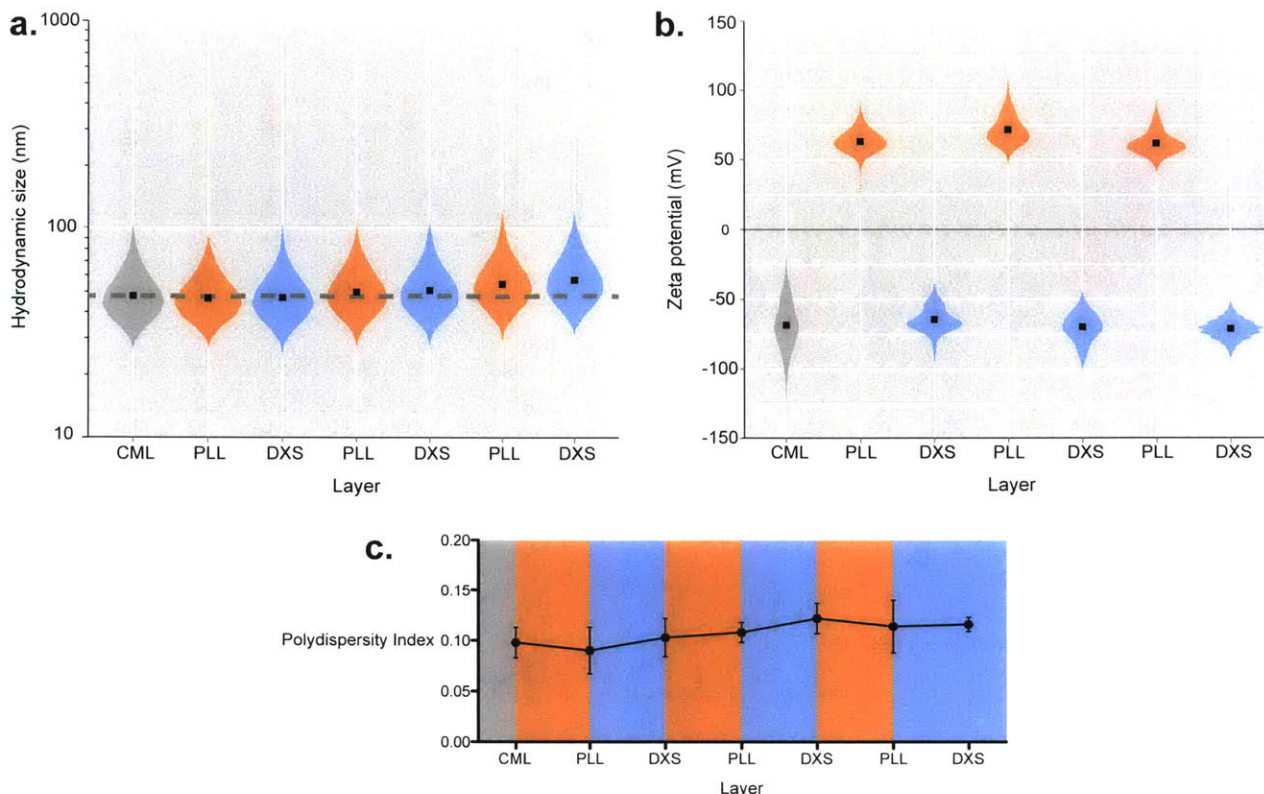
Appendix A Figure 2. Solid-core LbL particles were prepared by coating 40 nm, carboxy-modified latex particles with three bilayers of poly(L-lysine) and dextran sulfate (40CML-[PLL/DXS]$_3$). This formulation was prepared using the TFF-assisted protocol to demonstrate compatibility with smaller LbL substrates. **(a)** We tracked the hydrodynamic size using dynamic light scattering and plotted the particle size distribution on a violin plot to demonstrate controlled growth. Violin plots display the estimated kernel density of the size or charge distribution, and allow the visualization of population-wide evolution of LbL nanoparticle characteristics during synthesis. The black squares denote the mean hydrodynamic size for each layer. **(b)** The zeta potential reversal at each stage of the layering process confirms successful LbL assembly. This was tracked with laser Doppler electrophoresis, and the charge distributions were plotted as a violin plot. The blacks squares denote the mean zeta potential for each layer. **(c)** The polydispersity index was measured by dynamic light scattering, and remained small throughout LbL assembly indicating good uniformity. Error represents SD of three technical replicates. Gray denotes latex core, orange denotes PLL layers, and light blue denotes DXS layers.
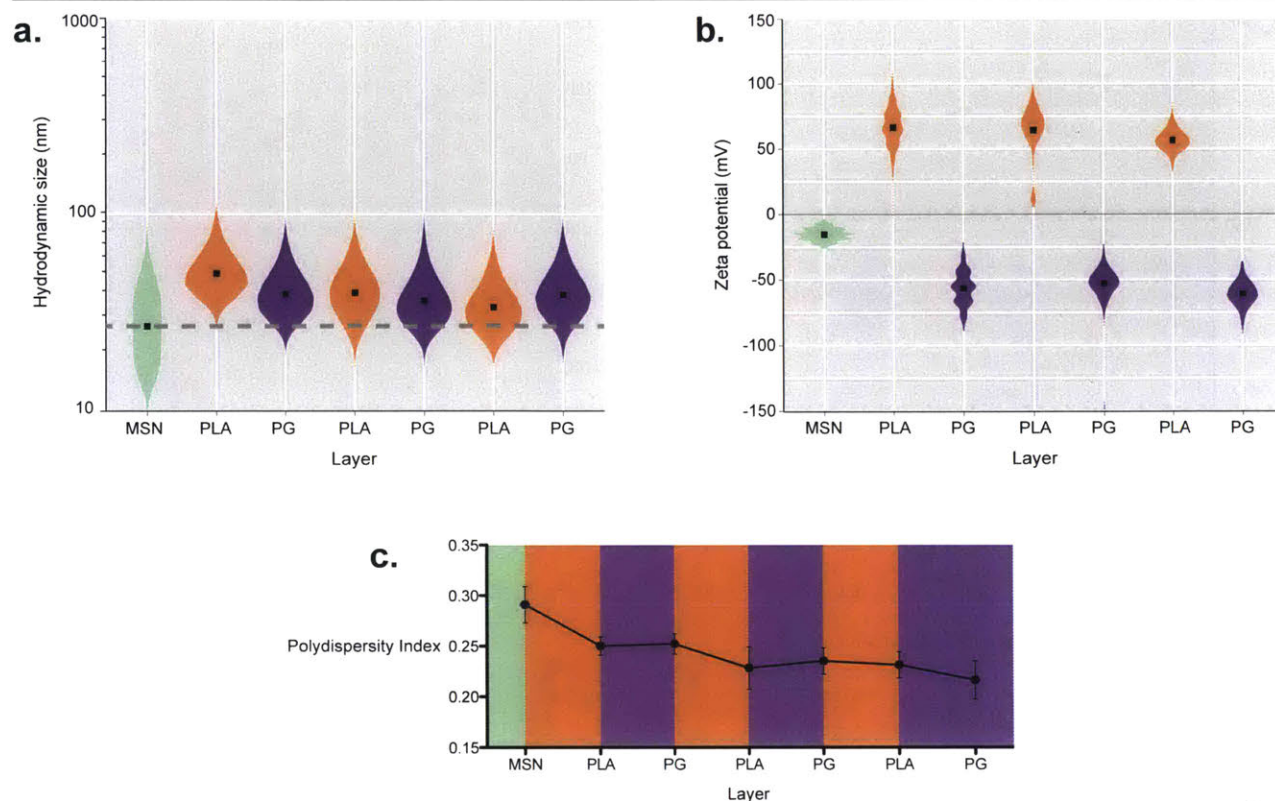
Appendix A Figure 3. Mesoporous-core LbL particles were prepared by coating 50 nm, mesoporous silica nanoparticles with three bilayers of poly(L-arginine) and poly(L-glutamic acid) (50MSN-[PLL/DXS]₃). This formulation was prepared using the TFF-assisted protocol to demonstrate compatibility with a solid, drug-loadable substrate. **(a)** We tracked the hydrodynamic size using dynamic light scattering and plotted the particle size distribution on a violin plot to demonstrate controlled growth. Violin plots display the estimated kernel density of the size or charge distribution, and allow the visualization of population-wide evolution of LbL nanoparticle characteristics during synthesis. The black squares denote the mean hydrodynamic size for each layer. We observed improvement in the size distribution during LbL modification which maybe due to the introduction of stronger electrostatic stabilization thanks to the polymer coating. The initial increase in size at the first layer is thought to be the generation of a relatively thick "fuzzy" polymer surface, which is then compacted by deposition of the next layer. **(b)** The zeta potential reversal at each stage of the layering process confirms successful LbL assembly. This was tracked with laser Doppler electrophoresis, and the charge distributions were plotted as a violin plot. The blacks squares denote the mean zeta potential for each layer. The weak charge on the initial MSN substrate led to relatively broader and less uniform charge distributions for the earlier layers, which eventually gives way to more uniform, tight charge distribution by layer 4. **(c)** The polydispersity index was measured by dynamic light scattering, and decreased throughout LbL assembly indicating improving uniformity. This is consistent with the observations made in the shape of the size distribution. Error represents SD of three technical replicates. Green denotes mesoporous silica core, orange denotes PLA layers, and purple denotes PG layers.
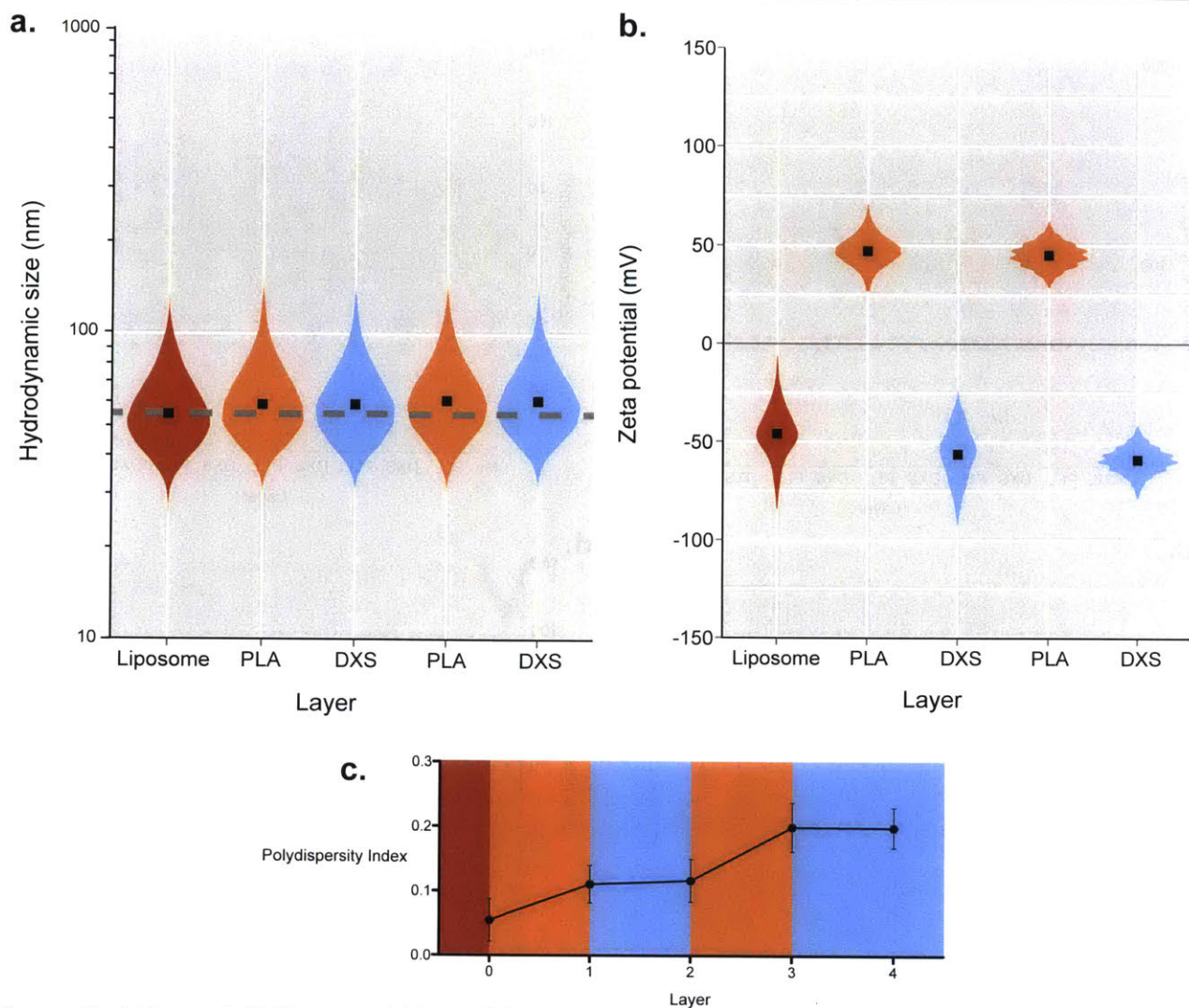
Appendix A Figure 4. Hollow-core LbL particles were prepared by coating 70 nm, doxorubicin-loaded liposomes with two bilayers of poly(L-arginine) and dextran sulfate (Lipo-[PLA/DXS]$_2$). This formulation was prepared using the TFF-assisted protocol to demonstrate compatibility with liposomal substrates, which are important for drug delivery. This formulation was also used to assess long-term storage options for LbL liposomes (see Main Figure 7). **(a)** We tracked the hydrodynamic size using dynamic light scattering and plotted the particle size distribution on a violin plot to demonstrate controlled growth. Violin plots display the estimated kernel density of the size or charge distribution, and allow the visualization of population-wide evolution of LbL nanoparticle characteristics during synthesis. The black squares denote the mean hydrodynamic size for each layer. **(b)** The zeta potential reversal at each stage of the layering process confirms successful LbL assembly. This was tracked with laser Doppler electrophoresis, and the charge distributions were plotted as a violin plot. The blacks squares denote the mean zeta potential for each layer. **(c)** The polydispersity index was measured by dynamic light scattering, and remained small throughout LbL assembly indicating good uniformity. Error represents SD of three technical replicates. Red denotes liposomal core, orange denotes PLA layers, and light blue denotes DXS layers.
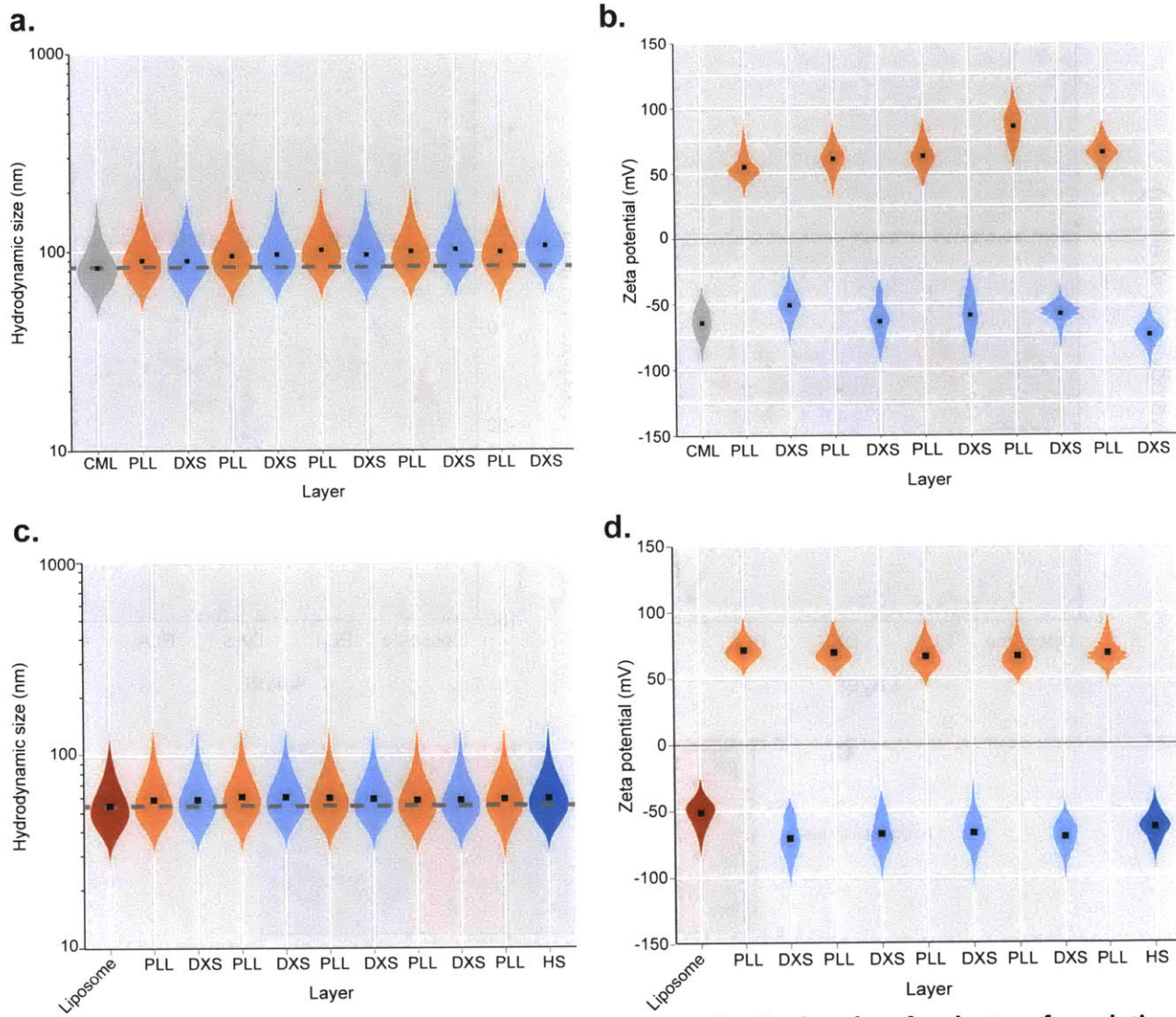
Appendix A Figure 5. This figure displays the size and charge distribution data for the two formulations featured in the main document; 100CML-[PLL/DXS]₅ and Lipo-[PLL/DXS]₄-PLL-HS. (a, c) We tracked the hydrodynamic size using dynamic light scattering and plotted the particle size distribution on a violin plot to demonstrate controlled growth. Violin plots display the estimated kernel density of the size or charge distribution, and allow the visualization of population-wide evolution of LbL nanoparticle characteristics during synthesis. The black squares denote the mean hydrodynamic size for each layer. **(b, d)** The zeta potential reversal at each stage of the layering process confirms successful LbL assembly. This was tracked with laser Doppler electrophoresis, and the charge distributions were plotted as a violin plot. The blacks squares denote the mean zeta potential for each layer. For polydispersity index data see the main document. Gray denotes latex core, red denotes liposomal core, orange denotes PLL layers, light blue denotes DXS layers, and dark blue denotes HS layers.
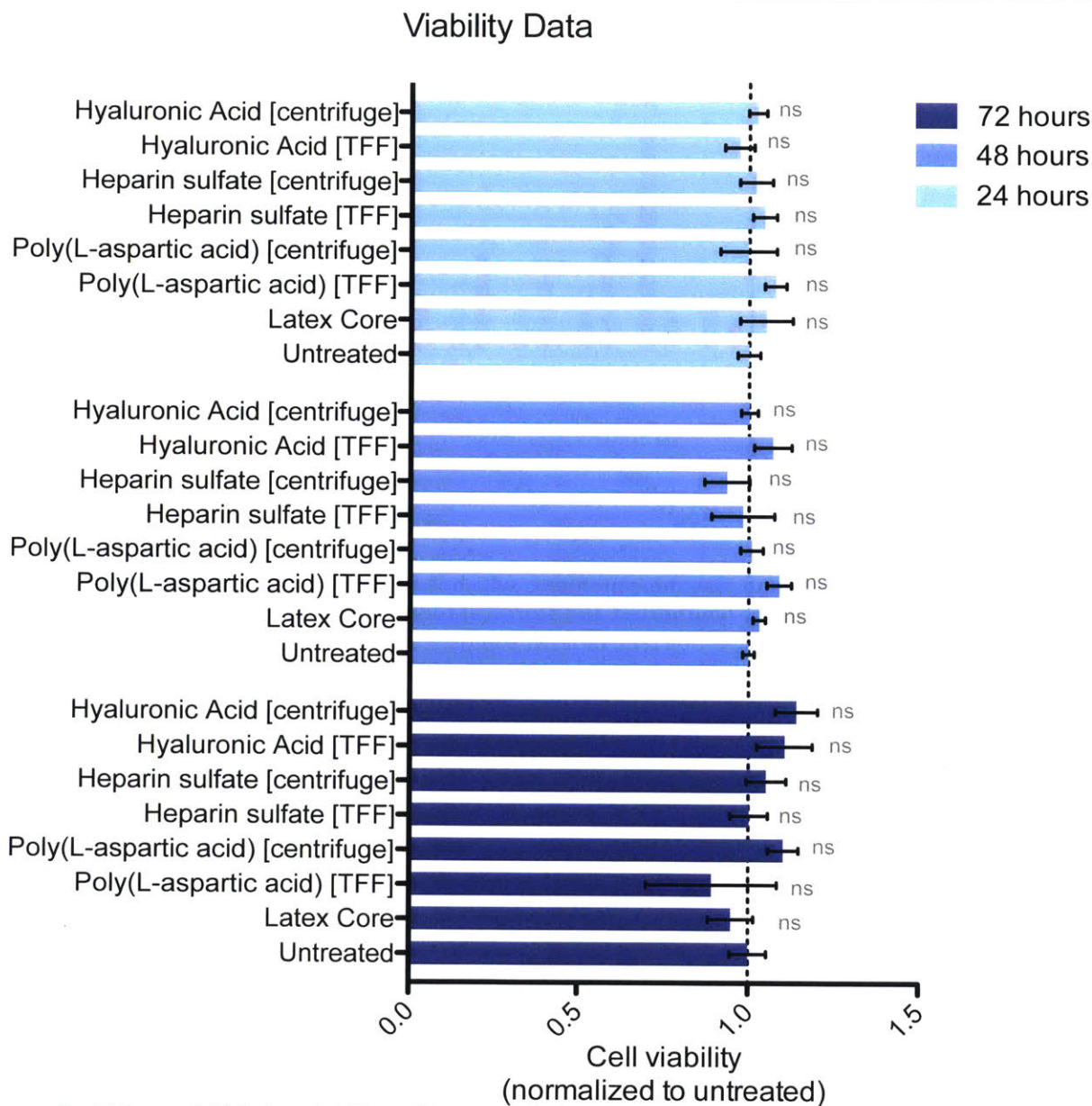
Viability Data

Appendix A Figure 6. Cellular viability of SKOV3 cells for 24, 48, and 72 hours following treatment by LbL nanoparticles indicate that these materials are not nonspecifically toxic. No statistically significant differences in viability were detected for any formulation, at any of the tested incubation times. Significance was evaluated using one-way ANOVA with the Dunnet post-test, comparing each formulation to the untreated control group for each incubation time. Error represents SD of three biological replicates.
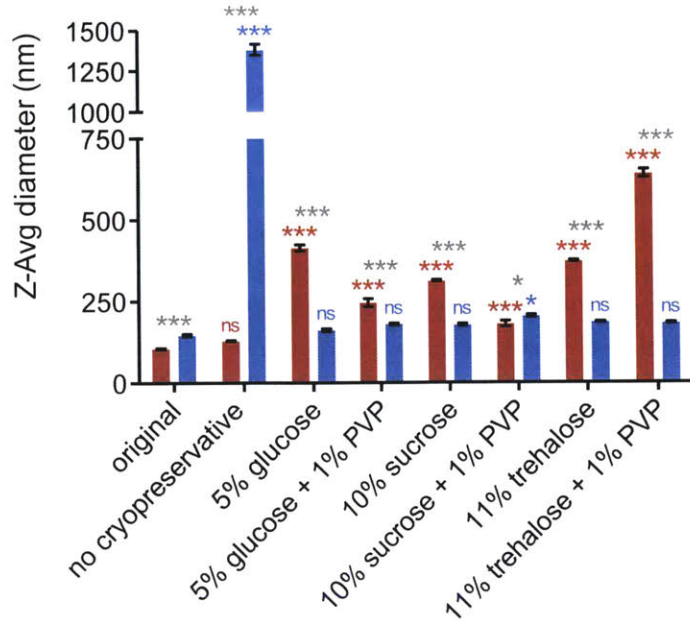
Appendix A Figure 7. The z-average size measurement, which is more sensitive to aggregation, further indicates that LbL liposomes can be lyophilized and stored at room temperature without loss of colloidal stability. This requires the use of a cryoprotectant, otherwise large-scale aggregation occurs as indicated above. Notably, bare liposomal formulations stored with cryoprotectants exhibit statistically significant z-average size increases that were not observed by the number average measurements, indicating the presence of an aggregating population. This finding supports the observation from the main document that polydispersity index increases for bare liposomes during long-term storage with cryoprotectants. Error represents SD of three technical replicates. Red denotes bare liposomes and blue represents LbL liposomes, Lipo-[PLL/DXS]$_2$.
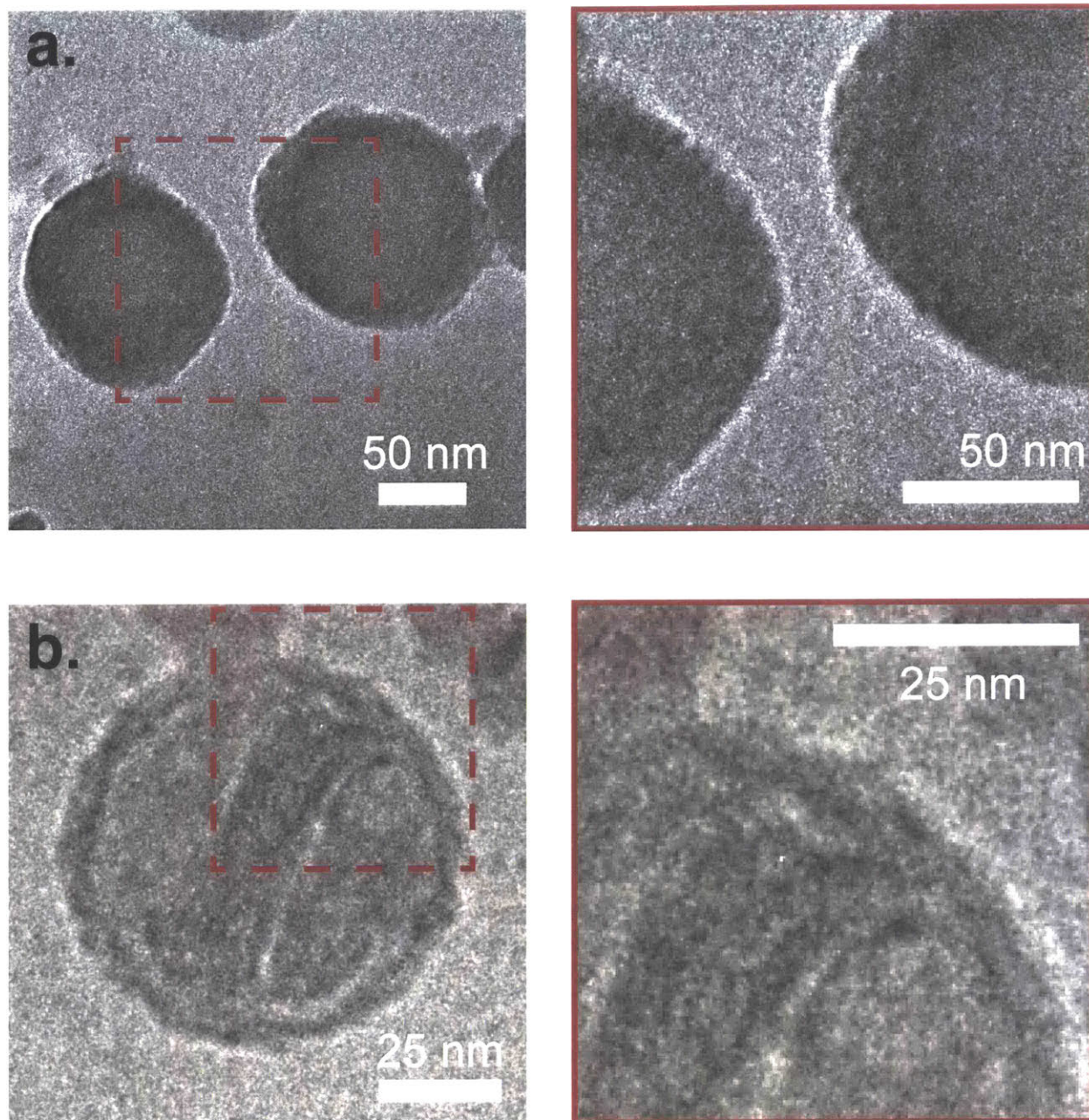
Appendix A Figure 8. Further detail of the surface of LbL nanoparticles is provided by the magnification of the Cryogenic TEM images of LbL nanoparticles. The region indicated by the dashed red line is magnified 200% in the right panel. **(a)** LbL-coated carboxy-modified latex (CML-[PLL/DXS]$_5$); **(b)** LbL-coated, doxorubicin-loaded liposome (Lipo-[PLL/DXS]$_4$-PLL-HS).
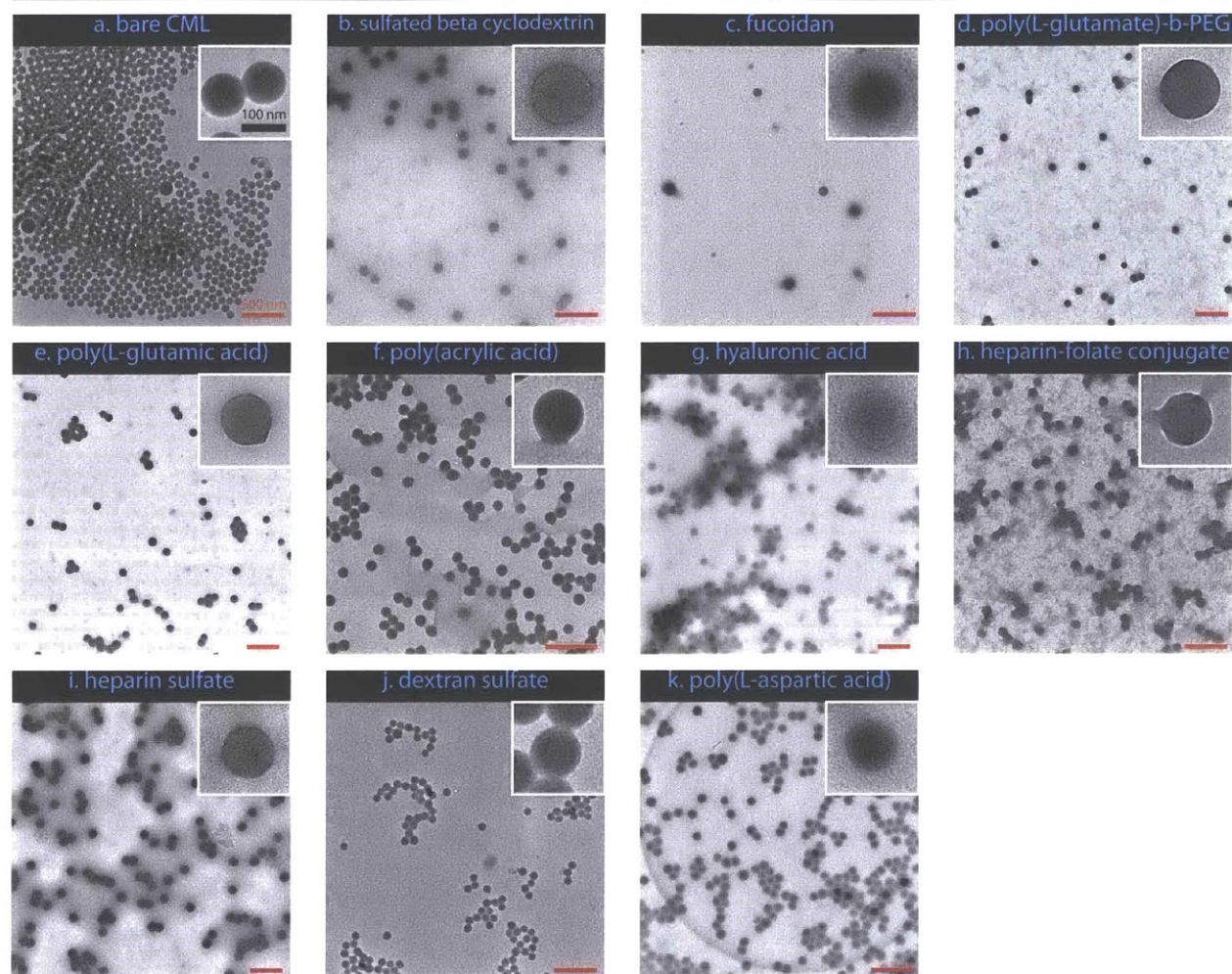
Appendix A Figure 9. Conventional TEM images of the LbL nanoparticle library, taken after three months of storage at 4 degrees Celsius in pure water, provide evidence that the morphology of these nanoparticles are preserved. Specimens were drop-casted from a 10 µg/mL solution onto a mesh copper grid coated with a continuous carbon film and then imaged on a JEOL 2011 High Contrast Digital TEM (120 kV). The red scale bar denotes 500 nm in each image. The inset shows a high-magnification view of a single nanoparticle, and the black scale bar from panel **(a)** represents 100 nm for all insets.

Supplemental methods

Synthesis of Heparin-bound Folic acid:

Activation of folic acid was performed according to the protocol as described by Lowe et al.[1] Folic acid (FA, 1.0 g) was reacted with 0.5 g of N-hydroxysuccinimide (NHS) in the presence of 0.5 mL of triethylamine in 25 mL DMSO at 40°C with stirring. Subsequently, 0.9 g of N,N'-Dicyclohexylcarbodiimide (DCC) was added to the solution and the mixture was stirred in the dark at room temperature overnight. After the reaction, the insoluble byproduct, dicyclohexylurea, was removed by filtration. After vacuum distillation of the solution to reduce DMSO volume, NHS-folate was precipitated by addition of 10x volume of acetone/diethylether (30:70). The precipitate pellet was centrifuged at 10,000 x g for 10 min, and washed three times with acetone/diethylether (30:70). The pellet was dried for 1h followed by vacuum drying, and stored in the dark at 4°C. Aminated FA was prepared according to the protocol of Huh et al. whereby FA-NHS, ethylenedi-amine (EDA, 2.0 equivalent of FA-NHS) and pyridine (0.1 equiv.) were allowed to react in DMSO overnight at room temperature.[2] Excess acetonitrile was added to the reactant solution to precipi-tate the product and remove excess EDA. The aminated FA was collected by centrifugation and dried under vacuum.

For conjugation of aminated FA to heparin sulfate, the later (0.05 g) was dissolved in pH 5.5 MES buffer followed by the addition of NHS and 1-Ethyl-3-(3-dimethylaminopropyl)carbodiimide (EDC) (1.2 equiv. of the targeted functionalization level (5%) of heparin carboxylic acid). The solution was allowed to stir for 30 minutes after which aminated FA (at 5% targeted functionalization level of heparin carboxylic acid group) was dissolved in DMSO, and were added in a drop-wise pattern to the solution of activated heparin sulfate. After 12h reaction period, the product was dialyzed through regenerated cellulose membrane (MWCO 2,000 g mol^{-1}) against deionized water for 16h. Degree of functionalization of folic acid on heparin sulfate was quantified by UV-Vis spectroscopic method. Degree of functionalization of folic acid on heparin sulfate was confirmed and quantified by UV-Vis spectroscopic method considering the folate absorption signal at 363 nm (**Figure S10**).

1. NHS, DCC, DMSO, 12h

2. H_2N $\diagup\diagdown$ NH_2 , pyridine

3. Heparin sulfate, EDC, NHS
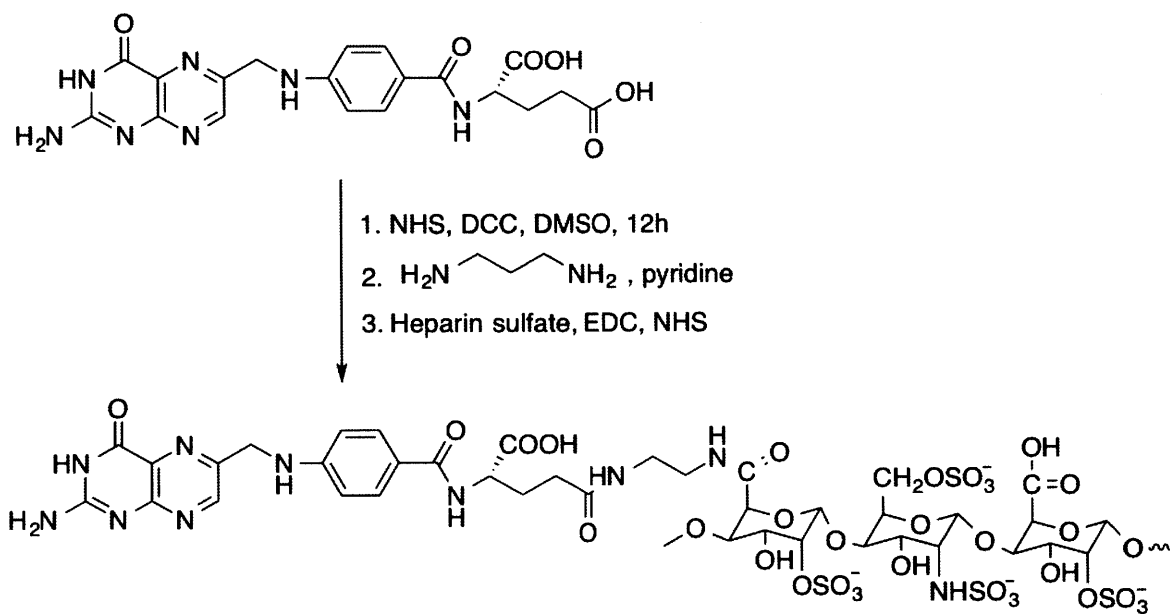
Appendix A Scheme 1
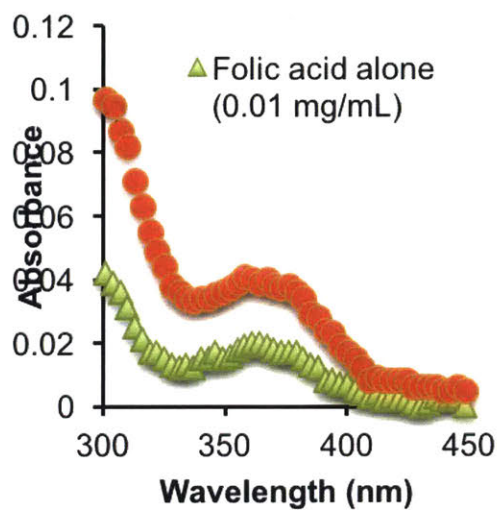
Appendix A Figure 10. Appendix A Figure 10: UV-Visible spectrum of folic acid decorated heparin (after dialysis) indicating the immobilization of folic acid as evident by the characteristic shoulder of folate at 363 nm.

References

1.   Lee, R. J.; Low, P. S., Folate as a Targeting Device for Proteins Utilizing Folate Receptor-Mediated Endocytosis. In *Drug Targeting: Strategies, Principles, and Applications*, Francis, G. E.; Delgado, C., Eds. Humana Press: Totowa, NJ, 2000; pp 69-76.

2.   Tran, T. H.; Bae, B.-c.; Lee, Y.-k.; Na, K.; Huh, K. M., Heparin-folate-retinoic acid bioconjugates for targeted delivery of hydrophobic photosensitizers. *Carbohydr Polym* **2013,** *92* (2), 1615-1624.

Appendix B

Appendix B.

Supporting information for Chapter 3: *Discovery of ovarian cancer targeting surface chemistries through a library approach* is provided here.

Appendix B Figures

Appendix B Figure 1. TEM was performed on all nanoparticle formulations to demonstrate the synthesis of uniform LbL-NPs with an approximate diameter of 100 nm. Specimens were drop-casted from a 10 µg/mL solution onto a mesh copper grid coated with a continuous carbon film and then imaged on a JEOL 2011 High Contrast Digital TEM (120 kV). The scale bar in the low-magnification image denotes 500 nm and the scale bar for the insets represents 100 nm.
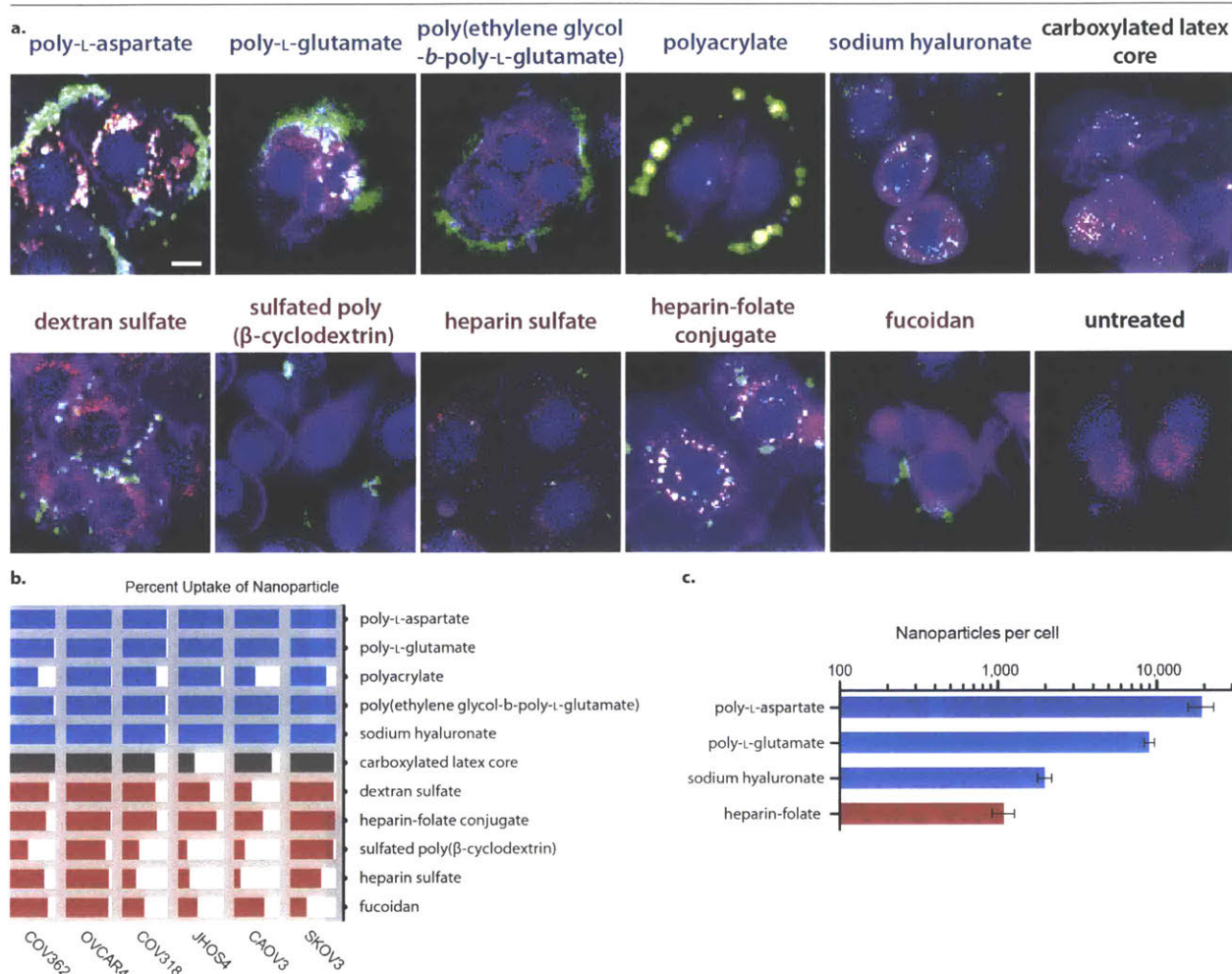
Appendix B Figure 2. Surface chemistry mediates important differences in nanoparticle uptake and trafficking, with major differences apparent between sulfated and carboxylated formulations as well as differences within the surface chemistry families. a) Live cell confocal imaging of JHOS4 ovarian cancer cells demonstrates that carboxylated LbL-NPs bind JHOS4 cells more efficiently than sulfated formulations. The JHOS4 cells treat the carboxylated formulations differently, sometimes accumulating particles on the surface in the case of poly-L-glutamate or internalizing them efficiently in the case of sodium hyaluronate. Inclusion of the folate on the heparin sulfate-coated system provides enhances accumulation and internalization relative to the corresponding heparin sulfate NP. Nanoparticle signal shown in green, lysotracker signal shown in red, cell membrane shown in magenta, nuclei shown in blue. Scale bar in the first micrograph denotes 10 μm for all images. b) Sulfated formulations fail to bind to all cells after 24 hours, whereas carboxylated systems are more uniformly bound to cancer cells, with the exception of polyacrylate. Notably, the bare latex core binds to a fewer percentage of cells than the majority of the carboxylated LbL-NPs. Percentage of nanoparticle positive cells was determined by flow cytometry following a 24-hour incubation with 20 pM LbL-NP. c) The number of nanoparticles per cell was determined for four LbL-NP formulations of interest, and demonstrates a 4-fold and 10-fold increase in nanoparticles bound per cell for poly-L-glutamate and poly-L-aspartate systems relative to sodium hyaluronate-coated particles. Nanoparticle quantification was performed by lysing a known number of NP-treated cells and measuring nanoparticle-associated fluorescence using a plate reader. Fluorescence units were converted to a number of NP using a standard curve of NP prepared in cell lysate from untreated cells. Error bars represent standard deviation.

Sodium hyaluronate (HA)   Poly-L-glutamate (PLE)   Poly-L-aspartate (PLD)   Heparin folate conjugate (HF)
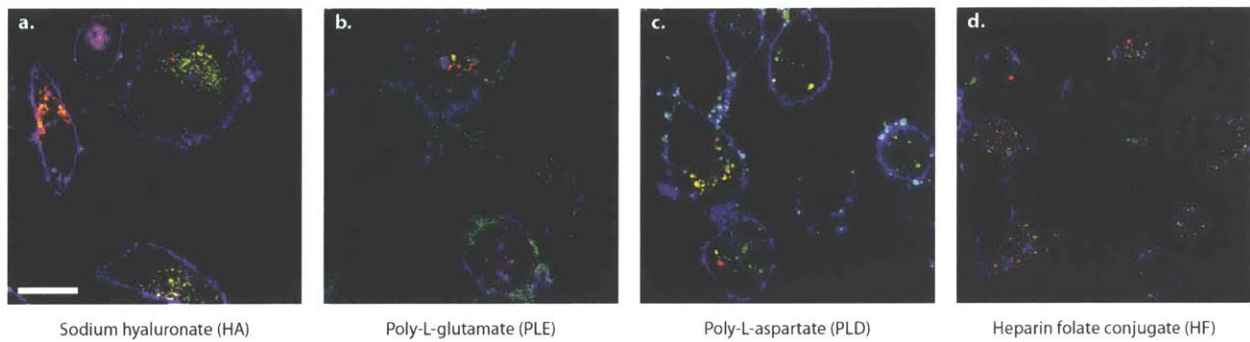
Appendix B Figure 3. COV362 ovarian cancer cells demonstrate consistent subcellular trafficking patterns for key LbL-NPs. Cells were incubated with 20 pM concentrations of LbL-NPs and imaged live using a confocal microscope. a) HA-coated NPs were observed mostly internalized by the cell. b) PLE-coated NPs again demonstrated a fibrous surface coating morphology with limited penetration into the cell. c) The PLD-coated NPs appeared as punctate signals from within the cells and on the membrane and cellular projections. d) HF-coated NPs were mostly internalized at this time point, but were less abundant relative to the carboxylated LbL-NPs. Nanoparticle signal shown in green, lysotracker signal shown in red, and cell membrane shown in magenta. Scale bar in the first micrograph denotes 10 μm for all images.

Sodium hyaluronate (HA)　　　　Poly-L-aspartate (PLD)
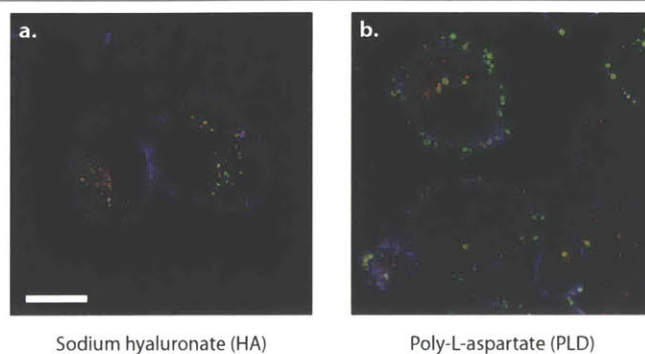
Appendix B Figure 4. Caov3 ovarian cancer cells also process HA and PLD-coated NPs in a manner consistent with results from other ovarian cancer lines. Cells were incubated with 20 pM concentrations of LbL-NPs and imaged live using a confocal microscope. a) HA-coated NPs are internalized and organized inside or near lysosomes. b) PLD-coated LbL NPs are observed as punctate spots on the membrane surface as well as co-localized with lysosomes. Nanoparticle signal shown in green, lysotracker signal shown in red, and cell membrane shown in magenta. Scale bar in the first micrograph denotes 10 µm for both images.
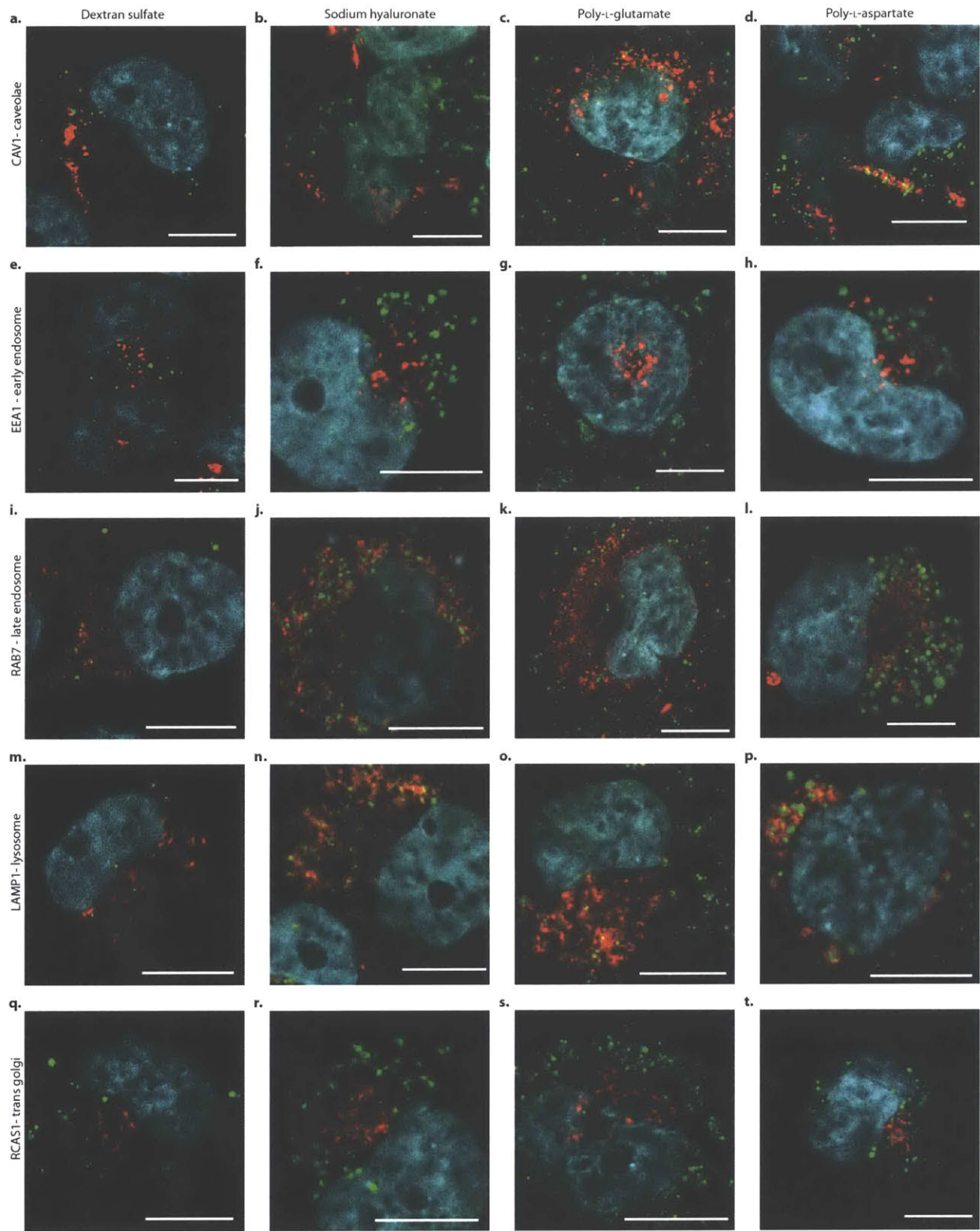
Appendix B Figure 5. LbL-NPs have distinct subcellular fates depending on their terminal coating. We probed whether nanoparticles associate with caveolae (CAV1 positive vesicles, a-d), early endosomes (EEA1 positive vesicles, e-h), late endosomes (RAB7 positive vesicles, i-j), lysosomes (LAMP1

positive vesicles, m-p), and trans golgi (RCAS1 positive vesicles, q-t). Dextran sulfate (DXS), sodium hyaluronate (HA), poly-L-glutamate (PLE), and poly-L-aspartate (PLD) coated LbL-NPs showed differences primarily in lysosomal and caveolar association in OVCAR8 cells at 24 hours. Micrographs of OVCAR8 cells were obtained using an Olympus FV1200 confocal microscope following incubation with 20 pM LbL-NP. Nanoparticle signal shown in green, organelle signal shown in red, nuclei shown in cyan. Scale bar denotes 10 μm.
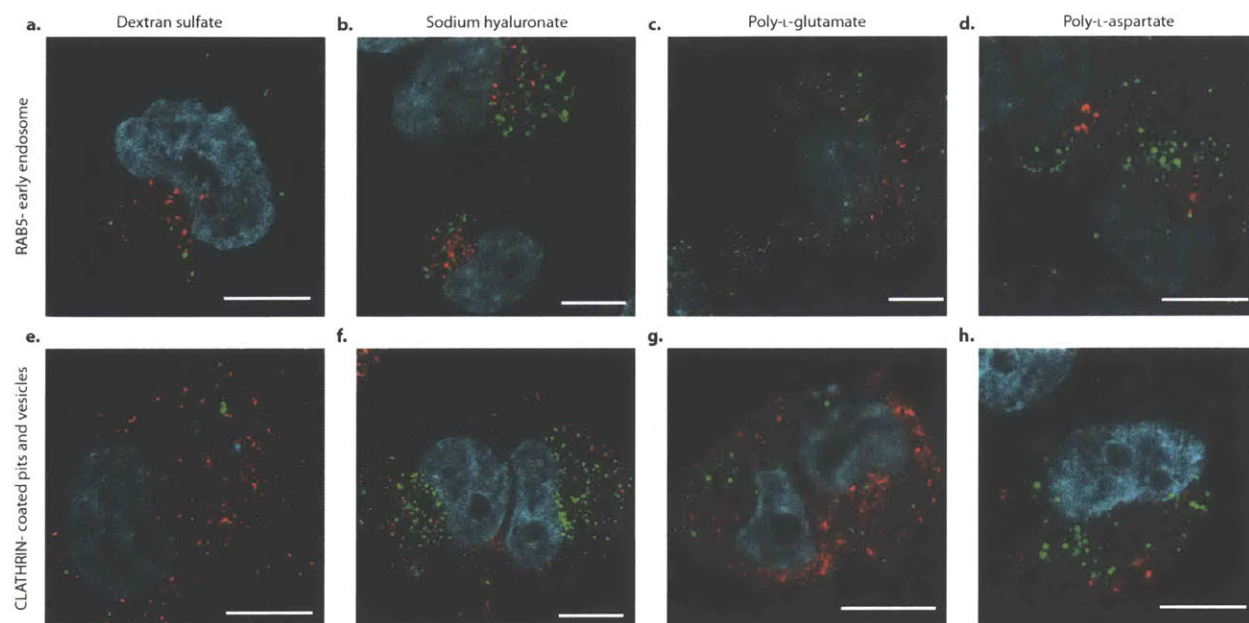
Appendix B Figure 6. LbL-NPs are not associated with the early endosome or in clathrin-coated vesicles after 24 hours. Confocal microscopy of OVCAR8 cells looked at LbL-NP co-localization with clathrin-coated vesicles (e-h) and early endosome (Rab5 positive, a-d). Nanoparticle signal shown in green, vesicle signal shown in red, nuclei shown in cyan. Scale bar denotes 10 μm.

| | **a.** Dextran sulfate | **b.** Sodium hyaluronate | **c.** Poly-L-glutamate | **d.** Poly-L-aspartate |

Rows: LAMP1/RAB7 - late endolysosomes, Nanoparticle, Merge, Detail (Late endolysosomes / NP / Nucleus), (Membrane / NP / Nucleus), Z-projection
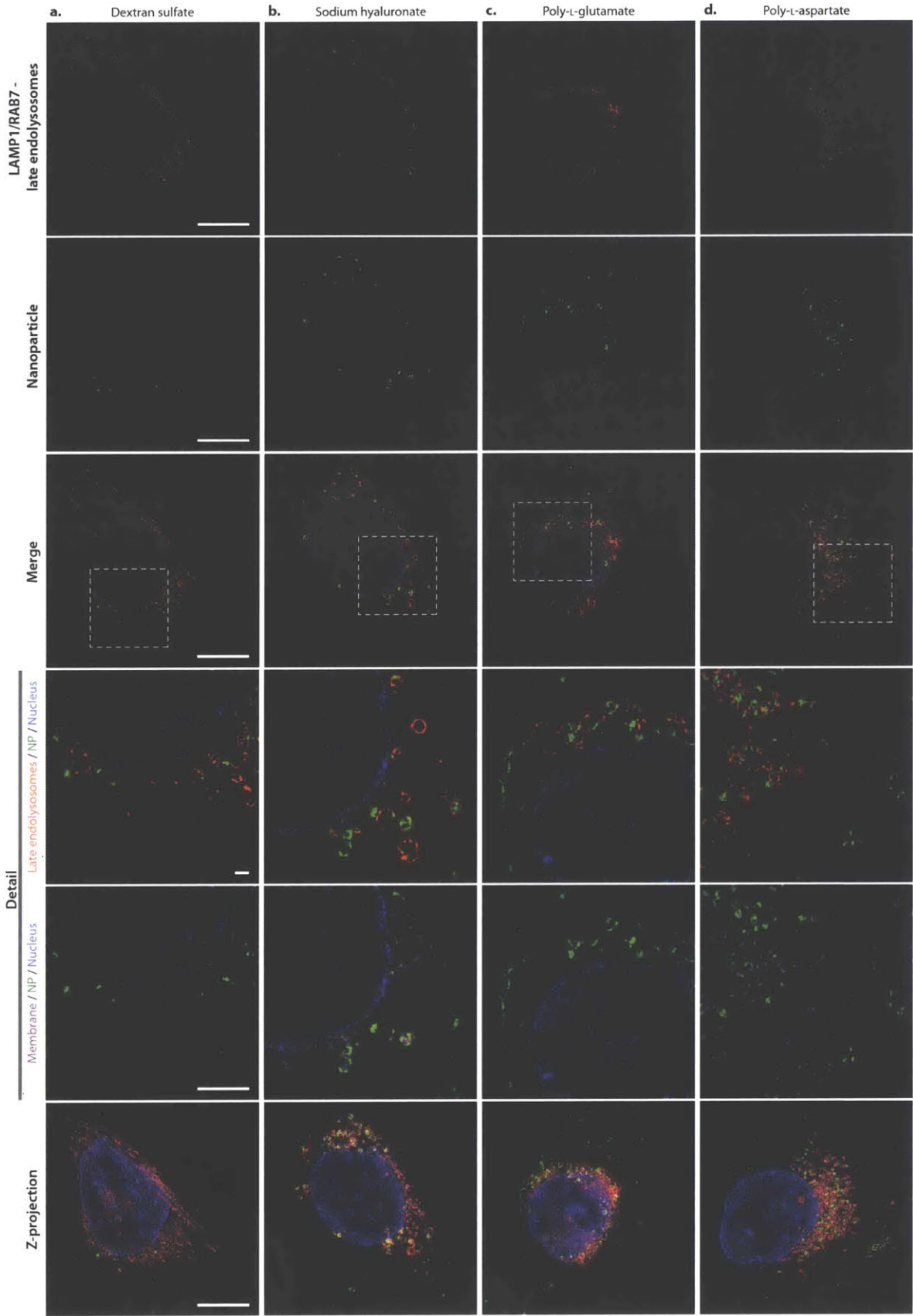
Appendix B Figure 7. Internalized LbL NPs navigate to the late endosomal-lysosomal compartment in OVCAR8 cells. Cells were treated with 4 pM LbL NP for 24 hours and then fixed and processed for super resolution microscopy. LAMP1 and Rab7 proteins are stained to label the lysosomal and late endosomal compartments, and are shown in red. Wheat germ agglutinin (WGA) was used to stain membranes (including outer membrane, some vesicular membranes and the nuclear membrane) and is shown in magenta. Nanoparticles are shown in green and nuclei in blue. Scale bars denote 10 microns, with the exception of the scale bar for the detail panels, where they denote 1 micron. All internalized NPs appear to be contained within this compartment at this time point.
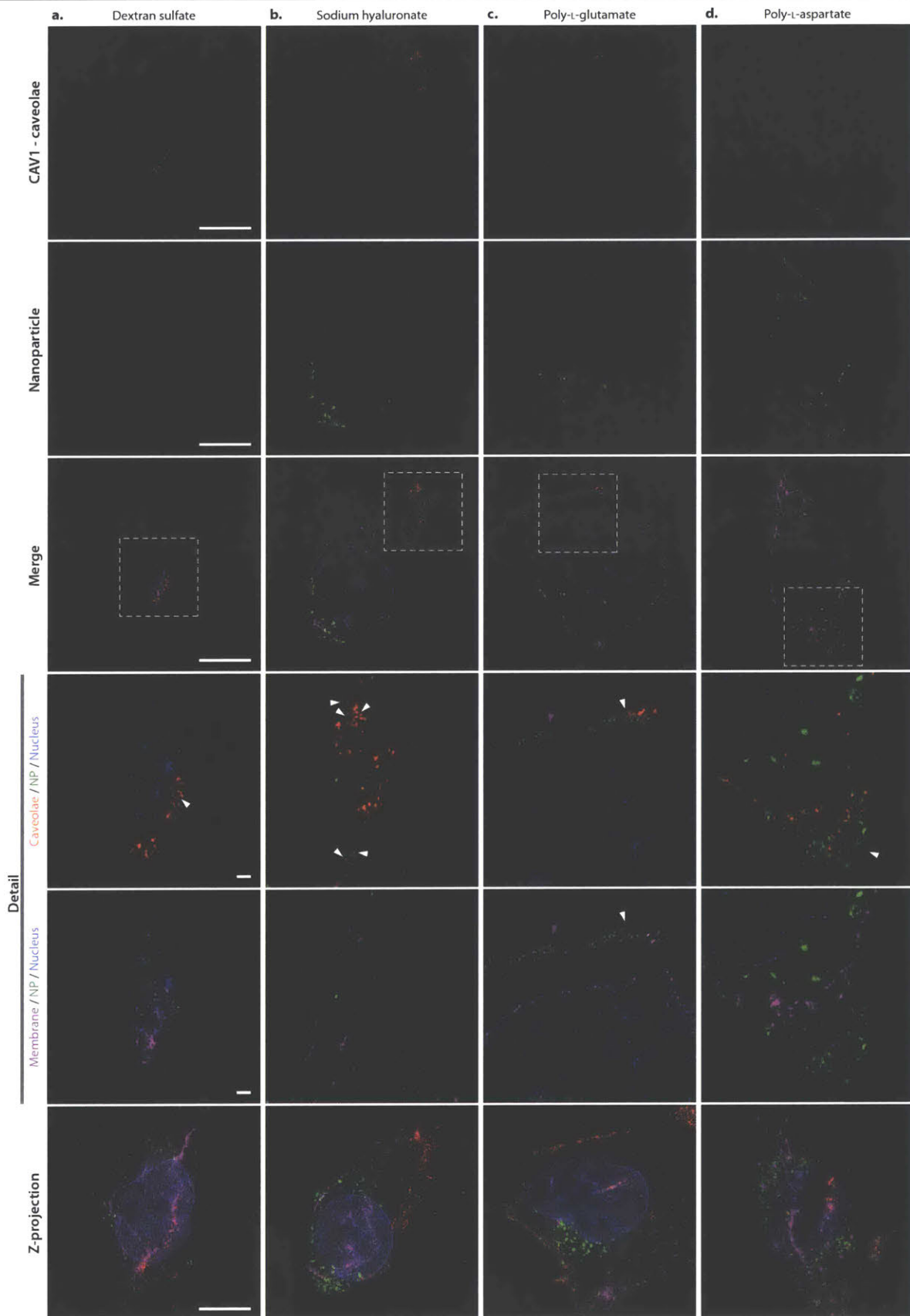
Appendix B Figure 8. Surface bound LbL-NPs have different degrees of interaction with caveolae at 24 hours in OVCAR8 cells. Cells were treated with 4 pM LbL NP for 24 hours and then fixed and processed for super resolution microscopy. CAV1 proteins are stained to label the caveolar compartment, and are shown in red. Wheat germ agglutinin (WGA) was used to stain membranes (including outer membrane, some vesicular membranes and the nuclear membrane) and is shown in magenta. Nanoparticles are shown in green and nuclei in blue. Scale bars denote 10 microns, with the exception of the scale bar for the detail panels, where they denote 1 micron. a) Although almost entirely internalized, some faint dextran sulfate-coated NP signal was noted near a caveolar ridge. b) Surface-bound fractions of sodium hyaluronate-coated NPs also appear to be within caveolae. c) Poly-L-glutamate (PLE)-coated NPs have surface bound fractions that are not associated with caveolae as indicated by the purple arrow, although most caveolar regions are enriched with PLE-NPs as indicated by the white arrow. d) In contrast, the considerable fraction of poly-L-aspartate-coated NPs found on the surface are almost always associated with the caveolar compartment.
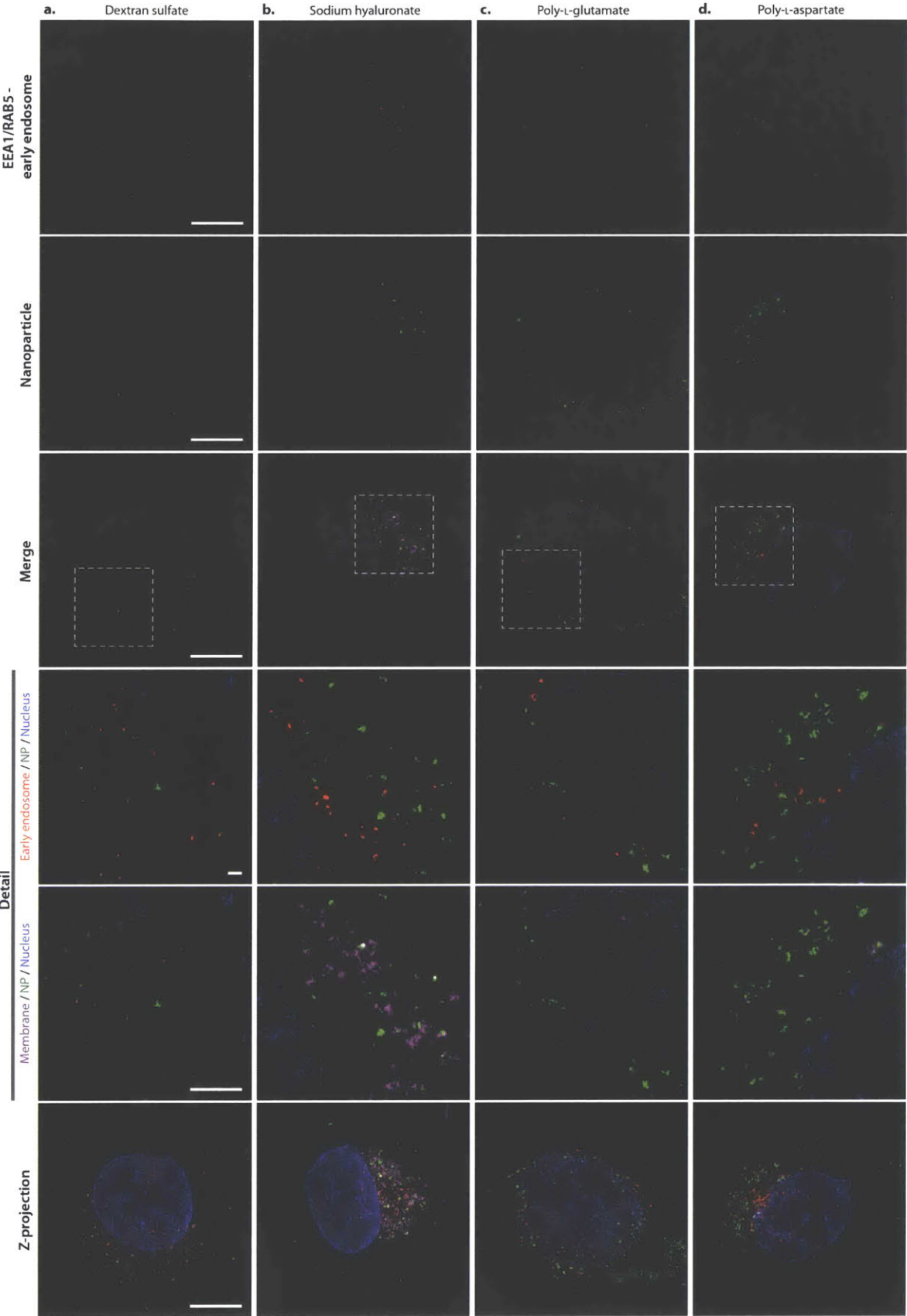
Appendix B Figure 9. By 24 hours, LbL NPs do not appear to co-localize with any early endosomal compartments. Cells were treated with 4 pM LbL NP for 24 hours and then fixed and processed for super resolution microscopy. EEA1 and Rab5 proteins are stained to label the early endosomal compartments, and are shown in red. Wheat germ agglutinin (WGA) was used to stain membranes (including outer membrane, some vesicular membranes and the nuclear membrane) and is shown in magenta. Nanoparticles are shown in green and nuclei in blue. Scale bars denote 10 microns, with the exception of the scale bar for the detail panels, where they denote 1 micron.
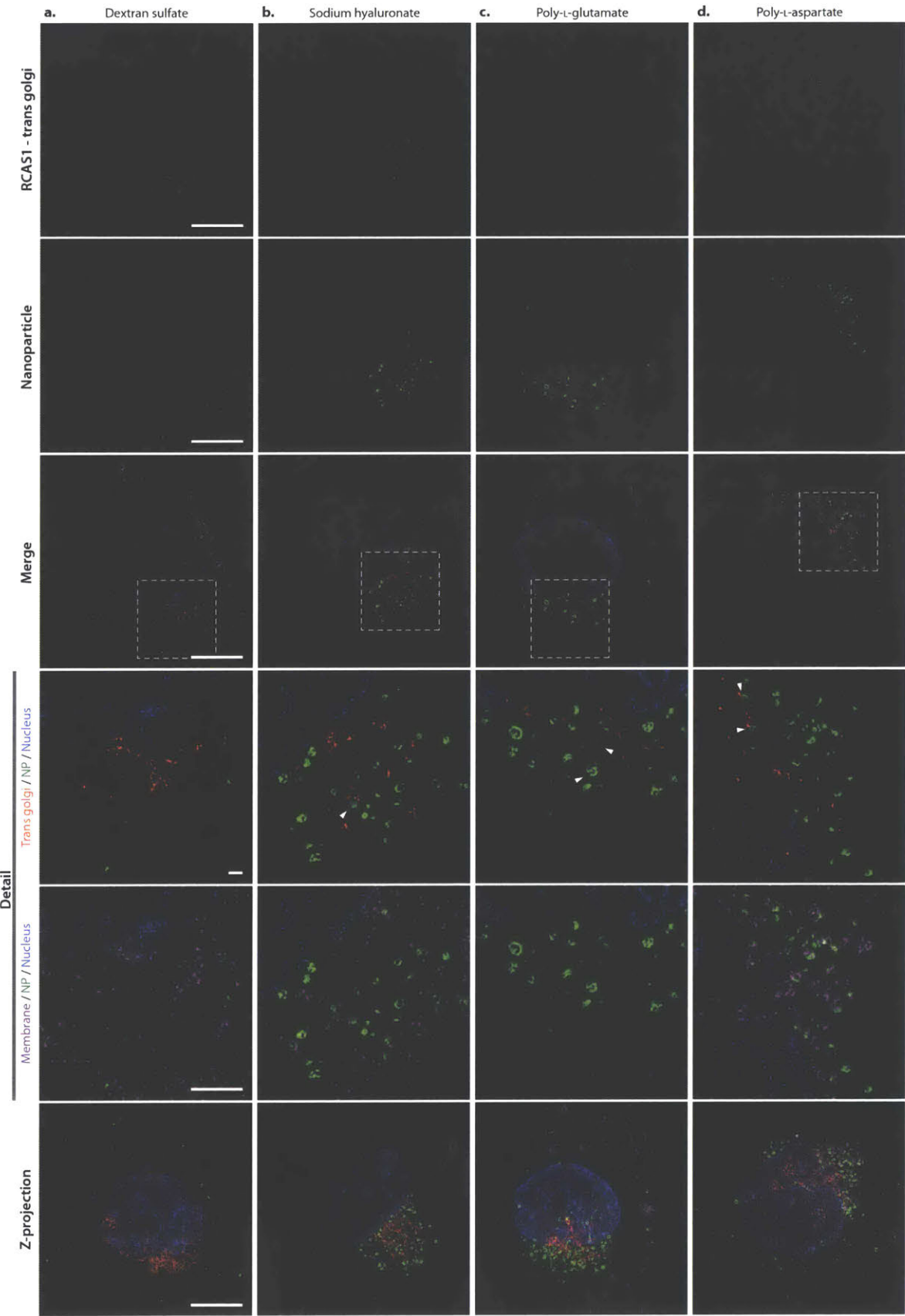
Appendix B Figure 10. Carboxylated LbL-NPs can be found near and in between trans golgi stacks, but not inside them. Cells were treated with 4 pM LbL NP for 24 hours and then fixed and processed for super resolution microscopy. RCAS1 proteins are stained to label the trans golgi compartment, and are shown in red. Wheat germ agglutinin (WGA) was used to stain membranes (including outer membrane, some vesicular membranes and the nuclear membrane) and is shown in magenta. Nanoparticles are shown in green and nuclei in blue. Scale bars denote 10 microns, with the exception of the scale bar for the detail panels, where they denote 1 micron. a) Dextran sulfate-coated NPs do not appear in close proximity to the trans golgi, though this may be a function of overall amount of NP in the cell. b-d) Sodium hyaluronate, poly-L-glutamate, and poly-L-aspartate-coated NPs are observed near golgi stacks, sometimes in very close proximity as denoted by the arrows. While provocative, it is unclear the extent to which these NPs may be engaged with the trans golgi, and should be the focus of future studies.
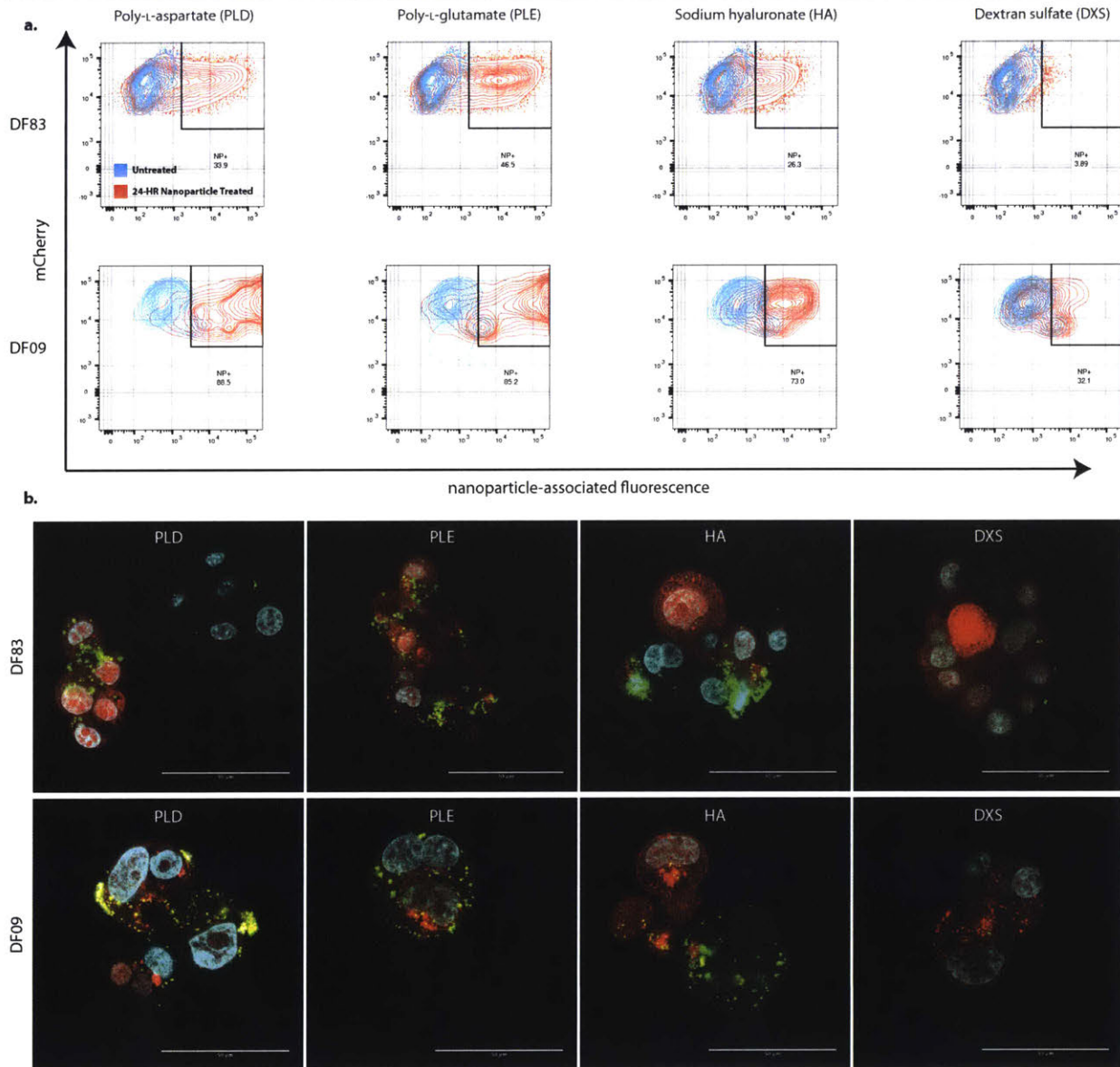
Appendix B Figure 11. LbL-NP surface chemistry determines binding affinity towards patient-derived xenograft (PDX) ovarian cancer spheroids. Four LbL formulations were tested for binding affinity to PDX spheroids, fluorescent latex nanospheres were coated with poly-L-arginine and then either with poly-aspartic acid, poly-L-glutamic acid, hyaluronic acid or dextran sulfate. Following 24 hour incubation in either growing or assay media, the PDX spheroids DF83 and DF09 were processed into single cell suspensions for flow cytometry. Live cells were identified using the PDX cell mCherry signal and nanoparticle positive populations were identified based on untreated controls. a) Carboxylated LbL nanoparticles show improved spheroid binding for both cell lines. Percent nanoparticle+ cell populations also confirm that carboxylated LbL formulations bind to more cells in the spheroids than do dextran sulfate-coated particles. b) Confocal microscopy z-slices of PDX spheroids following 24 hour incubation with LbL nanoparticles. The confocal data supports the quantitative results from flow cytometry. Notably, the poly-L-aspartic and poly-L-glutamic formulations appear to have significant surface accumulations, whereas the hyaluronic acid formulation is primarily internalized.
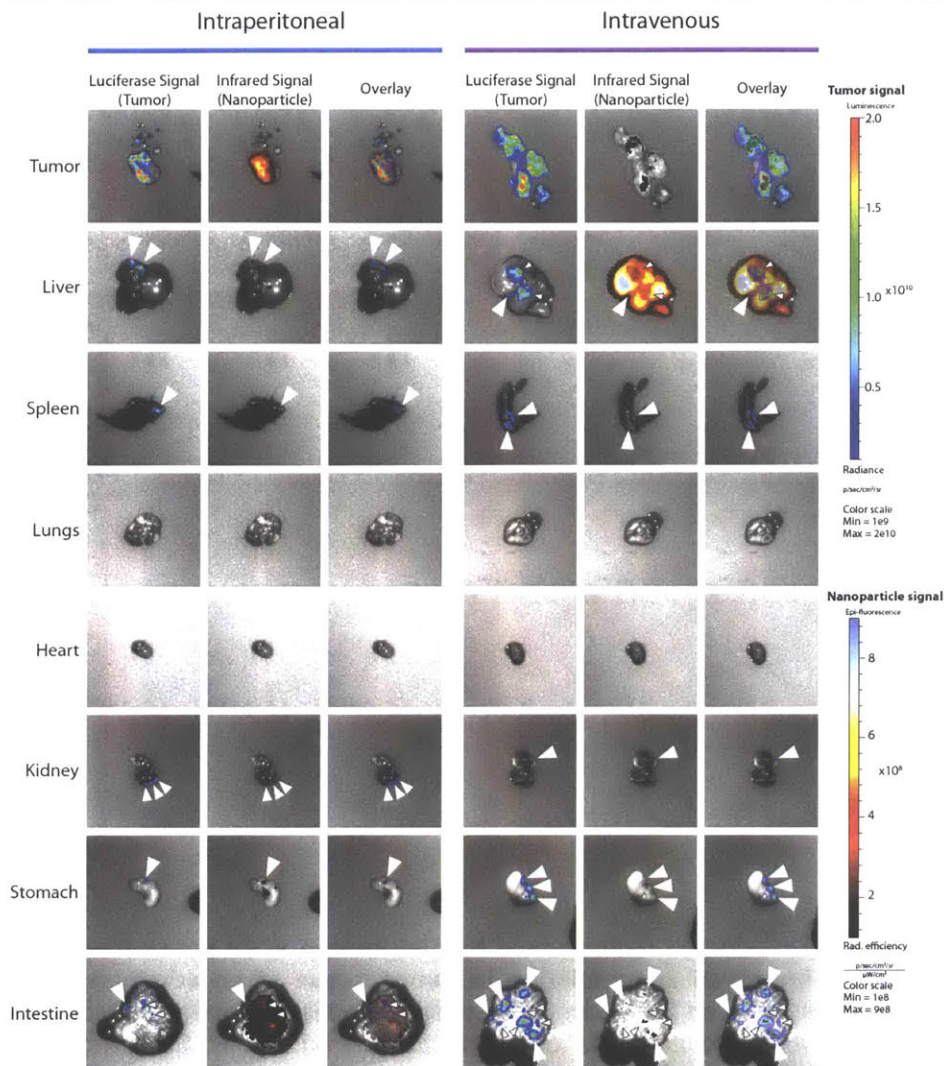
Appendix B Figure 12. Representative images of the biodistribution of the unmodified CML core particles at 24 hours after either IV or IP-administration. Luciferase signal from tumor cells and infrared fluorescence from nanoparticles were measured for each organ using an IVIS imaging device. Arrows denote locations of metastases on organs. The core particle co-localized well with the primary tumor tissue when administered IP. There is some co-localization with the primary tumor and some intestinal metastasis following IV administration, but the co-localization is highly heterogeneous and diminished compared to the results of IP-administration.
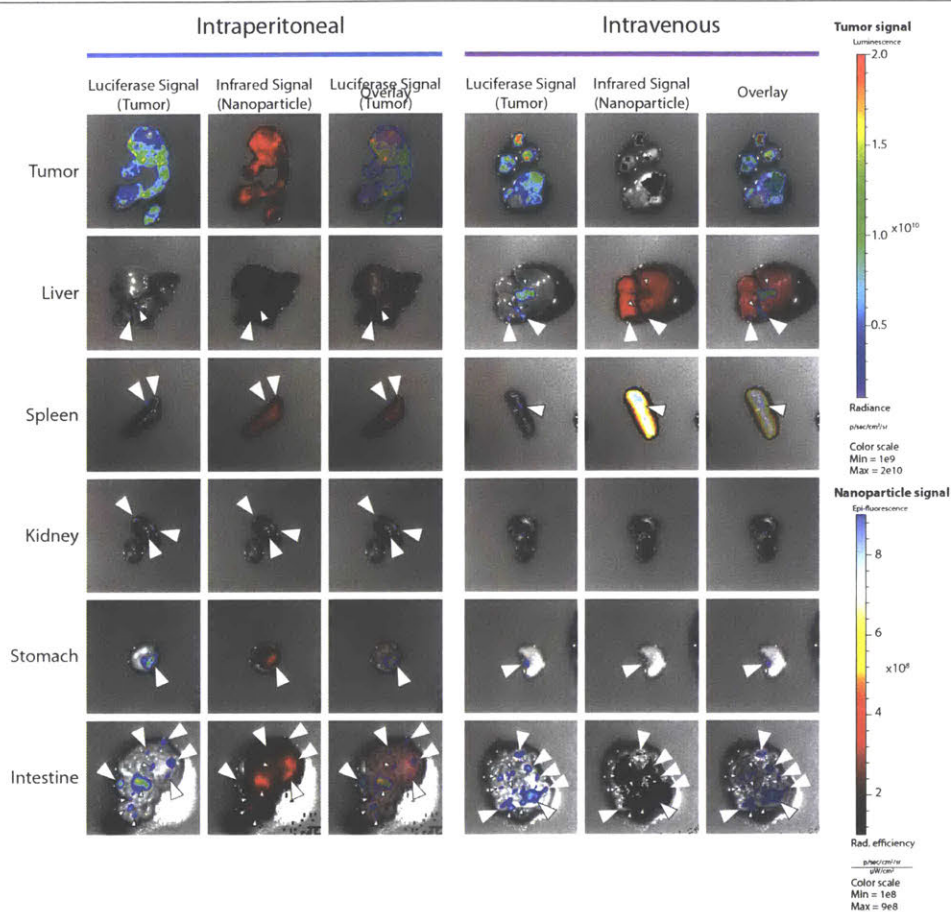
Appendix B Figure 13. PEG-coated nanoparticle biodistribution at 24 hours following IP or IV administration indicates improved accumulation in tumor tissue when administered IP. Luciferase signal from tumor cells and infrared fluorescence from nanoparticles were measured for each organ using an IVIS imaging device. Arrows denote locations of metastases on organs. Similar to the biodistribution of the unmodified CML core (Appendix B Figure 12), the IV administration route leads to heterogeneous co-localization with the primary tumor, though some co-localization with intestine metastatic nodules is observed. The amount of NP delivered to tumors appears diminished in the IV-administration condition compared to the IP-administered condition. There is diffuse NP signal throughout the intestine that is not co-localized to tumor nodules. Notably, diffuse NP signal is detected throughout the liver and spleen for both IP and IV, in contrast to results from the other nanoparticles shown in the Appendix.
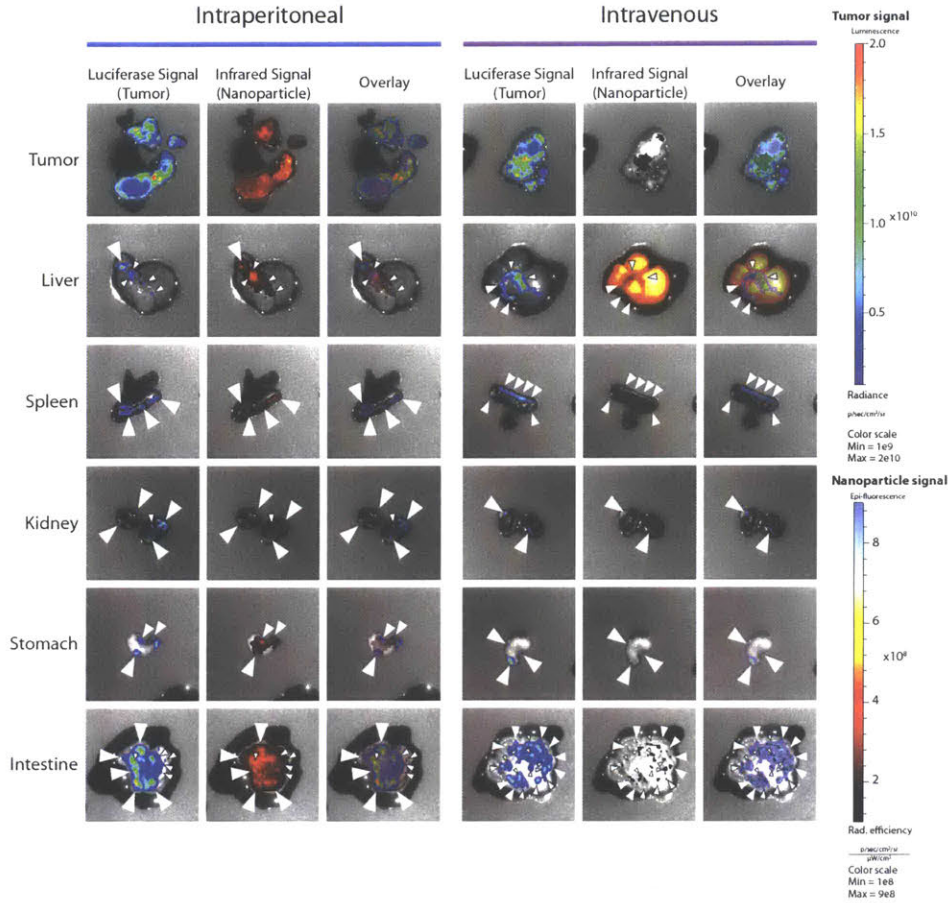
Appendix B Figure 14. The biodistribution of DXS-coated LbL NPs at 24 hours following IV or IP-administration follows similar trends between the two administration methods. Luciferase signal from tumor cells and infrared fluorescence from nanoparticles were measured for each organ using an IVIS imaging device. Arrows denote locations of metastases on organs. Most of the DXS NP is lost to the liver following IV administration, but some heterogeneous co-localization with the primary tumor is noted, as well as co-localization with intestinal metastases. More NP signal is detected from neoplastic tissues following IP-administration, including in metastases on the other IP organs.
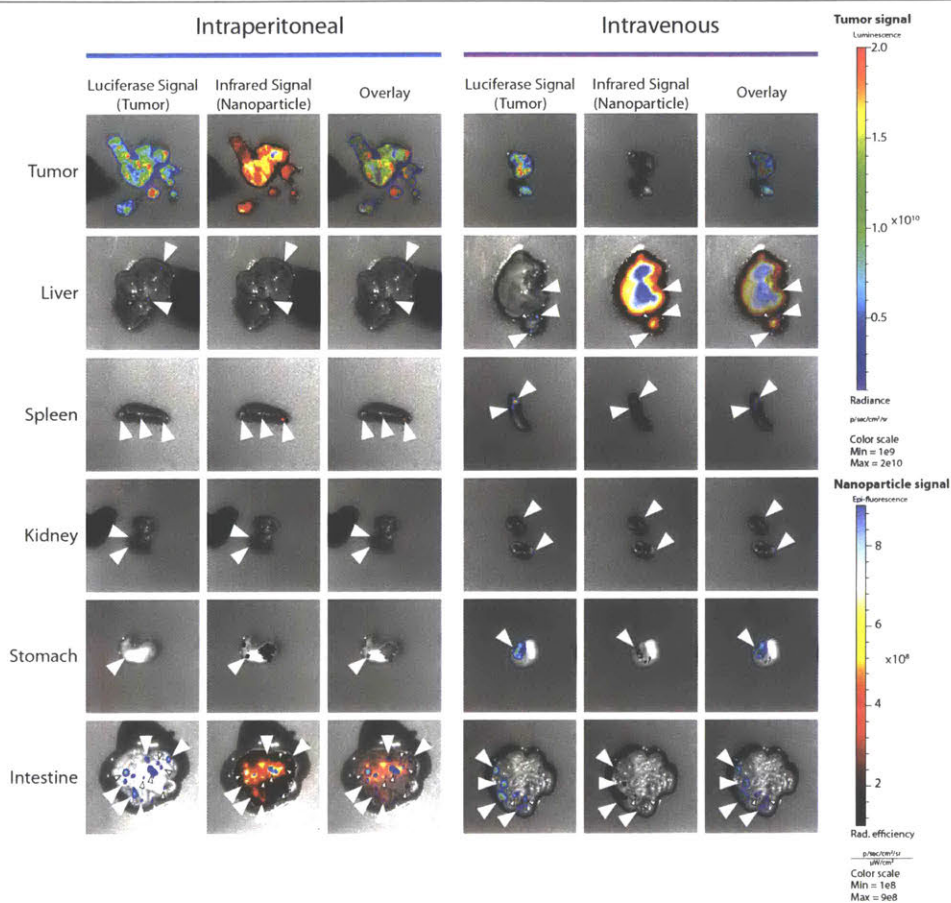
Appendix B Figure 15. PLE-coated NP biodistribution at 24 hours after either IV or IP-administration indicate improved NP delivery to tumors when using IP-administration. Luciferase signal from tumor cells and infrared fluorescence from nanoparticles were measured for each organ using an IVIS imaging device. Arrows denote locations of metastases on organs. IV-administration of PLE NPs leads to significant accumulation in the liver, and reduced but diffuse accumulation in the Spleen. However, NP signal is detected heterogeneously through the primary tumor mass and some metastatic nodules in the stomach and intestine for IV-administered conditions. Much stronger NP signal is detected from tumors of IP-administered mice. Very good co-localization of PLE NP with metastases on the intestine are noted in the IP-administered model.
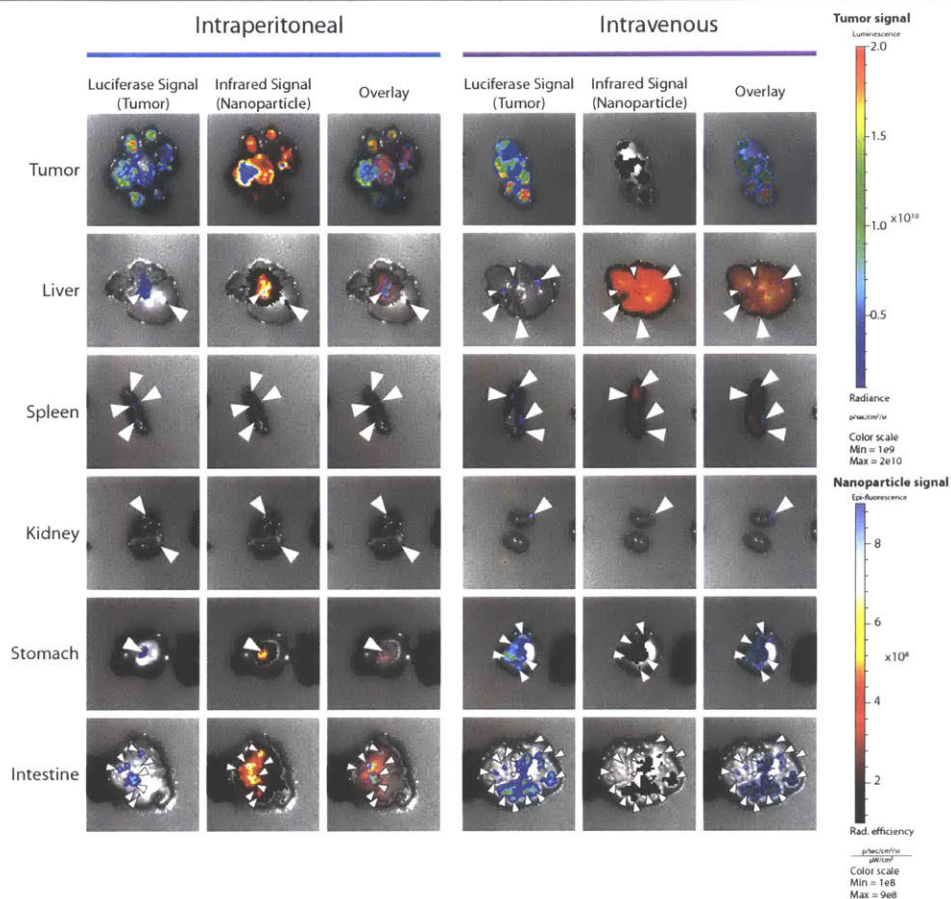
Appendix B Figure 16. The biodistribution of PLD-coated LbL NPs at 24 hours after either IV or IP-administration indicated improved delivery of NP to tumors for IP-routes. Luciferase signal from tumor cells and infrared fluorescence from nanoparticles were measured for each organ using an IVIS imaging device. Arrows denote locations of metastases on organs. IV administration of PLD NPs leads to diffuse signal in the liver and spleen, indicating loss to these filtration organs. However, good co-localization of NP with the metastatic nodules of the intestine and stomach indicate a good tumor-homing ability. Interestingly, NP signal from the primary tumor mass is heterogeneous. Despite this, the overall amount of NP signal from neoplastic tissue is low after IV-administration when compared to the results of IP-administration. IP-administered PLE NPs appear to be present throughout the primary tumor and in all detectable metastatic nodules in the other IP organs.
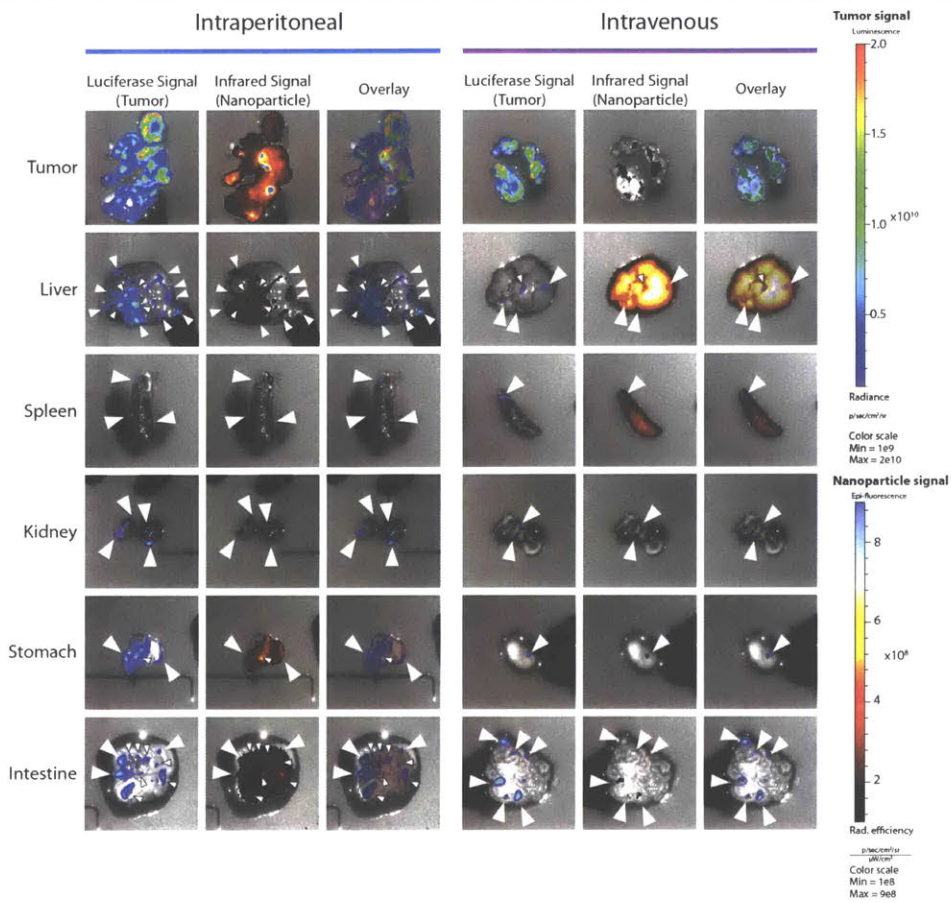
Appendix B Figure 17. HA-coated LbL NP biodistribution 24 hours after either IP or IV administration. Luciferase signal from tumor cells and infrared fluorescence from nanoparticles were measured for each organ using an IVIS imaging device. Arrows denote locations of metastases on organs. HA NPs have a heterogeneous accumulation in the primary tumor following IV-administration, consistent with the other NPs tested. The NPs appear to have co-localization with several of the metastatic lesions on the stomach and intestine as well. However, the majority of the dose appears to be in the liver and spleen. On the other hand, IP-administration of HA NPs leads to NP signal throughout the primary tumor as well as the majority of the malignant lesions throughout the other IP organs.
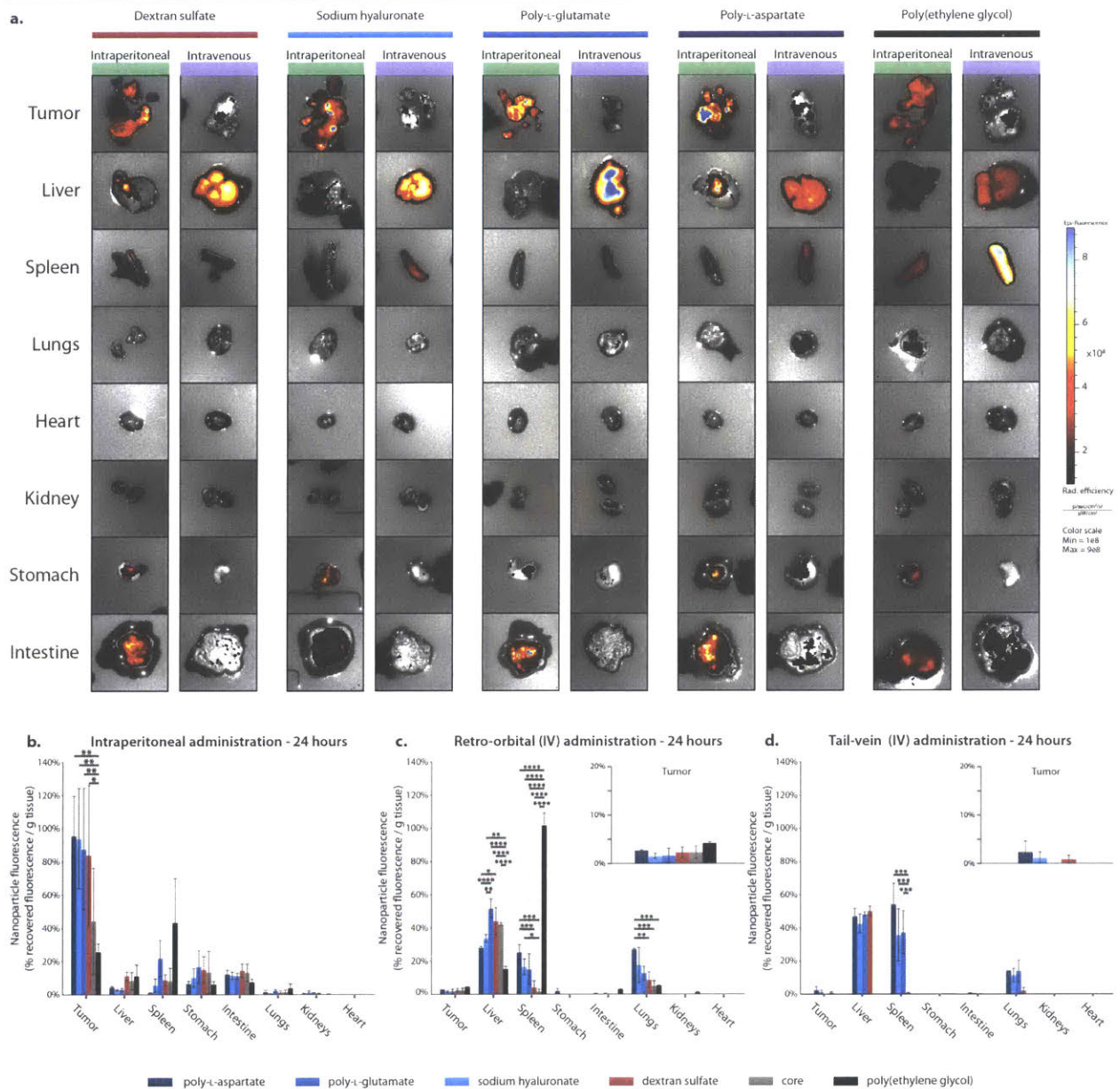
Appendix B Figure 18. NP biodistribution is strongly impacted by route of administration, and by 24 hours this effect dominates any tumor-targeting contribution from surface chemistry. Infrared fluorescence from nanoparticles were measured for each organ using an IVIS imaging device. a) Retro-orbital IV administration was compared to IP-administration for poly-L-aspartate (PLD), pol-L-glutamate (PLE), sodium hyaluronate (HA), dextran sulfate (DXS), poly(ethylene glycol) coated CML core, and unmodified CML core. In all instances, IV-administration skews NP biodistribution towards the liver and to a lesser extent the spleen. IP-administration skews NP distribution to neoplastic tissues. b) Quanitification of the IVIS results shows that LbL NPs, but not unmodified CML core, have a significant and improved accumulation in the primary tumor relative to PEGylated NPs. c) Quantification of the results from retro-orbital IV injections indicate that surface chemistry may influence degree of accumulation in the liver spleen and lungs, but not accumulation in the tumor at this time point. d) A smaller study comparing only LbL NPs was conducted using a tail-vein injection instead of retro-orbital injection. Interestingly, this approach led to undetectable PLE NP signal in the tumors, but no significant differences for tumor accumulations observed with the other formulations. Tail-vein injection also reduced the amount of PLD NP delivered to the lungs. Other than this,

the distribution to the liver and spleen remained consistent with retro-orbital injection. Error bars represent SEM, and statistical analysis was done using a two-way ANOVA with a Tukey post-hoc test and an alpha of 0.5.
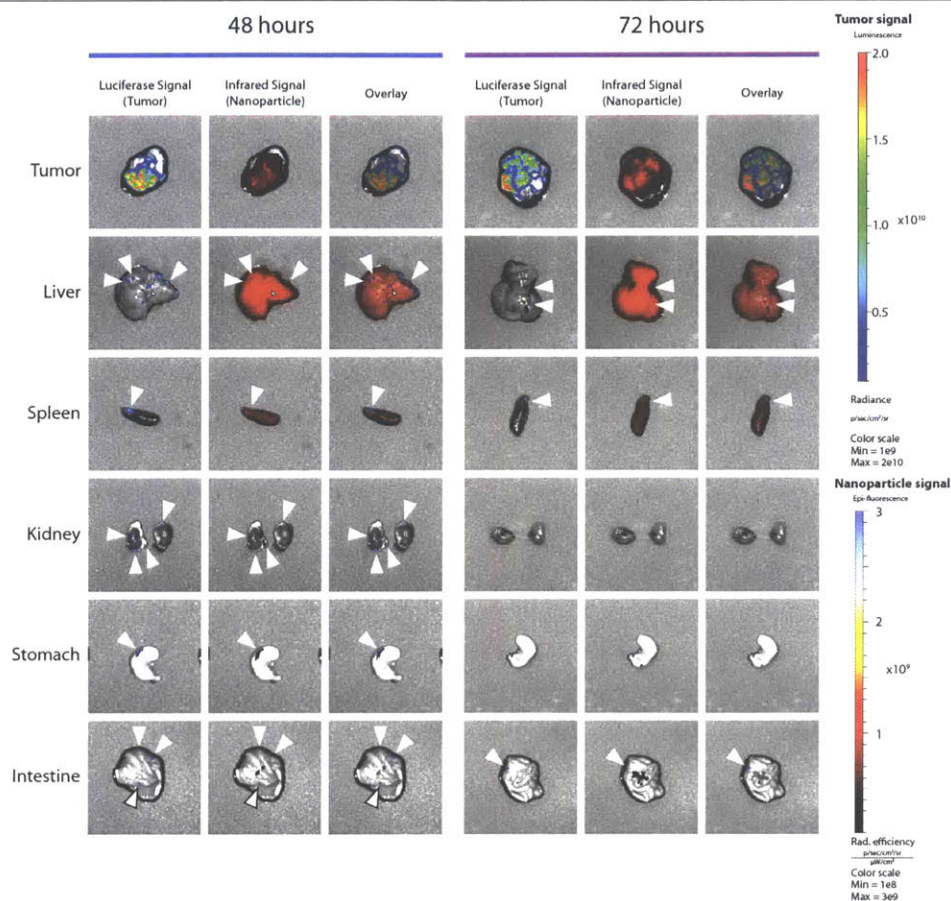
Appendix B Figure 19. Biodistribution of PEGylated CML cores at 48 and 72 hours following IP administration indicates a spillover into the liver and spleen compartments. Luciferase signal from tumor cells and infrared fluorescence from nanoparticles were measured for each organ using an IVIS imaging device. Arrows denote locations of metastases on organs. PEG NPs appear to have less co-localization with metastatic lesions at these times. These results may indicate the clearance of the NP from the IP cavity via the lymphatic system.
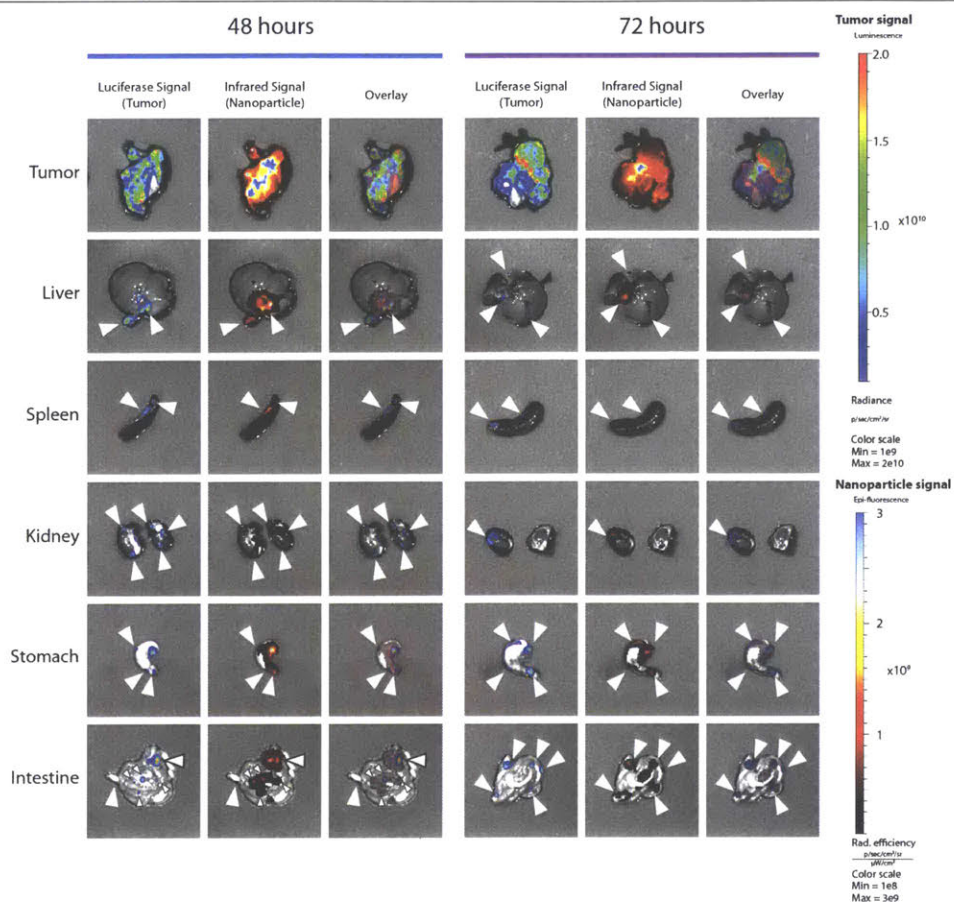
Appendix B Figure 20. DXS-coated LbL NP biodistribution at 48 and 72 hours following IP administration indicates continued co-localization with neoplastic tissue. Luciferase signal from tumor cells and infrared fluorescence from nanoparticles were measured for each organ using an IVIS imaging device. Arrows denote locations of metastases on organs. Signal from the primary tumor appears dimmer at 72 hours which may imply a clearance pathway, although the lack of NP in the liver or spleen would suggest the NPs may be captured somewhere between the IP cavity and the lymphatic drainage into the venous compartment.
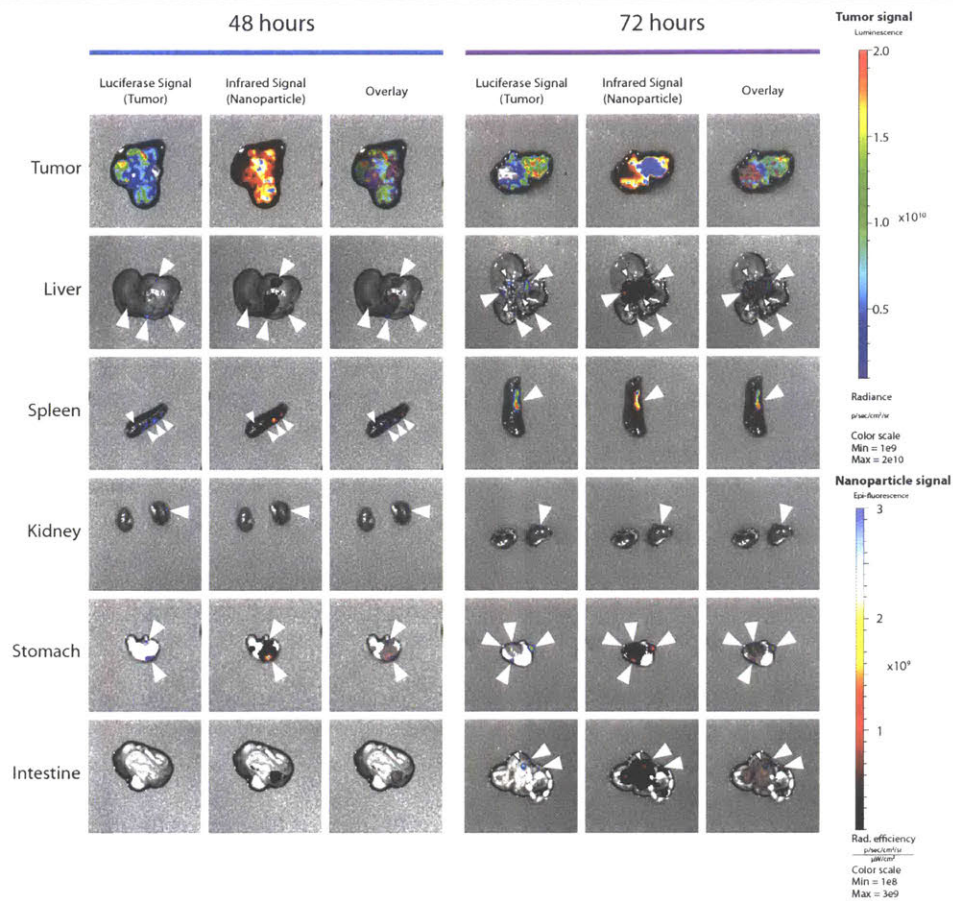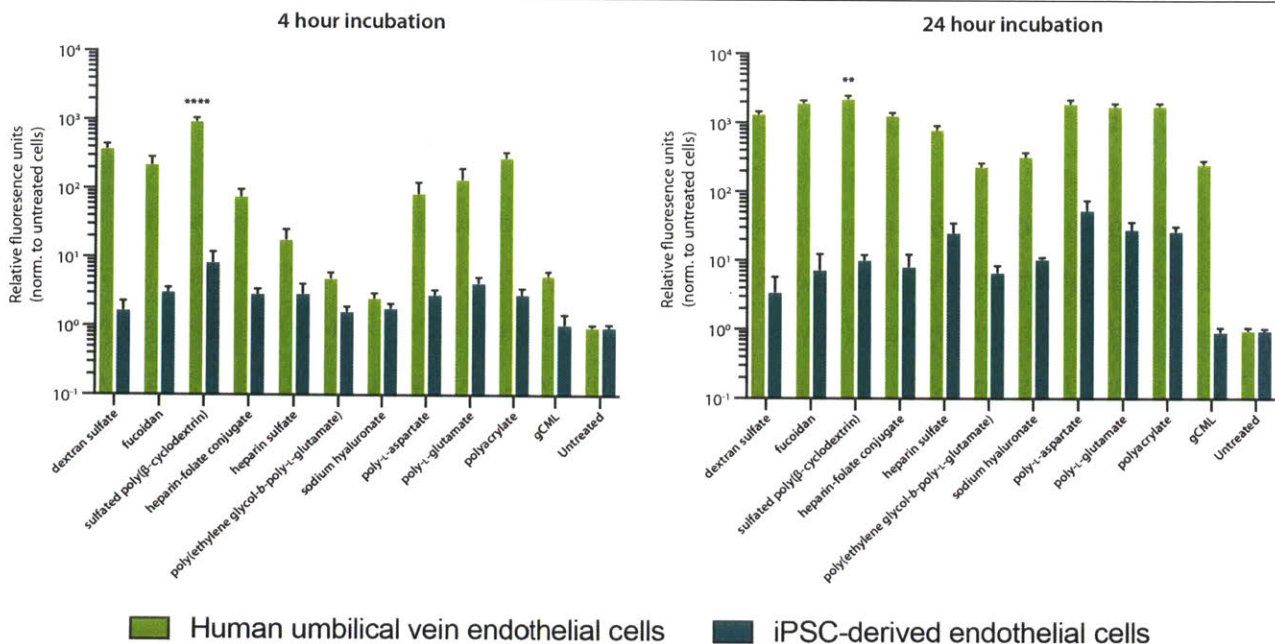
Appendix B Figure 21. PLE-coated LbL NP biodistribution at 48 and 72 hours following IP administration indicates continued co-localization with neoplastic tissue. Luciferase signal from tumor cells and infrared fluorescence from nanoparticles were measured for each organ using an IVIS imaging device. Arrows denote locations of metastases on organs. Some diffuse NP signal in the intestines and stomach is not co-localized with detectable lesions, but the majority of signal appears to co-localize with tumor bioluminescence.
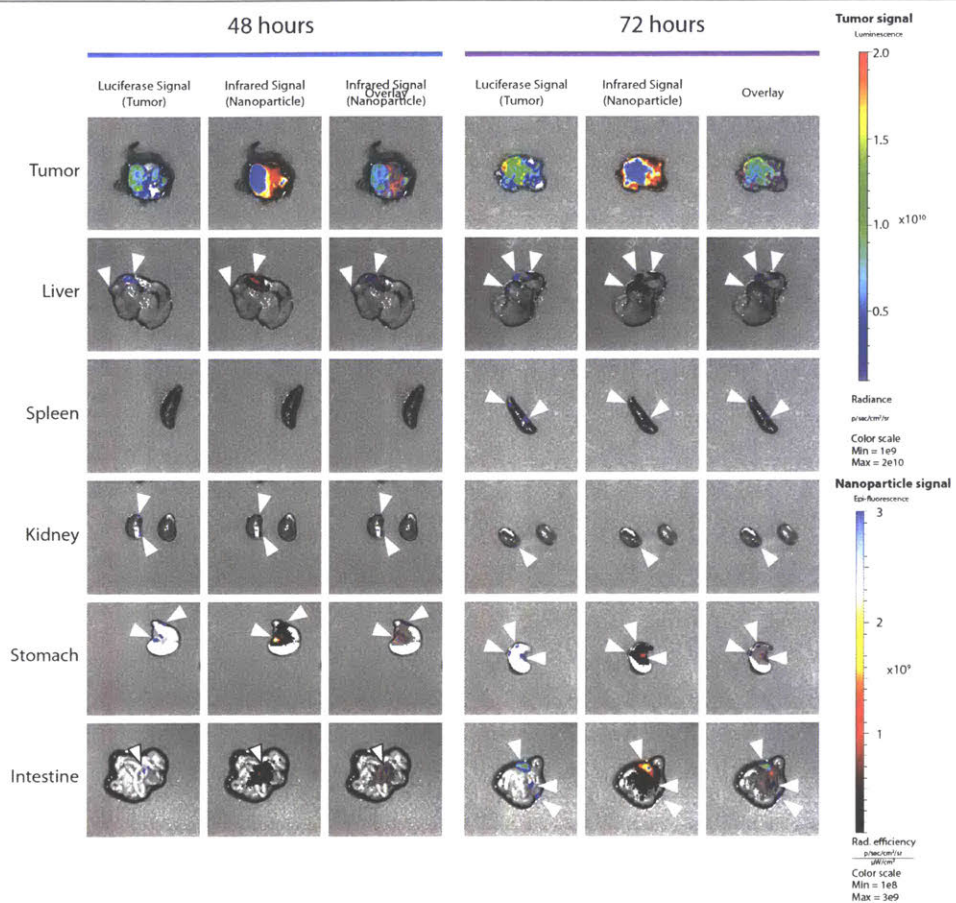
Appendix B Figure 22. PLD-coated LbL NP biodistribution at 48 and 72 hours following IP administration indicates continued co-localization with neoplastic tissue. Luciferase signal from tumor cells and infrared fluorescence from nanoparticles were measured for each organ using an IVIS imaging device. Arrows denote locations of metastases on organs. PLD-coated NPs co-localize with the tumor bioluminescence.
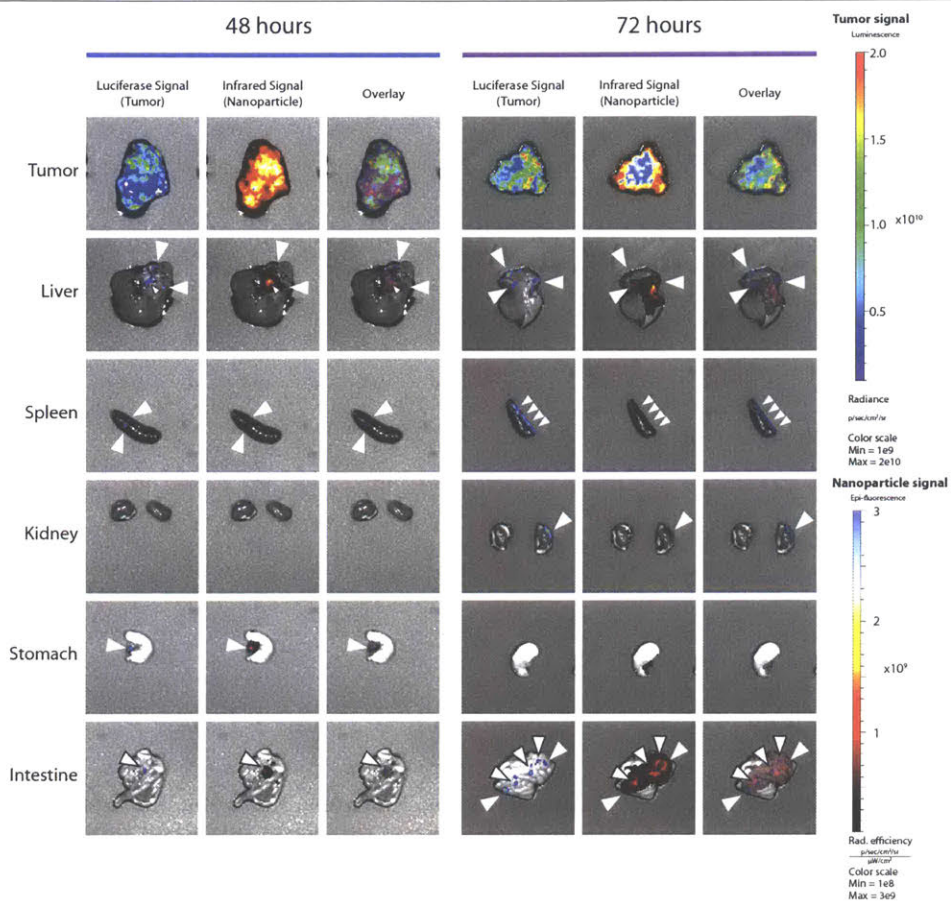
Appendix B Figure 23. HA-coated LbL NP biodistribution at 48 and 72 hours following IP administration indicates continued co-localization with neoplastic tissue. Luciferase signal from tumor cells and infrared fluorescence from nanoparticles were measured for each organ using an IVIS imaging device. Arrows denote locations of metastases on organs. Some diffuse NP signal in the intestines and stomach is not co-localized with detectable lesions, but the majority of signal appears to co-localize with tumor bioluminescence.
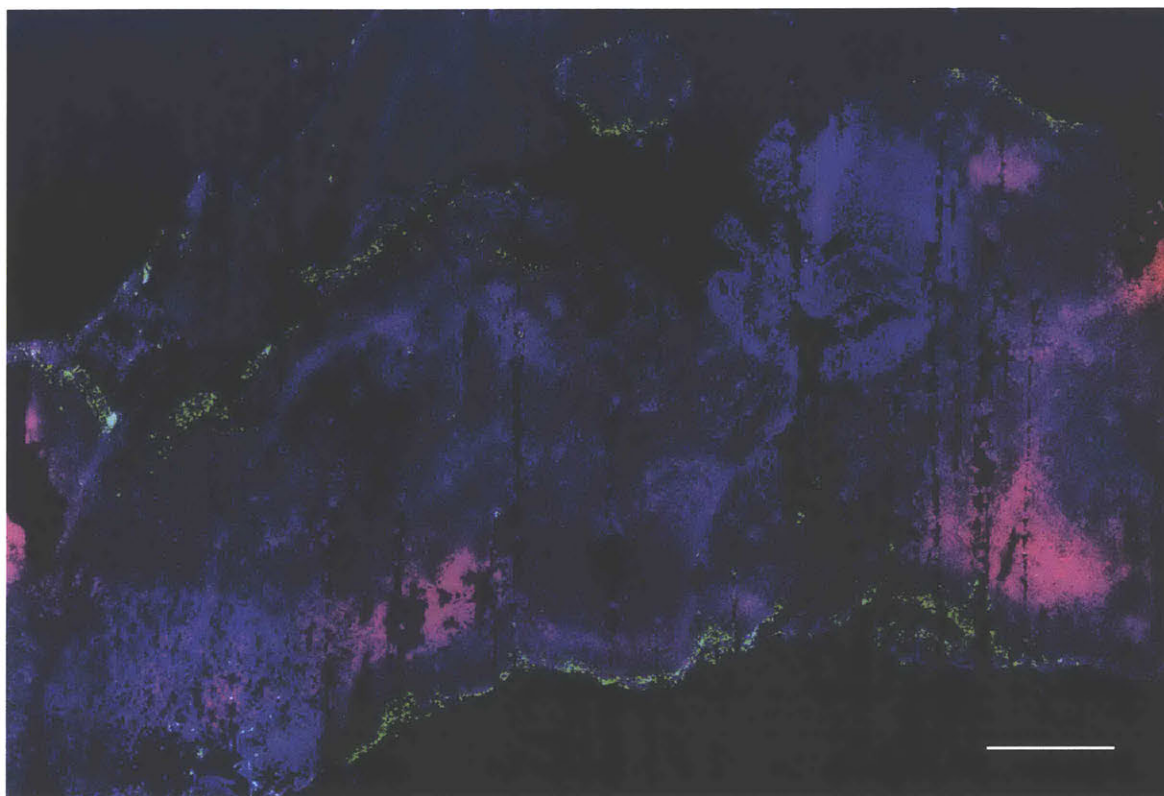
Appendix B Figure 24. Cryohistology of tumor tissue from PLE-NP treated mice indicates how pristine tissues have more NP signal on the periphery than what is seen on the more heavily processed tissues discussed in the main text.

4 hour incubation

24 hour incubation

■ Human umbilical vein endothelial cells   ■ iPSC-derived endothelial cells

Appendix B Figure 25. Sulfated poly(β-cyclodextrin) (SBC)-coated LbL NPs have an affinity towards endothelial cells. SBC-NPs are enriched in iPSC endothelial cells at four hours, although the observation is not statistically significant, and the trend dissipates at 24 hours. But for HUVEC cells, the SBC-NPs are significantly enriched at both 4 and 24-hour time points. Error bars represent SEM and statistical analysis was performed using two-way ANOVA with a Dunnett's post-hoc test (comparing all results to SBC-NP treated cells) and alpha of 0.5.

Endothelial targeting LbL nanoparticles

While SO_3-LbL-NPs were largely unsuccessful at mediating improved uptake in OvCa cells, we noted an intriguing trend with SBC-coated NPs that indicated improved uptake in endothelial cells. We first noted this behavior in the context of iPSC-derived endothelial cells. After 4 hour incubation, all other LbL-NPs had MFR values ranging from 1.1 to 4.4 and no clear correlation between surface chemistry family was apparent. In contrast, SBC-coated NPs had an MFR of 8.7. The effect does not carry to later time points however, and several formulations accumulate better in iPSC-derived endothelial cells at 24 hours. However, we also noted that spleen stromal cells bound SBC-coated NPs more than any other NP both at 4 and 24 hours (MFR of 2.7 and 4.4, respectively). The next best MFR for spleen stroma was fucoidain-coated NP with a MFR of 1.5 at 4 hoursand HA-coated NP with a MFR of 2.0 at 24 hours. Since a significant portion of the stromal compartment is likely endothelial cells, we followed up on this observation by performing a similar uptake experiment on HUVEC cells. Notably, HUVECs had a remarkable capacity for binding all types of nanoparticles almost indiscriminately, but in spite of this we do observe a preference for SBC-coated NPs (**Appendix B Figure 25**). SBC-coated NPs have a MFR of 978.5 at 4 hours, relative to the other LbL NPs that range from 2.6 to 389.4. At 24 hours, SBC-coated NPs retain the highest MFR - 2271.2 - while the rest of the LbL NPs have MFRs ranging from 238.1 to 1977.8. While further study is needed to determine if these differences could lead to meaningful shifts in nanoparticle targeting, we find the results interesting. If SBC-coated NPs can exhibit an endothelial-targeting behavior they could have applications for the development of anti-angiogenesis nanomedicines as well as nanotherapies aimed at treating cardiovascular disease.

Supplemental methods

Human umbilical vein endothelial cells (HUVECs, Lonza), were a kind gift from the Grifith Lab at MIT. They were grown using Lonza EGM-2 Endothelial Cell Growth Medium-2 BulletKit. Patient-derived xenograft (PDX) cell lines were a kind gift from the Brugge Lab at Harvard, and were grown with a homemade media provided by the lab.

For all experiments, these cells were seeded in 96 well plates according to the methods for the flow cytometry binding assay described in the main methods section. HUVEC cells were processed in the same manner described in the main text.

The PDX cells were processed similarly to the splenocytes described in the main text, with one small exception: samples of the PDX spheroid suspension were first taken and preserved for microscopy. Afterwards, the spheroid suspension was pelleted using centrifugation (RCF 300, 5 minutes) and washed. PDX spheroids were incubated in 1x TrypLE Express 30 for 10 minutes. The suspension was then passed 3x through 70 micron and 40 micron cell strainers and 2x through a FACS filter cap (BD). The samples were analyzed using a BD LSR2 cytometer, and detected mCherry signal (produced by the PDX cells) and nanoparticle signal in the FITC channel.

For confocal microscopy of the PDX spheroids, the samples isolated prior to flow analysis were taken and pelleted in FACS tubes (300 RCF, 5 minutes). The cells were resuspended in 300 uL PBS, and then 100 uL of 16% methanol-free formaldehyde (Pierce) was added. The cells were fixed at room temperature for 10 minutes, then washed via centrifugation and resuspended in 300 uL of PBS. The spheroid suspension was then added to chambered coverslips and imaged directly using an Olympus FV1200, as described in the fixed cell imaging methods in the main text.
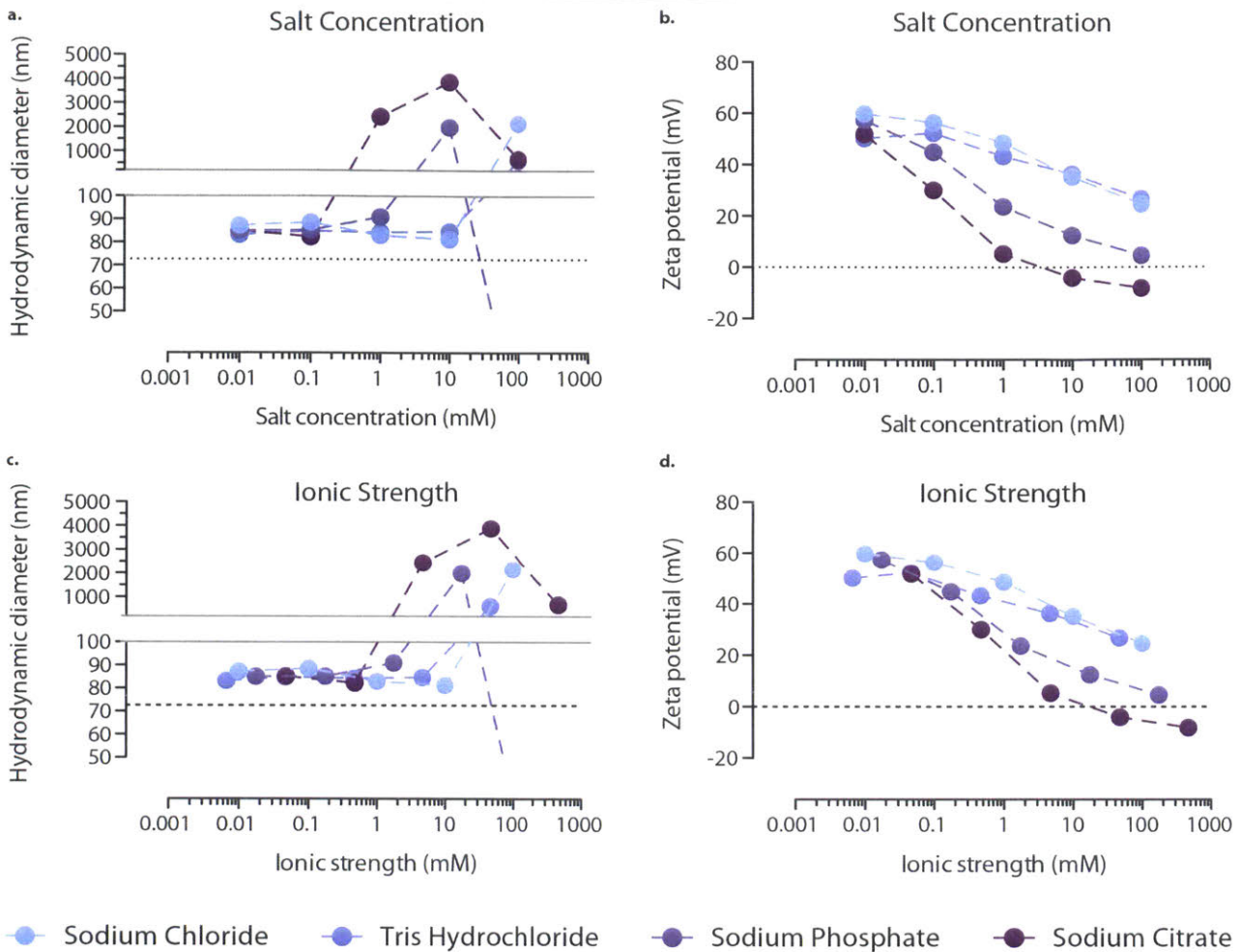
Appendix C

Appendix C.

Supporting information for Chapter 4: *The role of solution conditions in the robust synthesis of layer-by-layer liposomes* is provided here.
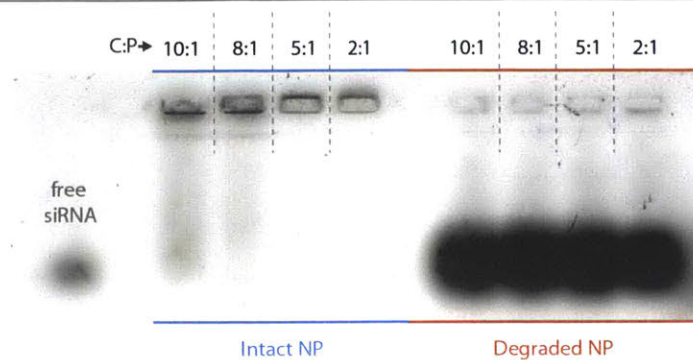
Appendic C Figures

a. Salt Concentration

b. Salt Concentration

c. Ionic Strength

d. Ionic Strength

Legend: Sodium Chloride — Tris Hydrochloride — Sodium Phosphate — Sodium Citrate

Appendix C Figure 1. The salt screen from Figure 1 was replotted to directly compare the impact of different salt species on PLR adsorption onto anionic liposomes. The (a) size and (b) zeta are replotted to demonstrate the impact of salt identity. Salt concentration is not able to completely explain the aggregation and loss of charge seen with the multivalent species. When the data is replotted based on each condition's ionic strength (c-d), the data converges somewhat, but it remains apparent that there is an impact due to valency that is not fully recapitulated by considering ionic strength alone. HEPES is omitted because a straightforward means to calculate ionic strength of a zwitterion was not found. Size and polydispersity data were acquired by dynamic light scattering, and zeta potential data was measured using laser Doppler electrophoresis.
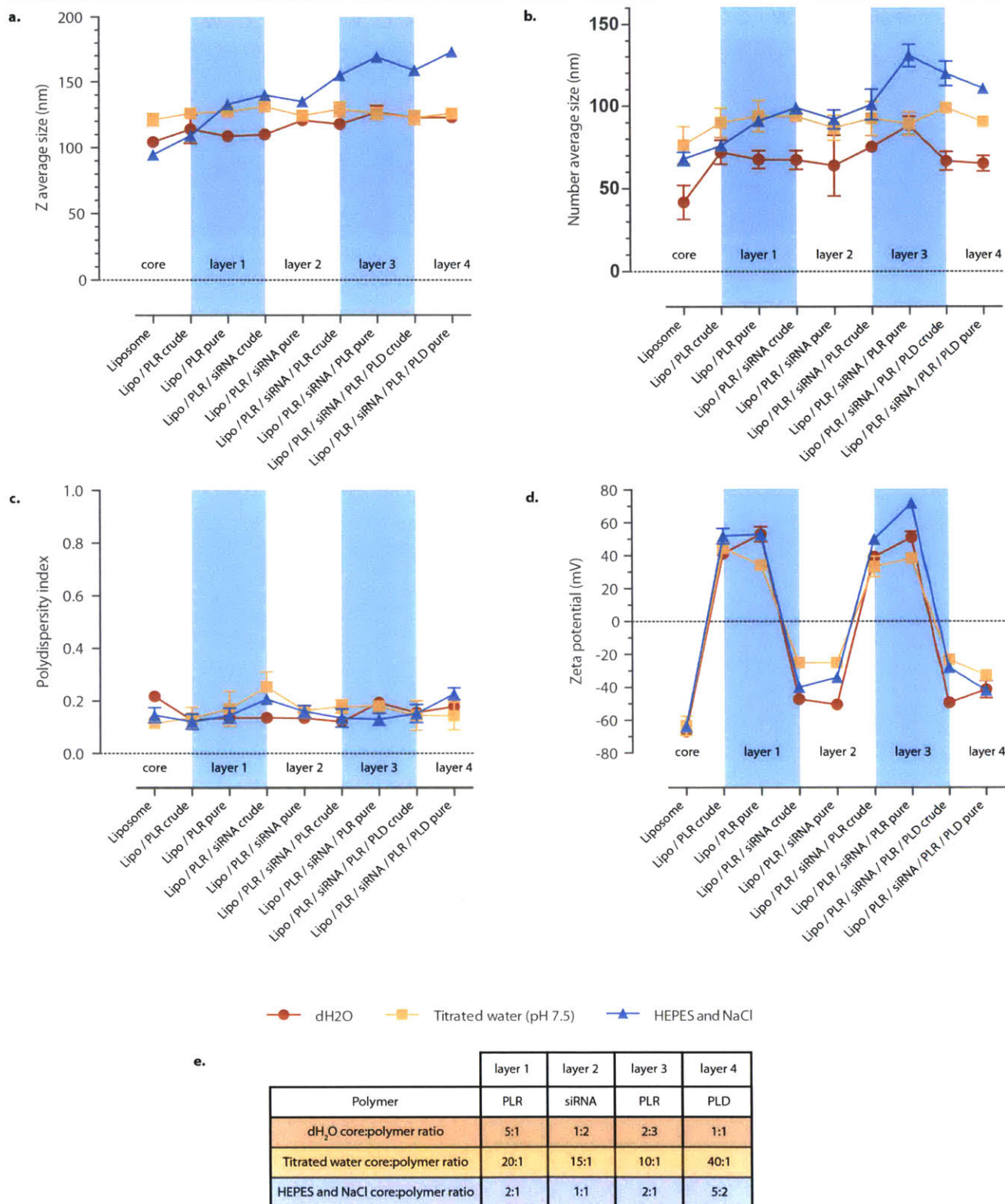
Appendix C Figure 2. Addition of the third layer, composed of poly(L-arginine), does not lead to loss of siRNA from the second layer. In fact, as the optimal C:P ratio is achieved (5:1), the PLR layer shields siRNA from the effects of electrophoresis, which causes partial migration of the siRNA-PLR complexes into the gel for ratios 10:1 and 8:1. Heparin-degraded particles on the right-hand side of the gel readily release the entrapped siRNA into the gel.
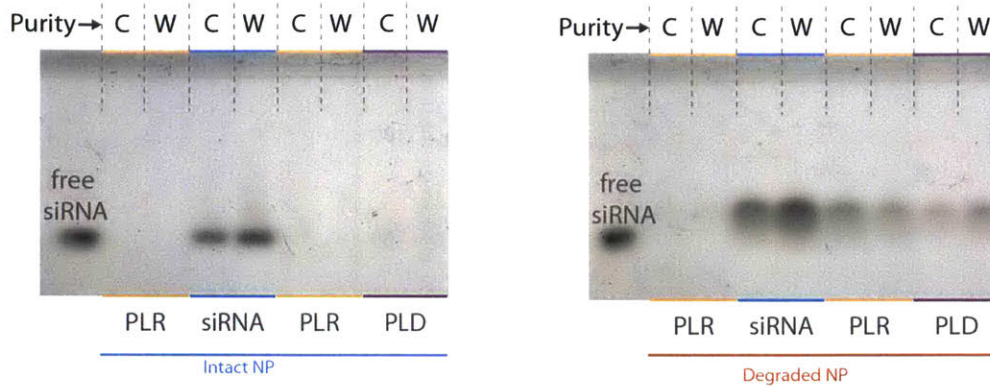
Appendix C Figure 3. Agarose gel of the degraded LbL nanoparticle from 4c, showing that layers 3 and 4 were deposited and purified without additional loss of siRNA due to layering. Some loss of siRNA is reflective of process loss during handling during the additional layering and purification steps.

Legend: ● dH2O ■ Titrated water (pH 7.5) ▲ HEPES and NaCl

e.

	layer 1	layer 2	layer 3	layer 4
Polymer	PLR	siRNA	PLR	PLD
dH$_2$O core:polymer ratio	5:1	1:2	2:3	1:1
Titrated water core:polymer ratio	20:1	15:1	10:1	40:1
HEPES and NaCl core:polymer ratio	2:1	1:1	2:1	5:2

Appendix C Figure 4. The size, uniformity and surface charge properties of LbL liposomes prepared in either deionized water (dH2O), pH 7.5 titrated water (20 µM Na$_2$HPO$_4$), or 25 mM HEPES 20 mM NaCl. The HEPES NaCl condition is buffer exchanged to water during the interlayer purification steps. a) LbL liposomes prepared in the presence of HEPES and NaCl develop thicker layers, producing a steady

increase in z-average hydrodynamic diameter during the synthesis. Formulations prepared without NaCl do not exhibit the same steady growth in size. b) Number average size illustrates the same trend. c) All syntheses generate uniform particles with PDI remaining below 0.025, and d) complete charge conversion during the addition of different layers. e) In order to achieve these stable syntheses, we note that the C:P ratio varies significantly with the different bulk conditions. Size and polydispersity data were acquired by dynamic light scattering, and zeta potential data was measured using laser Doppler electrophoresis. Error bars represent standard deviation of three technical replicates.
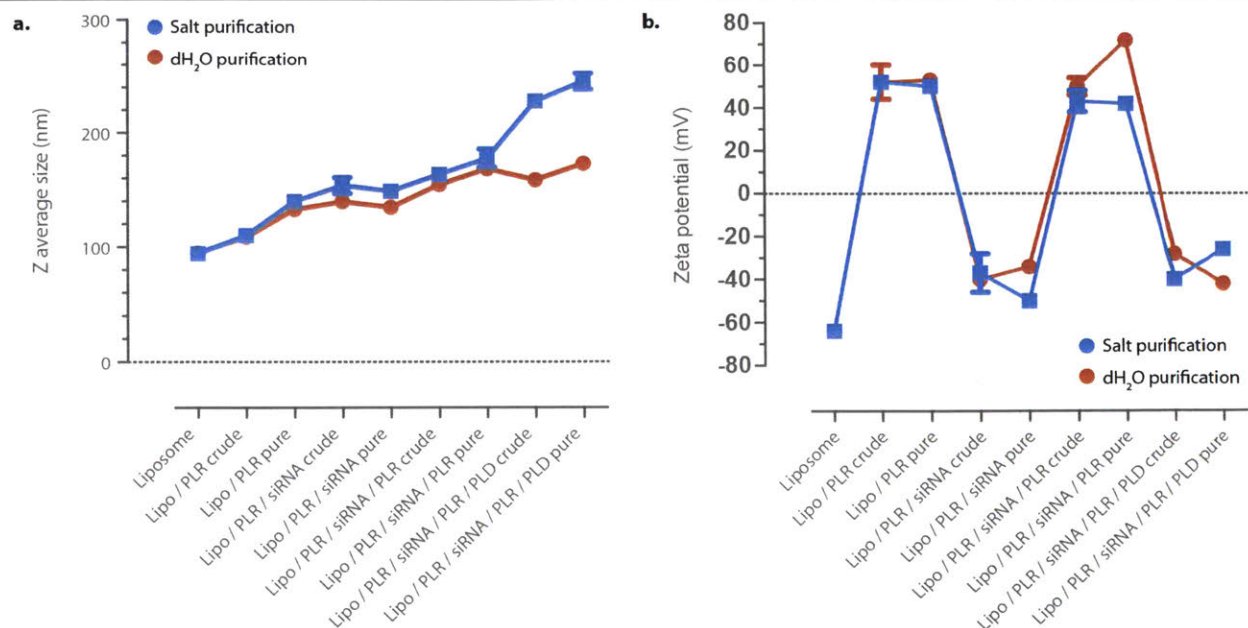
Appendix C Figure 5. Purification bulk conditions can impact nanoparticle size and charge properties. a) Use of salts in the exchange buffer increases Z average hydrodynamic diameter, and may indicate particle bridging or mild aggregation. b) Although C:P ratios were chosen that yielded similar zeta potential in the crude state, purification in salt led to slight decrease in the magnitude of surface charge during the purification of anionic layers, which could be indicative of shedding or rearrangement of the LbL film during purification. Loss of charge could also mediate some of particle aggregation hypothesized in panel a. Size data were acquired by dynamic light scattering, and zeta potential data was measured using laser Doppler electrophoresis. Error bars represent standard deviation of three technical replicates.
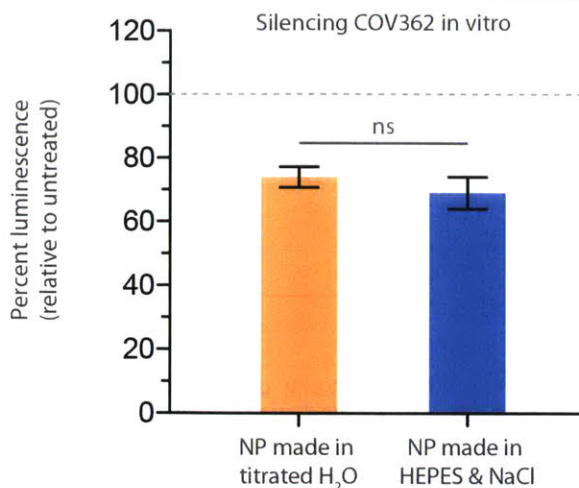
Appendix C Figure 6. Easier to transfect cell lines like COV362 do not exhibit significantly improved knockdown with bulk condition-optimized formulations. COV362 cells were treated with 30 nM siRNA using nanoparticles generated from either pH 7.5 titrated water or the optimized HEPES/NaCl method, and knockdown of the luciferase reporter gene was assayed after 24 hours. Error bars represent the SD of triplicates. All statistical tests were performed using one-way ANOVA (alpha = 0.05), with the Tukey post-test, on PRISM graphing software.
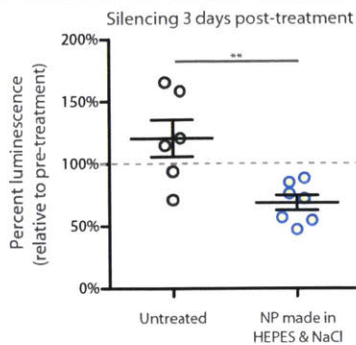
Appendix C Figure 7. Results from siRNA delivery using LbL liposomes prepared using the optimized HEPES/NaCl bulk conditions described in Figures 3 and 4. Subcutaneous flank xenografts of luciferized OVCAR8 cells were treated with 0.5 mg/kg siLuciferase and evaluated periodically for silencing of the reporter gene. These data represent silencing 3 days after injection, and show significant downregulation of the luciferase gene relative to untreated mice. All statistical tests were performed using one-way ANOVA (alpha = 0.05), with the Tukey post-test, on PRISM graphing software.
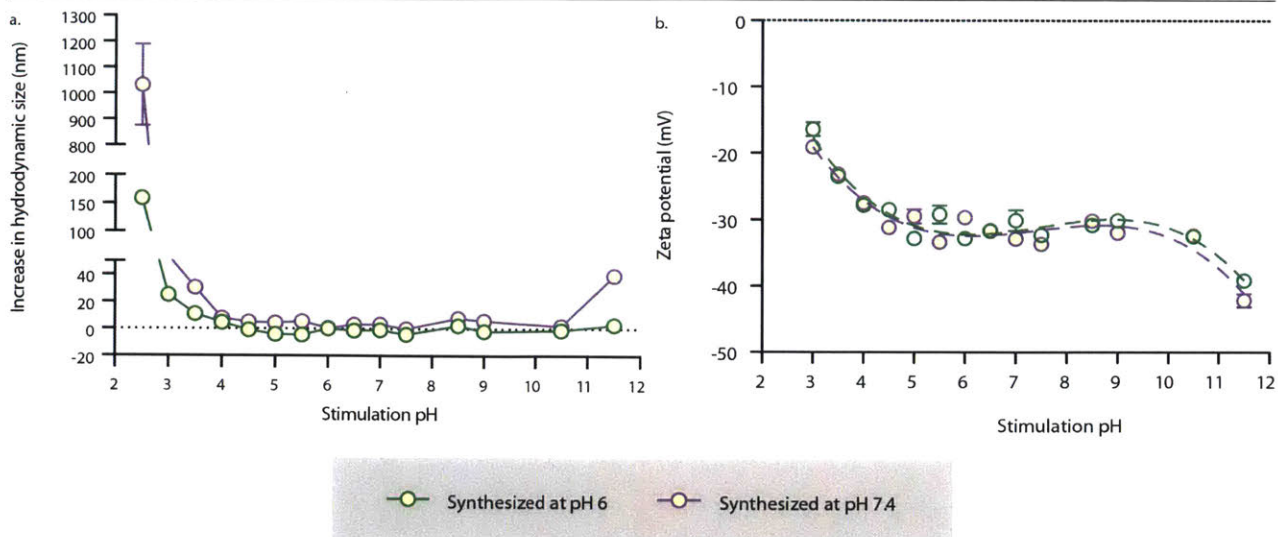
Appendix C Figure 8. LbL nanoparticles (CML/PLR/HA) were synthesized at different pHs and then stimulated to induce swelling via exposure to different pH solutions. a) Nanoparticle prepared at pH 7.4 exhibit swelling behavior at pH 3.5 and 11.5, whereas particles prepared at pH 6 only begin exhibiting a similar degree of swelling at pH 3. b) Both nanoparticles exhibit similar changes in ionization state thoughout this pH range, with the HA-coated particle losing its charge rapidly as the system is protonated at acidic pH.
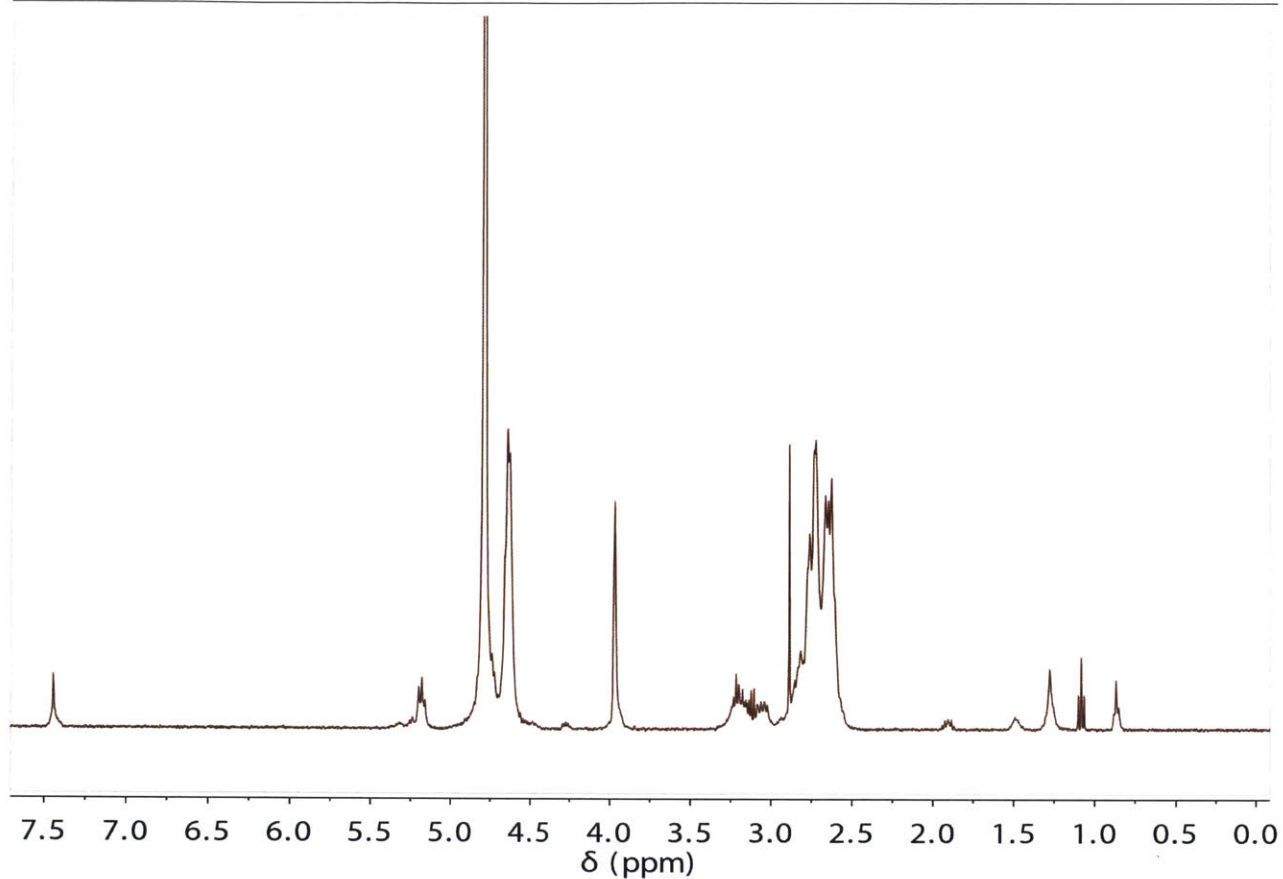
Appendix D

Appendix D.

Supporting information for Chapter 5: *Developing theranostic layer-by-layer nanoparticles through clickable terminal layers* is provided here.
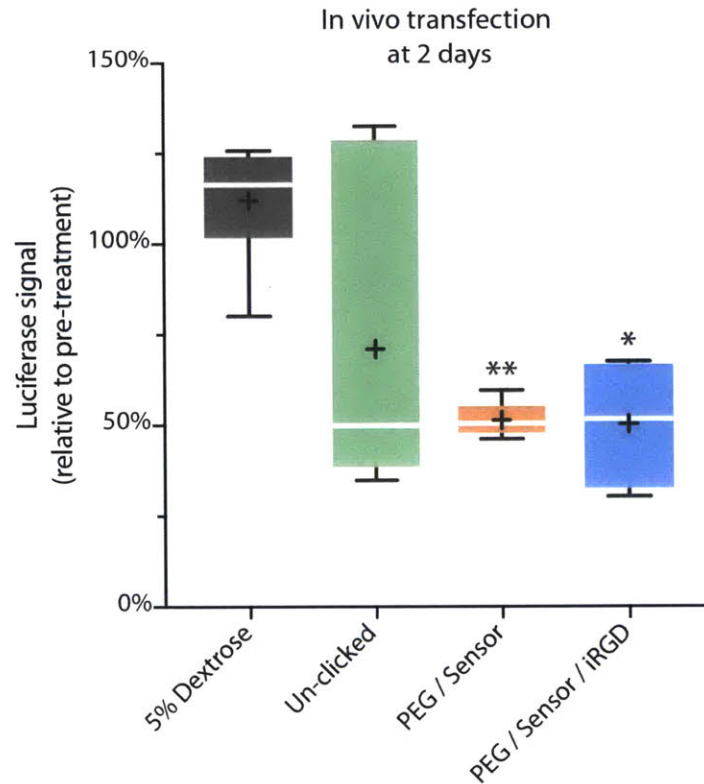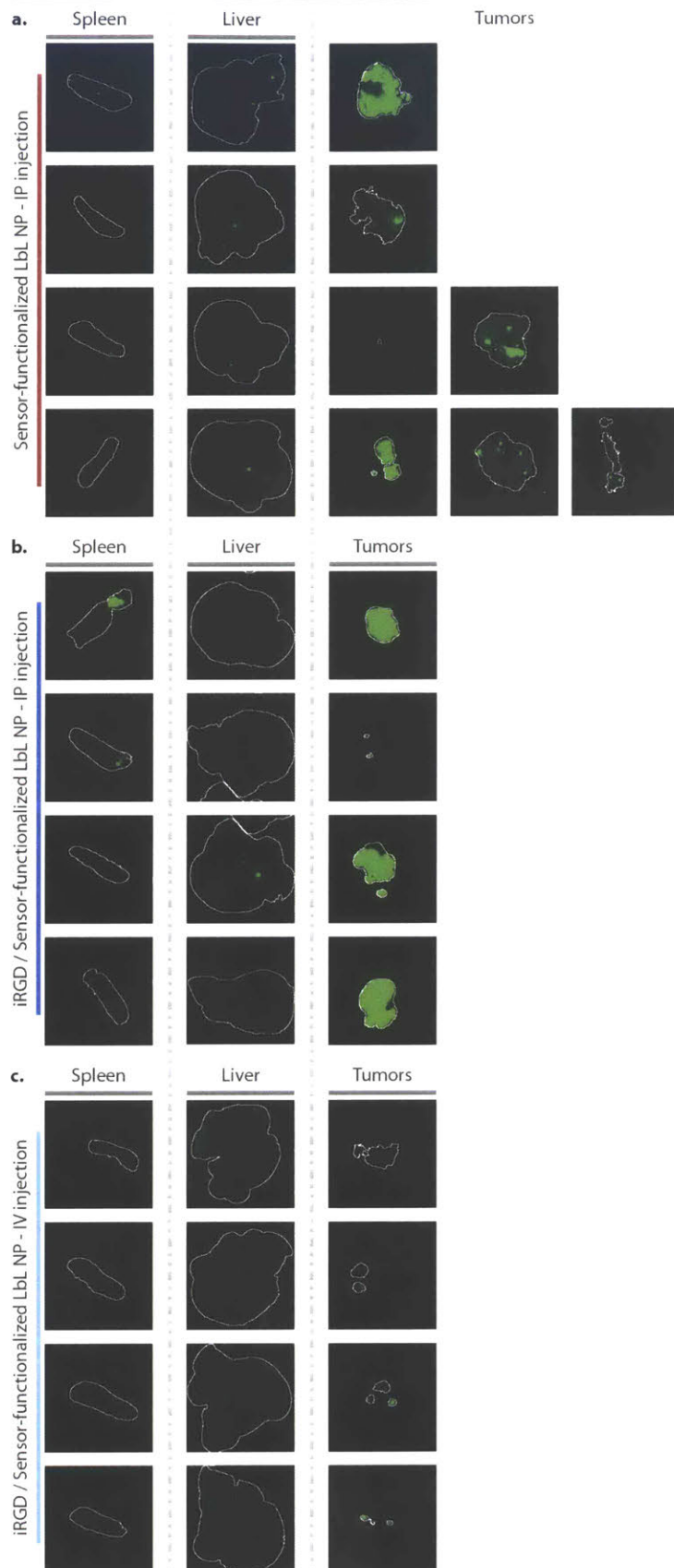
Appendix D Figures

Appendix D Figure 1. NMR trace of propargyl-modified poly-L-aspartate. Peaks: 4.7 is residual solvent, 4.5 is alpha hydrogen, 4.0/3.0 is from propargyl amine, and 2.5-3.0 is side chain. Small peaks are either from solvent initiator or residual salt from the reaction

Appendix D Figure 2. In vivo transfection of flank ovarian cancer model, two days after injection with theranostic LbL NPs. Un-clicked LbL NPs mediate transfection but it is variable at this time point. Meanwhile, both PEG/Sensor and PEG/Sensor/iRGD functionalized LbL NPs mediate transfections, knocking down roughly 50% of luciferase expression on average. The results are statistically significant when compared to the control condition. Statistical analysis was performed with a one-way ANOVA with a Tukey post-hoc test and alpha of 0.05.

Appendix D

Appendix D Figure 3. Spleens, livers, and tumors from mice treated with Cy7-labeled theranostic LbL NP. White outlines denote the region of interest as defined by tissue autofluorescence in the 700 nm channel. Green signal corresponds to fluorescence from LbL liposomes in the 800 nm channel.